

DEVELOPMENT OF THREE WAY CATALYTIC CONVERTER FOR  
AUTOMOTIVE EXHAUST GAS

A THESIS SUBMITTED TO  
THE GRADUATE SCHOOL OF NATURAL AND APPLIED SCIENCES  
OF  
MIDDLE EAST TECHNICAL UNIVERSITY

BY

BİLAL BAYRAM

IN PARTIAL FULFILLMENT OF THE REQUIREMENTS  
FOR  
THE DEGREE OF DOCTOR OF PHILOSOPHY  
IN  
CHEMICAL ENGINEERING

JULY 2021



Approval of the thesis:

**DEVELOPMENT OF THREE WAY CATALYTIC CONVERTER FOR  
AUTOMOTIVE EXHAUST GAS**

submitted by **BİLAL BAYRAM** in partial fulfillment of the requirements for the degree of **Doctor of Philosophy in Chemical Engineering, Middle East Technical University** by,

Prof. Dr. Halil Kalıpçılar  
Dean, Graduate School of **Natural and Applied Sciences**

Prof. Dr. Pınar Çalık  
Head of the Department, **Chemical Engineering**

Prof. Dr. Görkem Külah  
Supervisor, **Chemical Engineering, METU**

Prof. Dr. Işık Önal  
Co-Supervisor, **Chemical Engineering, METU**

**Examining Committee Members:**

Prof. Dr. Emrah Özensoy  
Chemistry, Bilkent University

Prof. Dr. Görkem Külah  
Chemical Engineering, METU

Assoc. Prof. Dr. Alper Uzun  
Chemical and Biological Engineering, Koç University

Assist. Prof. Dr. Bahar İpek Torun  
Chemical Engineering, METU

Assist. Prof. Dr. Gökhan Çelik  
Chemical Engineering, METU

Date: 09.07.2021

**I hereby declare that all information in this document has been obtained and presented in accordance with academic rules and ethical conduct. I also declare that, as required by these rules and conduct, I have fully cited and referenced all material and results that are not original to this work.**

Name, Last name: Bilal Bayram

Signature :

## ABSTRACT

### DEVELOPMENT OF THREE WAY CATALYTIC CONVERTER FOR AUTOMOTIVE EXHAUST GAS

Bayram, Bilal

Doctor of Philosophy, Chemical Engineering

Supervisor: Prof. Dr. Görkem Külah

Co-Supervisor: Prof. Dr. Işık Önal

June 2021, 171 pages

In this study, a novel perovskite-based three-way catalyst ( $\text{LaFe}_{0.57}\text{Co}_{0.37}\text{Pd}_{0.06}\text{O}_3/\text{Ce}_{0.8}\text{Zr}_{0.2}\text{O}_2/\text{Al}_2\text{O}_3$ ) with high performance, thermal stability and  $\text{SO}_2$  poisoning resistance was developed. The performance of the developed catalyst was compared to a standard catalyst based on dispersed metal ( $\text{Pd/Rh}/\text{Ce}_{0.8}\text{Zr}_{0.2}\text{O}_2/\text{Al}_2\text{O}_3$ ). Performance evaluations were carried out in a dynamic activity test system that simulates redox fluctuations in the exhaust of gasoline engines. ICP-OES, BET surface area, X-ray diffraction, TEM-EDX spectroscopy, DRIFTS and CO chemisorption techniques were used for the characterization of catalysts. The performances of the catalysts before aging were obtained close to each other. After hydrothermal aging at 1273 K, perovskite-based catalyst was able to maintain its activity to a great extent. However, there was a serious activity loss in the standard catalyst, and NO and  $\text{C}_3\text{H}_8$  conversions could not exceed 20% even at 600 °C. XRD revealed palladium substitution in the B site of the perovskite structure, which was seen as evidence of thermal stability. The growth of the Pd crystallite size from 3.4 nm to 28.1 nm was evaluated as evidence of the activity loss for standard catalyst. The CO chemisorption findings were also in parallel with the activity test, according

to which the standard catalyst lost 85% and the perovskite-based catalyst lost only 30% CO uptake capacity.

Keywords: Three-way Catalysts, Thermal Stability, Pd-Perovskite, SO<sub>2</sub> Poisoning

## ÖZ

### OTOMOTİV EGZOZ GAZI İÇİN ÜÇ YOLLU KATALİTİK DÖNÜŞTÜRÜCÜ GELİŞTİRİLMESİ

Bayram, Bilal  
Doktora, Kimya Mühendisliği  
Tez Yöneticisi: Prof. Dr. Görkem Külah  
Ortak Tez Yöneticisi: Prof. Dr. Işık Önal

Haziran 2021, 171 sayfa

Bu çalışmada, yüksek performansa, termal kararlılığa ve SO<sub>2</sub> zehirlenmesine karşı dirence sahip, yeni bir perovskit bazlı üç yollu katalizör ( $\text{LaFe}_{0.57}\text{Co}_{0.37}\text{Pd}_{0.06}\text{O}_3/\text{Ce}_{0.8}\text{Zr}_{0.2}\text{O}_2/\text{Al}_2\text{O}_3$ ) geliştirilmiştir. Geliştirilen katalizörün performansı, dağılmış metale (Pd/Rh/  $\text{Ce}_{0.8}\text{Zr}_{0.2}\text{O}_2 / \text{Al}_2\text{O}_3$ ) dayalı standart bir katalizörle karşılaştırıldı. Performans değerlendirmeleri, benzinli motorların egzozlarındaki redoks dalgalanmalarını simüle eden bir dinamik aktivite test sisteminde gerçekleştirildi. Katalizörlerin karakterizasyonu için ICP-OES, BET yüzey alanı, X-ışını kırınımı, TEM-EDX spektroskopisi, DRIFTS ve CO kemisorpsiyon teknikleri kullanılmıştır. Katalizörlerin yaşlanma öncesi performansları birbirine yakın olarak elde edildi. 1273 K'de hidrotermal yaşlanmanın ardından, perovskit bazlı katalizör aktivitesini büyük ölçüde sürdürebildi. Bununla birlikte, standart katalizörde ciddi bir aktivite kaybı tespit edildi, ki NO ve C<sub>3</sub>H<sub>8</sub> dönüşümleri 600 °C'de bile %20'yi geçemedi. XRD, perovskit yapısının B bölgesinde termal stabilitenin kanıtı olarak görülen paladyum ikamesini ortaya çıkardı. Pd kristalit boyutunun 3.4 nm'den 28.1 nm'ye büyümesi, standart katalizör

için aktivite kaybının kanıtı olarak değerlendirildi. CO kemisorpsiyonu, standart katalizörün %85 ve perovskit bazlı katalizörün yalnızca % 30 CO tutma kapasitesini kaybettiği ortaya çıkarmış, bu da performans sonuçları ile paralellik göstermiştir.

Anahtar Kelimeler: Üç Yollu Katalitik Dönüştürücü, Isıl Direnç, Pd-Perovskite, SO<sub>2</sub> Zehirlenmesi



To my family

## ACKNOWLEDGMENTS

I wish to express my sincere gratitude to my supervisors Prof. Dr. Işık Önal and Prof. Dr. Görkem Külâh for their support, guidance and help, in all the possible way, throughout my study. Without their encouragements and practical solutions to problems, I would not have achieved this work with success.

I would like to express my gratitude to all my thesis examining committee members Prof. Dr. Emrah Özensoy, Dr. Bahar İpek, Assoc. Prof. Dr. Alper Uzun, Dr. Gökhan Çelik and Dr. Damla Erođlu for their valuable suggestions for this study.

I would like to especially thank to my wife Esra and my son Demir Ege for their love, patience and support during the study.

Heartfelt thanks to my colleague Barış Erdoğan for his advices and contributions to see the whole picture during the study. I would also thank to Buse Efil for her cooperation during the laboratory studies. Zeynep Buse Şendil's help while completing the work was invaluable, I would like to thank her as well.

I wish to thank to my parents, Selma and Kemal Bayram, my brother Süleyman Bayram, my mother-in-law and my father-in-law Esmâ and Mahmut Demircan for their endless love and encouragement.

The financial support provided by Scientific Research Project Coordination Unit of Middle East Technical University [grant numbers BAP-03-04-2017-007, BAP-07-02-004-224] is gratefully acknowledged.

## TABLE OF CONTENTS

ABSTRACT.....	v
ÖZ.....	vii
ACKNOWLEDGMENTS.....	x
TABLE OF CONTENTS.....	xi
LIST OF TABLES.....	xv
LIST OF FIGURES.....	xvi
LIST OF ABBREVIATIONS.....	xix
LIST OF SYMBOLS.....	xx
1 INTRODUCTION.....	1
1.1 The Principle of Catalysis.....	1
1.2 Three Way Automotive Catalysts.....	3
1.2.1 Exhaust Gases.....	4
1.2.2 Evolution of Gasoline Automotive Catalysts: Regulations, Reactions and Catalyst Compositions.....	6
1.2.3 TWC Catalytic Components and Their Functions on Reaction Mechanisms.....	14
1.3 Perovskites.....	23
1.3.1 Structure and Properties of Perovskites.....	23
1.3.2 Synthesis Techniques of Perovskites.....	26
1.3.3 Redox Properties of Perovskites.....	28
1.3.4 Oxygen Mobility Properties of Perovskites.....	30

1.3.5	Adsorption Properties of Perovskites .....	34
1.3.6	Thermal Stability of Perovskites .....	36
2	LITERATURE REVIEW .....	39
3	EXPERIMENTAL .....	51
3.1	Materials .....	51
3.2	Equipment .....	51
3.3	Catalyst Preparation .....	53
3.3.1	Preparation of Oxygen Storage Powder .....	53
3.3.2	Preparation of Pseudoboehmite .....	53
3.3.3	Impregnation of Metal .....	54
3.3.4	Preparation of Perovskite Powders .....	54
3.3.5	Preparation of Washcoating Slurry .....	55
3.3.6	Monolith Coating .....	57
3.4	Catalyst Characterization .....	57
3.5	Catalyst Activity Test System .....	59
3.5.1	Catalyst Aging .....	61
3.5.2	SO <sub>2</sub> Poisoning of Catalysts .....	62
4	RESULTS AND DISCUSSION .....	63
4.1	Catalysts Tested in the Study .....	63
4.2	Performance and Durability Comparison of C1 and C2 Catalysts .....	65
4.3	Effect of Noble Metal Loading on the Performance and Durability of the Perovskite-based Catalyst .....	80
5	CONCLUSIONS .....	85
	REFERENCES .....	89

APPENDICES .....	115
APPENDIX A .....	115
CATALYST PREPARATION .....	115
A.1 Preparation of Ceria-Zirconia Oxide ( $\text{Ce}_{0.8}\text{Zr}_{0.2}\text{O}_2$ ) .....	115
A.2 Preparation of Pseudoboehmite .....	116
A.3 Metal Impregnation on Ceria-Zirconia Oxide .....	116
A.4 Preparation of C1 Catalyst .....	117
A.5 Preparation of $\text{LaFe}_{0.57}\text{Co}_{0.37}\text{Pd}_{0.06}\text{O}_3$ .....	118
A.6 Preparation of $\text{LaFe}_{0.57}\text{Co}_{0.37}\text{Rh}_{0.06}\text{O}_3$ .....	119
A.7 Preparation of C2 Catalyst .....	120
A.8 Preparation of C3 Catalyst .....	121
A.9 Preparation of C4 Catalyst .....	121
APPENDIX B .....	123
NOBLE METAL LOADING CALCULATION .....	123
APPENDIX C .....	124
MASS FLOW CONTROLLER CALIBRATION .....	124
APPENDIX D .....	129
MASS SPECTROMETER CALIBRATION .....	129
APPENDIX E .....	133
CATALYTIC PERFORMANCE TEST CALCULATIONS .....	133
E.1 Volumetric Gas Flow Rate Determination .....	133
E.2 MFC Flow Rate Calculation .....	133
APPENDIX F .....	135

PERFORMANCES OF PEROVSKITE BASED CATALYST WITHOUT NOBLE METAL LOADINGS.....	135
F.1 Performance and Characterization of $\text{LaFe}_{0.6}\text{Co}_{0.4}\text{O}_3$ Catalyst.....	135
F.2 Performance and Characterization of $\text{LaFe}_{0.57}\text{Co}_{0.37}\text{Mn}_{0.06}\text{O}_3$ Catalyst..	137
F.3 Performance and Characterization of $\text{LaFe}_{0.57}\text{Co}_{0.37}\text{Ru}_{0.06}\text{O}_3$ Catalyst...	138
APPENDIX G .....	141
PERFORMANCES CURVES OF THE TESTED CATALYSTS.....	141
G.1 Performances Curves of fresh C1 Catalyst .....	141
G.2 Performances Curves of fresh C2 Catalyst .....	144
G.3 Performances Curves of fresh C3 Catalyst .....	146
G.4 Performances Curves of fresh C4 Catalyst .....	149
G.5 Performances Curves of Hydrothermally Aged C1 Catalyst.....	151
G.6 Performances Curves of Hydrothermally Aged C2 Catalyst.....	154
G.7 Performances Curves of Hydrothermally Aged C3 Catalyst.....	156
G.8 Performances Curves of Hydrothermally Aged C4 Catalyst.....	159
G.9 Performances Curves of $\text{SO}_2$ Poisoned C1 Catalyst.....	161
G.10 Performances Curves of $\text{SO}_2$ Poisoned C2 Catalyst .....	163
G.11 Performances Curves of $\text{SO}_2$ Poisoned C3 Catalyst .....	166
G.12 Performances Curves of $\text{SO}_2$ Poisoned C4 Catalyst .....	168
CURRICULUM VITAE .....	171

## LIST OF TABLES

### TABLES

Table 1.1 CO, HC and NO <sub>x</sub> emission limits for United States [5,14,30,38,39].....	7
Table 3.1 Operational Parameters for Performance Test System .....	60
Table 4.1. Nominal dry based composition of the catalysts studied.....	64
Table 4.2. ICP-OES analysis: measured noble metal concentrations of fresh and aged catalysts. ....	68
Table 4.3. Textural properties of fresh and hydrothermally aged catalysts.....	69
Table 4.4. Total CO uptake for tested catalyst samples.....	77

## LIST OF FIGURES

### FIGURES

Figure 1.1. Catalyzed and uncatalyzed reaction pathways for a heterogeneous catalytic reaction [3].	2
Figure 1.2 Four-time stroke engine a) intake of fuel and air, b) compression, c) spark and combustion d) exhaust. Adapted from ref [12].	5
Figure 1.3 History of tightening of exhaust emission limits [44].	7
Figure 1.4 Air/fuel ratio and stoichiometry [21]	11
Figure 1.5 EPA FTP-75 exhaust test procedure including cold start [93].	13
Figure 1.6 EPA SCO3 exhaust test procedure with air condition system [93].	14
Figure 1.7 An illustration of a catalytic converter that is packed within a stainless-steel container [12,42].	15
Figure 1.8 TWC position in a vehicle. [12].	15
Figure 1.9 Reactant and product concentrations as a function of temperature for NO reduction reactions over Pd/SiO <sub>2</sub> . (A) 2000 ppm NO+1000 ppm H <sub>2</sub> +N <sub>2</sub> balance. (B) 2900 ppm NO+3450 ppm CO+N <sub>2</sub> balance [121].	20
Figure 1.10. Structure of ABO <sub>3</sub> type perovskite [150,155].	24
Figure 1.11 Orthorhombic (a) and rhombohedral (b) distortions of the perovskite [150].	25
Figure 1.12. A) Reduction and reoxidation of LaCoO <sub>3</sub> indicated temperatures. B Temperature programmed reduction of LaCoO <sub>3</sub> [193]	29
Figure 1.13 TPD spectra of O <sub>2</sub> from sample La <sub>0.99</sub> Co <sub>0.86</sub> Fe <sub>0.15</sub> O <sub>3-δ</sub> calcined at various temperatures [178].	31
Figure 1.14 TPD curves of oxygen from La <sub>1-x</sub> Sr <sub>x</sub> CoO <sub>3</sub> [197].	32
Figure 1.15 Scheme of oxygen Exchange on LaCoO <sub>3</sub> [216].	33
Figure 1.16 Extent of total (open circles) and reversible (filled circles) oxygen adsorption on clean LaMO <sub>3</sub> surfaces [226].	36



Figure 2.1 Catalytic oxidation of H <sub>2</sub> , CO and CH <sub>4</sub> over LaMnO <sub>3</sub> and LaCoO <sub>3</sub> . Same concentrations of H <sub>2</sub> , CO and CH <sub>4</sub> (1.5%) + 17.6% O <sub>2</sub> + 4.1% CO <sub>2</sub> + 1.5% H <sub>2</sub> O [147].	41
Figure 2.2 CO oxidation over La <sub>1-x</sub> Ce <sub>x</sub> MnO <sub>3</sub> perovskite catalysts. Reaction conditions: 1% CO + 1% O <sub>2</sub> + 98% He. [165]	42
Figure 2.3 NO conversion to N <sub>2</sub> on powder La <sub>0.8</sub> Sr <sub>0.2</sub> Fe <sub>0.9</sub> Pd <sub>0.1</sub> O <sub>3</sub> : (A) 1000 ppmv NO, 4000 ppmv H <sub>2</sub> , He balance and (B) 1000 ppmv NO, 10.000 ppmv H <sub>2</sub> , 5% O <sub>2</sub> , He balance [254].	45
Figure 3.1 CO Pulse Chemisorption setup	59
Figure 3.2. Schematic representation of TWC performance test system.	60
Figure 3.3. Catalyst aging system.	62
Figure 4.1 Fresh performance comparison of C1 and C2 catalysts.	66
Figure 4.2. Performance comparison of hydrothermally aged C1 and C2 catalysts.	67
Figure 4.3. XRD pattern of fresh and aged C1 catalyst. (a: Ce <sub>0.8</sub> Zr <sub>0.2</sub> O <sub>2</sub> b: $\gamma$ -Al <sub>2</sub> O <sub>3</sub> c: delta-Al <sub>2</sub> O <sub>3</sub> ).	70
Figure 4.4. XRD pattern of fresh and aged C2 catalyst. (a: LaFe <sub>0.57</sub> Co <sub>0.37</sub> Pd <sub>0.06</sub> O <sub>3</sub> b: Ce <sub>0.8</sub> Zr <sub>0.2</sub> O <sub>2</sub> c: $\gamma$ -Al <sub>2</sub> O <sub>3</sub> ).	71
Figure 4.5 XRD patterns of LaCoO <sub>3</sub> , LaFe <sub>0.6</sub> Co <sub>0.4</sub> O <sub>3</sub> and LaFe <sub>0.57</sub> Co <sub>0.37</sub> Pd <sub>0.06</sub> O <sub>3</sub> structures.	72
Figure 4.6. TEM Image and EDX pattern for the marked point for fresh C1 catalyst.	73
Figure 4.7. TEM Image and EDX pattern for the marked point for hydrothermally aged C1 catalyst.	73
Figure 4.8. TEM Image and EDX pattern for the marked point for fresh C2 catalyst.	74
Figure 4.9. TEM Image and EDX pattern for the marked point for hydrothermally aged C2 catalyst.	74
Figure 4.10. Performance comparison of SO <sub>2</sub> poisoned C1 and C2 catalysts.	75

Figure 4.11. CO pulse chemisorption graph of fresh C1 (a), hydrothermally aged C1 (b), SO <sub>2</sub> poisoned C1 (c), fresh C2 (d), hydrothermally aged C2 (e), SO <sub>2</sub> poisoned C2 (f) catalyst samples. ....	76
Figure 4.12. DRIFTS Absorbance Spectra for Fresh and SO <sub>2</sub> Poisoned C1 catalyst sample. ....	79
Figure 4.13. DRIFTS absorbance spectra for fresh and SO <sub>2</sub> -poisoned C2 catalyst samples. ....	80
Figure 4.14. Fresh performance comparison of C1, C2, C3, C4 catalysts. ....	81
Figure 4.15. Performance comparison of C1, C2, C3, C4 catalysts after hydrothermal aging. ....	82
Figure 4.16. Performance comparison of C1, C2, C3, C4 catalysts after SO <sub>2</sub> poisoning. ....	83

## LIST OF ABBREVIATIONS

### ABBREVIATIONS

A/F	Air to Fuel Ratio
g	Gram
rpm	Revolution per minute
Hr.	Hour
AO	Aluminum Oxide
CZO	Cerium Zirconium Oxide
GHSV	Gas Hourly Space Velocity
HC	Hydrocarbon
MFC	Mass Flow Controller
MS	Mass Spectrometer
NO <sub>x</sub>	Nitrogen Oxides
OSC	Oxygen Storage Capacity
TWC	Three Way Catalyst
m/z	Mass-to-charge ratio

## LIST OF SYMBOLS

### SYMBOLS

<b>Symbol</b>	<b>Definition</b>	<b>Units</b>
T	Temperature	°C
T <sub>50</sub>	Light-off Temperature	°C
V <sub>eff</sub>	Effective Volume	cm <sup>3</sup>
γ	Gamma phase	-
v	Flow rate	ml/min

## **CHAPTER 1**

### **INTRODUCTION**

This chapter gives general information related to the catalysis area by underlining the three-way catalysis (TWC) and its applications. Following that, properties, structure and characteristics of perovskite systems are discussed.

#### **1.1 The Principle of Catalysis**

Catalysis technology allows us to produce many products that can be difficult or expensive to manufacture. In addition to production processes, catalysis also plays a vital role in controlling environmental pollution [1].

Catalysts help to reduce free energy of activation of a reaction by changing the reaction pathway [2]. If alternative routes exist, a catalyst can enhance product selectivity by enhancing just one of the competing reaction sequences, also it can increase the reaction rate or enable the reaction at lower temperature[3]. The primary effect of a catalyst on a chemical reaction is to increase its rate coefficient, without being consumed in the process [3].

In catalysis, there are two fields that can be distinguished, homogeneous and heterogeneous catalysis [3]. In homogenous catalysis, both the reactant and catalyst are in the same phase and that brings about the ease of electronic and steric properties control of the catalysts [3]. Therefore, activity and selectivity obtained in this field of catalysis are better compared to that of in heterogeneous catalysis [3]. They are mainly used in small batch reaction processes that have demands for

pure and selective products, for instance, in the pharmaceutical industry [3]. In heterogeneous catalysis, catalysts are not in the same physical state as the reactants [4–8]. For a gas-solid system, shown in Figure 1.1, the reaction happens on the surface provided by the catalyst [1]. It attracts the reactant molecules on particular centers of its surface where interfaces between the catalyst and the reactant molecules exist [9]. Multiple catalytic active sites usually coexist on the surface of the support, therefore the structural characterization monitored by most of the spectroscopic techniques give insight into the average surface structure [8,10,11]. The strength of heterogeneous catalysts is in the ease of catalyst recovery and product separation [1,3]. Due to this fact, heterogeneous catalysis is extensively preferred in the petrochemical industry and in large-scale production of base chemicals [3].

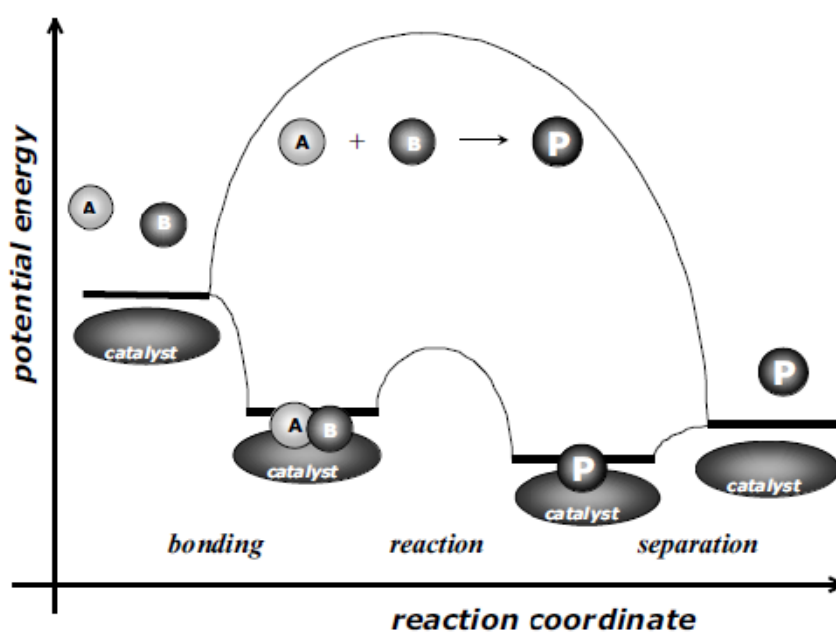


Figure 1.1. Catalyzed and uncatalyzed reaction pathways for a heterogeneous catalytic reaction [3].

Resistances occurring in the transport of reactants and products between the solid surface and the gas system limits the reaction rate in heterogeneous catalytic reactions [8]. Therefore, heterogeneous catalysis research necessitates a deep knowledge of transport phenomena and surface chemistry [3].

Heterogeneous catalysts are extensively used in everyday life for the removal of pollutants from automobile exhausts [8,12]. A gasoline engine exhaust gas contains numerous harmful compounds such as nitrogen oxides ( $\text{NO}_x$ ), carbon monoxide (CO) and unburnt hydrocarbons (HC) [1,5,6,8,12,13]. Because of the expanded interest for low-emission vehicles, most automobiles are at present provided with a three-way catalytic (TWC) exhaust system for concurrent abatement of CO,  $\text{NO}_x$ , HC [12].

## **1.2 Three Way Automotive Catalysts**

Gasoline-powered passenger cars are known to emit hydrocarbon (HC), carbon monoxide (CO) and nitrogen oxides ( $\text{NO}_x$ ) compounds that are harmful to the environment and human health [14–18]. This issue began to pose a critical problem in the mid-20th century [2,12,18,19]. For the first time in 1970, the "Clean Air Act" regulation aimed at reducing these harmful compounds started to be implemented in the US [6,12,18]. In parallel with this regulation, catalytic converters were used in automobiles for the first time in 1975 [5,19,20]. Requirements for the first converters were 90% CO and HC, 50% NO conversion and 50 000 mil endurance [6,21].  $\text{NO}_x$  reduction was at first achieved non-catalytically by a mechanical framework called exhaust gas recirculation (EGR) [12,14,21,22]. A controlled sum of engine effluent gas, rich in  $\text{H}_2\text{O}$ ,  $\text{CO}_2$  and  $\text{N}_2$ , was fed back into the engine upstream, in this manner expanding the heat capacity and bringing down the

elevated temperature accomplished, driving to a diminish in NO<sub>x</sub> formation from the N<sub>2</sub> and O<sub>2</sub> reaction [5,12,16,23]. This was adequate for meeting the NO<sub>x</sub> regulations according to the 1975 emission standard [21]. This approach was supplanted by the appearance of three-way catalysis (TWC), with which NO<sub>x</sub>, CO and HC conversions greater than 90% were accomplished [6,8,12]. In this section details of exhaust gases, reaction mechanisms taking place on a TWC and legislative limits for pollutant emissions are explained.

### **1.2.1 Exhaust Gases**

Gasoline is a refined product of petroleum comprising of a blend of hydrocarbons, added substances, and blending agents [24–26]. The composition of gasolines changes broadly, depending on the crude oils utilized, the refinery facilities and the market demand dependent mostly on climatic conditions [24]. The commonplace composition of gasoline hydrocarbons (by volume) is: 4-8% alkanes; 2-5% alkenes; 25-40% isoalkanes; 3-7% cycloalkanes; 1-4% cycloalkenes; and 20-50% total aromatics (0.5-2.5% benzene) [24,25]. The gasoline blend is a homogeneous mixture of hydrocarbons having 4 to 12 carbon atoms (C<sub>4</sub> to C<sub>12</sub>) [24]. Proportions of C<sub>4</sub>, C<sub>5</sub>, C<sub>6</sub>, C<sub>7</sub>, C<sub>8</sub> and C<sub>9</sub>-C<sub>12</sub> in gasoline are 2%, 20-25%, 30-35%, 10-15%, 11-15% and 10-20% by weight, respectively [24,25].

Gasoline engines, spark-ignited engines, rely on the fuel combustion to produce power [12,13,27,28]. Spark-ignited engines operate according to Otto cycle, in which air and gasoline mixture burn inside the internal combustion engine and the volume of the cylinder remains constant in quasi-static manner [23,29]. Volumetric compression ratio remains low and constant for gasoline engines [13,23]. In a four-time stroke gasoline engine, as can be seen in Figure 1.2, the first step is air and fuel injection [12,30]. It is followed by volumetric compression, which is low enough compared to that of Diesel engine [12,30]. Combustion takes place at the



third step in constant volume in which the piston does not move until the combustion ends [12,30]. Finally, a temperature increase within the system is used to move the piston [12,30].

For gasoline engines, stoichiometric weight-based air to fuel ratio (A/F) is 14.7 and the molar ratio at this level is denoted as  $\lambda=1$  [2,6,12,17,21,31]. Stoichiometry has a significant effect on fuel efficiency and exhaust composition [2,6,12,17,21].

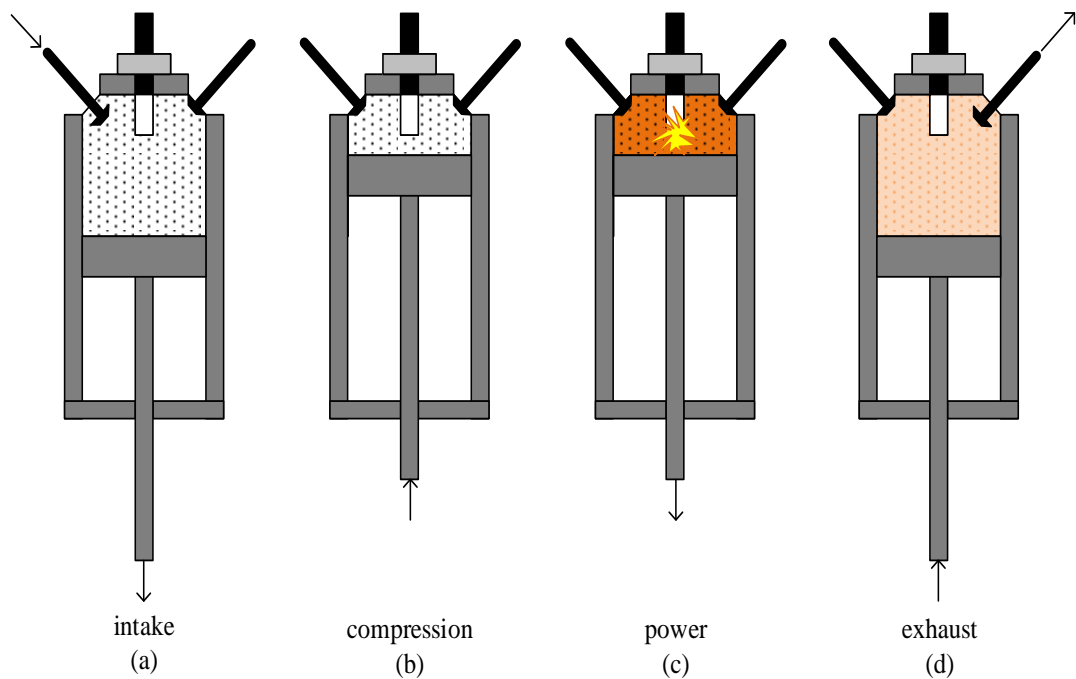


Figure 1.2 Four-time stroke engine a) intake of fuel and air, b) compression, c) spark and combustion d) exhaust. Adapted from ref [12].

Engine exhaust gases are complicated mixtures and directly affected by factors such as acceleration/deceleration, start-up, urban use, intercity use and fuel content [5,12,32]. Total hydrocarbon content varies between 500 to 5000 ppm. Hydrocarbon types are 30-40% aromatics, 20-30% olefins, 25-35% alkanes and a small amount oxygenates (CHO) [21,24,33]. CO content can vary between 1000-60000 ppm. NO<sub>x</sub> content can vary between 100 and 4000 ppm [2,12,32,34]. Depending on the fuel type, SO<sub>2</sub> content can be between 15-60 ppm [12,35–37]. O<sub>2</sub> is in continuous oscillation between 2000 and 20000 ppm. CO<sub>2</sub> is around 10-15% [12,34]. H<sub>2</sub>O content is about 10% [12,34]. Finally, nitrogen gas provides the balance of the mixture [5,12].

### **1.2.2 Evolution of Gasoline Automotive Catalysts: Regulations, Reactions and Catalyst Compositions**

In this section, how the three-way catalysts have evolved from the time they were first applied to the present day and related developments in the catalyst content and reactions on the catalyst will be explained. In addition to these, with the state of the art achieved today and the expected innovations / additional constraints in the future, the direction in which the technology will evolve will be mentioned.

Persistent tightening of regulations is the most important factor within the advancement of automotive catalysts, as can be seen in Figure 1.3 and Table 1.1 [21,26,38–40]. In 1970, “Clean Air Act” regulation in the United States was based only on 90% HC and 90% CO oxidations [5,6,13,16,18,21,41]. It has been found that the most active and stable catalysts to achieve mentioned oxidations are platinum and palladium, as shown in equations 1 and 2 [5,18,42,43].

## The Road to Cleaner Cars...

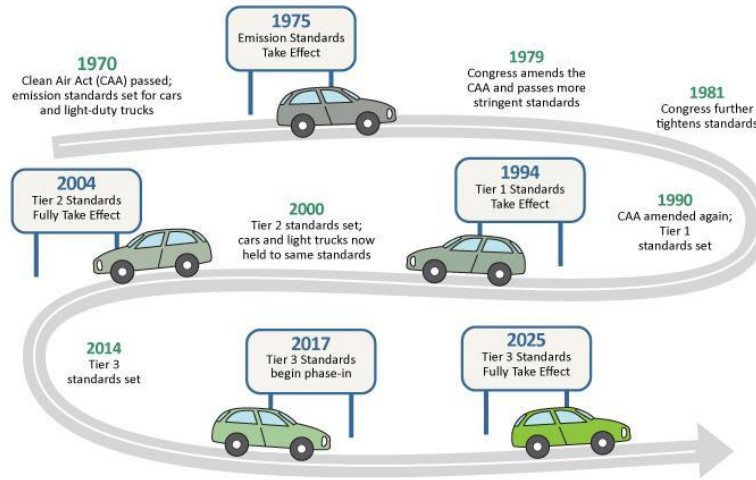
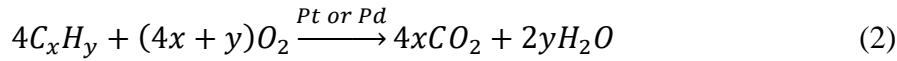


Figure 1.3 History of tightening of exhaust emission limits [44].

Table 1.1 CO, HC and NO<sub>x</sub> emission limits for United States [5,14,26,38,39]

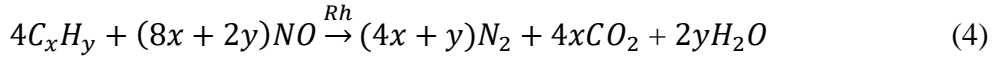
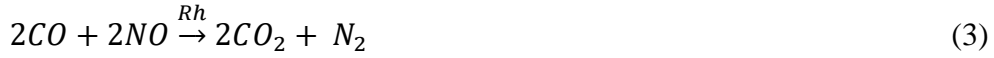
Year	Emission Limit in US (mg/mile)		
	CO	HC	NO <sub>x</sub>
1972 (Clean Air Act)	39000	3200	3200
1975 (Congress amend)	9000	900	2000
1980 (Congress amend)	8000	410	1000
1993-2003 (Tier 1)	3400	250	400
2003-2016 (Tier 2)	2100	55	40
2016-2025 (Tier 3)	1000	30	30



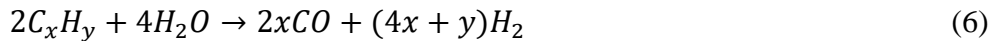
For NO conversion, 50% conversion was found to be sufficient by applying non-catalytic EGR technology [2,6,12,21]. With this method, some of the combustion gases coming out of the engine were fed back to the engine inlet, and the formation of NO gas resulting from the reaction of N<sub>2</sub> and O<sub>2</sub> was reduced by reducing the temperatures formed in the cylinder [6,21,45].

The regulation, which was later put into effect in 1975, required improvements in both engine, fuel and catalyst technology. Tetraethyl lead (TEL), which was used as an anti-knocking agent, was removed from the gasoline content due to extreme poisoning effect of Pb on catalysts [5,16,23,46,47]. It was substituted by organic additive methyl tert-butyl ether (MTBE) [5,6,21]. Following this composition change, engines with lower compression ratios, that can operate even at lower octane ratings, was developed [5,26,41]. In parallel with all these, more active and more durable catalysts were developed by anchoring the active components of the catalysts to the strong stabilizers Al<sub>2</sub>O<sub>3</sub> and CeO<sub>2</sub>-ZrO<sub>2</sub> with the help of heat treatment [20]. Also, in this period, catalysts were coated on cordierite monoliths (2MgO-5SiO<sub>2</sub>-2Al<sub>2</sub>O<sub>3</sub>) with low thermal expansion coefficient and 75-85% open frontal area [42,48,49]. Thus, the efficiency of the catalysts were increased with lower pressure drop and higher mass transfer.

In 1980, the NO<sub>x</sub> conversion was increased from 50% to 90% [21]. It was understood that this tightening specific to NO<sub>x</sub> could not be achieved only with the EGR system. Studies conducted in this period revealed that rhodium is an effective catalyst in the NO / NO<sub>2</sub> reduction reaction, shown in equation 3-5 [42,50,51].



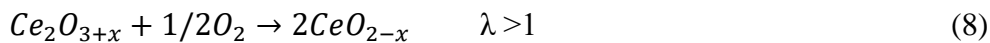
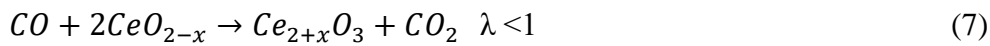
The stoichiometric level is defined as 14.7 kg air / kg fuel [18,52,53]. TWC catalysts are designed to operate at the stoichiometric level and can run both reduction and oxidation reactions at stoichiometric conditions [21,54]. These properties are unique to TWC catalysts [21]. The division of the instantaneous kg air / kg fuel level to the stoichiometric level during the operation is defined as lambda ( $\lambda$ ) [5,7,12,31,55]. Fuel-rich levels ( $\lambda < 1$ ) bring about increase in NOx conversion and engine power [12,56]. The steam reforming reaction shown in equation 6 is an endothermic reaction and allows CO and H<sub>2</sub> to be obtained from hydrocarbons at high temperatures [18,57,58]. H<sub>2</sub> and CO formed play a vital role in NO reduction as seen in equations 3 and 5 as reducing agents [12,21]. In the case where  $\lambda > 1$ , lean conditions, oxidation reactions are favorable, fuel efficiency increases, but NOx conversion is interrupted [59–62].



Deviation from stoichiometry can be caused by many reasons such as fuel, season, acceleration, deceleration, and idle [21]. This situation directly affects engine efficiency, catalyst efficiency and fuel economy [12,61]. For this reason, the  $\lambda$  level at which the system operates is a parameter that must be measured instantaneously and must be constantly controlled [2,63,64]. Due to this requirement, the feedback

system, which is used to adjust the amount of fuel supply, started to be used in vehicles in the mid-1980s [63]. The critical component of this feedback system is the oxygen sensor that communicates with the on-board computer [21]. This sensor measures the oxygen level in atmospheric air by comparing the oxygen level at the engine outlet [21,65].

The  $\lambda$  sensor measuring at the engine outlet naturally reacts with a delay and therefore there is a continuous oscillation in the oxygen level at the exhaust outlet around the stoichiometric level [12,17,21,55,66]. In order to minimize the effect of this oscillation on the conversion performance of the catalyst, the oxygen storage component has been used in the catalyst formulation [55,67]. Usually a mixture of  $CeO_2$ - $ZrO_2$  is preferred for this purpose [68,69]. They can easily transfer oxygen atoms in the structure when exposed to the reducing environment, shown in equation 7 [21,70,71]. Ceria can easily transfer oxygen atoms both from the surface and from the bulk [72,73]. Its crystal structure allows the oxygen atoms in the bulk to easily diffuse to the surface [74]. Zirconia is mostly used to increase the thermal resistance of ceria [56,68,75–78]. Molecular oxygen transferred from the structure can come back when the environment reaches oxidizing conditions, shown in equation 8 [79–81]. The addition of different oxides into Ceria and its effect on oxygen mobility has been tested in many studies, and since the 1980s, studies are still being carried out on this subject to increase oxygen mobility and thermal resistance [71,72,76,82]. The most important reason for this is that catalysts must be exposed to increasingly higher temperatures (1000 °C) in order to respond to the more stringent regulations [12,13,18,21,54,82,83].



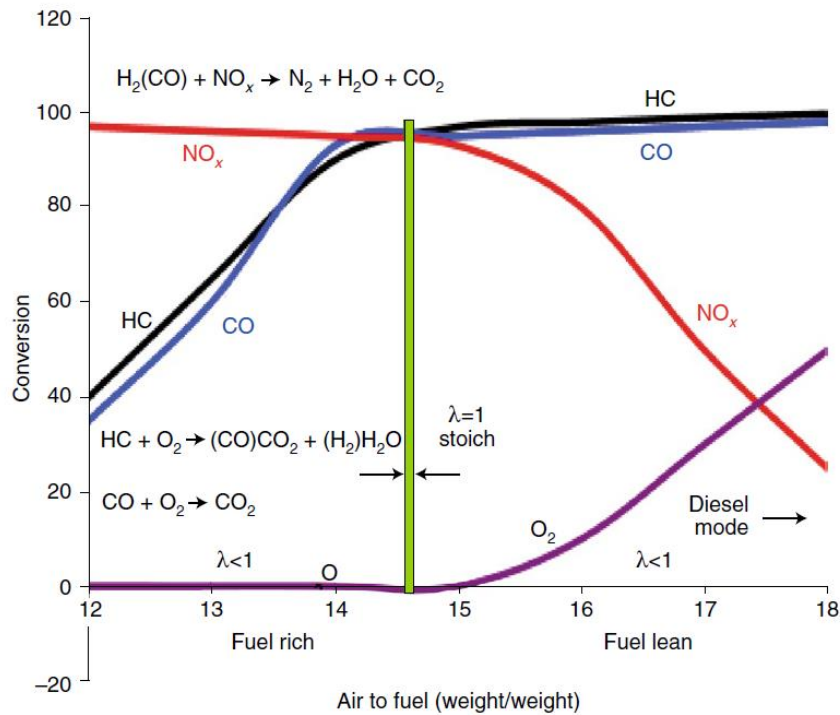


Figure 1.4 Air/fuel ratio and stoichiometry [21]

In the early 1990s, tier 1 regulation was implemented and according to this regulation, it is planned that the conversion of NO<sub>x</sub>, HC and CO will reach 94-96% within 10 years [39,84]. In addition, in this regulation, it was mandatory to reduce the sulfur content in the fuel. With the reduction of sulfur in fuel in the early 90s, the efficiency and stand-alone use of the Pd-only catalyst came to the fore [21,54,61,74,85,86]. However, in response to the more stringent regulations, the requirement that the efficiency of the catalyst in the cold-start period should be below 30 seconds continued by first approximating the catalyst to the engine and then adding rhodium to the structure with the realization that palladium could not respond to this [2,6,21,54].

In the early 2000s, tier 2 regulation, the requirement that the catalyst convert 99% of the pollutants and be durable for 150000 mil, began to be implemented [39]. During this period, mainly catalysts were used as Pd / Rh catalysts, while Pt / Rh

catalysts remained in the background [12,21,54]. Again, in this period, there had been developments in both catalyst and engine operation. Better control of combustion processes and more efficient fuel injection technologies were material has become [64,68,69,75,87,88]. In addition, the stability of the oxygen storage material is increased [56,69,72,75,85]. Palladium was preferred because it was cheaper, especially compared to platinum. Today, palladium price is around 2.5 times of platinum [2,6,7,21].

Tier 3 regulation published in 2014 necessitated the conversion of these pollutants at the extent of 99.5% [26]. In parallel with this, Europe, China and India planned to implement a very close conversions target [21]. Most of the countries of the world agreed and act together on both fuels saving and environmental protection [21,40]. The most prominent indicator of this has been that the countries in question have recently updated their emission control procedures. Federal Test Protocol (FTP-75) and Supplemental Federal Test Procedure (SFTP) applied in the USA are used to test catalyst systems in automobiles [21,89]. The procedure of simulating driving modes by means of dynamometers and measuring emissions with analytical equipment under these conditions was added to the FTP-75. Thus, it can be seen how the high temperatures and exhaust flow changes in the exhaust of the engine under load reflect on the catalytic performance. In addition, the efficiency of the catalyst systems in the cold start period has been added to the procedure, see Figure 1. 5. According to this, catalytic systems that cannot initiate light-off within 30 seconds directly fail the test [21]. The Environmental Protection Agency also mandates in SCO3 procedure to measure emission under conditions where the vehicle's air conditioning systems are active, see Figure 1.6 . Meanwhile, vehicle manufacturers included sudden transition of lean / rich conditions and exposure to high exhaust temperatures to catalyst testing procedures to simulate the execution of the chassis tests [21]. Catalysts are tested by being exposed to thermal aging conditions ranging from 950-1100 °C for 50-100 hours in order to meet the requirement of durability of 150000 miles [21].



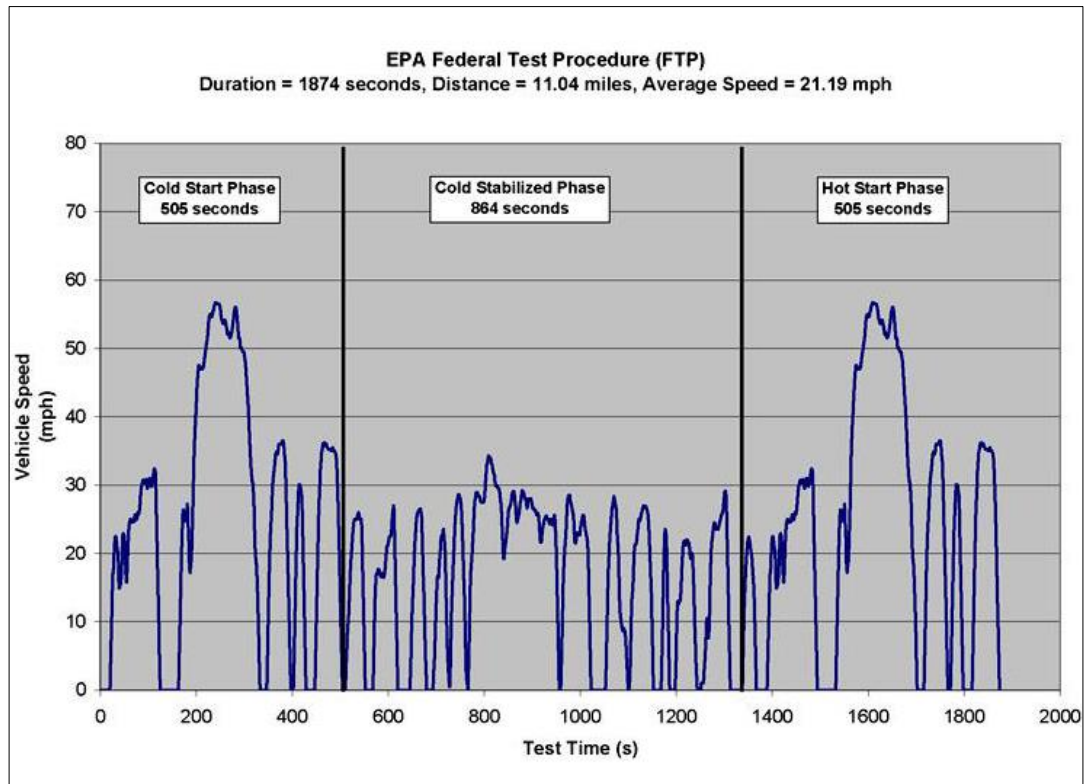


Figure 1.5 EPA FTP-75 exhaust test procedure including cold start [89].

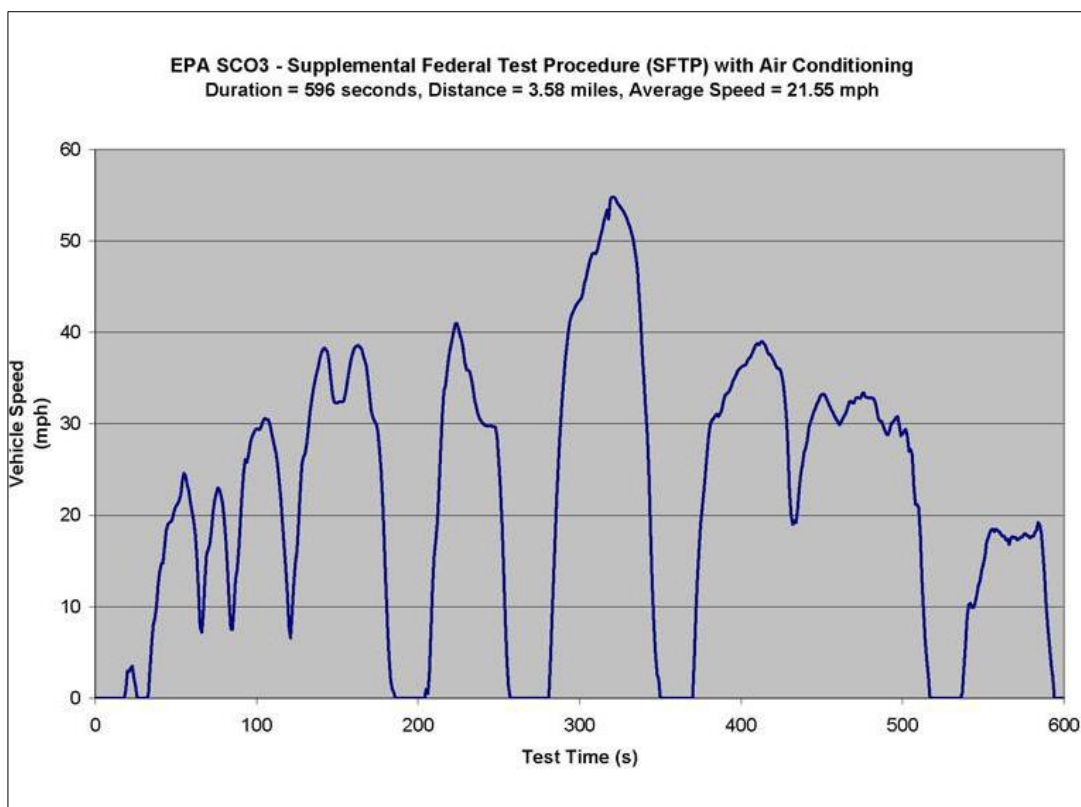


Figure 1.6 EPA SC03 exhaust test procedure with air condition system [89].

The requirements to be met by catalysts are getting more stringent in the coming years. Providing light-off conditions between 200-250 °C and at the same time being resistant to temperatures of 1000 °C are challenging requirements [5,12,54,69,88,90–93]. Reducing precious metal content or developing catalysts from alternative materials are ongoing development issues for TWC area.

### 1.2.3 TWC Catalytic Components and Their Functions on Reaction Mechanisms

TWCs are basically active material coated honeycomb shaped cordierite or metallic monoliths are packed within a stainless steel container (Figure 1.7) and installed

on the exhaust pipeline (Figure 1.8) [2,5,6,12,42,94].

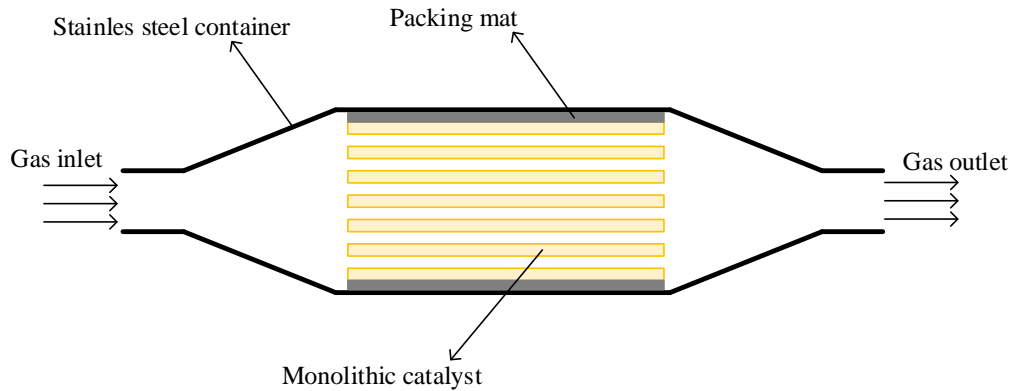


Figure 1.7 An illustration of a catalytic converter that is packed within a stainless-steel container [12,42].

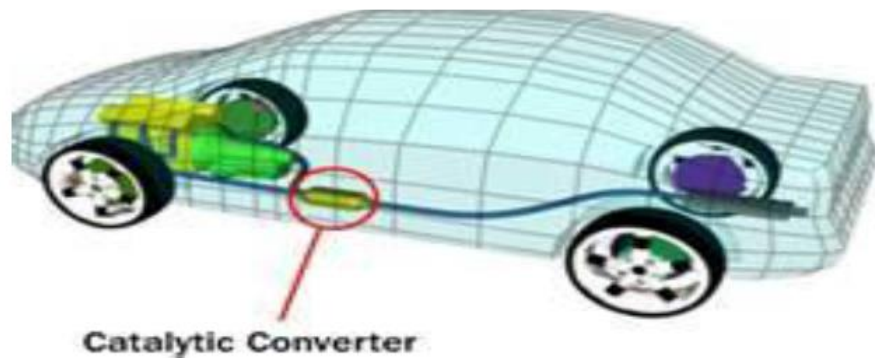
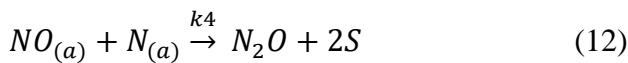
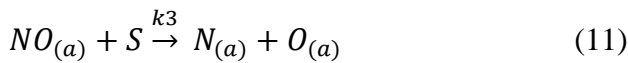


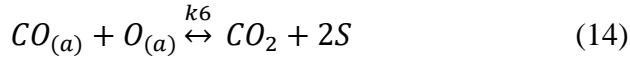
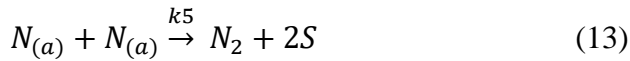
Figure 1.8 TWC position in a vehicle. [12].

A typical TWC catalyst consists of three or four components which are; 1) high surface area support material, 2) oxygen storage material, 3) active metals or platinum group metals (Pt, Pd and Rh) and 4) promoter used to affect the reaction mechanism [7,54,95]. It is known that many reactions occur simultaneously in the three-way catalysis system (equations 1-6) [9,95–97]. Mechanisms and kinetics of

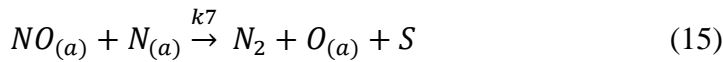
these reactions have been extensively investigated in many studies in the past years [13,54,96–103]. In this section, the mechanisms of NO reduction, HC and CO oxidation reactions will be examined.

Steps of NO reduction reaction mechanism in which CO is used as a reducing agent shown in equations 9 to 14 have been suggested by many researchers [9,54,97]. This reaction mechanism is a classical Langmuir-Hinshelwood mechanism based on surface chemistry [63,97,104–108]. Accordingly, first, NO and CO are reversibly adsorbed from the gas phase to the surface. Muraki et al. found that CO adsorption at 350 °C on the Pd / Al<sub>2</sub>O<sub>3</sub> catalyst was much faster and the adsorption of NO in the NO conversion reaction was a rate limiting step [109]. In the same study, they found that CO covers the surface sites and this inhibits the NO conversion rate. According to their proposed reaction rate equation, the NO conversion rate is directly proportional to the NO partial pressure and inversely proportional to the CO partial pressure [109]. On the contrary, Mamede et. al. found in their study that the rate limiting step was NO dissociation (equation 11) [106]. However, they noticed that as temperature increased, the rate limiting step changed as oxygen removal (equation 14) step from the surface.





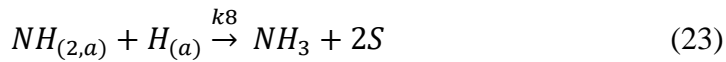
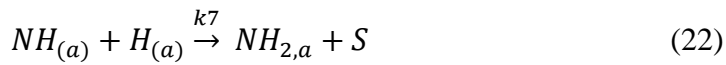
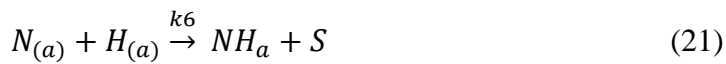
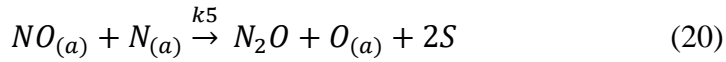
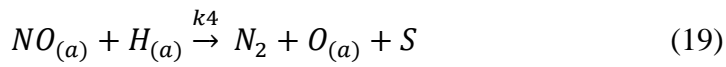
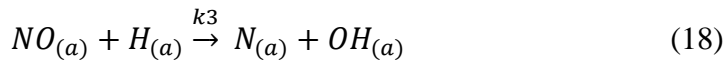
In the kinetic study of Granger et. al. on the Pd / Al<sub>2</sub>O<sub>3</sub> catalyst, they found that the palladium surface was covered by chemisorbed CO and NO molecules [110]. They suggested that the N<sub>2</sub> formation step (equation 13) is dependent on surface diffusion and, therefore, very little of this step occurs [111]. Instead, they suggested an alternative step specified in equation 15.

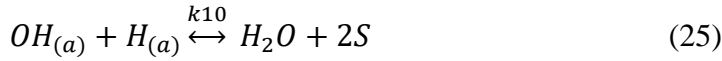


It has been determined that rhodium is more selective to the N-pairing step (equation 13) when performing the same reaction on Pd and Pt surfaces [111]. The reason for it is that the dissociative chemisorption of NO is favored by the Rh surface [111]. This outcome is to a great extent a result of the right arrangement of the Fermi levels of the metals relative to the atomic orbitals of the adsorbed NO; in Rh the Fermi level is found over the antibonding orbitals, whereas in Pd and Pt it is below [97,108]. Hence, extra charge is exchanged from the Rh surface into the antibonding orbitals of NO, debilitating the N-O bond [97,108].

In light duty vehicle emission, the H<sub>2</sub> concentration is about one-fifth of the CO concentration [5,7,12,26,39]. However, in NO reduction, H<sub>2</sub> is also involved in the mechanism, especially at low temperatures (equation 16-25) [9,112–115]. The reaction was studied in Pd / Al<sub>2</sub>O<sub>3</sub> catalyst and according to the findings obtained rate limiting step was determined as dissociation of NO in this reaction [112]. A similar study was carried out on the Pd / LaCoO<sub>3</sub> catalyst and it was determined that the rate of reaction varies directly with the H<sub>2</sub> partial pressure and inversely with the NO pressure [113]. Accordingly, it was concluded that NO was strongly

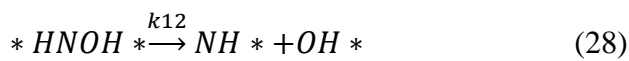
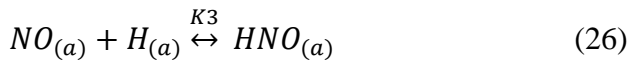
adsorbed to the surface and the reaction rate was slowed due to the weak probability of the two H atoms required for dissociation to be located in adjacent sites [112,113]. The main handicap of the NO + H<sub>2</sub> reduction reaction is the selectivity of palladium to the N<sub>2</sub>O formation (equation 20) at low temperatures [116]. While the selectivity of palladium to N<sub>2</sub>O formation at 120 °C was around 70%, it decreased rapidly with the increase in temperature [116,117].





Chambers et. al. examined the N<sub>2</sub> selectivity of CO + NO and NO + H<sub>2</sub> reactions in Pd / SiO<sub>2</sub> catalyst [117]. Under 250 °C, the main product of the NO + H<sub>2</sub> reaction was N<sub>2</sub>O, whereas in the CO + NO reaction, N<sub>2</sub>O was observed to occur above 250 °C. NH<sub>3</sub> formation was seen between 150-225 °C and disappeared as the temperature increased, Figure 1.9 [117]. Rahkamaa-Tolonen et al., in the hydrogen-deuterium exchange experiment, determined that the formation of NH<sub>3</sub> took place step by step (equations 21-23) [115]. Oh and Triplett, on the other hand, showed that in the reaction of 4500 ppm H<sub>2</sub>, 1500 ppm NO, 18000 CO, 1000 ppm C<sub>3</sub>H<sub>6</sub>, 9000 ppm O<sub>2</sub>, 10% CO<sub>2</sub> and 10% H<sub>2</sub>O, the Pd / Al<sub>2</sub>O<sub>3</sub> catalyst has 100% NH<sub>3</sub> selectivity between 400-500 °C [118]. They also found that temperature increase, CeO<sub>2</sub> addition as OSC or replacement of Pd with Rh completely inhibited NH<sub>3</sub> [118].

Iglesia et. al. suggested that the breaking of the bonds of diatomic molecules with strong chemical bonds is possible only by inclusion of atoms having low coordination number located in the steps and terraces [9]. However, they claimed that during the reaction, the steps and terraces in question were also inhibited by the adsorbed molecules. For this reason, they proposed intermediate reaction steps, stating that high-energy bonds must first be weakened via the bimolecular pathways and then the bond cleavage will occur (equations 26-28) [9].



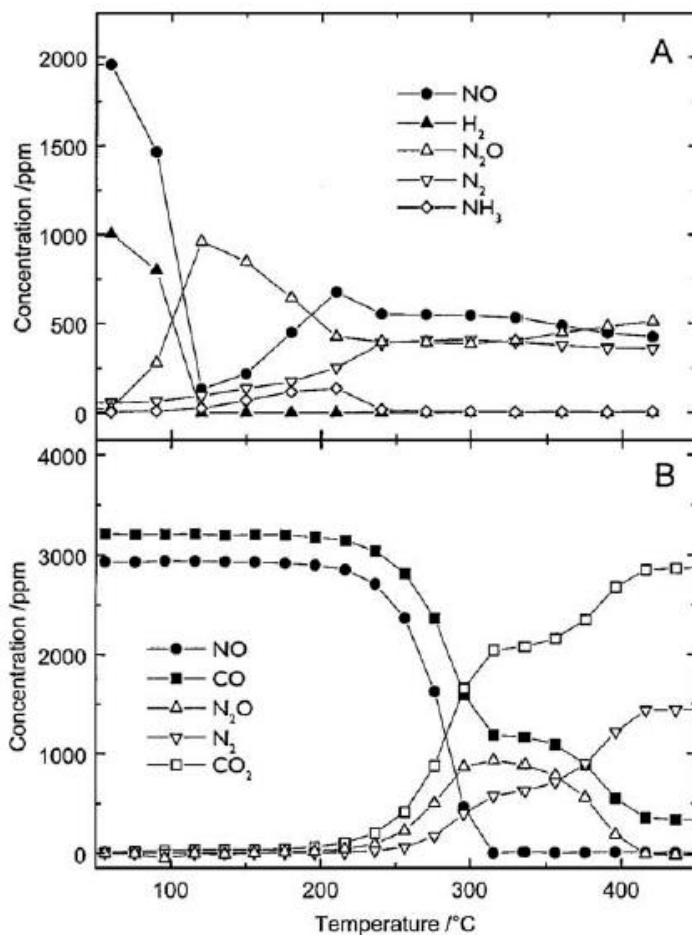
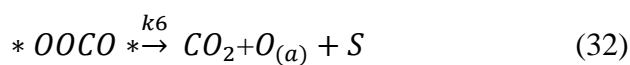
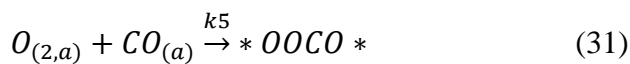
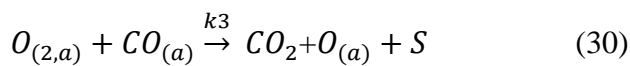


Figure 1.9 Reactant and product concentrations as a function of temperature for NO reduction reactions over Pd/SiO<sub>2</sub>. (A) 2000 ppm NO+1000 ppm H<sub>2</sub>+N<sub>2</sub> balance. (B) 2900 ppm NO+3450 ppm CO+N<sub>2</sub> balance [117].

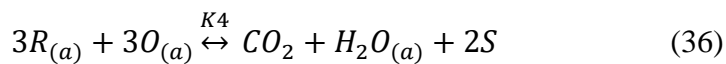
CO oxidation is another major reaction in three-way catalysis. Many researchers have suggested that this reaction is driven by the Langmuir-Hinshelwood mechanism [119–127]. Engel and Ertl made a mechanism comparison in their study and could not detect evidence of the Eley-Rideal mechanism [120]. Schwab and Gossner found that the rate-limiting step was the conversion of adsorbed CO and molecular oxygen to CO<sub>2</sub> in their study on the Pd-based catalyst (equation 30) [127]. According to this study, the reaction rate is inversely proportional to the CO concentration and directly proportional to the O<sub>2</sub> concentration [127]. Szanyi et. al.



determined that the rate-limiting step is the desorption of CO [121]. They found in their study that the Pd surface is covered with CO. Additionally, in this study, it was emphasized that the reaction between CO+O and finally desorption of CO<sub>2</sub> took place very quickly [121]. Xu and Goodman studied the reaction kinetics on the Pd / SiO<sub>2</sub> catalyst. In this study, the temperature was changed between 77 and 727 °C [122]. Xu and Goodman found that the reaction rate increased up to a maximum with increasing temperature and then decreased with increasing temperature. Parker and Föttinger found that hydroxyl groups on the Pd surface increase the reaction rate [124,125]. In these studies, they suggested that carbon monoxide forms carbonate species with hydroxyl groups, which facilitates the breaking of the C-O bond. Similarly, Iglesia et al emphasized that for the cleavage of the C-O bond in CO occurs after intermediate compounds weakens the C-O bond and direct dissociation is not possible on metal surfaces easily (equation 31 and 32) [9]. Rajasree et al. investigated the relationship between the CO oxidation reaction rate and the concentration of H<sub>2</sub>O and CO<sub>2</sub> on the Pd / CeO<sub>2</sub>-ZrO<sub>2</sub> catalyst [126]. According to this study, H<sub>2</sub>O in the environment directly increased the reaction rate. On the other hand, the increase in CO<sub>2</sub> concentration decreased the reaction rate, due to the reduction of the oxygen-storing sites by CO<sub>2</sub>.



There are many complex elementary steps in the propane and propene oxidation reaction [96,128–132]. Ma et. al. has proposed a reaction mechanism as shown in equations 33-36 [96]. In this mechanism, P represents two carbon and R represents single carbon cracking products. In the end, R combines with the adsorbed oxygen to produce H<sub>2</sub>O and CO<sub>2</sub>. Cullis et. al. and Yao's studies showed that CO<sub>2</sub> desorption does not affect the reaction rate due to its rapid occurrence [130,131]. On the other hand, H<sub>2</sub>O molecule slows down the reaction rate due to the formation of palladium hydroxide. Aryafar et. al. has shown that the adsorption of propane and propene are the rate limiting steps [132]. Yao have found that the reaction rate in the Pd / Al<sub>2</sub>O<sub>3</sub> catalyst was inversely proportional to the propene concentration under O<sub>2</sub> rich conditions [128]. In contrast, he found that when the catalyst was Pd / CeO<sub>2</sub> / Al<sub>2</sub>O<sub>3</sub>, the reaction rate varied in direct proportion to the propene concentration [128]. The reason for this difference was suggested as that CeO<sub>2</sub> removes the inhibitory effect of propene. In another study by Yao et al., it was determined that the reaction rate in Pd-based catalysts is always directly proportional to the propane concentration [131]. Basically, the biggest difference between propane and propene reaction kinetics is that propene adsorbs more strongly to palladium [133].



## 1.3 Perovskites

### 1.3.1 Structure and Properties of Perovskites

First found for  $\text{CaTiO}_3$ , perovskite type oxides can be shown with a common formula of  $\text{ABO}_3$  [134,135]. A typical perovskite crystal structure is comprised of two cation A and B and an anion Oxygen [8]. These structures, whose properties such as morphology, surface, electrical conductivity, thermal conductivity, magnetism, can be tailored by using different cations at sites A and B, continue to be the main subject of many different studies [136–139]. Perovskites are used as catalysts in oxidation, reduction, hydrogenation, photocatalysis, electrocatalysis, VOC elimination [140], water deposition and reforming reactions. In this section, properties of perovskites used as catalysts in oxidation, reduction and pollution control reactions will be discussed [141–150].

With the beginning of the 1970s, the extraordinary catalytic properties of perovskites began to be reported [8,151]. It is widely considered today to replace precious metals by perovskites [8,139,152–155]. The reasons for this are that they are easy to synthesize, cheap compared to precious metals, and many properties can be tailored by adding different cations to the structure [139,156]. The A cation in the perovskite structure can be from the lanthanide, alkaline or alkaline earth group. The B cation can be a transition metal with a 3d, 4d or 5d configuration. Therefore, the perovskite to be formed can be in  $\text{A}^{\text{I}}\text{B}^{\text{V}}\text{O}_3$ ,  $\text{A}^{\text{II}}\text{B}^{\text{IV}}\text{O}_3$  or  $\text{A}^{\text{III}}\text{B}^{\text{III}}\text{O}_3$  structure depending on electroneutrality [8,146,151]. The ideal perovskite structure is a cubic structure with a  $\text{Pm}\bar{3}\text{m}$  space group, Figure 1.10 [151]. The corners of the cube are occupied by cation A and the cation B is located in the center of the cube [151]. In addition to that, oxygen anions are present at the centers of faces [151]. Twelve and six oxygen anions coordinate A and B cation, respectively [146]. So, the A cation need to be larger than the B cation. To have interaction between A, B and oxygen, atomic radii sum of B cation and oxygen anion should be equal

to  $\sqrt{2}$  times the sum of the atomic radii of A cation and oxygen anion [157]. As shown in equation 37, the tolerance factor is defined as the division of the sums mentioned above. If the tolerance factor of a compound is between  $0.8 < t < 1.0$ , then perovskite structure can be formed [8,146,151,157].

$$t = \sqrt{2} \frac{R_A + R_O}{R_B + R_O} \quad (37)$$

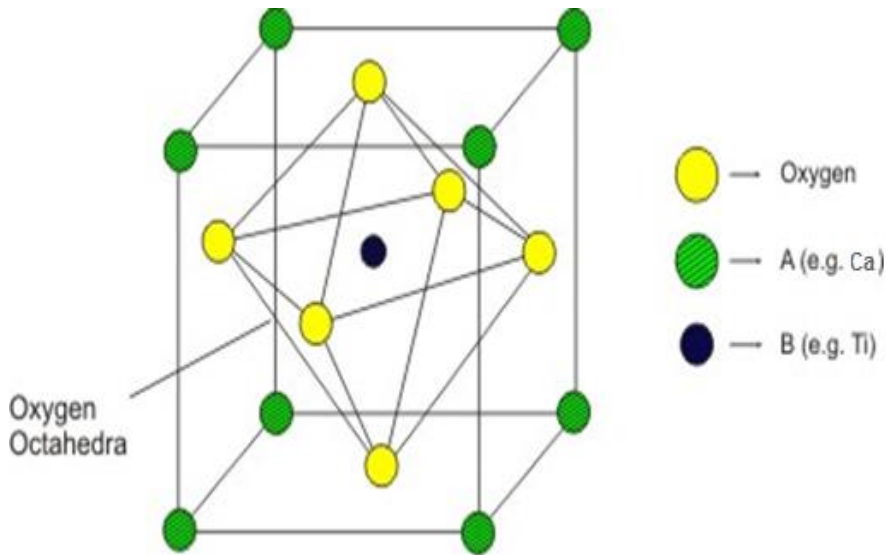


Figure 1.10. Structure of  $ABO_3$  type perovskite [146,151].

One of the preferences of the perovskite structure is in this way the plausibility to receive a wide extend of diverse compositions, changing either the A or the B cation or somewhat substituting each cation by other cations of the same or distinctive valences [8,151,157]. Ternary perovskite-type oxides is divided into  $A^{1+}B^{5+}O_3$ ,  $A^{2+}B^{4+}O_3$ ,  $A^{3+}B^{3+}O_3$  and complex oxides  $A^{2+}(B_{0.67}^{3+}B_{0.33}^{6+})O_3$ ,  $A^{2+}(B_{0.5}^{3+}B_{0.5}^{5+})O_3$ ,  $A^{2+}(B_{0.5}^{2+}B_{0.5}^{6+})O_3$ ,  $A^{2+}(B_{0.5}^{1+}B_{0.5}^{7+})O_3$ ,  $A^{3+}(B_{0.5}^{2+}B_{0.5}^{4+})O_3$  [157]. None of the material have the ideal cubic perovskite structure. There are few examples like  $LaAlO_3$  are slightly distorted. The stable structure of the crystal

depends on geometric factors [146]. Although the tolerance factor is not equal to 1, the perovskite structure can be formed and by the addition of different A cations to the structure, it can create distortion in the sequence of the six O anions surrounding the B cation, which leads to the formation of orthorhombic or rhombohedral crystal structures [8,66,101,146,152,158].

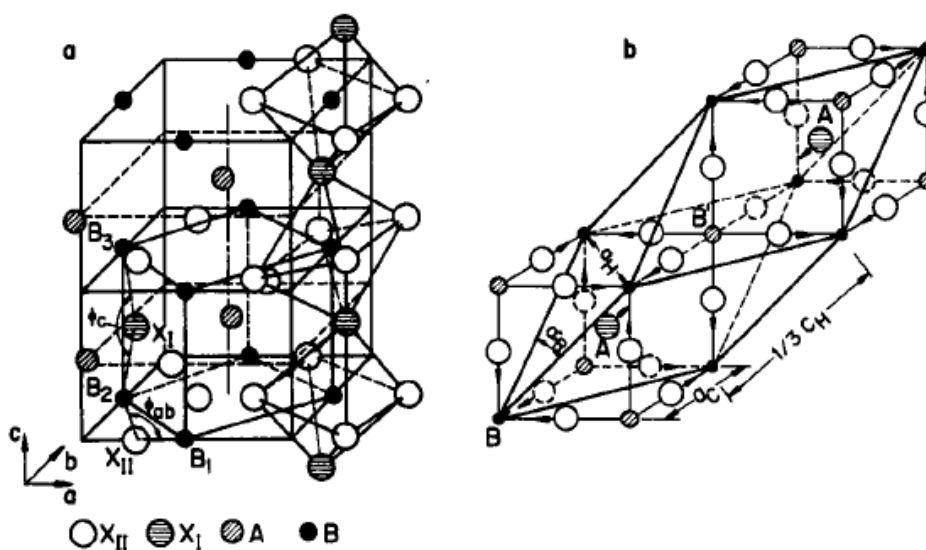


Figure 1.11 Orthorhombic (a) and rhombohedral (b) distortions of the perovskite [146].

Complex oxides are usually applied in the catalysis area, due to their anion or cation vacant possibilities [151,157,159]. It is possible to accommodate more than one cation in the A and/or B site of the perovskite structure such as  $A_{1-x}A'_xB_3O_3$  or  $AB_{1-x}B'_xO_3$  or  $A_{1-x}A'_xB_{1-x}B'_xO_3$  [8,151]. Moreover, oxygen excess or deficiency such as in the formula  $A_{1-x}A'_xB_{1-x}B'_xO_{3\pm\delta}$  ( $\delta$  subscript shows non-stoichiometry) also possible to obtain without losing the perovskite structure [154,158,160]. Accommodation of different cation without destroying perovskite structure, (i.e., non-stoichiometry) helps the researcher to tailor the electronic and surface structure of compounds. Moreover, these multi component perovskite materials perform interestingly promising catalytic properties for carbon monoxide oxidation and NO reduction with CO or H<sub>2</sub> [149,158,161].

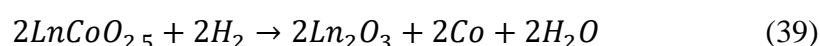
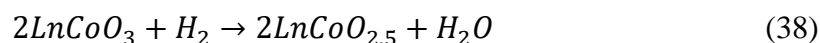
### 1.3.2 Synthesis Techniques of Perovskites

The synthesis technique is critical in improving the weak textural properties of perovskites [8,138]. In catalyst applications, the specific surface area can be increased by modifications in the synthesis routes, which can improve the accessibility of the surfaces. Solid-solid [162–164], coprecipitation [165,166], complexation [167,168], freeze / spray drying [165,166,169,170], sol-gel [171], high-energy ball milling [172] and mesostructuration [173–175] are synthesis techniques known to be common. Solid-solid was the most widely used method in the 1970s and this method is mainly based on solid state diffusion and is carried out by exposing two different metal oxides to high temperature (higher than 1000 °C) for a long time (more than 12h) [162,163]. In this technique, heat treatment and grinding steps are repeated, which positively affects the purity of the perovskite obtained, but extends the synthesis time very much. With this technique, materials with a crystal size of 10-100  $\mu\text{m}$  and a specific surface area of 1-2  $\text{m}^2/\text{g}$  can be obtained [162,163]. Coprecipitation, complexation, sol-gel, and freeze / spray drying are the techniques that use solution chemistry [8]. These techniques gained popularity in the 1980s [8,146,151,165,167,171]. In these techniques, metal oxides formed in solution are first dried and then subjected to calcination. Since the products obtained in solution chemistry are homogeneous, calcination temperatures in these techniques can be between 500-900 °C [165,166]. Owing to the calcination applied at lower temperatures than the calcination temperature applied in the solid-solid method, it can be possible to obtain materials with relatively higher surface area [167,168]. Specific surface areas of materials produced with solution chemistry can vary between 5-40  $\text{m}^2/\text{g}$  [8]. High calcination temperatures may also be required in these applications to remove the precursors such as citrate or carbonate, which can reduce the specific surface area obtained to

3-5 m<sup>2</sup>/g level [176,177]. The reactive grinding technique has gained polarity over the past 10 years [8]. In this technique, two metal oxides are mixed in a high-energy ball-mill to form perovskite, usually at room temperature to obtain perovskites. Pure perovskites can be obtained after an average of 10-20 hours of operation at a rotational speed of around 700 rpm. Since high temperature calcination is not applied in this method, materials with a specific surface area of 40 m<sup>2</sup>/g can be produced. In order to increase the surface area of the perovskite to be produced, inclusion of additives (like ZnO or NaCl) in the ball-milling media has been investigated in many studies [178–182]. Later, these additives are bleached and taken from the content of the desired products. With this method, perovskites having high specific surface area (82 m<sup>2</sup>/g) and a few nanometer-sized crystals were obtained [183]. These high-field products have shown promising performance in CO [184] oxidation, methane oxidation and N<sub>2</sub>O [185] decomposition reactions. Although the performance of the catalysts obtained by the reactive grinding method is promising, the long grinding duration and the expensive bleaching processes are the obstacles to the practicality of this method and therefore to its widespread use. With the elimination of these handicaps, this method has the potential to gain popularity in the future [8]. Another important synthesis technique found in the literature is mesostructuration (or nanocasting). This method is based on the use of structures with known porosity as template (nano-cast) [173–175]. In the study of Wang et al., vinyl silica was used as a nano-cast and the desired perovskite precursors were complexed on this structure with solution chemistry [173]. After the calcination process, vinyl silica, was abraded with the help of NaOH solution. With this method, LaCoO<sub>3</sub> and LaMnO<sub>3</sub> with a specific surface area of 97 m<sup>2</sup>/g and 155 m<sup>2</sup>/g, respectively, could be produced [173]. These high surface area catalysts produced showed remarkable activity in methane oxidation and methanol oxidation [175]. It is promising to achieve high surface area and remarkable activities in catalysts produced by this method [8,174,175,185]. On the other hand, the use of a template and then the separation of this template makes this technique expensive [8].

### 1.3.3 Redox Properties of Perovskites

Intrinsic redox properties of perovskites, which allow them to involve in many oxidation reaction mechanisms, is the most important reason for their preference as catalysts [146,151,171]. In a structure in the form of  $\text{LnBO}_3$  (if Ln is an alkaline earth metal) the redox is generally determined by the B site [186,187]. The contribution of the A site to the redox properties can be of secondary importance in hydrocarbon oxidation reactions and when they have  $A^{\text{III}}$  value [188,189]. Two different peaks were observed in the  $\text{H}_2$ -TPR experiments of the alkaline earth cobaltites [85,188,190]. Whereas, only one peak is observed in TPR experiment of  $\text{Co}_3\text{O}_4$  around 350 °C [189]. The first of these peaks is observed around 400 °C and is due to the transformation of  $\text{Co}^{+3}$  in the perovskite structure to  $\text{Co}^{+2}$  as indicated in equation 38 [189]. If the temperature is not increased any further, the reduction degree of 1  $e^-$ / molecule cannot be exceeded Figure 1.12-A. As the temperature was increased, the reduction of cobalt from  $\text{Co}^{+2}$  to  $\text{Co}^0$  occurred (equation 39) Figure 1.12-B [189].





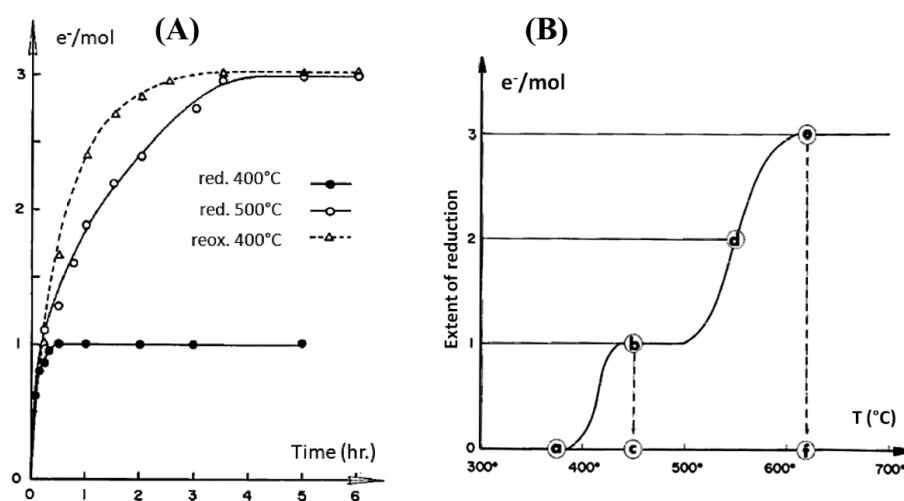


Figure 1.12. A) Reduction and reoxidation of LaCoO<sub>3</sub> indicated temperatures. B Temperature programmed reduction of LaCoO<sub>3</sub> [189]

Cobalt takes longer to turn completely into metallic form, mainly because the reduction reaction takes place according to the contracting sphere model [151]. According to this model, first the outer layer of the sphere is reduced and then the reduction reaction slows down due to the diffusion resistances [191]. As a matter of fact, it can be seen that this model works in the Figure 1.12-A, where complete reduction has lasted for about 6 hours. Reduced to metallic state, cobalt continues to be found in the A cations in the perovskite matrix [146,151,171]. If it is oxidized slowly again (around 400 ° C), the perovskite structure can be restored [151]. However, when the material reduced to the metallic phase is exposed to high temperature (1000 °C) in an inert atmosphere, the cobalt atoms are sintered and the perovskite structure cannot be obtained by re-oxidizing [189]. Irusta et al. found that the temperatures at which TPR peaks were formed increased with increasing calcination temperature applied to the material [140]. This is explained by the increase in the crystal size of the material and the extension of the diffusion times naturally [140,169,188,192,193]. Many studies have been conducted to determine the effect of A site on the reduction process in cobaltites. Futai et al. found that surface oxygen binding energy is correlated with T<sub>max</sub> peaks obtained with TPR

[188]. Accordingly, the order of  $\text{LaCoO}_3 < \text{PrCoO}_3 < \text{NdCoO}_3 < \text{SmCoO}_3 < \text{EuCoO}_3$  was determined depending on the ease of reduction [188]. The effect of having more than one A cation in the structure on the ease of reduction was investigated by Irusta et. al. on the  $\text{La}_{0.8}\text{Sr}_{0.2}\text{CoO}_{3-x}$  catalyst. Adding Sr to the  $\text{LaCoO}_3$  structure prevented the crystalline size of the material from growing and thus facilitated reduction [140]. In this study, it was determined that the first TPR peak was around 200 °C [140]. Nakamura et al. Determined that the addition of Sr to the structure affects the formation of unstable  $\text{Co}^{+4}$  and, consequently, oxygen vacancies [193]. Similarly, the reducibility on the  $\text{LaFeO}_3$  catalyst in the form of  $\text{ABO}_3$  was studied by Tejuca et al [146]. According to this study, excess oxygen (more than 3 e<sup>-</sup>/molecules) was detected in the structure and the reason for this was proposed as evidence for the presence of  $\text{Fe}^{+4}$  ions [146]. Ciambelli et al. Studied the change of the ratio of  $\text{Fe}^{+4}$  ions on the catalyst  $\text{LaFe}_{1-x}\text{Mg}_x\text{O}_3$  ( $x = 0.1-0.5$ ). In this study, it was understood that the ratio of  $\text{Fe}^{+4}$  ions increased until the level of  $x = 0.2$  and the ratio remained the same at higher levels [137,194]. Marti et al. Studied the relation of A site (A = La, Pr, Nd, and Gd) with the nonstoichiometry of the Fe cation. In this study, it was determined that only  $\text{LaFeO}_3$  catalyst contained  $\text{Fe}^{+4}$  ion [195].

### 1.3.4 Oxygen Mobility Properties of Perovskites

Oxygen mobility can be characterized by temperature programmed desorption TPD or isotopic oxygen exchange methods [8]. Oxygen mobility has been extensively studied as it elucidates the properties of the perovskite catalyst that are directly related to its performance, such as oxygen storage capacity, crystal irregularities in its structure, and oxygen nonstoichiometry [160,193,203–209,195–202]. Perovskites can adsorb and desorb two types of oxygen,  $\alpha$  and  $\beta$ . The first oxygen peak in TPD tests belongs to the weakly bound alpha oxygen and this peak is usually obtained below 500 °C [174,210]. The amount of  $\alpha$  oxygen is less compared

to the full oxygen coverage of the sample [202,203,205,207]. It has been suggested that  $\alpha$  oxygen is the  $O^-$  and  $O_2^-$  species that bounded weakly to the B site on surface.  $\beta$  oxygen can be detected in the form of a sharp peak and at higher temperatures Figure 1.13 [174].  $\beta$  oxygen is desorbed from the bulk of the material and reversibly occurs in perovskite structures [151].

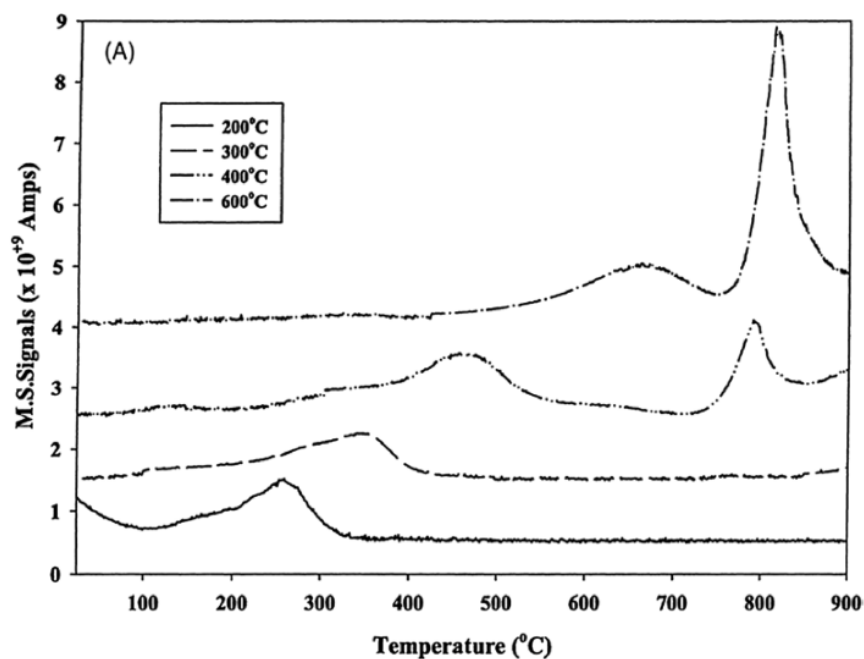


Figure 1.13 TPD spectra of  $O_2$  from sample  $La_{0.99}Co_{0.86}Fe_{0.15}O_{3-\delta}$  calcined at various temperatures [174].

The relation of the desorption amount of  $\alpha$ - $O_2$  with the cation addition made to site A has been studied by many researchers on the  $La_{1-x}Sr_xCoO_3$  catalyst [193,204,211]. As the rate of Sr addition increased, a very high amount of oxygen desorption was detected, and this was because the Sr addition created oxygen vacancies in the crystal lattice, Figure 1.14 [193].

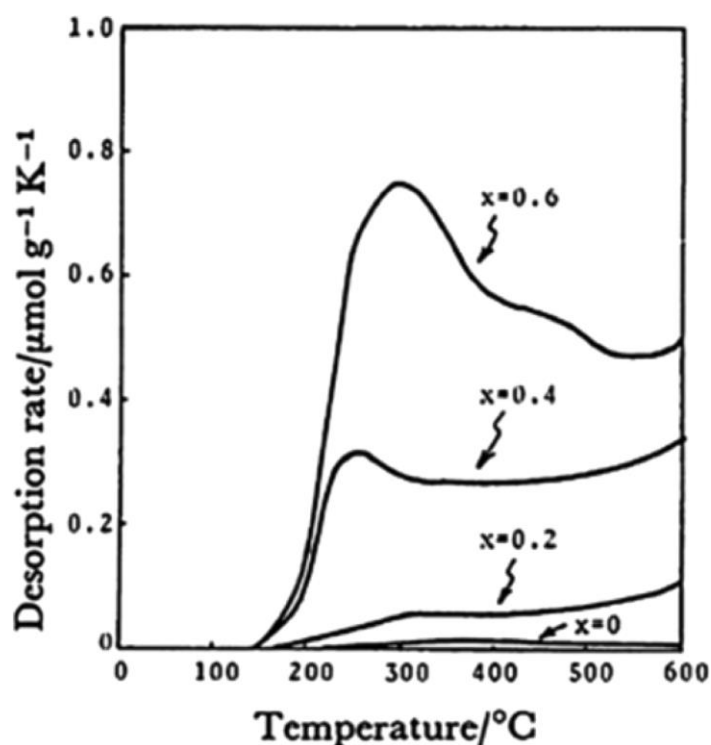


Figure 1.14 TPD curves of oxygen from  $\text{La}_{1-x}\text{Sr}_x\text{CoO}_3$  [193].

The isotopic exchange method helps to understand the behavior of the catalyst in the reaction mechanism [8,212]. With this technique, it is basically possible to separate the oxygen from adsorbing/desorbing on/from the surface of the catalyst and the oxygen dissociating and diffusing it into the lattice [213,214]. The second can give information about the intrinsic reactivity of the catalyst. In this technique, the gas mixture consisting of  $^{18}\text{O}_2$  and  $^{16}\text{O}_2$  isotopes is sent to the sample and it is possible to determine how the mass over charge ratio ( $m/z$ ) of 36 ( $^{18}\text{O}_2$ ), 34 ( $^{18}\text{O}^{16}\text{O}$ ), 32 ( $^{16}\text{O}_2$ ) in the effluent change compared to the upstream [214,215]. For the dissociative adsorption to take place, the reaction of the oxygen in the structure of the catalyst and the change of 32/36 mass ratio accordingly is taken as basis [213,214]. Dissociation of oxygen molecule and diffusion of molecular oxygen in to the crystal lattice brings about the possible combination of oxygen atoms coming from gas and bulk, i.e. heteroexchange [213–216]. Royer et. al. studied the heteroexchange mechanism, demonstrated in Figure 1.15 [212]. According to their

proposal, oxygen diffusion between crystal particles occurs faster than oxygen diffusion between the catalyst bulk and its surface. Therefore, particle size reduction will positively affect the rate of reactions dependent to oxygen adsorption / desorption kinetics.

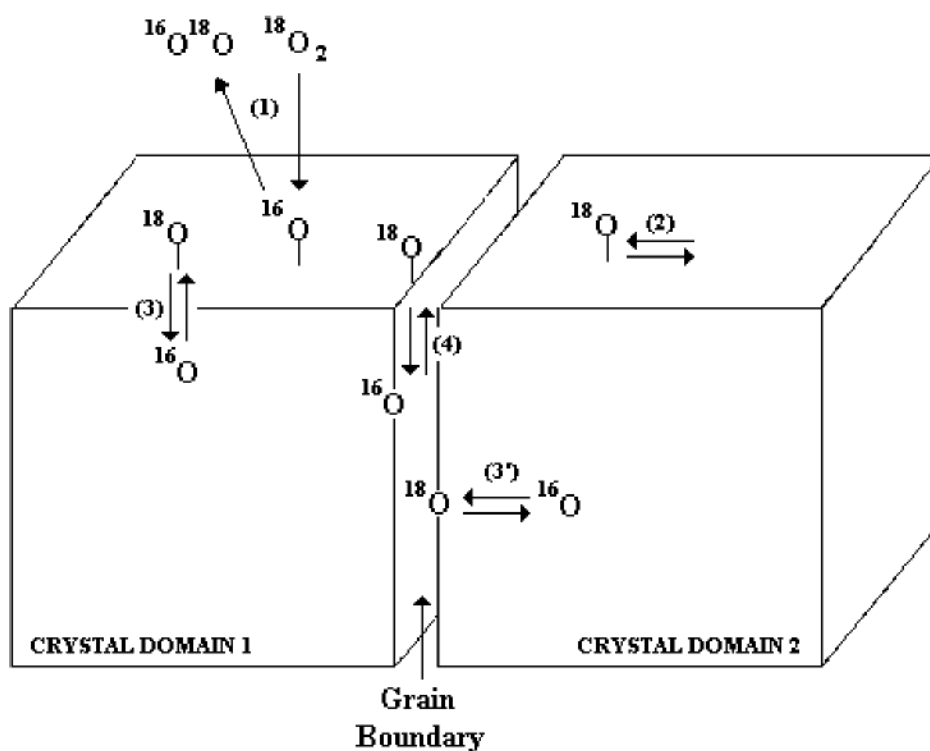


Figure 1.15 Scheme of oxygen Exchange on  $\text{LaCoO}_3$  [212].

Nakamura et al., using  $^{18}\text{O}_2$  on the  $\text{La}_{1-x}\text{Sr}_x\text{CoO}_3$  catalyst, studied whether heteroexchange occurred and the effect of the Sr ratio on the heteroexchange rate [193]. Below  $150^\circ\text{C}$  (for  $x = 0$  or  $0.2$ ) there was no positive effect of the Sr ratio on the heteroexchange rate [193]. On the other hand, it was determined that the Sr inclusion increased the heteroexchange rate at  $300^\circ\text{C}$ . For  $x = 0.6$  heteroexchange was detected even at  $150^\circ\text{C}$ . According to the findings, it was understood that the most important factor affecting the heteroexchange rate is the diffusion of oxygen from the lattice to the surface [193]. Cherry et. al. proposed that the oxygen vacancy would not be the only reason affecting diffusion, in addition, the size of the A and

B cations may also be effective [217]. According to this study, the reduction of the size of the A cation (optimum 0.095nm) and the growth of the size of the B cation (0.075nm) provide optimum conditions for the migration of oxygen from bulk to the surface [217]. When these findings are associated with the tolerance factor, it has been determined that the optimum tolerance factor level that facilitates the diffusion of oxygen to the surface is approximately 0.81 [218].

### **1.3.5 Adsorption Properties of Perovskites**

The probe molecule adsorption technique provides information about the nature, structure and possible involvement of sites on perovskite surfaces [151,219]. The equilibrium level, adsorption kinetics and desorption of these molecules are frequently studied [219–223]. It has been determined that the amount of CO adsorption in the perovskites in the form of  $\text{LaBO}_3$  (B = transition metal) is determined by the cation in the  $\text{B}^{+3}$  site [219]. Maximum CO adsorption was obtained with  $\text{Fe}^{+3}$  cation, and isobutene adsorption was parallel to CO adsorption [219]. In the  $\text{CO}_2$ -CO sequential adsorption test on the  $\text{LaCrO}_3$  surface, it was found that both molecules were adsorbed on the same sites [224]. On the other hand, in the  $\text{O}_2$ -CO sequential adsorption test, it was determined that both molecules were adsorbed as much as they were on the clean surface, and it was found that these two molecules were attached to different sites [219,222,225]. It has been determined that CO binds to surface oxygen by metallic ions and depending on the temperature (298-773 K), the amount of CO adsorbed increases [186,225]. In the NO adsorption study on  $\text{LaBO}_3$  perovskite catalysts, it was determined that the adsorption reached the maximum level in the case of Co as the B site [219]. Unlike CO adsorption, NO adsorption on  $\text{LaFeO}_3$ ,  $\text{LaNiO}_3$  catalysts did not increase with increasing temperature (273-673K) [219]. On the other hand, for  $\text{LaCrO}_3$ ,  $\text{LaMnO}_3$  and  $\text{LaRhO}_3$  catalysts, the change in temperature provided only 20% increase [225,226]. In the light of these findings, it was determined that

NO molecule adsorption is a process that progresses without the need for activation by temperature. The amount of NO adsorbed on the above-mentioned perovskites is very close to the amount adsorbed from simple oxides. Infrared adsorption spectra showed that NO molecule was adsorbed on  $\text{LaMnO}_3$  in the form of dinitrosyl, nitrite and nitrate. According to this result, NO can interact with both  $\text{Mn}^{+3}$  and  $\text{O}^{-2}$  ions [226]. In the sequential NO-CO and CO-NO adsorption tests, when NO was adsorbed first, the adsorption of CO was inhibited and this led to the conclusion that NO was adsorbed more strongly [219]. As a matter of fact, NO and CO adsorption thermodynamic parameters were compared on  $\text{LaCrO}_3$  and NO was found to have higher adsorption enthalpy and lower adsorption entropy [219,225].

Oxygen adsorption profiles are studied due to the use of perovskites in oxidation-reduction reactions. The amount of oxygen adsorption in  $\text{LaMO}_3$  ( $\text{M} = \text{Cr, Mn, Fe, Co, Ni}$ ) catalysts was tested by Kremenec et al [222]. It was determined that the Mn and Co profiles reached the maximum, shown in Figure 1.16. This result was also consistent with the findings of Iwamoto et. al. [223]. Many studies have found that most oxygen adsorption is irreversible [193,199,222,223,227–229].

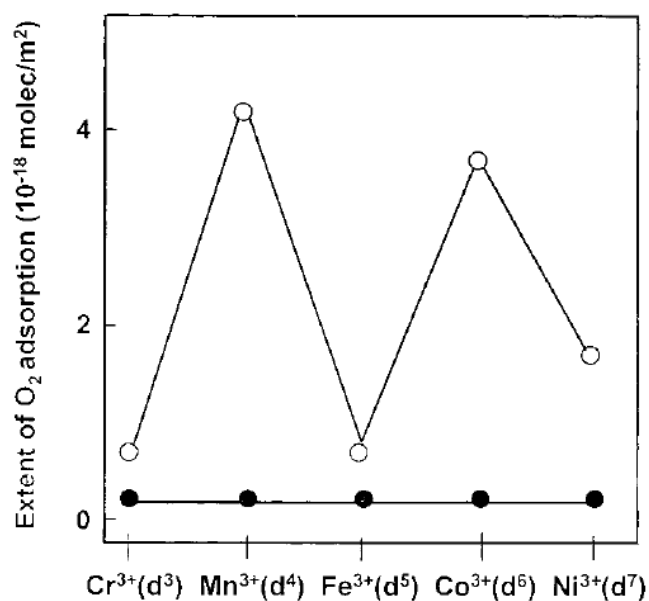


Figure 1.16 Extent of total (open circles) and reversible (filled circles) oxygen adsorption on clean LaMO<sub>3</sub> surfaces [222].

### 1.3.6 Thermal Stability of Perovskites

The thermal stability of perovskites is mostly affected by A cations [151]. In order to understand its thermal stability, the mechanisms by which perovskites are deformed at elevated temperatures have been examined in many studies [188,230–232]. The reduction of the cation at B site in reducing environments and then its sintering with the effect of temperature irreversibly destroys the perovskite structure [8,151]. Arakawa et al. investigated the reduction extent in LnCoO<sub>3</sub> (Ln = lanthanide cations) catalysts and found that the growth of the cation diameter at site A decreased the reduction extent [230]. In this study, improvement of the thermal stability of perovskites with the increasing size of A cation has shown experimentally. In a systematic study carried out by Katsura et. al., Gibbs free energy of formation ( $\Delta G^\circ$ ) analysis was performed between 1150-1300 K on LnFeO<sub>3</sub> catalysts [232]. The findings showed that increasing the cation diameter in the A site increased the negativity of the  $\Delta G^\circ$  value, which theoretically supported



the work of Arakawa et. al. [230,232]. In another study, the relationship between tolerance factor  $t$  and stability  $\text{LnCoO}_3$  ( $\text{Ln} = \text{La, Pr, Nd, Sm, Gd}$ ) was studied [192]. In this study, the reduction peaks occurred around 633 K ( $\text{Co}^{+3}$  to  $\text{Co}^{+2}$ ) and around 800 K ( $\text{Co}^{+2}$  to  $\text{Co}^0$ ) during reduction process. It was revealed that the factor preventing the sintering of cobalt in its reduced form at the  $\text{Co}^0$  state in the perovskite matrix is the increasing diameter of the A cation and therefore the  $t$  factor. The study revealed that thermal stability increases with the increase of the  $t$  factor (equation 37) [192].



## CHAPTER 2

### LITERATURE REVIEW

Gasoline engine exhausts, containing unburned or partially burned hydrocarbons (HCs), carbon monoxide (CO) and nitrogen oxides (NO<sub>x</sub>) as primary pollutants [12], are treated with three-way catalysts (TWCs) to convert these pollutants to less harmful compounds (CO<sub>2</sub>, H<sub>2</sub>O) for environmental pollution control [58,154]. Noble metals are extensively preferred as active components in TWC applications [20] due to their ability to change their oxidation states easily with the alteration of environments between oxidative and reductive conditions [139]. Metallic Pd or Pt supported on metal oxides, mostly Al<sub>2</sub>O<sub>3</sub> as support and/or ceria as oxygen storage material was reported extensively as effective catalysts for oxidation reactions [5,54,154]. In addition to that, inclusion of Rh in the formulation was found to favor the NO reduction reactions [32,154,233,234]. Both the morphology, i.e. high specific surface area of the support, and the extent of dispersion, i.e. a few nanometer-sized noble metal clusters, are the key factors for the performance of dispersed noble metal catalysts, but these properties are very sensitive to exposed temperatures and poisoning chemicals [69,142,144,234,235]. Catalysts, mounted closer to the engine exhaust (i.e., close-coupled catalyst or CCC) for shorter cold-start period, are exposed to high temperatures even ranging up to 1000 °C [2,12,235,236] resulting in the loss of surface area of the support material [154], sintering of active components [13,237] and consequently, causing an irreversible deactivation of the catalyst [238,239]. As higher and higher targets for performance and durability are pushed forward by legislators, dispersed noble metals, which can start sintering around 500-700 °C, started not to meet the requirements [12,26]. Thermal stability remains as an issue that necessitates ongoing material

development due to the stringent emission standards [26,38,39]. Another important catalyst deactivation mechanism is the poisoning, which occurs due to chemisorption of lead (Pb), sulfur (S), and phosphorus (P) by catalytically active components [45,52,240,241]. With an increase in the extent of poisoning, the deactivation of active sites and pore blockage occur, which result in a decrease in catalytic activity [91]. Therefore, exploration of new catalytic materials that possess high thermal endurance and good poisoning resistance remain as an ongoing technological advancement area to solve the problem associated with three way catalysis [7,54,84]. Over the past two decades, perovskite-based materials have been extensively studied in TWC applications due to their thermal stability and adjustable surface and bulk properties [8,21,54,151]. Within the scope of these studies, perovskites were tested as OSCs [66,87,150,156,242], as precious metal substitutes [11,143,164,194,201–203,243–245], as supports to stabilize precious metals [65,101,102,150,152,246,247] and as hosts that take precious metals into their structures [18,64,66,102,116,142,144,245,248]. Synthesis techniques, textural properties, and intrinsic properties of perovskite structures have been developed since the 1970s [163,165–168,172,176,185,196,208]. These materials are known to exhibit remarkable performance in CO, HC oxidation and NO reduction reaction [8,146,151]. In addition, it has been shown in many studies that they can protect their structures even at high temperatures, and thus delay/prevent the sintering of precious metals added/supported in their structures [54,139,142,242,249,250]. Today, the use of these perovskites together with noble metals (NMs) or directly as an alternatives to NMs in TWC applications are the subjects of many studies [18,64,66,87,142,144,154,248].

The activities of perovskites have been studied on CO, HCs oxidation and NO reduction reactions [11,101,137,154,194,201,251–253]. The effect of substitution of A or B cations with other cations on critical parameters such as anion deficiency or anion excess or lattice oxygen mobility has been investigated in many studies on these reactions [66,101,256,257,150,154,162,185,212,251,254,255].

Perovskites containing divalent cations at B sites can generally be active in oxidation reactions [8]. Mostly  $\text{LnBO}_3$  ( $\text{Ln} = \text{lanthanides}$ ) perovskites show high activity in CO and HC oxidation reaction when B site is Mn, Co, Ni or Fe [151]. In Royer et al.'s study of the oxidation of  $\text{H}_2 + \text{CO} + \text{CH}_4$  gas mixture on  $\text{LaCoO}_3$  and  $\text{LaMnO}_3$  catalysts (shown in Figure 2.1) revealed that  $\text{LaCoO}_3$  showed slightly higher activity [143]. It was also determined that CO was converted first, then  $\text{H}_2$  and finally  $\text{CH}_4$ . The same conversion sequence was obtained with the Pd catalyst, but the conversion temperatures obtained with the Pd catalyst were  $70^\circ\text{C}$  lower for CO and  $\text{H}_2$  and  $180^\circ\text{C}$  lower for  $\text{CH}_4$  [143].

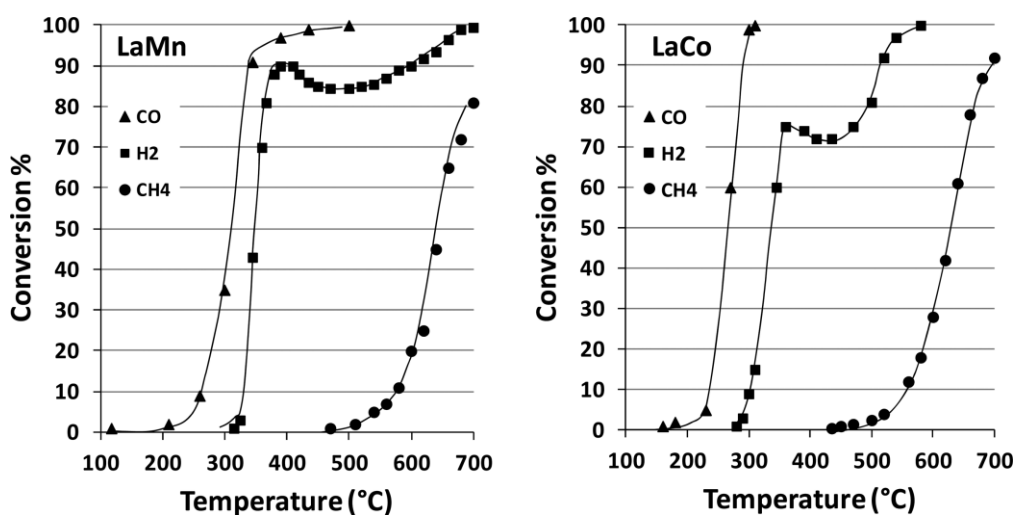


Figure 2.1 Catalytic oxidation of  $\text{H}_2$ , CO and  $\text{CH}_4$  over  $\text{LaMnO}_3$  and  $\text{LaCoO}_3$ . Same concentrations of  $\text{H}_2$ , CO and  $\text{CH}_4$  (1.5%) + 17.6%  $\text{O}_2$  + 4.1%  $\text{CO}_2$  + 1.5%  $\text{H}_2\text{O}$  [143].

Suprafacial mechanisms in CO oxidation and intrafacial mechanisms similar to Mars and Van Krevelen mechanism in  $\text{CH}_4$  oxidation were found to be effective [143]. High temperatures are required for intrafacial mechanisms to come into play. Therefore,  $\text{CH}_4$  conversion started between  $450\text{--}500^\circ\text{C}$  Figure 2.1. Cobaltite and manganite perovskites are very active catalysts for CO oxidation because the B site cations contained in these catalysts can exist in more than one oxidation state ( $\text{Co}^{+2}/\text{Co}^{+3}$  and  $\text{Mn}^{+3}/\text{Mn}^{+4}$ ) which generates excess oxygen on the catalyst surface

[11]. Cations in a higher oxidation state on the surface play an active role in CO activation and can easily transfer excess oxygen in their structure to CO [11]. They can recover the oxygen they lost from the oxygen in the gas phase. It has been found that the substitution of Ce at site A in the  $\text{LaMnO}_3$  ( $\text{La}_{1-x}\text{Ce}_x\text{MnO}_3$ ) catalyst contributes to the anion diffusivity so that the oxygen contained in bulk can also assist in surface reactions [161]. As a result, dramatic improvements in CO light-off temperature were observed, shown in Figure 2.2 [161]. Similar situations are also valid for the  $\text{LaCoO}_3$  catalyst, and the substitution of Sr to A site in this catalyst showed that the light-off temperature decreased to 180 °C in the CO oxidation reaction [258].

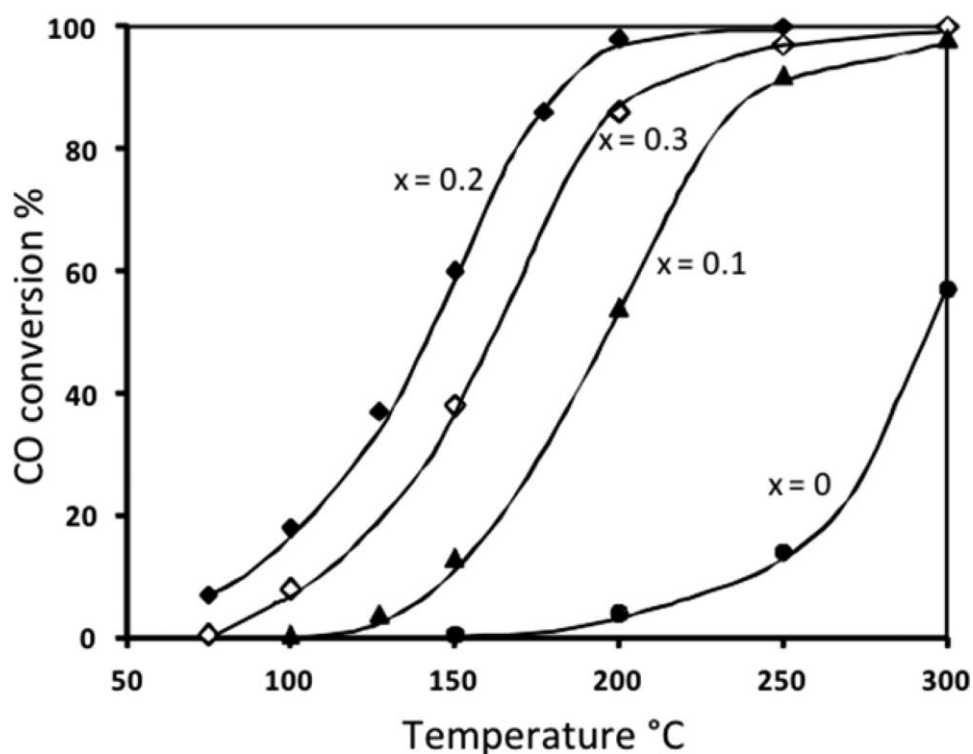


Figure 2.2 CO oxidation over  $\text{La}_{1-x}\text{Ce}_x\text{MnO}_3$  perovskite catalysts. Reaction conditions: 1% CO + 1%  $\text{O}_2$  + 98% He. [161]

Zhang-Steenwinkel et al. studied the mechanism of CO oxidation on manganites and determined that the rate determining step of the reaction as the CO adsorption from the gas phase to the surface [145]. In the same study, it was also determined

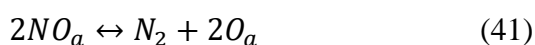
that the adsorption of oxygen to sites at low temperatures decreases the reaction rate, but this effect disappears as the temperature increases [145]. In addition, it was determined that lattice oxygen migration was involved in the reaction with the increase of temperature [145]. It has been found that this positive effect of temperature compensates for the negative effect of the decreasing specific surface area on the reaction rate [145].

Ferrites ( $\text{LaFeO}_3$ ) show less activity in CO oxidation compared to cobaltites and manganites [11,243]. Nevertheless, the fact that iron is cheap and abundant maintains a constant interest in this metal [11,194,259,260]. The reducibility of iron, present in the  $\text{Fe}^{+3}$  and  $\text{Fe}^{+4}$  oxidation states within the perovskite structure, directly affects the CO oxidation performance [11,194,259,260]. The effect of Sr, Ca, Nd, Sm substitution in the A site on oxidation performance evaluated by Ciambelli et. al. and it was found that Nd had the highest activity with a light off temperature of 321 °C [194,261]. In addition, the substitution of Cu, Mg, Cu and Pd in to the B site did not dramatically increase the oxidation performance. However, it has been observed with isotopic exchange technique that Cu and Pd substitution increases the bulk oxygen mobility in  $\text{LaFeO}_3$  ( $\text{LaFe}_{1-x}\text{Pd}_x\text{O}_3$ ,  $\text{LaFe}_{1-x}\text{Cu}_x\text{O}_3$ ) catalyst [116,262].

Propane oxidation has been studied in many studies on ferrites [263–265], manganites [266], cobaltites [267] and double-substituted catalysts [268]. Song et al. Studied the oxidation mechanism of propane on the  $\text{La}_{0.66}\text{Sr}_{0.34}\text{Ni}_{0.3}\text{Co}_{0.7}\text{O}_3$  catalyst [268]. It has been determined that the most suitable mechanism for the oxidation of propane is the Mars and van Krevelen mechanism [268]. According to the findings of the studies conducted, it was determined that propane oxidation started at 200 °C and the light-off temperature around 300 °C [268]. These light-off levels were found to be close to the levels obtained with Pt, Pd and Rh catalysts [131,269,270]. Spinicci et al. [271] compared the oxidation performance of alkanes on the  $\text{LaBO}_3$  (B = Mn, Co, and Fe) catalyst with that of the  $\text{PdO} / \text{Al}_2\text{O}_3$  catalyst.

Surprisingly, they found that ferrites were the most active catalysts in the oxidation of alkanes and even demonstrated better activity in the PdO catalyst. It has been suggested that the main reason for this is that ferrites have higher bulk oxygen mobility than the other two perovskites [269,271].

There are many studies in the literature on reduction of nitrogen oxides [272]. Direct decomposition of NO and N<sub>2</sub> selectivity as a product have been studied on many perovskite structures (equations 40 and 41) [273]. However, without reducing agents such as H<sub>2</sub> or CO in the reaction medium, this reaction has not been found in the literature that this reaction takes place on a perovskite catalyst without precious metal [8,29,101,274]. The Selective Catalytic Reduction (SCR) process works in TWC applications [8,151,251,253,254]. In this process, NO<sub>x</sub> are continuously reduced with the help of reducing agents H<sub>2</sub>, CO [101,251,274].



The H<sub>2</sub>-SCR reaction, mechanism specified in equations 9-16, has been studied on perovskite catalysts in stoichiometric or oxygen-rich media [101,253]. Rodriguez et al. Studied the H<sub>2</sub>-SCR reaction on BaTiO<sub>3</sub> and BaTi<sub>0.95</sub>Pd<sub>0.05</sub>O<sub>3</sub> catalysts [101]. The BaTi<sub>0.95</sub>Pd<sub>0.05</sub>O<sub>3</sub> catalyst converted 85-95% of NO (even in the presence of CO<sub>2</sub> and H<sub>2</sub>O in the feed). However, the N<sub>2</sub> selectivity was 50% [101,134,253]. In addition, without Pd, NO<sub>x</sub> conversion did not occur under these conditions. Palladium-containing perovskites have been extensively studied in NO reduction [110,275–277]. In the study performed on LaCoO<sub>3</sub> catalyst, a maximum conversion of 5% was achieved under excess oxygen, with bulk LaCoO<sub>3</sub>. Complete conversion of NO with 63% N<sub>2</sub> selectivity was achieved at 148 °C with the inclusion of Pd to the structure (LaCo<sub>1-x</sub>Pd<sub>x</sub>O<sub>3</sub>) [110]. The reason for the low activity of LaCoO<sub>3</sub> in NO conversion is due to the formation of stable nitrates on the catalyst, and the



addition of Pd to the structure removes the nitrates from surface [110,277].

Furfori et al. synthesized ferrites with different cation substitutions at sites A and B ( $\text{LaFeO}_3$ ,  $\text{La}_{0.8}\text{Sr}_{0.2}\text{FeO}_3$ ,  $\text{Pd/La}_{0.8}\text{Sr}_{0.2}\text{FeO}_3$ ,  $\text{La}_{0.8}\text{Sr}_{0.2}\text{Fe}_{0.9}\text{Pd}_{0.1}\text{O}_3$ ,  $\text{La}_{0.7}\text{Sr}_{0.2}\text{Ce}_{0.1}\text{FeO}_3$ ,  $\text{Pd/La}_{0.7}\text{Sr}_{0.2}\text{Ce}_{0.1}\text{FeO}_3$ ,  $\text{La}_{0.7}\text{Sr}_{0.2}\text{Ce}_{0.1}\text{Fe}_{0.9}\text{Pd}_{0.1}\text{O}_3$ ) [251]. Among these catalysts, the activity of  $\text{La}_{0.8}\text{Sr}_{0.2}\text{Fe}_{0.9}\text{Pd}_{0.1}\text{O}_3$  was the highest. As seen in Figure 2.3, in an oxygen-free environment and  $40000\text{ h}^{-1}$  GSVH conditions, all of the NO was converted into  $\text{N}_2$  at  $200\text{ }^\circ\text{C}$ . However, in the feed containing 5% oxygen, a maximum conversion to 55%  $\text{N}_2$  was achieved and then  $\text{N}_2\text{O}$  and  $\text{NO}_2$  formation was observed with the effect of increasing temperature. The authors stated that the performance and selectivity of this catalyst under stoichiometric conditions would be promising and argued that the activity of this catalyst was due to the oxidation state of iron being suitable for NO and  $\text{H}_2$  adsorption [251].

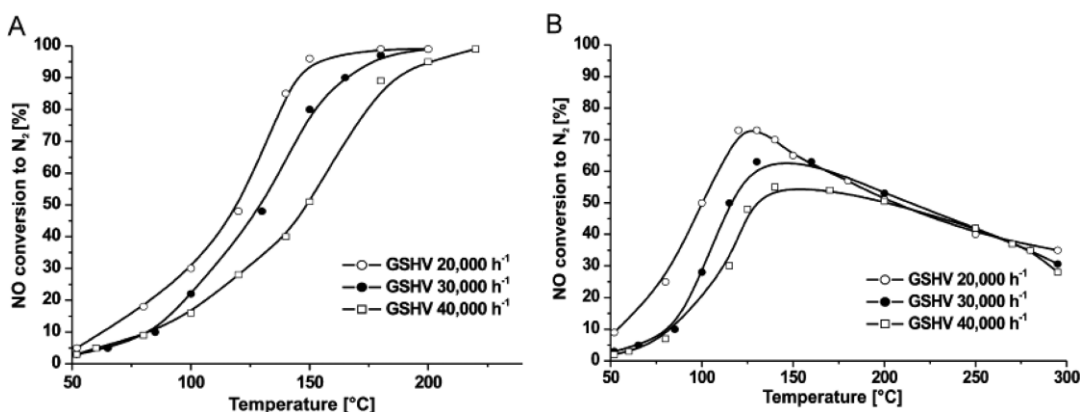


Figure 2.3 NO conversion to  $\text{N}_2$  on powder  $\text{La}_{0.8}\text{Sr}_{0.2}\text{Fe}_{0.9}\text{Pd}_{0.1}\text{O}_3$ : (A) 1000 ppmv NO, 4000 ppmv  $\text{H}_2$ , He balance and (B) 1000 ppmv NO, 10,000 ppmv  $\text{H}_2$ , 5%  $\text{O}_2$ , He balance [251].

The  $\text{C}_3\text{H}_6$ -SCR reaction ( $\text{NO} + \text{C}_3\text{H}_6 + \text{O}_2$ ) has attracted the attention of many studies [254,256,278,279]. It has been understood that Fe-based materials are the most effective NO reducers in perovskite catalysts [278,279]. Zhang et al. found that 81% of NO at  $450\text{ }^\circ\text{C}$  and 97% of NO at  $700\text{ }^\circ\text{C}$  was converted to  $\text{N}_2$  (3000 ppm NO, 3000 ppm  $\text{C}_3\text{H}_6$ , and 1%  $\text{O}_2$  in helium at a space velocity of  $50\ 000\text{ h}^{-1}$ )

[256]. The reason for successful conversion at this level was emphasized by the authors that iron increases the oxygen mobility in the lattice, which in turn improves the reducibility of the catalyst. In addition, it was among the findings of the study that adding Pd to the perovskite structure decreases the transformation temperatures [147,256].

Perovskite catalysts have also been tested in TWC applications where both reduction and oxidation reactions occur together under gasoline-powered engine exhaust conditions [18,64,66,142,144]. In the study conducted by Zhou *et al.* [18] performances of palladium-substituted perovskite ( $\text{LaFe}_{0.77}\text{Co}_{0.17}\text{Pd}_{0.06}\text{O}_3$ ) and perovskite-supported palladium ( $\text{Pd}/\text{LaFe}_{0.8}\text{Co}_{0.2}\text{O}_3$ ) catalysts were compared and the doped catalyst was found to be more active at the same Pd loading. However, the performance change after thermal aging or  $\text{SO}_2$  poisoning was not investigated. Guillaume *et al.*, compared the performance and oxygen storage capacity of perovskite based  $\text{LaMn}_{0.976}\text{Rh}_{0.024}\text{O}_{3+\delta}$  catalyst to that of a reference dispersed metal based  $\text{Pt-Rh}/\text{CeO}_{2-\gamma}\text{Al}_2\text{O}_3$  catalyst under oscillating conditions and in the presence of steam in the reaction mixture [66]. It was found that the perovskite-based catalyst also had promising oxygen storage capacity and good performance, but the performance change after hydrothermal treatment or poisoning effect was not studied. Furthermore, the use of powder catalyst instead of structured monolithic catalysts, no alkane (i.e.  $\text{C}_3\text{H}_8$ ) presence in reacting gas mixture and very low GHSV ( $13000\text{h}^{-1}$ ) preference makes the study far from simulating real exhaust conditions. However, only a limited number of studies are available on the investigation of the effect of hydrothermal aging [64] and poisoning [142,144] on the performance of perovskite based-TWC catalysts. Nishihata *et al.*, compared the three-way catalytic performances of  $\text{Pd}/\text{Al}_2\text{O}_3$  and  $\text{LaFe}_{0.57}\text{Co}_{0.38}\text{Pd}_{0.05}\text{O}_3$  catalysts after 100h aging at  $900\text{ }^\circ\text{C}$  under real exhaust conditions. They observed that the former catalyst lost about 10% of its activity due to noble metal sintering. On the other hand, the perovskite-based catalyst preserved its activity and maintained the high dispersion of Pd particles after aging. Accordingly, they

proposed that, under slightly reducing environment, Pd particles segregate out of the perovskite crystal and under oxidative atmosphere they dissolve back into bulk perovskite structure. Therefore, the reversible movement of palladium into and out of the perovskite matrix in response to cyclic redox fluctuations of the exhaust gas composition suppressed the sintering of palladium particles. In this study, the effect of hydrothermal aging at 900 °C was studied but the effect of hydrothermal aging at higher temperatures and the effect of poisoning on the activity of the catalyst remained as issues to be investigated. Tzimpilis *et al.* studied performance, thermal durability and SO<sub>2</sub> poisoning resistance of two perovskite based natural gas vehicle catalysts: La<sub>0.91</sub>Mn<sub>0.85</sub>Ce<sub>0.24</sub>Pd<sub>0.05</sub>O<sub>z</sub> and La<sub>1.034</sub>Mn<sub>0.966</sub>Pd<sub>0.05</sub>O<sub>z</sub> [142,144]. Both catalysts showed better thermal stability and poisoning resistance compared to that of commercial Pd-based catalyst. However, these studies were performed under steady state reactant concentration and the results cannot represent the fluctuating redox conditions of gasoline vehicle exhaust. The catalytic converters of gasoline engines have to satisfy high performance, thermal stability and SO<sub>2</sub> resistance requirements under realistic conditions in which severe mass transfer limitations and fluctuating stoichiometry take place. Most of the studies on three-way catalysis prefer powder catalysts usage at low gas hourly space velocity (GHSV < 15000 h<sup>-1</sup>) [18,158] or steady stoichiometric conditions [18,142,144].

Current FTP-75 and SC03 catalyst performance test protocols are based on dynamic driving conditions [89,280]. These protocols force the engine to operate between fuel rich and fuel lean conditions in a transient manner [89]. During these transitions, the exhaust gas temperature can instantly rise up to 950 °C to 1100 °C [281]. As Tier 3 standard mandates 150000 mil catalyst life, catalysts can be exposed to these temperatures between 50 and 100 hours during their lifetime [26,38].

The catalyst previously developed by our working group has shown that it has superior properties in terms of performance and thermal resistance than a

commercial catalyst [282]. Therefore, the performance, thermal stability and SO<sub>2</sub> poisoning resistance of the catalyst we developed within the scope of this study will be compared with the catalyst previously developed by our group (hereinafter referred to as benchmark catalyst or C1). According to Tier 3 standard and FTP-75 protocol, the catalyst must reach its light-off within 30 seconds [89]. In most vehicles, the catalyst bed reaches 300 °C within 30 seconds, so a light-off of 300 °C or less will also be considered in the catalyst performance evaluation [2,5,21,26]. The benchmark catalyst contains 0.75% by weight of noble metal (0.1% Rh and 0.65% Pd) nominally. Noble metal loading at the same weight ratio was also preferred in the perovskite-based catalyst formulation. The benchmark catalyst contains 27.3 wt % Ce<sub>0.8</sub>Zr<sub>0.2</sub>O<sub>2</sub>. In order to make an efficient comparison, this ratio was kept the same for the perovskite-based catalyst. The precious metals are supported on Ce<sub>0.8</sub>Zr<sub>0.2</sub>O<sub>2</sub> in the benchmark catalyst. In the perovskite-based catalyst, noble metals were substituted into the B sites of perovskites (LaFe<sub>0.57</sub>Co<sub>0.37</sub>Rh<sub>0.06</sub>O<sub>3</sub> and LaFe<sub>0.57</sub>Co<sub>0.37</sub>Pd<sub>0.06</sub>O<sub>3</sub>). LaFe<sub>x</sub>Co<sub>y</sub>Pd<sub>1-x-y</sub>O<sub>3</sub> structure was preferred in perovskite-based catalyst formulation. Iron can increase oxygen mobility within the perovskite structure and has good activity in NO reduction reaction [110,112,113,251,253,274,276]. Because of these properties, iron was used in Site B. Fe and Pd substituted catalysts provide complete NO conversion, but N<sub>2</sub> selectivity remains around 60% [251,274]. Therefore, Rh, which has high performance in NO activation, NO dissociation and N<sub>2</sub> selectivity in NO conversion, was added to the catalyst structure [5,105,111]. The reason for the substitution of cobalt to the B site is that it can hold excess oxygen on the catalyst surface and increase the surface oxidation reaction rates that conform to the Langmuir–Hinshelwood mechanism [8,11,185]. There are several reasons for the substitution of palladium at site B; 1) Pd atoms accessible on the surface accelerate oxygen exchange in many intermediate steps, 2) Pd accelerates bulk oxygen mobility in the catalyst, 3) Pd prevents the formation of nitrates on the catalyst surface, 4) Pd atoms accessible on the surface play an active role in the activation of NO, CO and HC [18,34,274,283,64,87,102,142–144,245,253]. It is known that

the A site is not directly involved in the reaction mechanism, instead, it is known that oxygen deficiency can be created in the structure with the substitution of more than one cation in A site [146,151,188,189]. Considering that the same effect can be achieved by adding Fe cation to site B [8,146,251], it was preferred to use only La cation in site A. The reason for La selection is that this cation provides an effective thermal stabilization in reducing environments [188,230,231].  $\gamma$ -Al<sub>2</sub>O<sub>3</sub> has been used as a support material in both benchmark and perovskite-based catalysts.  $\gamma$ -Al<sub>2</sub>O<sub>3</sub> concentrations are 72.7% wt. in the benchmark and 45.3% wt. in the perovskite-based catalyst. Inductively coupled plasma optical emission spectroscopy (ICP-OES), Brunauer, Emmett and Teller (BET) surface area, X-Ray diffraction, Transmission electron microscopy (TEM) energy-dispersive X-ray spectroscopy (TEM-EDX), diffuse reflectance infrared Fourier transform spectroscopy (DRIFTS), and CO pulse chemisorption techniques were used to determine the various physical and chemical changes that occurred within the catalysts with hydrothermal aging as well as SO<sub>2</sub> poisoning.

## **2.1 Objective of the Study**

The objective of this study is to develop a three-way catalyst with high thermal stability, promising SO<sub>2</sub> poisoning resistance and performance comparable to dispersed noble metal catalysts. Considering the aforementioned protocols and standards, performance evaluation is done under oscillating stoichiometry and 1000 °C aging temperature is applied in this study. In addition, the catalysts are tested by coating them on a monolith in order to approach severe mass transfer limitations in real conditions.



## CHAPTER 3

### EXPERIMENTAL

#### 3.1 Materials

For promoter Cerium (III) nitrate hexahydrate ( $\text{CeN}_3\text{O}_9 \cdot 6\text{H}_2\text{O}$ ) (Aldrich, 99%) and Zirconyl nitrate hexahydrate ( $\text{N}_2\text{O}_7\text{Zr}_{\text{aq}}$ ) (Fluka, % 27 & Zr (gravimetric)), Hydrogen peroxide ( $\text{H}_2\text{O}_2$ ) (J.T. Baker, 30% v/v), ammonium hydroxide solution ( $\text{NH}_4\text{OH}$ ) (Aldrich, 33%  $\text{NH}_3$ ) and iso-propanol ( $\text{CH}_3\text{CHOHCH}_3$ ) (J.T. Baker) are used. For pseudoboehmite aluminum-tri-sec-butoxide (ATSB) ( $\text{Al}(\text{OC}_4\text{H}_9)_3$ ) (Aldrich, 97%) hydrochloric acid HCl (Aldrich, min 37%) are used. For perovskite synthesis, Lanthanum(III) nitrate hexahydrate ( $\text{La}(\text{NO}_3)_3 \cdot 6\text{H}_2\text{O}$ ) (Sigma-Aldrich, %99.99), Cobalt(II) nitrate hexahydrate ( $\text{Co}(\text{NO}_3)_2 \cdot 6\text{H}_2\text{O}$ ) (Sigma-Aldrich, %98), Iron(III) nitrate nonahydrate ( $\text{Fe}(\text{NO}_3)_3 \cdot 9\text{H}_2\text{O}$ ) (Sigma-Aldrich, %99.5), Manganese(II) nitrate hydrate ( $\text{Mn}(\text{NO}_3)_2 \cdot x\text{H}_2\text{O}$ ) (Sigma-Aldrich, %97), Palladium(II) nitrate hydrate ( $\text{Pd}(\text{NO}_3)_2 \cdot x\text{H}_2\text{O}$ ) (Sigma-Aldrich, ~40% Pd basis), Rhodium(III) nitrate solution hydrate ( $\text{Rh}(\text{NO}_3)_3 \cdot x\text{H}_2\text{O}$ ) (Sigma-Aldrich, ~36% Rh basis), Ruthenium(III) nitrosyl nitrate solution in dilute nitric acid  $\text{Ru}(\text{NO})(\text{NO}_3)_x(\text{OH})_y$ ,  $x+y=3$  (Sigma-Aldrich, ~1.5% Ru basis) are used as metal nitrates.

#### 3.2 Equipment

Rotary vacuum evaporator is used for vacuum drying of the slurries, (0-1000 rpm, 0-100 mbara, with temperature-controlled water bath, IKA Brand). Stirring is carried out by laboratory stirrers, (0-2000 rpm, with temperature control, IKA Brand). Normal drying is carried out in a laboratory oven, (RT to 250 °C, PID controlled, Protherm Brand). Calcination is carried out inside a tubular reactor that

has 38 mm inner diameter and up to 1200 °C temperature control range.

For the catalytic performance measurement, a dynamic catalytic test system is used which is comprised of five mass flow controllers, an evaporator, two heated gas transfer lines, a temperature-controlled quartz reactor, Mass Spectrometer (MS) (Hiden HPR-20 Q/C), non-dispersive infrared CO Analyzer (Teledyne model 7600) and software. Five different Teledyne Hastings Instruments HFC202 model mass flow controllers are assembled on the downstream of five different gas supply cylinders. A fast-acting solenoid valve and a flow restrictor line is used to alternate the oxygen content of the reaction environment. The solenoid valve is oscillated at 1 Hz and the downstream of the oscillating line is directly connected to the reactor inlet. In order to enrich the water vapor composition of the gas mixture, nitrogen stream is bubbled through a temperature-controlled water tank. In order to have 10% water vapor concentration both the flow rate and the temperature of the water in the tank can be adjusted, but in most of the application water tank is kept at 55 °C and nitrogen stream is kept constant. Five different gas streams are mixed in a heated manifold and then transferred to the reactor through a heated line. Both the manifold and the heated line operates at 110 °C. The quartz reactor having 80 cm length is comprised of two different sections. The reaction gas is preheated in the first section of the reactor which is actually a 30 cm long spiral quartz tubing. The heated gas mixture reaches the second section of the reactor which is actually a quartz chamber that contains a monolithic catalyst. The temperature of the reactor is measured and controlled with the aid of a K-type thermocouple (with 3 mm diameter and Inconel 600 shielding) which is immersed in a quartz well that touches the top of the monolith consequently. The reactor temperature is controlled by the feedback system to which this thermocouple is connected. The measurement accuracy of the thermocouple is  $\pm 1$  °C degree for 100-1200 °C range. The control system can keep the reactor temperature constant with deviations in the  $\pm 0.5$  °C band from the set value. The reactor is designed for monolithic catalysts having 22 mm diameter and 13 mm diameter.



### **3.3 Catalyst Preparation**

Perovskite based catalyst preparation consists of five sections which are OSC powder production, pseudoboehmite production, perovskite production, washcoat production and monolith coating. On the other hand, in the dispersed metal-based catalyst preparation process, there is a metal impregnation process instead of perovskite production. Only general synthesis route for catalyst preparation is explained in this section. The detailed catalyst synthesis procedure is shown in Appendix A.

#### **3.3.1 Preparation of Oxygen Storage Powder**

A co-precipitation technique was used for the synthesis of  $\text{Ce}_{0.8}\text{Zr}_{0.2}\text{O}_2$  powder [284]. Nitrate forms of cerium (Ce) and zirconium (Zr) were mixed in distilled water with a Ce:Zr atomic ratio of 4:1. Hydrogen peroxide ( $\text{H}_2\text{O}_2$ ) was then added to water in a volume ratio of 1:3. The mixture was poured into an excess ammonium hydroxide solution ( $\text{NH}_4\text{OH}$ , Aldrich, 33%  $\text{NH}_3$ ). The solution was kept for 2 days in order to achieve a complete precipitation. Product was dried at  $150^\circ\text{C}$  for 12 h and finely ground. It was further calcined in the oven with dry air at  $600^\circ\text{C}$  for 5h.

#### **3.3.2 Preparation of Pseudoboehmite**

Pseudoboehmite was used as a binder material in the wash coating slurry. In the work of Nguefack (2003), the sol-gel method was used to synthesize pseudoboehmite [285]. Aluminum-tri-sec-butoxide (ATSB) was first hydrolyzed and then condensed with the addition of hydrochloric acid (HCl). The obtained gel was dried at  $150^\circ\text{C}$  for 12 h and then calcined at  $300^\circ\text{C}$  for 5 h, under dry airflow.

### 3.3.3 Impregnation of Metal

Palladium and rhodium are used as noble metals. Palladium (II) chloride solution (Aldrich, PdCl<sub>2</sub>, 5 wt% solution in 10 wt% HCl) and Rhodium (III) nitrate solution (Aldrich, Rh(NO<sub>3</sub>)<sub>3</sub> ~ 10 wt% Rh in 5 wt% nitric acid (HNO<sub>3</sub>) are the precursors for the noble metals. Depending on the desired nominal loading of the noble metal in the final recipe, (0.65wt.% for Pd, and 0.1 wt.% for Rh were chosen) the noble metal is weighed. The weighed metal is dissolved in water and the amount of water is determined according to the water hold capacity of the sample that is going to be impregnated, 1.5 times of the water hold capacity is used in this work. Prior to the impregnation process, the noble metal solution is mixed in a rotary vacuum evaporator flask for half an hour. Then, the solid material is added to the flask, rotational speed is set to 130 rpm, pressure is set to 450 mbar and temperature is set to 80°C. The sample is mixed until all the water in the flask evaporates. Then drying at 150°C for 12 h is carried out. Finally, the sample is calcined at 550°C for 1 h under excess air flow.

### 3.3.4 Preparation of Perovskite Powders

Sol-gel citrate complexation method was used to prepare perovskite catalysts. This method is suitable for the production of pure single phases without any contaminations caused by impurities [146]. Compared to other solid-solid mixture production techniques, lower calcination temperatures are required in sol-gel technique, as a result perovskite obtained experience a lesser extent of sintering and have a higher specific surface area. Moreover, sol-gel technique allows homogenous mixing of precursors which results in the formation of homogenous perovskite [286]. The reactions taking place between precursor metals and citric acid are all exothermic and the generated heat during reactions helps the formation of the perovskite crystallites to a certain extent [160].

In the sol-gel citrate complexation technique, nitrate salts of precursors are dissolved in deionized water. The same amount of citric acid in the coordination number basis of metal ions is added to the solution in order to replace the nitrates located in metal coordinates with citrates. This step is called as citrate complexation and lasts until a spongy material is obtained. Finally, the obtained material is grounded and calcined under excess air flow [15,161].

$\text{LaFe}_{0.6}\text{Co}_{0.4}\text{O}_3$ ,  $\text{LaFe}_{0.57}\text{Co}_{0.37}\text{Pd}_{0.06}\text{O}_3$ ,  $\text{LaFe}_{0.57}\text{Co}_{0.37}\text{Ru}_{0.06}\text{O}_3$ ,  $\text{LaFe}_{0.57}\text{Co}_{0.37}\text{Mn}_{0.06}\text{O}_3$ ,  $\text{LaFe}_{0.57}\text{Co}_{0.37}\text{Rh}_{0.06}\text{O}_3$  will be used as a candidate for active perovskite and their synthesis route is explained here. The reasons for choosing these catalyst formulations are described in a literature review section. The nitrate salts of metals are first dissolved in deionized water. Lanthanum(III) nitrate hexahydrate ( $\text{La}(\text{NO}_3)_3 \cdot 6\text{H}_2\text{O}$ ), Cobalt(II) nitrate hexahydrate ( $\text{Co}(\text{NO}_3)_2 \cdot 6\text{H}_2\text{O}$ ), Iron(III) nitrate nonahydrate ( $\text{Fe}(\text{NO}_3)_3 \cdot 9\text{H}_2\text{O}$ ), Manganese(II) nitrate hydrate ( $\text{Mn}(\text{NO}_3)_2 \cdot x\text{H}_2\text{O}$ ), Palladium(II) nitrate hydrate ( $\text{Pd}(\text{NO}_3)_2 \cdot x\text{H}_2\text{O}$ ), Rhodium(III) nitrate solution hydrate ( $\text{Rh}(\text{NO}_3)_2 \cdot x\text{H}_2\text{O}$ ), Ruthenium(III) nitrosyl nitrate solution in dilute nitric acid  $\text{Ru}(\text{NO})(\text{NO}_3)_x(\text{OH})_y$ ,  $x+y=3$  are used as metal nitrate salts. The desired amount of citric acid is separately dissolved in the same amount of distilled water as used in precursor solution and then added to the precursor solution under vigorous stirring. The desired amount of promoter is also added into the final solution. Then, the solution is stirred at 60 °C until the viscous gel is obtained. Further drying process at 100 °C for 5h is also applied to obtain a spongy material. Finally, the calcination is applied at 700 °C for 5 h [211].

### 3.3.5 Preparation of Washcoating Slurry

Two different catalyst type were prepared. The first type was perovskite free TWC catalyst. This catalyst was for benchmark purposes. Second type catalysts were perovskite containing catalyst. In this section synthesis route of both catalyst type will be explained.

### **3.3.5.1 Preparation of Washcoating Slurry for Perovskite Free Catalyst**

This procedure has been adapted from the work of Nijhuis et. al. [287]. Gamma phase aluminum oxide (AO) ( $\gamma\text{-Al}_2\text{O}_3$ ) and impregnated promoter are mixed within a flask in which weight percentage of the Ce is 19. Then, the solid solution is weighed and deionized water is added by 2/3 of weight solid solution. After that, 3mm diameter alumina balls are placed in the flask for the milling process. The slurry is milled on an orbital shaker for 48 hours at 275 rpm. Then drying at 150°C for 12 h and calcination at 550 °C for 1 hr processes are followed. In order to improve interparticle adhesion between AO and particles that tend to ionize at elevated temperatures pseudoboehmite should be added into washcoat slurry. Therefore, obtained powder is mixed with pseudoboehmite and water again for the milling process. Added pseudoboehmite is one tenth of AO by the weight and water is again 2/3 by the weight of the solid solution. This time two stage of milling is applied, firstly 2 hours of milling is applied. Before second stage of milling, nitric acid (Merck, 65%  $\text{HNO}_3$ ) is added to the solution until the pH of the solution reaches to 1. The second stage of milling is carried out for 6 hours.

### **3.3.5.2 Preparation of Washcoating Slurry for Perovskite Containing Catalyst**

This procedure has been adapted from the work of Nijhuis et. al. [287]. Gamma phase aluminum oxide (AO) ( $\gamma\text{-Al}_2\text{O}_3$ ) and perovskite-promoter mixed solid is mixed within a flask in which weight percentage of the Ce is 19. Here in this recipe AO weight percentage in total solid concentration is not constant as in the case of the benchmark catalyst, but it changes according to the perovskite (noble metal) loading. For 20 g/ft<sup>3</sup>, 10 g/ft<sup>3</sup> and 2 g/ft<sup>3</sup> nominal loading AO weight percentage are 39%, 53% and 65%, respectively. The same procedure is applied for perovskite

containing catalyst, but the addition of pseudoboehmite which is dependent to AO content is also altered accordingly.

### **3.3.6 Monolith Coating**

Cordierite monoliths that have 22 mm outer diameter, 13 mm length and 400 cells/in<sup>2</sup> cell density are used in this study. The monolith coating process starts with drying at 150 °C for 30 min. The dried monoliths are weighed to record bare weight, which will be helpful for uptake calculation. Then, monolith is dipped into the washcoat slurry and rotated upside down for 1 minute. After that, the monoliths is removed from the slurry and blocked channels of it is cleaned from the excess coating material via a pressurized air blow. After cleaning the excess washcoat the monolith is weighed again and checked whether or not wet basis weight change after coating process is in between 0.70 to 0.85 g. The coating process is repeated until the wet basis weight change reaches the desired level. Once coated properly, the monolith is dried. If the loading amount is appropriate, monoliths are firstly dried at 150 °C for 1 hour and calcined at 500 °C for 3 h [149]. The final product is weighed and weight change on the dry basis is recorded, which is helpful for noble metal loading calculation.

### **3.4 Catalyst Characterization**

The washcoat used in monolith coating has also been used for characterization. Namely, the same drying and calcination processes to which the monolith was exposed were applied to the washcoat to be used for characterization, and a powder catalyst sample was obtained for characterization with this method. Prepared powder catalysts are characterized with XRD, ICP-OES, BET, TEM-EDX, DRIFTS and Pulse Chemisorption techniques. X-ray diffractometer is operated at 2 degrees/min scan speed with Cu radiation at 40 kV and 40 mA power. Crystal structure, crystal phases and the crystallite are detected with this technique.

Inductively coupled plasma-optical emission spectrometry (Perkin Elmer DRC II) is used to analyze the noble metal content present in the dried and calcined washcoat powder, which is required for the calculation of the actual noble metal loading on monolith. BET surface area of a powder catalyst is obtained from the nitrogen adsorption isotherm at 77 K in a Quantachrome Corporation, Autosorb-6 analyzer. All the powder samples are degassed to  $10^{-4}$  Torr prior to measurements. EDX spectra and palladium particle growth of powder catalysts are obtained in a JEOL JEM 2100F HRTEM microscope. Perkin Elmer Spectrum One FTIR analyzer with DRIFTS attachment is used to investigate the formation of different phases after SO<sub>2</sub> poisoning. Finally, CO pulse chemisorption experiments are conducted via custom build test setup equipped with Sihamdzu MGS4 Gas Sampler and Hiden Analytical HPR 20 Mass Spectrometer (shown in Figure 3.1). The pulsed chemisorption is carried out within a micro reactor that has 6 mm outer diameter and 4 mm inner diameter. Samples, roughly 100 mg, are weighed accurately. Oxygen (Linde, %99.995) is fed to the micro reactor, kept 300 °C, at 70 ml/min flow rate, for 1 hour. After that, the sample is cooled down to room temperature under the helium flow. Then, the reactor is heated to 400 °C with 10 °C/min ramp rate and kept at that temperature under reduction gas flow (5 %H<sub>2</sub>/He (Linde, %99.995)) at 70 mL/min. The reduction step is followed by helium flushing for 2 hours at 400 °C. Before chemisorption pulses, the sample is left to cool down to room temperature within helium atmosphere. 2 ml of sorption gas (2900 ppm CO in He (Air Liquide, %99.0), balance He (Linde, %99.995) are pulsed until the area of the peaks obtained began to be equal.

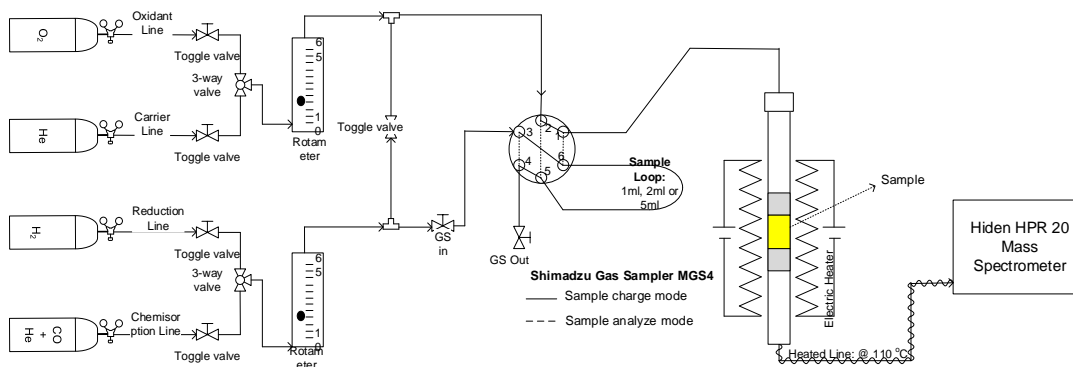


Figure 3.1 CO Pulse Chemisorption setup

Catalyst loading on the monolith is also recorded. As shown in Table B. 1, weight change after loading is recorded for each monolith and noble metal loading is calculated accordingly. Each monolith holds  $4.75 \pm 0.10$  g solid catalyst. Theoretical noble metal loading for catalysts is approximately  $20.0 \pm 1.0$  g/ft<sup>3</sup>.

### 3.5 Catalyst Activity Test System

Schematic of the performance test system is shown in the Figure 3.2. Mass flow controllers are used to blend a gas mixture that simulates the engine exhaust. Calibration procedure for mass flow controllers is explained in Appendix C. The composition and other operational parameters of performance test are given in Table 3.1. Oxygen concentration is oscillated between 5800 to 9400 ppm at 1 Hertz frequency via a fast-acting solenoid valve. A heated line operating at 110 °C is used to transfer the upstream gas mixture at  $50000 \text{ h}^{-1}$  space velocity to the quartz reactor. As it enters the quartz reactor it is firstly heated through a preheating section before reaching the monolithic catalyst sample with a 22 mm diameter and 13 mm length. The downstream gas of the catalytic reactor is sampled via hot zone sampling. The concentration of the sampled gas is analyzed with a mass

spectrometer and an infrared CO analyzer. The calibration procedure for mass spectrometer is explained in Appendix D. Real time concentration and temperature data are acquired by data acquisition software. A typical test starts by programmed a temperature increase from 150 °C to 600 °C at a rate of 5 °C/ min. Once 600 °C temperature is reached the reactor is left to natural cooling. Acquired data during the cooling period are used to report light-off temperature.

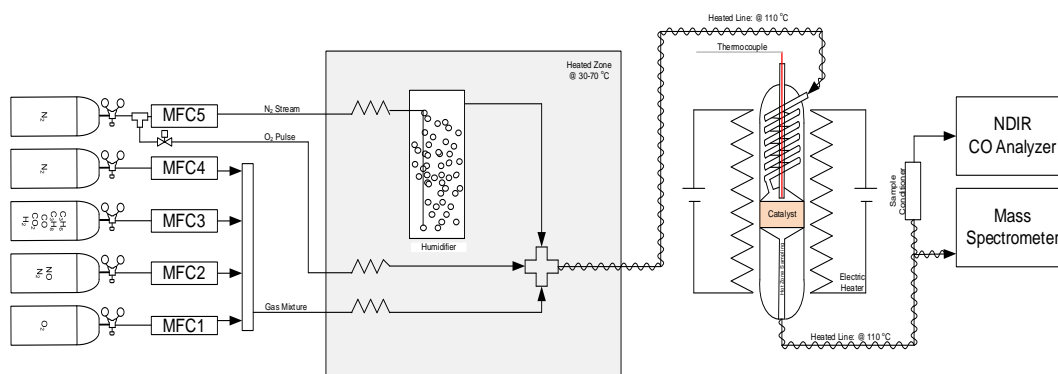


Figure 3.2. Schematic representation of TWC performance test system.

Table 3.1 Operational Parameters for Performance Test System

<b>Performance Test Conditions</b>	
C <sub>3</sub> H <sub>6</sub>	370 ppm
C <sub>3</sub> H <sub>8</sub>	120 ppm
CO	10000 ppm
H <sub>2</sub>	2310 ppm
CO <sub>2</sub>	10.000 %
NO	1500 ppm
SO <sub>2</sub>	0.000/20 ppm
O <sub>2</sub>	5800-9400 ppm
H <sub>2</sub> O	10 %



Table 3.1 (cont'd)

N <sub>2</sub>	Balance
Temperature	600 °C to r.t. by natural cooling
GHSV	50000 h <sup>-1</sup>

### 3.5.1 Catalyst Aging

Produced catalysts are aged under a wet air stream (1:10 water:air, mol/mol). The volumetric flow rate of air is set to 2240 ml/min and the liquid water flow rate is set to 0.18 ml/min. GHSV is kept at 50000 h<sup>-1</sup> which is equal to activity test conditions. As illustrated in the Figure 3.3, the monolithic catalyst sample is installed in a quartz reactor having 22 mm diameter. The tubular reactor is operated vertically and the flow is directed from up to down, as in the activity test system. Temperature reading is obtained inside the reactor just over the catalyst and temperature control is managed according to this reading. Catalysts are aged at 1000°C for 3 hours. The tubular furnace is heated at a rate of 5°C/min and after aging is completed the wet air flow is stopped and the reactor cools down naturally.

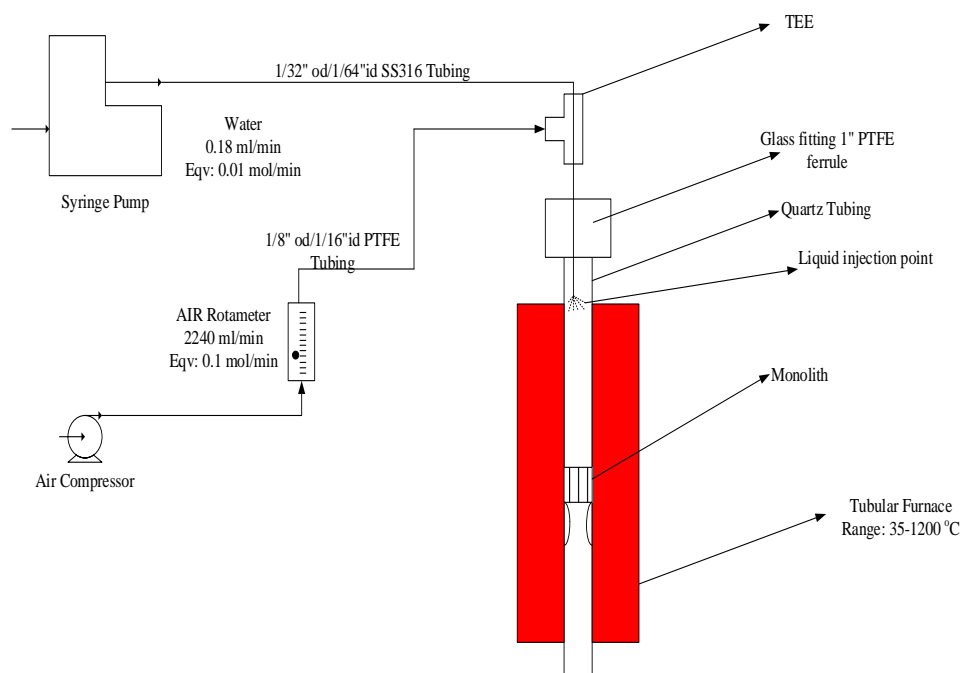


Figure 3.3. Catalyst aging system.

### 3.5.2 SO<sub>2</sub> Poisoning of Catalysts

Both monolithic and powder catalysts are poisoned under reaction conditions shown in Table 3.1 with 20ppm SO<sub>2</sub> inclusion to upstream gas mixture. The volumetric flow rate of air is set to 2240 ml/min and the GHSV is kept at 50000 h<sup>-1</sup>. Poisoning starts by programmed a temperature increase from 150 °C to 600 °C at a rate of 5 °C/ min. Once 600 °C temperature is reached the reactor is hold at that temperature for three hours and then left to natural cooling. In order to investigate the effect of poisoning, treated catalyst again subjected to the standard test procedure without any SO<sub>2</sub> presence in reactant mixture. The detailed calculations for catalytic performance evaluation are presented in Appendix E.

## CHAPTER 4

### RESULTS AND DISCUSSION

#### 4.1 Catalysts Tested in the Study

The catalytic performances of four (C1-C4) different catalysts are reported in this study. Their dry-based nominal compositions and actual noble metal loadings are summarized in Table 4.1. The details of calculation for actual noble metal loading is shown in Appendix B. The benchmark catalyst, C1, is chosen due to its promising fresh, thermally aged and SO<sub>2</sub> poisoned performances obtained in the study conducted in our laboratory previously [282]. C1 catalyst is produced by following the same procedure used in the aforementioned study, the procedure is given in the Appendix A. C1 catalyst, wash-coated on a cordierite monolith, is comprised of dispersed noble metals impregnated on Ce<sub>0.8</sub>Zr<sub>0.2</sub>O<sub>2</sub> and  $\gamma$ -Al<sub>2</sub>O<sub>3</sub>. Palladium and rhodium are used as noble metals with nominal loadings of 0.65% wt. and 0.1% wt., respectively. C2 is the novel catalyst that contains perovskite as active material. It is wash-coated on a cordierite monolith and comprised of LaFe<sub>0.57</sub>Co<sub>0.37</sub>Pd<sub>0.06</sub>O<sub>3</sub>, LaFe<sub>0.57</sub>Co<sub>0.37</sub>Rh<sub>0.06</sub>O<sub>3</sub>, Ce<sub>0.8</sub>Zr<sub>0.2</sub>O<sub>2</sub> and  $\gamma$ -Al<sub>2</sub>O<sub>3</sub>. C2 also contains 0.10% wt. rhodium and 0.65% wt. palladium, nominally but unlike C1 these metals are located in perovskite structure. C3 and C4 are produced for the investigation of the noble metal decrease on the TWC performance of the perovskite-based catalyst C2.

Table 4.1. Nominal dry based composition of the catalysts studied.

	<b>Ce<sub>0.8</sub>Zr<sub>0.2</sub>O<sub>2</sub></b> <b>(wt. %)</b>	<b>Al<sub>2</sub>O<sub>3</sub></b> <b>(wt. %)</b>	<b>Perovskite</b> <b>(wt. %)</b>	<b>Rh</b> <b>(wt. %)</b>	<b>Pd</b> <b>(wt. %)</b>	<b>Actual NM Loading</b> <b>(g/ft<sup>3</sup>)</b>
C1	27.300	71.950	0.000	0.100	0.650	20.165
C2	27.300	42.650	29.300	0.100	0.650	20.332
C3	27.300	57.675	14.650	0.050	0.325	10.383
C4	27.300	69.695	2.930	0.010	0.065	2.038

Catalytic performance of each fresh catalyst is tested in the dynamic test system. In order to evaluate the performance of a catalyst, %50 (T50) conversion temperatures of H<sub>2</sub>, CO, O<sub>2</sub>, C<sub>3</sub>H<sub>6</sub>, C<sub>3</sub>H<sub>8</sub> and NO (i.e., light-off temperature) are used as the performance indicators. In order to eliminate temperature irregularities during heating period of reactor, only the data during cooling period, which happens by natural convection, are reported. Moreover, in order to ensure repeatability, each catalyst is tested at least three times. The detailed S curves for cooling period of catalytic performance tests is presented in Appendix F and Appendix G.

In addition to fresh performance tests, all of four catalysts are further investigated on their resistances towards hydrothermal aging and SO<sub>2</sub> poisoning. The changes in the activities of the catalysts after thermal and chemical aging are compared. Obtained performance change characteristics are tried to be explained via characterizations techniques such as XRD, BET, ICP-OES, TEM-EDX, DRIFTS-FTIR and pulse chemisorption.

## 4.2 Performance and Durability Comparison of C1 and C2 Catalysts

Catalysts not subjected to any thermal or chemical aging will be referred to as "fresh catalyst" in this study. The performance achieved with fresh catalyst will be referred to as "fresh performance". Fresh performance comparisons of C1 and C2 catalysts are presented in Figure 4.1. Performances obtained for H<sub>2</sub> and C<sub>3</sub>H<sub>6</sub> conversions were quite similar, but C1 showed 32 °C, 13 °C, and 29 °C better light-off temperatures for CO, C<sub>3</sub>H<sub>8</sub>, and NO conversions, respectively. The S curves of fresh C1 catalyst are shown in Appendix G in Figures G1-G5. The catalyst was able to perform H<sub>2</sub> and CO conversions at low temperatures. All of the H<sub>2</sub> is oxidized at about 250 °C. A break in the NO conversion curve is observed at temperatures between 180-230 °C, where the H<sub>2</sub> concentration decreases rapidly (Figure G 2 and Figure G 5). This break, apparent at temperatures between 180-230 °C, has been evaluated as evidence that the H<sub>2</sub>-CO SCR reaction contributes to the NO conversion at low temperatures (equations 5, 16-25). Similarly, a break in NO conversion was also detected between 280-330 °C. This was seen as proof that the CO-NO SCR reaction took place (equations 3, 9-15). The almost cessation of NO conversion from 280 °C to 330 °C, when the CO is completely depleted, showed that the CO-NO SCR reaction was the dominant reaction in the NO conversion. When the conversion curves of C2 catalyst are examined (Figure G6-G10), it was determined that NO conversion starts at 180 °C. At temperatures where the conversion rate of NO gradually increases (approaching the light-off), the depletion of H<sub>2</sub> happened. This has prevented us from understanding how much the H<sub>2</sub>-NO SCR reaction plays with the C2 catalyst. However, the depletion of CO (at 300 °C) stopped the NO conversion completely, and even the conversion gradually decreased, up to 400 °C (Figure G. 10). The resumption of NO conversion above 400 °C was interpreted as the activation of intrafacial mechanisms (mechanisms similar to Mars and Van Krevelen) on the perovskite catalyst [8,138,143,212].

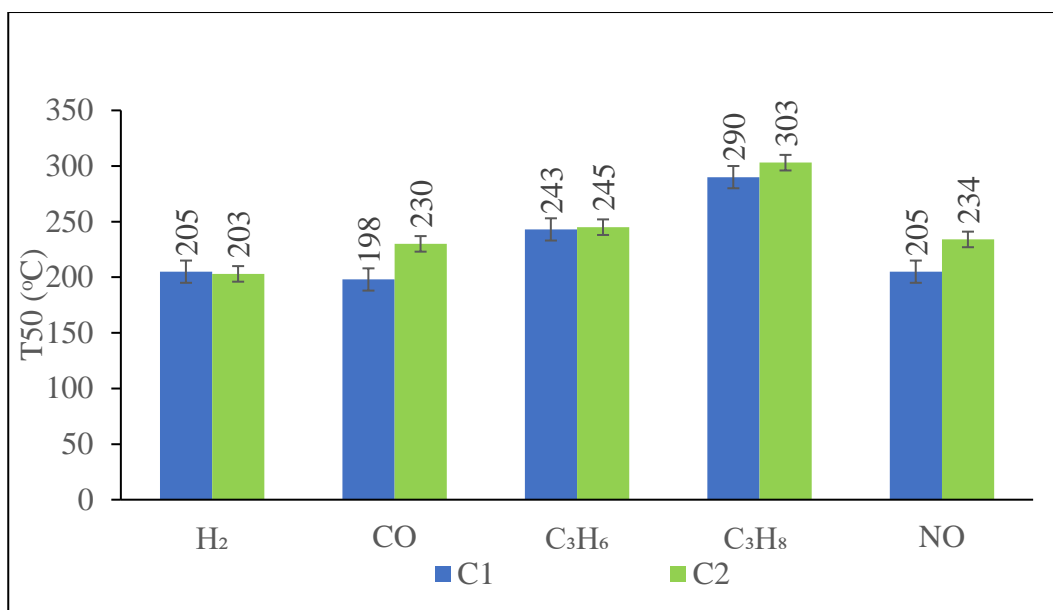


Figure 4.1 Fresh performance comparison of C1 and C2 catalysts.

Once they were hydrothermally aged, the C<sub>3</sub>H<sub>8</sub> and NO conversion performances of C1 catalysts were affected dramatically, as shown in Figure 4.2. The aged C1 catalyst converted 40% and 20% of C<sub>3</sub>H<sub>8</sub> and NO at 600°C, respectively (Figure G. 24 and G. 25). On the other hand, C2 highly preserved its performance upon aging with a 67°C and 32°C increase in light-off temperature for C<sub>3</sub>H<sub>8</sub> and NO, respectively. Here, the increase in the depletion of CO to 400 °C has similarly shifted the reduction and re-increase of the NO conversion to higher temperatures. Although both of the catalysts showed performance losses after aging, the benchmark catalyst C1 showed a more severe performance decrease.

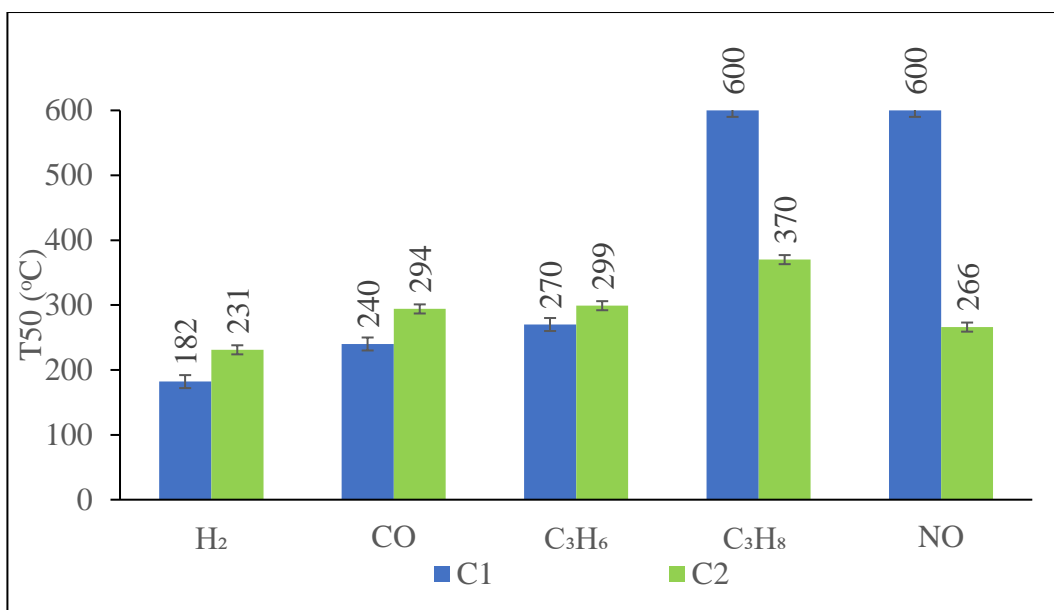


Figure 4.2. Performance comparison of hydrothermally aged C1 and C2 catalysts.

The catalyst samples required for characterization were not collected by scraping off the monolith, instead washcoat catalyst powders were produced, which were exposed to the same conditions as the monolithic catalyst. Noble metal concentration values obtained by ICP-OES analysis of the fresh and hydrothermally aged C1 and C2 catalysts are presented in Table 4.2. The results revealed that the noble metal concentrations were consistent with their corresponding nominal compositions and did not change with hydrothermal aging. This shows that the decrease in activity was not related to loss of noble metal content but was rather related to morphological and electronic changes that took place.

Table 4.2. ICP-OES analysis: measured noble metal concentrations of fresh and aged catalysts.

Catalyst	Measured Concentration	
	wt. %	
	Pd	Rh
C1-Fresh	$0.65 \pm 0.01$	$0.103 \pm 0.003$
C1-Aged	$0.65 \pm 0.01$	$0.104 \pm 0.003$
C2- Fresh	$0.65 \pm 0.01$	$0.101 \pm 0.003$
C2-Aged	$0.65 \pm 0.01$	$0.102 \pm 0.003$

BET surface areas, average pore volumes, and average pore diameters for fresh and aged catalysts are presented in Table 4.3. The results indicate that textural properties of both catalysts were damaged considerably with hydrothermal aging. The losses in surface areas (53% for C1 and 46% for C2) and pore volumes (60% for C1 and 54% for C2), together with the increases in pore diameter were evidence for the collapse of the smallest pores available in the structure. The close textural changes after thermal aging in both catalysts, and the inability of the C1 catalyst to maintain its activity to the same extent indicates that the activity was not directly related to textural changes.



Table 4.3. Textural properties of fresh and hydrothermally aged catalysts.

<b>Catalyst</b>	<b>BET Surface Area m<sup>2</sup>/g</b>	<b>Average Pore Volume cc/g</b>	<b>Average Pore Diameter Å</b>
<b>C1-Fresh</b>	51	0.15	31
<b>C1-Aged</b>	24	0.06	67
<b>C2- Fresh</b>	58	0.28	14
<b>C2-Aged</b>	31	0.13	28

Figure 4.3 shows the XRD patterns of the fresh and aged C1 catalyst.  $\gamma$ -Al<sub>2</sub>O<sub>3</sub> and Ce<sub>0.8</sub>Zr<sub>0.2</sub>O<sub>2</sub> diffraction peaks were clearly detected in fresh C1 sample. Apart from  $\gamma$ -Al<sub>2</sub>O<sub>3</sub> and Ce<sub>0.8</sub>Zr<sub>0.2</sub>O<sub>2</sub> peaks, no palladium or rhodium peaks were observed due to low loading. After aging the sample, peaks grew sharper and delta-Al<sub>2</sub>O<sub>3</sub> peaks appeared. The average crystallite size, calculated by Scherrer equation, increased from 2.9 nm ( $2\theta = 37.01^\circ$ , FWHM= 3.0°,  $\lambda = 1.54 \text{ \AA}$ ) to 9.0 nm ( $2\theta = 37.01^\circ$ , FWHM= 0.97°,  $\lambda = 1.54 \text{ \AA}$ ) and from 5.90 nm ( $2\theta = 28.86^\circ$ , FWHM= 1.52°,  $\lambda = 1.54 \text{ \AA}$ ) to 35.6 nm ( $2\theta = 28.86^\circ$ , FWHM= 0.241°,  $\lambda = 1.54 \text{ \AA}$ ) for  $\gamma$ -Al<sub>2</sub>O<sub>3</sub> and Ce<sub>0.8</sub>Zr<sub>0.2</sub>O<sub>2</sub>, respectively. Figure 4.4 shows the patterns of the C2 catalyst. In addition to  $\gamma$ -Al<sub>2</sub>O<sub>3</sub> and Ce<sub>0.8</sub>Zr<sub>0.2</sub>O<sub>2</sub> diffraction peaks, LaFe<sub>x</sub>Co<sub>1-x</sub>O<sub>3</sub> peaks were also detected for the fresh catalysts. Similarly, sharper peak growth and delta-Al<sub>2</sub>O<sub>3</sub> phase formations were observed for the C2 catalyst sample. The average crystallite size increased from 22.90 ( $2\theta = 22.86^\circ$ , FWHM= 0.37°,  $\lambda = 1.54 \text{ \AA}$ ) nm to 40.20 nm ( $2\theta = 22.86^\circ$ , FWHM= 0.21°,  $\lambda = 1.54 \text{ \AA}$ ), from 4.60 nm ( $2\theta = 41.01^\circ$ , FWHM= 1.9°,  $\lambda = 1.54 \text{ \AA}$ ) to 19.10 nm ( $2\theta = 37.01^\circ$ , FWHM= 0.46°,  $\lambda = 1.54 \text{ \AA}$ ), and from

6.50 nm ( $2\theta = 28.86^\circ$ , FWHM= 1.32°,  $\lambda = 1.54 \text{ \AA}$ ) to 27.40 nm ( $2\theta = 28.86^\circ$ , FWHM= 0.31°,  $\lambda = 1.54 \text{ \AA}$ ) for  $\text{LaFe}_{0.6}\text{Co}_{0.4}\text{O}_3$ ,  $\text{Al}_2\text{O}_3$ , and  $\text{Ce}_{0.8}\text{Zr}_{0.2}\text{O}_2$ , respectively. Figure 4.5 shows the XRD patterns of  $\text{LaCoO}_3$ ,  $\text{LaFe}_{0.6}\text{Co}_{0.4}\text{O}_3$  and  $\text{LaFe}_{0.57}\text{Co}_{0.37}\text{Pd}_{0.06}\text{O}_3$  structures. By adding iron to the  $\text{LaCoO}_3$  structure (PDF card no: 01-0186-1662),  $\text{LaFe}_{0.6}\text{Co}_{0.4}\text{O}_3$  (PDF card no: 01-073-2814) shifted the  $2\theta$  peak from  $32.98^\circ$  to  $32.72^\circ$ . The reason for this is that the ionic radii of  $\text{Fe}^{+3}$  is larger than that of  $\text{Co}^{+3}$  and the lattice expands accordingly. Similarly, adding palladium to the  $\text{LaFe}_{0.6}\text{Co}_{0.4}\text{O}_3$  structure also had the same effect on lattice expansion and the apparent  $2\theta$  peak at  $32.72^\circ$  shifted to  $32.60^\circ$ . These data are accepted as evidence of palladium inclusion into the perovskite structure.

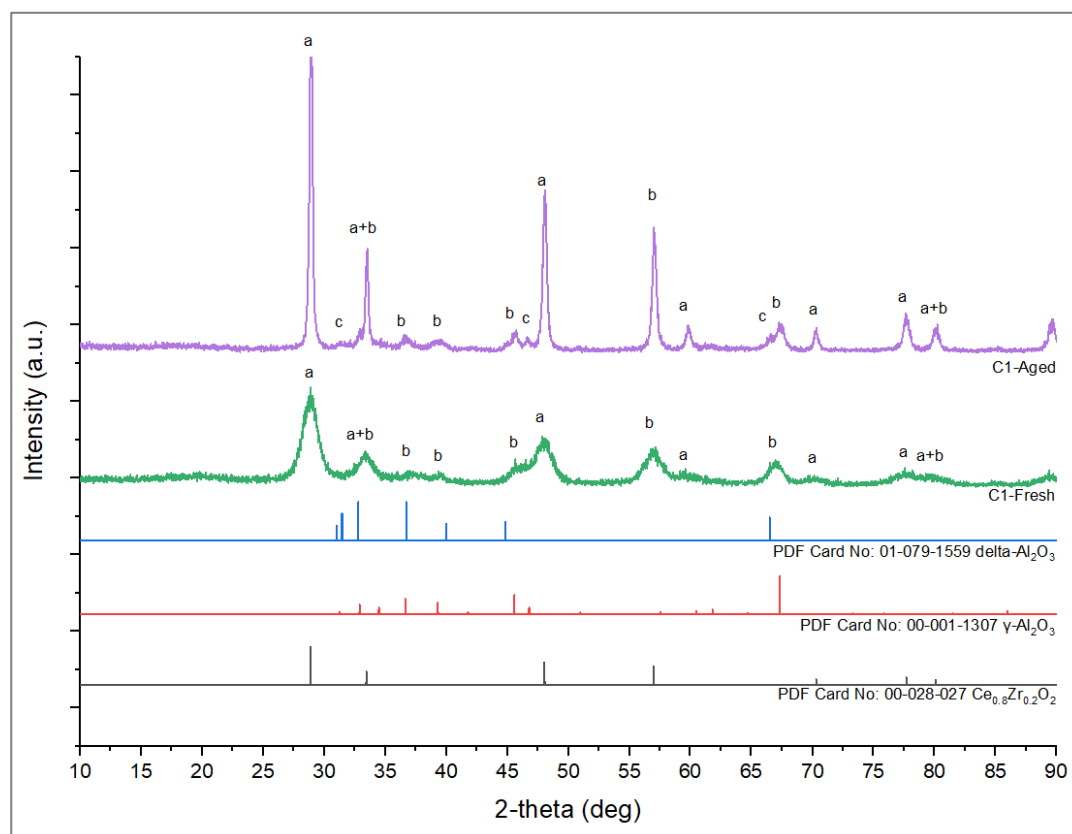


Figure 4.3. XRD pattern of fresh and aged C1 catalyst. (a:  $\text{Ce}_{0.8}\text{Zr}_{0.2}\text{O}_2$  b:  $\gamma\text{-Al}_2\text{O}_3$  c:  $\delta\text{-Al}_2\text{O}_3$ )

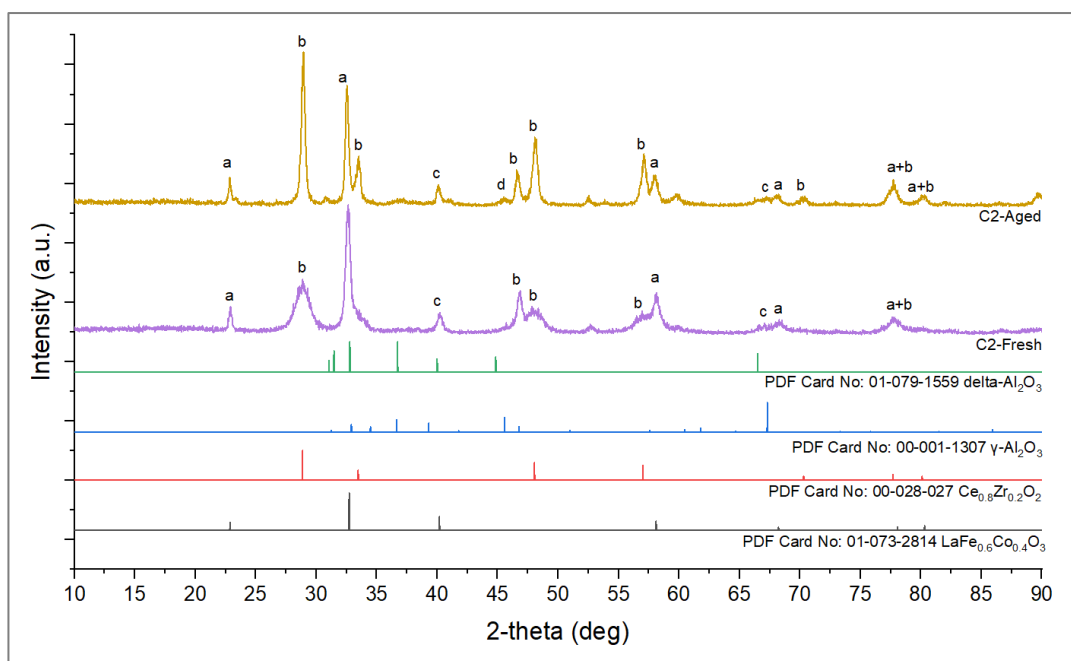


Figure 4.4. XRD pattern of fresh and aged C2 catalyst. (a:  $\text{LaFe}_{0.57}\text{Co}_{0.37}\text{Pd}_{0.06}\text{O}_3$  b:  $\text{Ce}_{0.8}\text{Zr}_{0.2}\text{O}_2$  c:  $\gamma\text{-Al}_2\text{O}_3$ )

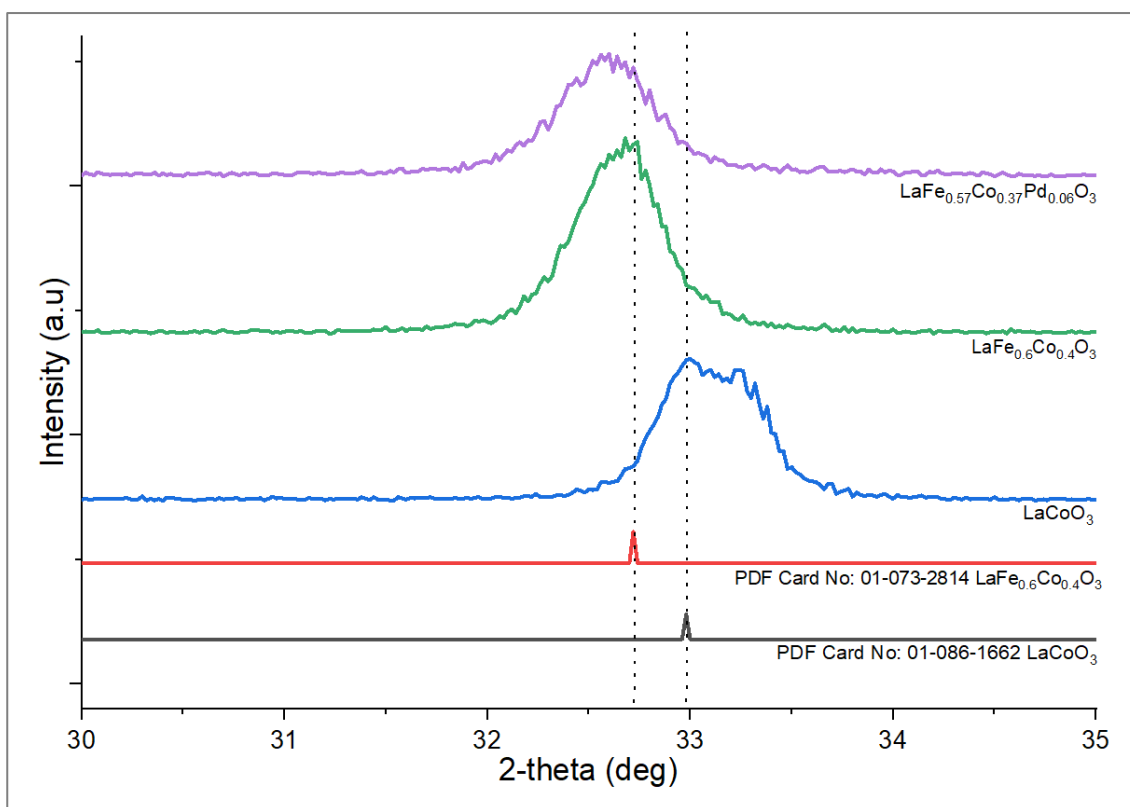


Figure 4.5 XRD patterns of  $\text{LaCoO}_3$ ,  $\text{LaFe}_{0.6}\text{Co}_{0.4}\text{O}_3$  and  $\text{LaFe}_{0.57}\text{Co}_{0.37}\text{Pd}_{0.06}\text{O}_3$  structures.

The TEM-EDX results for fresh and aged samples are shown in Figure 4.6-9. The crystallite size growth during the aging process was also evident in TEM images of both C1 and C2 catalyst samples, which was also in agreement with the BET and XRD characterization results. The beam was focused on small crystallites with spherical shape and weakly attached over surface that resemble Pd particles, and ten scans sampling of the sample were performed with EDX. Palladium peaks were observed for both fresh and aged C1 catalyst samples, as shown in Figure 4.6 and Figure 4.7. In contrast, no Pd peak was found in the EDX scan of the perovskite catalyst. The possibility that palladium atoms were not found in clusters was thought to be the reason for this, Figure 4.8-9.

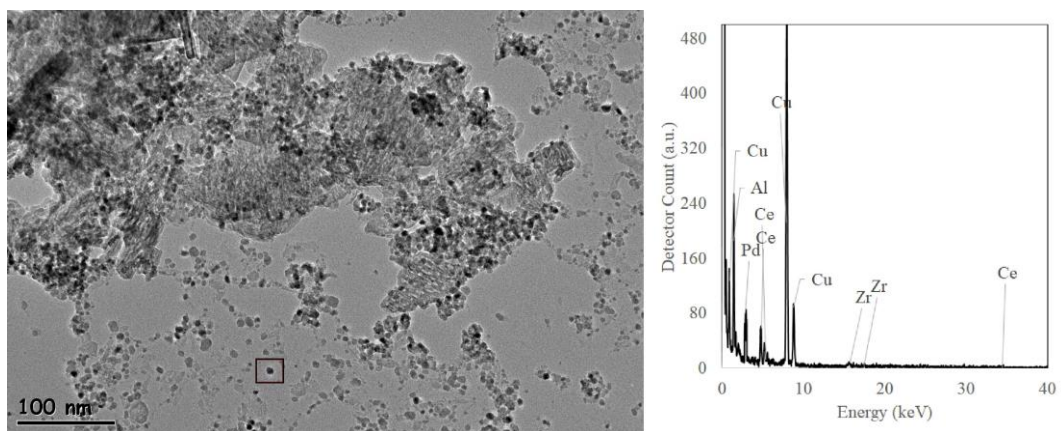


Figure 4.6. TEM Image and EDX pattern for the marked point for fresh C1 catalyst.

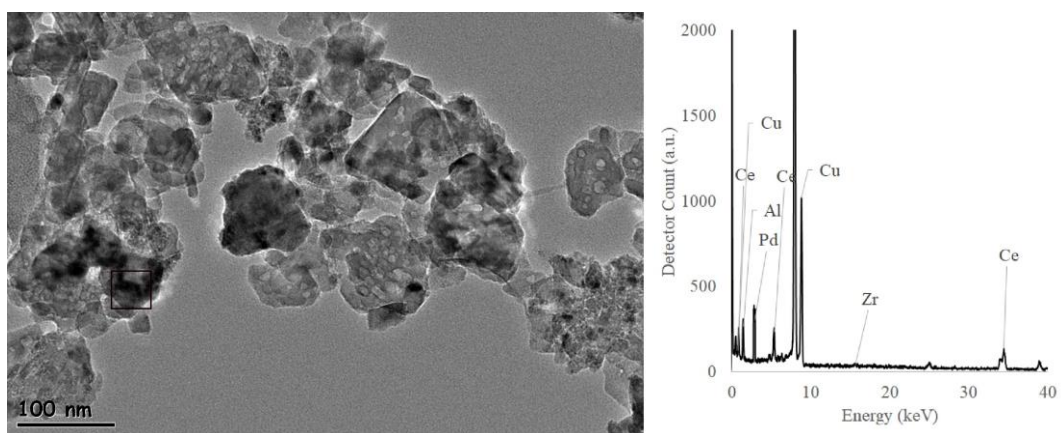


Figure 4.7. TEM Image and EDX pattern for the marked point for hydrothermally aged C1 catalyst.

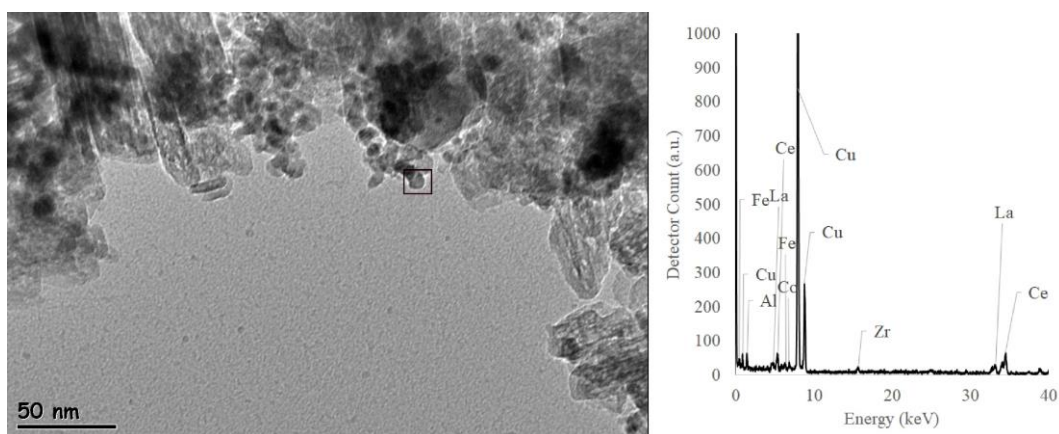


Figure 4.8. TEM Image and EDX pattern for the marked point for fresh C2 catalyst.

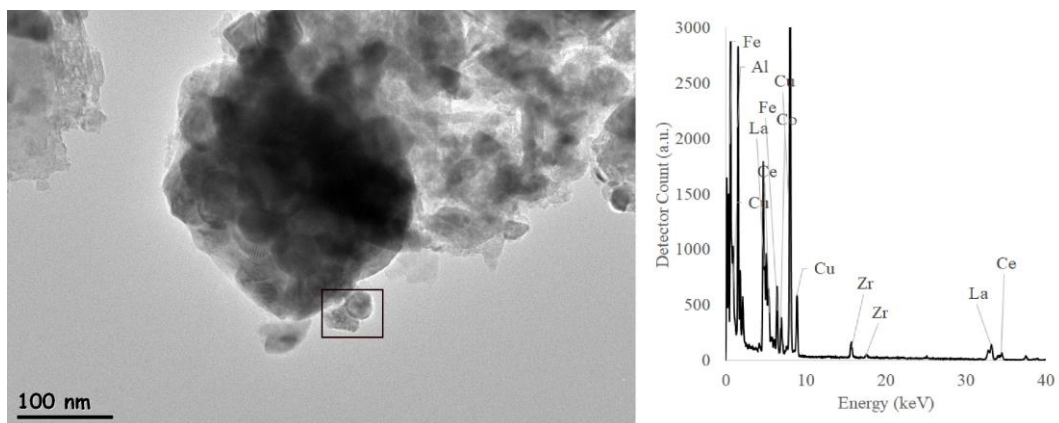


Figure 4.9. TEM Image and EDX pattern for the marked point for hydrothermally aged C2 catalyst.

The effects of SO<sub>2</sub> poisoning on the C1 and C2 catalysts are shown in Figure 4.10. Light-off temperature increase after SO<sub>2</sub> poisoning of C1 were measured as 35°C, 55°C, 26°C, 150°C and 35°C for H<sub>2</sub>, CO, C<sub>3</sub>H<sub>6</sub>, C<sub>3</sub>H<sub>8</sub>, and NO, respectively. On

the other hand, the light off temperature increase for C2 were measured as 38°C, 50°C, 5°C, 67°C, and 9°C for H<sub>2</sub>, CO, C<sub>3</sub>H<sub>6</sub>, C<sub>3</sub>H<sub>8</sub>, and NO, respectively. The C1 catalyst was affected more severely, especially for C<sub>3</sub>H<sub>6</sub>, C<sub>3</sub>H<sub>8</sub> and NO conversions compared to C2 catalyst.

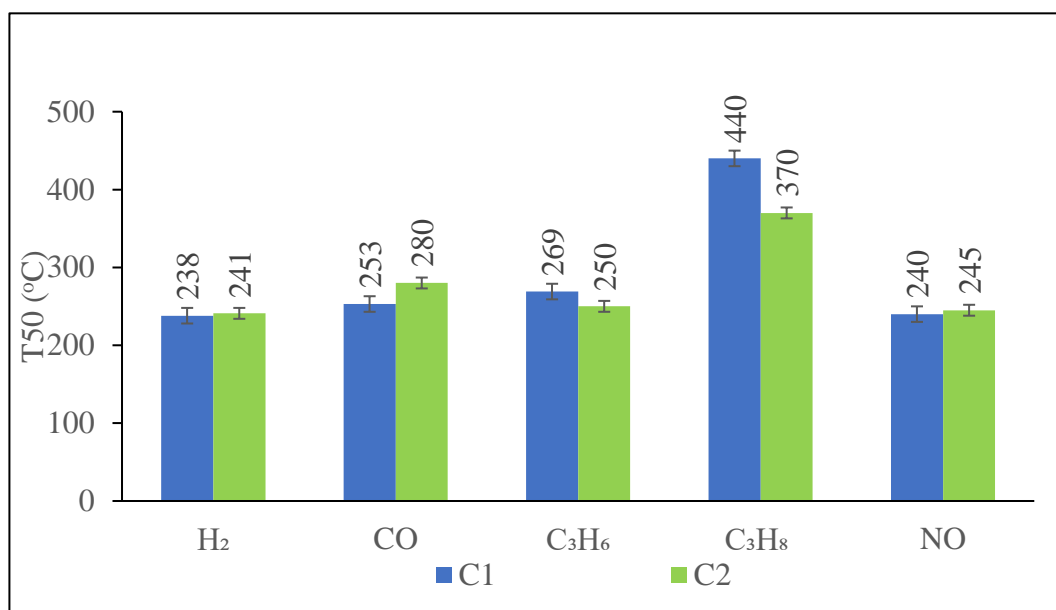


Figure 4.10. Performance comparison of SO<sub>2</sub> poisoned C1 and C2 catalysts.

To investigate the changes in the active sites after heat treatment and SO<sub>2</sub> exposure, CO pulse chemisorption experiments were carried out. With this method, the CO uptake capacity, the number of CO moles sorbed by gram of catalyst, is determined and this value is used as an indicator for the accessible active sites of the catalyst. The pulse chemisorption graph of each catalyst is presented in Figure 4.11-a-f), in which the area under each peak indicates the amount of CO that cannot be sorbed by the catalyst. According to the sorption dynamics, the first seven pulses were adsorbed by fresh C1 catalyst (Figure 4.11-a), with total sorption of the first five

pulses. For aged C1 only partial sorption of the first pulse (Figure 4.11-b) and SO<sub>2</sub>-poisoned C1 catalysts, only partial sorption of the first and earliest three pulses (Figure 4.11-c) were observed. The fresh C2 catalyst sample adsorbed the first six pulses, with only the first pulse adsorbed totally (Figure 4.11-d). The sorption of the first four pulses was recorded for aged and poisoned C2 catalyst samples, with total sorption only in the first pulses (Figure 4.11-e and f).

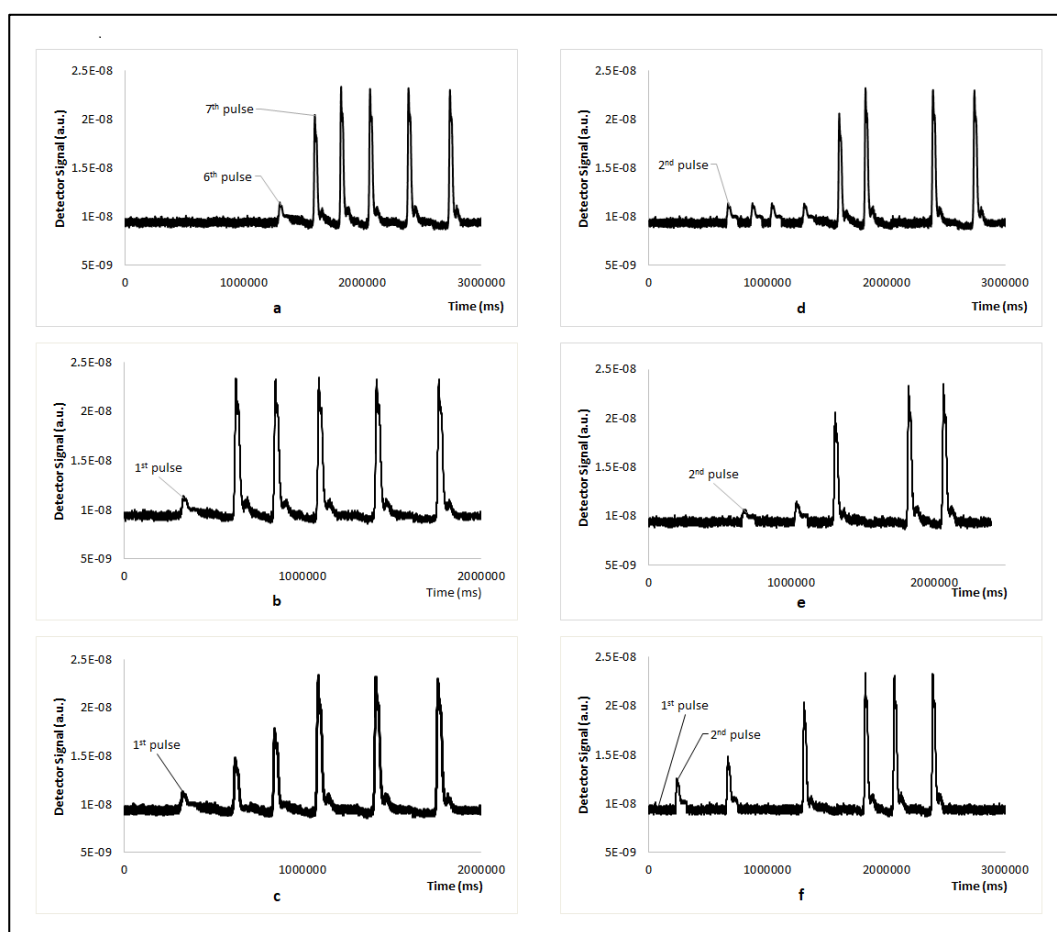


Figure 4.11. CO pulse chemisorption graph of fresh C1 (a), hydrothermally aged C1 (b), SO<sub>2</sub> poisoned C1 (c), fresh C2 (d), hydrothermally aged C2 (e), SO<sub>2</sub> poisoned C2 (f) catalyst samples.



The changes in the CO uptake capacities of C1 and C2 catalysts after heat treatment and SO<sub>2</sub> exposure is shown in Table 4.4. On the assumption that CO molecules are sorbed by Pd atoms in C1 catalyst, dispersion and average crystallite size of Pd atoms were calculated in this catalyst. Accordingly, hydrothermal aging caused the Pd crystallite size to grow from 3.4 nm to 28.1 nm. Instead of comparing dispersion to understand the effect of poisoning with SO<sub>2</sub>, the active Pd surface area comparison would be more realistic. Accordingly, with SO<sub>2</sub> poisoning, the active Pd surface area decreased from 0.9 (m<sup>2</sup>/g catalyst) to 0.4 (m<sup>2</sup>/g catalyst). As a result of these changes in C1 catalyst, total CO uptake (mmol/g catalyst) decreased 85% after aging and 60% after SO<sub>2</sub> poisoning of C1 catalyst sample. The assumption that CO molecules are only captured by Pd atoms in the C2 catalyst would not be a realistic assumption because CO molecules can be captured by both Fe<sup>+2/+3</sup> and Co<sup>+2/+3</sup> cations. Therefore, it was preferred to compare the changes in this catalyst only on the CO uptake capacity. The fresh C2 catalyst sample showed 30 % less CO uptake capacity compared to that of fresh C1 catalyst. However, aging did not affect the CO uptake capacity of the C2 catalyst as it did in the case of C1 catalyst; only a 25 % decrease in CO uptake was recorded. The CO pulse chemisorption results were consistent with the performance tests, suggesting that the dispersed metal catalyst was less resistant to thermal aging and poisoning.

Table 4.4. Total CO uptake for tested catalyst samples.

<b>Catalyst Sample</b>	<b>Uptake (mmol CO/g cat)</b>	<b>Active Pd Surface Area per g Catalyst (m<sup>2</sup>/g)</b>	<b>%Dispersion of Pd</b>	<b>Average Pd Crystallite Size (nm)</b>
Fresh C1	0.0112	0.9	27.6	3.4

Table 4.4 (cont'd)

Aged C1	0.0016	0.1	4.0	28.1
SO <sub>2</sub> poisoned C1	0.0044	0.4	NA	NA
Fresh C2	0.0077	NA	NA	NA
Aged C2	0.0058	NA	NA	NA
SO <sub>2</sub> poisoned C2	0.0040	NA	NA	NA

The DRIFTS-FTIR absorbance spectra of both for fresh and SO<sub>2</sub> poisoned C1 catalyst samples are shown in Figure 4.12. At 1160–1200 cm<sup>-1</sup>, the formation of bulk Al<sub>2</sub>(SO<sub>4</sub>)<sub>3</sub> on the poisoned catalyst was detected. Due to low Pd loading, the band at ~1435 cm<sup>-1</sup>, corresponding to  $\nu$  (S = O) of Pd-SO<sub>4</sub> was not found. However, together with aluminum sulfate formation, it is known that Al<sub>2</sub>O<sub>3</sub> favors the formation of PdSO<sub>4</sub> via spillover of sorbed SO<sub>x</sub> to PdO surface [27,288]. It can be assumed that other peaks are material-originated ones, as they existed in both spectra, and band positions were not changed or affected by poisoning. The formation of bulk aluminum sulfates and PdSO<sub>4</sub> were due to reactions that took place between Al<sub>2</sub>O<sub>3</sub> (the porous support material) and SO<sub>2</sub>. Consequently, formed bulk Al<sub>2</sub>(SO<sub>4</sub>)<sub>3</sub> and inhibition of active sites were the main reasons for the activity loss for the dispersed metallic catalyst.

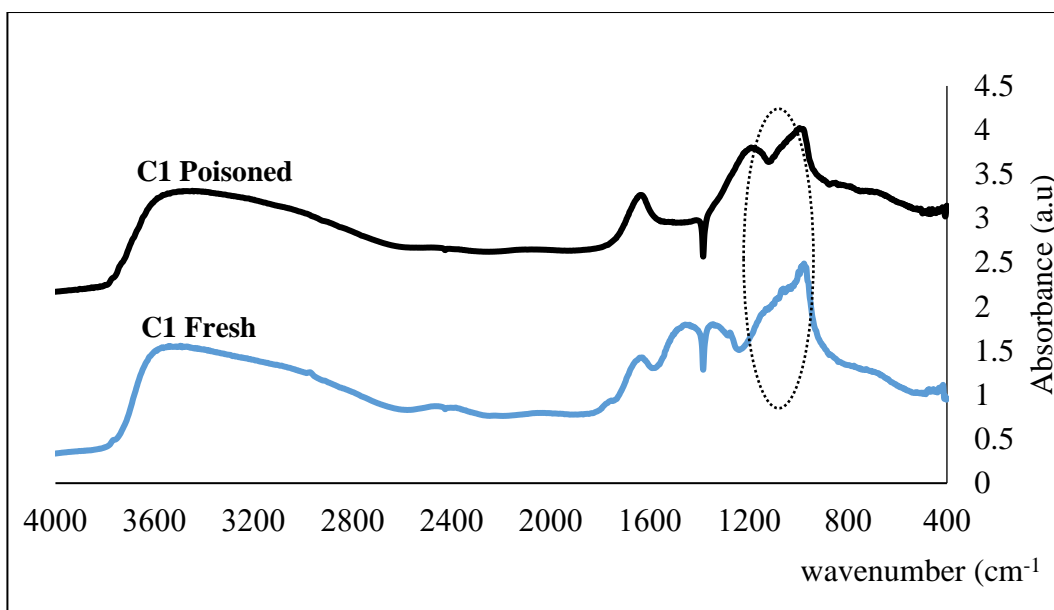


Figure 4.12. DRIFTS Absorbance Spectra for Fresh and SO<sub>2</sub> Poisoned C1 catalyst sample.

As shown in the DRIFTS-FTIR absorbance spectra of both for fresh and SO<sub>2</sub> poisoned C2 catalyst in Figure 4.13, at 1160–1200 cm<sup>-1</sup>, the formation of bulk Al<sub>2</sub>(SO<sub>4</sub>)<sub>3</sub> on the poisoned catalyst was not detected [288–290]. On the other hand, the bands at ~1635 cm<sup>-1</sup> and 3000–3600 cm<sup>-1</sup> indicated bulk FeSO<sub>4</sub> formation [291]. Moreover, the band at ~1435 cm<sup>-1</sup> that corresponded to the ν (S=O) of PdSO<sub>4</sub> was not found. It can be inferred that SO<sub>2</sub> attack was first focused on Fe atoms within the perovskite structure before the Al<sub>2</sub>O<sub>3</sub>. Formation of bulk FeSO<sub>4</sub> did not affect the performance of perovskite-based catalyst dramatically which may also mean the formation of PdSO<sub>4</sub> did not take place in perovskite-based catalyst as in the case of dispersed metallic catalyst.

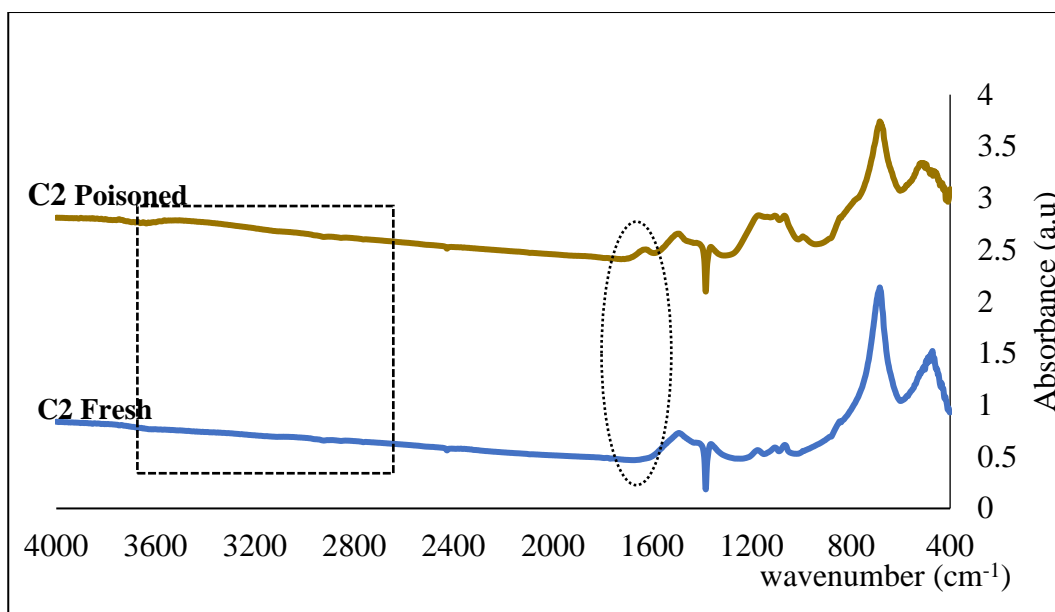


Figure 4.13. DRIFTS absorbance spectra for fresh and SO<sub>2</sub>-poisoned C2 catalyst samples.

### 4.3 Effect of Noble Metal Loading on the Performance and Durability of the Perovskite-based Catalyst

As shown in Table 4.1, noble metal loading of both benchmark and perovskite containing catalysts are 20g/ft<sup>3</sup>. It is also shown that the performance of benchmark catalyst was completely lost after hydrothermal aging. On the other hand, the performance of perovskite-based catalyst did not change significantly after hydrothermal aging. Considering these findings, a new experiment set is planned to investigate the effect of decreasing noble metal loading on the performance and durability of perovskite-based catalyst. According to the new experiment plan, 50% (10g/ft<sup>3</sup> noble metal loading, catalyst code C3) and 10% (2g/ft<sup>3</sup> noble metal loading catalyst code C4) of initial noble loading were tested for their fresh, hydrothermally aged and SO<sub>2</sub> poisoned performances. Detailed synthesis procedures for C3 and C4 are given in the Appendix A.

Fresh performance comparison of C1, C2, C3 and C4 are shown in Figure 4.14. It can be observed that C2 and C3 has almost the same performance. So, decreasing the noble metal loading from 20g/ft<sup>3</sup> to 10g/ft<sup>3</sup> did not change the performance of perovskite containing catalyst. Decreasing noble metal loading from 20g/ft<sup>3</sup> (C2) to 2g/ft<sup>3</sup> (C4) increased the 50% conversion temperature of C<sub>3</sub>H<sub>8</sub> and NO by 40 and 23 °C, respectively.

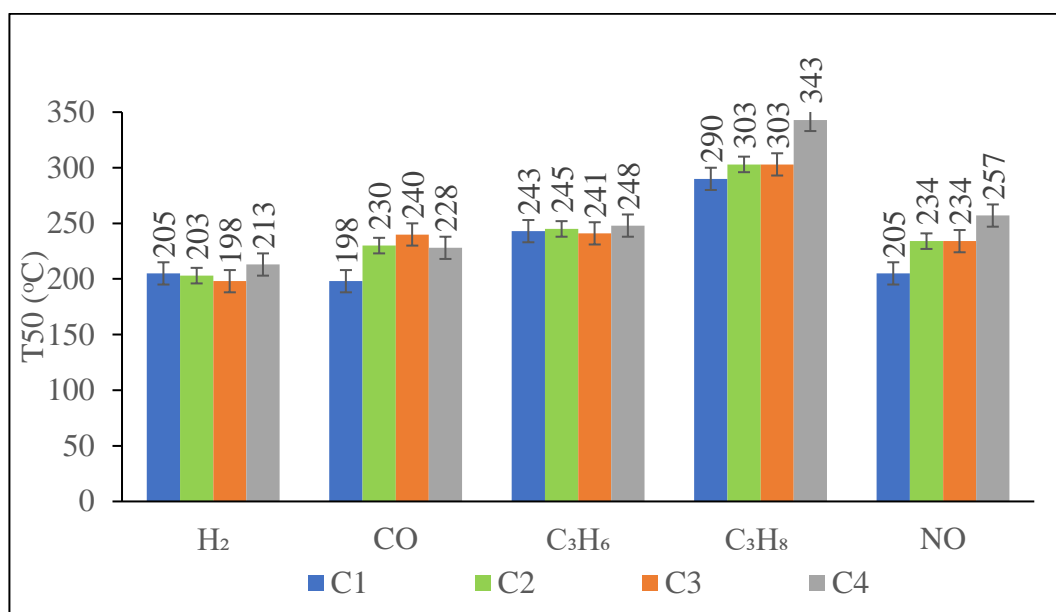


Figure 4.14. Fresh performance comparison of C1, C2, C3, C4 catalysts.

There were no dramatic differences between the fresh performances of C1, C2, C3 and C4 catalysts since complete conversion of all species were achieved. Performance change of C3 and C4 upon hydrothermal aging at 1000 °C for 3 hours and comparison of results to that of C1 and C2 is shown in Figure 4.15. It can be observed that hydrothermal aging at 1000 °C for 3 hours could not differentiate the performances of C2 and C3. In other words, perovskite containing catalyst having 10g/ft<sup>3</sup> noble metal loading (C3) shows the same thermal resistance with perovskite

containing catalyst having 20g/ft<sup>3</sup> noble metal loading (C2). Perovskite containing catalyst having 2g/ft<sup>3</sup> noble metal loading (C4) did not completely lose its performance as in the case of benchmark catalyst. That is the striking evidence for the thermal resistance of perovskite structure.

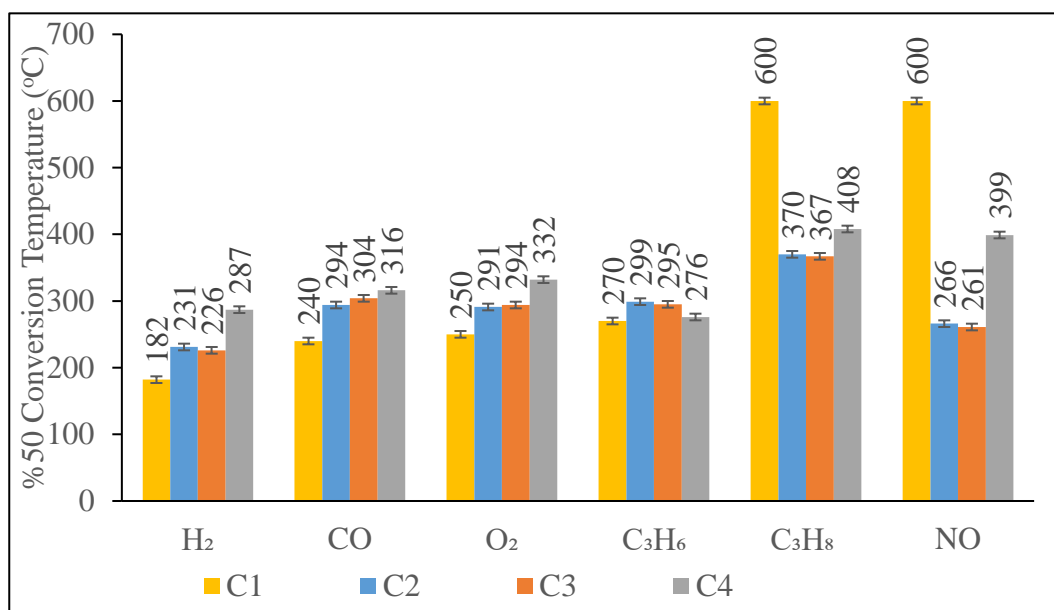


Figure 4.15. Performance comparison of C1, C2, C3, C4 catalysts after hydrothermal aging.

Considering the performances after SO<sub>2</sub> poisoning of four catalysts, shown in Figure 4.16, it can be observed that all of the catalysts lose its performance after SO<sub>2</sub> exposure. As mentioned earlier all four catalysts were exposed to SO<sub>2</sub> flow for 3 hours, under reaction conditions. However, performance decay of benchmark catalyst (C1) for C<sub>3</sub>H<sub>8</sub> conversion happened faster compared to that of perovskite containing catalyst. For example, after poisoning, C4 showed 30 °C better 50% conversion compared to C1. According to the results, the fresh performances of the perovskite-based catalyst and the benchmark catalyst were close to each other, but the perovskite-based catalyst was more resistant to hydrothermal aging and SO<sub>2</sub>

poisoning Considering the developments of Tier 3 regulation forcing catalysts to be exposed to higher temperature, the increase in precious metal prices, the almost zero sulfur content in fuels; Reducing the content of precious metals in the catalyst content and achieving thermal stabilization in parallel will be the subject of widespread work in the TWC field in the coming years. As further studies, testing and aging of the catalyst in real exhaust conditions should be considered.

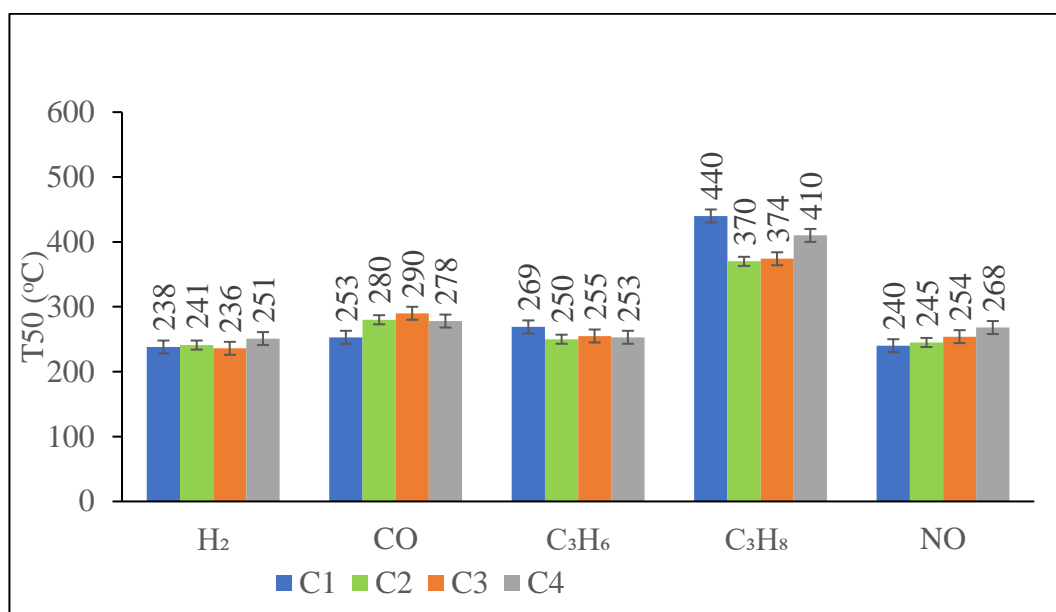


Figure 4.16. Performance comparison of C1, C2, C3, C4 catalysts after SO<sub>2</sub> poisoning.





## CHAPTER 5

### CONCLUSIONS

This study compared the three-way catalytic performance changes of the dispersed palladium/rhodium and the perovskite-based palladium/rhodium catalysts after hydrothermal aging and SO<sub>2</sub> poisoning. Dispersed palladium/rhodium-based catalyst, the benchmark catalyst or C1, is chosen due to its promising fresh, thermally aged and SO<sub>2</sub> poisoned performances obtained in the study conducted in our laboratory previously. C2 is the novel catalyst that contains LaFe<sub>0.57</sub>Co<sub>0.37</sub>Pd<sub>0.06</sub>O<sub>3</sub> and LaFe<sub>0.57</sub>Co<sub>0.37</sub>Rh<sub>0.06</sub>O<sub>3</sub> as active materials. Both C1 and C2 contain 20g/ft<sup>3</sup> nominal noble metal loading with 6.5 Pd/Rh wt./wt. ratio. C3 and C4 are also perovskite-based catalysts with the same active materials and Pd/Rh wt./wt. ratio. But, nominal noble metal loadings of C2 and C3 are 10g/ft<sup>3</sup> and 2g/ft<sup>3</sup>, respectively. Comparing the fresh performances of C1 and C2 catalysts, 50% conversion temperatures obtained with C1 were 32, 2, 13, 29 °C lower for CO, O<sub>2</sub>, C<sub>3</sub>H<sub>6</sub>, C<sub>3</sub>H<sub>8</sub> and NO, respectively, showing C1 has slightly better fresh performance.

Once they were hydrothermally aged, the C<sub>3</sub>H<sub>8</sub> and NO conversion performances of C1 catalysts were affected dramatically, such that, this catalyst was able to convert only 40% and 20% of C<sub>3</sub>H<sub>8</sub> and NO at 600°C, respectively. On the other hand, C2 highly preserved its performance upon aging with a 67°C and 32°C increase in light-off temperature for C<sub>3</sub>H<sub>8</sub> and NO, respectively. Although both of the catalysts showed performance losses after aging, the benchmark catalyst C1 showed a more severe performance decrease. According to the precious metal determination test with ICP-OES, it was understood that hydrothermal aging did not cause a decrease in the precious metal content, and the loss of performance was not related to the reduction of the precious metal amount. XRD revealed that,

adding palladium to the  $\text{LaFe}_{0.6}\text{Co}_{0.4}\text{O}_3$  structure brought about lattice expansion due to larger ionic radii of  $\text{Pd}^{+2}$  and the apparent  $2\theta$  peak at  $32.72^\circ$  shifted to  $32.60^\circ$ . These data were accepted as evidence of palladium inclusion into the perovskite structure. Considering the BET and XRD characterization results, it was confirmed that hydrothermal aging caused growth in crystallite sizes in both catalysts. Considering that the bulk textural properties are closely affected in the two catalysts, the loss of activity was found to be related to active sites.

TEM images also showed that hydrothermal aging caused growths in the bulk crystal chunks and clusters. This finding agrees with the BET and XRD findings. EDX analysis obtained via focusing beam on small crystallites with spherical shape and weakly attached over surface that resemble Pd particles, showed palladium peaks for both fresh and aged C1 catalyst samples. In parallel, CO pulse chemisorption revealed hydrothermal aging caused the Pd crystallite size to grow from 3.4 nm to 28.1 nm in C1 catalyst. On the other hand, Pd peak could not be observed for either fresh or aged C2 catalyst samples, which showed that Pd atoms took place in the perovskite lattice and did not sinter with hydrothermal aging. In addition, hydrothermal aging caused 85% of the CO uptake capacity loss in the dispersed metallic catalyst, which was only 30% in the perovskite-based catalyst.

Comparing the performance of fresh and  $\text{SO}_2$  poisoned benchmark catalyst, 50% conversion temperatures were increased 34, 53, 61, 24, 140 and 31 °C for  $\text{H}_2$ , CO,  $\text{O}_2$ ,  $\text{C}_3\text{H}_6$ ,  $\text{C}_3\text{H}_8$  and NO, respectively, due to poisoning. On the other hand, for the performance of fresh and  $\text{SO}_2$  poisoned perovskite containing catalyst, 50% conversion temperatures were increased 38, 50, 39, 5, 67 and 11 °C for  $\text{H}_2$ , CO,  $\text{O}_2$ ,  $\text{C}_3\text{H}_6$ ,  $\text{C}_3\text{H}_8$  and NO, respectively, due to poisoning. It can be observed that benchmark catalyst was affected more severely especially for  $\text{C}_3\text{H}_6$ ,  $\text{C}_3\text{H}_8$  and NO conversions compared to C2 catalyst. Exposure to 20ppm  $\text{SO}_2$  in the reactant mixture, especially under water vapor atmosphere gave rise to deactivation on both catalysts, but more severe deactivation was observed on the dispersed metallic-

based catalyst than the perovskite-based catalyst. Formation of aluminum sulfates in the dispersed metallic-based catalyst was also considered as an evidence for PdSO<sub>4</sub> formation, which also meant that the pore blockage and active site inhibition took place in this catalyst. On the other hand, only bulk FeSO<sub>4</sub> formation but no evidence of aluminum sulfate formation together with lesser extent of CO uptake capacity loss in perovskite-based catalyst can be attributed to the better poisoning resistance of this catalyst.

10g/ft<sup>3</sup> noble metal loaded perovskite-based catalyst, C3, and 2g/ft<sup>3</sup> noble metal loaded perovskite-based catalyst, C4, were tested for their fresh, hydrothermally aged and SO<sub>2</sub> poisoned performances. Considering the fresh performances, decreasing the noble metal loading from 20g/ft<sup>3</sup> to 10g/ft<sup>3</sup> did not affect the H<sub>2</sub>, CO, O<sub>2</sub>, C<sub>3</sub>H<sub>6</sub>, C<sub>3</sub>H<sub>8</sub> and NO conversions. Decreasing noble metal loading from 20g/ft<sup>3</sup> to 2g/ft<sup>3</sup> increased the 50% conversion temperature of C<sub>3</sub>H<sub>8</sub> and NO by 40 and 24 °C, respectively, but this much low loading still had significant performance. Even, 2g/ft<sup>3</sup> palladium loaded perovskite catalyst showed better performance compared to the benchmark catalyst after hydrothermal aging. So, newly developed catalyst formulations containing perovskite structure was much more thermally stable compared to doped benchmark catalyst. Perovskite containing catalyst having 10g/ft<sup>3</sup> palladium loading showed the same thermal resistance with perovskite containing catalyst having 20g/ft<sup>3</sup> palladium loading. Considering the performances after SO<sub>2</sub> poisoning, all four catalysts were affected in a similar manner but only faster performance decay of benchmark catalyst (C1) for C<sub>3</sub>H<sub>8</sub> conversion was observed compared to that of perovskite containing catalysts.

In summary, the perovskite-based catalyst showed satisfying thermal stability and SO<sub>2</sub> resistance under realistic conditions of gasoline powered engine exhaust where severe mass transfer limitations and fluctuating stoichiometry take place. These findings imply that perovskite-based catalysts can be a potential substitute of the

dispersed metal-based three-way catalysts. Despite the precious metal reduction in these catalysts, preserved performance and stability make them feasible to conduct pilot-scale trials as the next phase.

## REFERENCES

- [1] A. Haynes, *Concepts of Modern Catalysis and Kinetics*, 2005. doi:10.1055/s-2005-866709.
- [2] R.M. Heck, R.J. Farrauto, Automobile exhaust catalysts, *Appl. Catal. A Gen.* 221 (2001) 443–457. doi:10.1016/S0926-860X(01)00818-3.
- [3] I. Chorkendorff, J.W. Niemantsverdriet, *Concepts of Modern Catalysis and Kinetics*, 2nd edition, (2007).
- [4] J. Kašpar, P. Fornasiero, Nanostructured materials for advanced automotive de-pollution catalysts, *J. Solid State Chem.* 171 (2003) 19–29. doi:10.1016/S0022-4596(02)00141-X.
- [5] M. V. Twigg, Catalytic control of emissions from cars, *Catal. Today.* 163 (2011) 33–41. doi:10.1016/j.cattod.2010.12.044.
- [6] R.J. Farrauto, R.M. Heck, Catalytic converters: State of the art and perspectives, *Catal. Today.* 51 (1999) 351–360. doi:10.1016/S0920-5861(99)00024-3.
- [7] R.J. Farrauto, R.M. Heck, Environmental catalysis into the 21st century, *Catal. Today.* 55 (2000) 179–187. doi:10.1016/S0920-5861(99)00237-0.
- [8] S. Royer, D. Duprez, F. Can, X. Courtois, C. Batiot-Dupeyrat, S. Laassiri, H. Alamdari, Perovskites as substitutes of noble metals for heterogeneous catalysis: Dream or reality, *Chem. Rev.* 114 (2014) 10292–10368. doi:10.1021/cr500032a.
- [9] D. Hibbitts, E. Iglesia, Prevalence of bimolecular routes in the activation of diatomic molecules with strong chemical bonds (O<sub>2</sub>, NO, CO, N<sub>2</sub>) on catalytic surfaces, *Acc. Chem. Res.* 48 (2015) 1254–1262. doi:10.1021/acs.accounts.5b00063.
- [10] E. Ozensoy, D. Herling, J. Szanyi, NO<sub>x</sub> reduction on a transition metal-free  $\gamma$ -Al<sub>2</sub>O<sub>3</sub> catalyst using dimethylether (DME), *Catal. Today.* 136 (2008) 46–54. doi:10.1016/j.cattod.2007.12.095.
- [11] S. Royer, D. Duprez, Catalytic Oxidation of Carbon Monoxide over Transition Metal Oxides, *ChemCatChem.* 3 (2011) 24–65. doi:10.1002/cctc.201000378.
- [12] J. Kašpar, P. Fornasiero, N. Hickey, Automotive catalytic converters: Current status and some perspectives, *Catal. Today.* 77 (2003) 419–449. doi:10.1016/S0920-5861(02)00384-X.
- [13] M. Shelef, R.W. McCabe, Twenty-five years after introduction of

automotive catalysts: what next?, *Catal. Today*. 62 (2000) 35–50.  
doi:10.1016/S0920-5861(00)00407-7.

- [14] N. Hooftman, M. Messagie, J. Van Mierlo, T. Coosemans, A review of the European passenger car regulations – Real driving emissions vs local air quality, *Renew. Sustain. Energy Rev.* 86 (2018) 1–21.  
doi:10.1016/j.rser.2018.01.012.
- [15] P. Katara, Review Paper on Catalytic Converter for Automobile Exhaust Emission, *Int. J. Sci. Res.* 5 (2016) 30–33.  
<https://www.ijsr.net/archive/v5i9/ART20161460.pdf>.
- [16] S. Dey, N.S. Mehta, Automobile pollution control using catalysis, *Resour. Environ. Sustain.* 2 (2020) 100006. doi:10.1016/j.resenv.2020.100006.
- [17] K. Virpi, Poisoning of automotive exhaust gas catalyst components. The role of phosphorus in the poisoning phenomena, 2007.
- [18] K. Zhou, H. Chen, Q. Tian, Z. Hao, D. Shen, X. Xu, Pd-containing perovskite-type oxides used for three-way catalysts, *J. Mol. Catal. A Chem.* 189 (2002) 225–232. doi:10.1016/S1381-1169(02)00177-2.
- [19] E. Robinson, Global aspects of photochemical air pollution, *Adv. Chem. Ser.* 113 (1972) 1–15. doi:10.1021/ba-1972-0113.ch001.
- [20] H.S. Gandhi, G.W. Graham, R.W. McCabe, Automotive exhaust catalysis, *J. Catal.* 216 (2003) 433–442. doi:10.1016/S0021-9517(02)00067-2.
- [21] R.J. Farrauto, M. Deeba, S. Alerasool, Gasoline automobile catalysis and its historical journey to cleaner air, *Nat. Catal.* 2 (2019) 603–613.  
doi:10.1038/s41929-019-0312-9.
- [22] T. Johnson, Vehicular Emissions in Review, *SAE Int. J. Engines.* 7 (2014) 1207–1227. doi:10.4271/2014-01-1491.
- [23] T. Lattimore, Combustion and Emission Of a Direct Injection, *Sae Tech. Pap. Ser.* (2015) 256.
- [24] S. Sinha Majumdar, J.A. Pihl, Impact of Selected High-Performance Fuel Blends on Three-Way Catalyst Light off under Synthetic Spark-Ignition Engine-Exhaust Conditions, *Energy and Fuels.* 34 (2020) 12900–12910.  
doi:10.1021/acs.energyfuels.0c02102.
- [25] ATSDR, Chemical and Physical Information - Gasoline, (1990) 107.  
<https://www.atsdr.cdc.gov/toxprofiles/tp72-c3.pdf>.
- [26] R.K. Lattanzio, J.E. McCarthy, Tier 3 motor vehicle emission and fuel standards, U.S. EU Mot. Veh. Stand. Elem. Considerations Trade Issues. m (2014) 37–54.
- [27] D.L. Mowery, M.S. Graboski, T.R. Ohno, R.L. McCormick, Deactivation of

- PdO-Al<sub>2</sub>O<sub>3</sub> oxidation catalyst in lean-burn natural gas engine exhaust: Aged catalyst characterization and studies of poisoning by H<sub>2</sub>O and SO<sub>2</sub>, *Appl. Catal. B Environ.* 21 (1999) 157–169. doi:10.1016/S0926-3373(99)00017-X.
- [28] M. Tadrous, J.S. Wallace, Achieving Low Emissions From a Biogas Fueled SI Engine Using a Catalytic Converter, (2013) 523. doi:10.1115/icef2012-92090.
- [29] B.T. Screen, Platinum Group Metal Perovskite Catalysts, *Platin. Met. Rev.* 51 (2007) 87–92. doi:10.1595/147106707x192645.
- [30] D. Nevers, Chapter 2 Literature review 2.1 Automotive emissions, (2011). [http://en.wikipedia.org/wiki/Motor\\_vehicle](http://en.wikipedia.org/wiki/Motor_vehicle).
- [31] A. Suyabodha, Simulation of cyclic variability in gasoline engine under cold start conditions, *Film.* (2012).
- [32] R. Polvinen, M. Vippola, M. Valden, T. Lepistö, A. Suopanki, M. Härkönen, The effect of Pt-Rh synergism on the thermal stability of rhodium oxide on pure alumina and Ce-ZrO<sub>2</sub>-modified alumina-supported catalysts, *J. Catal.* 226 (2004) 372–381. doi:10.1016/j.jcat.2004.05.033.
- [33] J. R.H. Ross, *Catalysis: Science and Technology*, Vol. 5, 1984. doi:10.1016/s0166-9834(00)83350-3.
- [34] H. Tanaka, N. Mizuno, M. Misono, Catalytic activity and structural stability of La<sub>0.9</sub>Ce<sub>0.1</sub>Co<sub>1-x</sub>Fe<sub>x</sub>O<sub>3</sub> perovskite catalysts for automotive emissions control, *Appl. Catal. A Gen.* 244 (2003) 371–382. doi:10.1016/S0926-860X(02)00609-9.
- [35] H. Abdulhamid, E. Fridell, J. Dawody, M. Skoglundh, In situ FTIR study of SO<sub>2</sub> interaction with Pt/BaCO<sub>3</sub>/Al<sub>2</sub>O<sub>3</sub> NO<sub>x</sub> storage catalysts under lean and rich conditions, *J. Catal.* 241 (2006) 200–210. doi:10.1016/j.jcat.2006.04.034.
- [36] M.S. Wilburn, W.S. Epling, SO<sub>2</sub> adsorption and desorption characteristics of bimetallic Pd-Pt catalysts: Pd:Pt ratio dependency, *Catal. Today.* 320 (2019) 11–19. doi:10.1016/j.cattod.2017.08.054.
- [37] G. Gandhi, M. Shelef, Effects of Sulfur on Precious Metal Automotive Catalysts, *Appl. Catal.* 77 (1991) 175–186. <https://www.sciencedirect.com/science/article/pii/0166983491800633>.
- [38] F. Standards, F. Rule, Control of Air Pollution From Motor Vehicles: Tier 3 Motor Vehicle Emission and Fuel Standards, *Fed. Regist.* 79 (2014) 23414–23886.
- [39] U. States, Tier 2 Motor Vehicle Emission Standards and Gasoline Sulfur Control Requirements : Response to Comments, (1999).
- [40] US Environmental Protection Agency, Gasoline Sulfur Standards, (2016)

EPA-420-B-16-004.

- [41] A.O. Hasan, Influence of Prototype Three Way Catalytic Converter on Regulated and Unregulated Emissions from Gasoline HCCI / SI Engine by School of Mechanical Engineering, (2011).
- [42] G.J.K. Acres, Automobile emission control system, *Platin. Met. Rev.* 16 (1972) 74–86.
- [43] J. Zheng, S. Meyer, K. Köhler, Abatement of nitrous oxide by ruthenium catalysts: Influence of the support, *Appl. Catal. A Gen.* 505 (2015) 44–51. doi:10.1016/j.apcata.2015.07.019.
- [44] EPA, Global greenhouse gas emissions data app, Epa.Gov. (2014) U.S. Department of Energy, Oak Ridge, Tennessee. <https://www.epa.gov/ghgemissions/global-greenhouse-gas-emissions-data#Sector> (accessed January 1, 2021).
- [45] V. Kröger, Poisoning of Automotive Exhaust Gas Catalyst Components, 2007. <http://jultika.oulu.fi/files/isbn9789514286087.pdf>.
- [46] L.R. Sassykova, Y.A. Aubakirov, S. Sendilvelan, Z.K. Tashmukhambetova, M.F. Faizullaeva, K. Bhaskar, A.A. Batyrbayeva, R.G. Ryskaliyeva, B.B. Tyussyupova, A.A. Zhakupova, M.A. Sarybayev, The Main Components of Vehicle Exhaust Gases and Their Effective Catalytic Neutralization, *Orient. J. Chem.* 35 (2019) 110–127. doi:10.13005/ojc/350112.
- [47] B.W. Williamson, H.K. Stepien, H.S. Gandhi, Poisoning of Platinum-Rhodium Automotive Three-Way Catalysts : Behavior of Single-Component Catalysts and Effects of Sulfur and Phosphorus, *Environ. Sci. Technol.* 14 (1980) 319–324. doi:10.1021/es60163a008.
- [48] W.A. Grohon, June 26, 1973, (1973).
- [49] E.H. Meguerian, G.H.; Hirschberg, Catalyst for treating exhaust gas from internal combustion engine, US Pat. 4006103 (1977).
- [50] J. Mooney, C.D. Keith, N. J, A. William, United States Patent ( 19 ), (1979).
- [51] J.C. Hegedus, L & Summer, United States Patent (19), 1977.
- [52] U. Lassi, Deactivation correlations of Pd/Rh Three'way catalysts designed for Euro IV emission limits. Effects of aging atmosphere, temperature and time., Oulu Univ. Press. (2003) 1–180.
- [53] M. Şen, A.O. Emirođlu, M.B. Çelik, CO and C<sub>3</sub>H<sub>8</sub> oxidation activity of Pd/ZnO nanowires/cordierite catalyst, *Appl. Therm. Eng.* 99 (2016) 841–845. doi:10.1016/j.applthermaleng.2016.01.134.
- [54] J. Wang, H. Chen, Z. Hu, M. Yao, Y. Li, A review on the Pd-based three-way catalyst, *Catal. Rev. - Sci. Eng.* 57 (2015) 79–144.



doi:10.1080/01614940.2014.977059.

- [55] J. Kašpar, P. Fornasiero, M. Graziani, Use of CeO<sub>2</sub>-based oxides in the three-way catalysis, *Catal. Today*. 50 (1999) 285–298. doi:10.1016/S0920-5861(98)00510-0.
- [56] T. Masui, T. Ozaki, K.I. Machida, G.Y. Adachi, Preparation of ceria-zirconia sub-catalysts for automotive exhaust cleaning, *J. Alloys Compd.* 303–304 (2000) 49–55. doi:10.1016/S0925-8388(00)00603-4.
- [57] I.A. Carbajal-Ramos, M.F. Gomez, A.M. Condó, S. Bengió, J.J. Andrade-Gamboa, M.C. Abello, F.C. Gennari, Catalytic behavior of Ru supported on Ce<sub>0.8</sub>Zr<sub>0.2</sub>O<sub>2</sub> for hydrogen production, *Appl. Catal. B Environ.* 181 (2016) 58–70. doi:10.1016/j.apcatb.2015.07.025.
- [58] S. Matsumoto, Recent advances in automobile exhaust catalysts, *Catal. Today*. 90 (2004) 183–190. doi:10.1016/j.cattod.2004.04.048.
- [59] W.S. Epling, A. Yezerets, N.W. Currier, The effects of regeneration conditions on NO<sub>x</sub> and NH<sub>3</sub> release from NO<sub>x</sub> storage/reduction catalysts, *Appl. Catal. B Environ.* 74 (2007) 117–129. doi:10.1016/j.apcatb.2007.02.003.
- [60] M. Lyubovsky, L.L. Smith, M. Castaldi, H. Karim, B. Nentwick, S. Etemad, R. LaPierre, W.C. Pfefferle, Catalytic combustion over platinum group catalysts: Fuel-lean versus fuel-rich operation, *Catal. Today*. 83 (2003) 71–84. doi:10.1016/S0920-5861(03)00217-7.
- [61] J.A. Lupescu, J.W. Schwank, K.A. Dahlberg, C.Y. Seo, G.B. Fisher, S.L. Peczonczyk, K. Rhodes, M.J. Jagner, L.P. Haack, Pd model catalysts: Effect of aging environment and lean redispersion, *Appl. Catal. B Environ.* 183 (2016) 343–360. doi:10.1016/j.apcatb.2015.10.018.
- [62] I. Mejía-Centeno, G.A. Fuentes, Nitrous oxide formation during light-off over a commercial Pd-containing three-way catalytic converter: The effect of low-sulfur gasoline, *Chem. Eng. Commun.* 196 (2009) 1140–1151. doi:10.1080/00986440902831664.
- [63] H. Muraki, H. Shinjoh, H. Sobukawa, K. Yokota, Y. Fujitani, Palladium-Lanthanum Catalysts for Automotive Emission Control, *Ind. Eng. Chem. Prod. Res. Dev.* 25 (1986) 202–208. doi:10.1021/i300022a014.
- [64] Y. Nishihata, J. Mizuki, T. Akao, H. Tanaka, M. Uenishi, M. Kimura, T. Okamoto, N. Hamada, Self-regeneration of a Pd-perovskite catalyst for automotive emissions control, *Nature*. 418 (2002) 164–167. doi:10.1038/nature00893.
- [65] S.A. Malamis, R.J. Harrington, M.B. Katz, D.S. Koerschner, S. Zhang, Y. Cheng, L. Xu, H.W. Jen, R.W. McCabe, G.W. Graham, X. Pan, Comparison

- of precious metal doped and impregnated perovskite oxides for TWC application, *Catal. Today*. 258 (2015) 535–542. doi:10.1016/j.cattod.2014.11.028.
- [66] N. Guilhaume, M. Primet, Three-way catalytic activity and oxygen storage capacity of perovskite  $\text{LaMn}_{0.976}\text{Rh}_{0.024}\text{O}_{3+\delta}$ , *J. Catal.* 165 (1997) 197–204. doi:10.1006/jcat.1997.1481.
- [67] H.G. Stiegler, A structure for access control lists, *Softw. Pract. Exp.* 9 (1979) 813–819. doi:10.1002/spe.4380091003.
- [68] F.C. Gennari, C. Neyertz, G. Meyer, P. Fornasiero, M. Graziani, Kinetics of hydrogen chemisorption on high surface area Pd/Ce  $0.8\text{Zr}_{0.2}\text{O}_2$ , *J. Alloys Compd.* 404–406 (2005) 317–322. doi:10.1016/j.jallcom.2004.10.096.
- [69] Z. Zhan, L. Song, X. Liu, J. Jiao, J. Li, H. He, Effects of synthesis methods on the performance of Pt + Rh/Ce  $0.6\text{Zr}_{0.4}\text{O}_2$  three-way catalysts, *J. Environ. Sci. (China)*. 26 (2014) 683–693. doi:10.1016/S1001-0742(13)60444-1.
- [70] R. Ran, H. Zhang, X. Wu, J. Fan, D. Weng, Structure and oxygen storage capacity of Pd/Pr/CeO<sub>2</sub>-ZrO<sub>2</sub> catalyst: Effects of impregnated praseodymia, *J. Rare Earths*. 32 (2014) 108–116. doi:10.1016/S1002-0721(14)60039-9.
- [71] Y. Cao, R. Ran, X. Wu, B. Zhao, J. Wan, D. Weng, Comparative study of ageing condition effects on Pd/Ce $_{0.5}\text{Zr}_{0.5}\text{O}_2$  and Pd/Al<sub>2</sub>O<sub>3</sub> catalysts: Catalytic activity, palladium nanoparticle structure and Pd-support interaction, *Appl. Catal. A Gen.* 457 (2013) 52–61. doi:10.1016/j.apcata.2013.03.002.
- [72] L. Lan, S. Chen, Y. Cao, M. Zhao, M. Gong, Y. Chen, Preparation of ceria-zirconia by modified coprecipitation method and its supported Pd-only three-way catalyst, *J. Colloid Interface Sci.* 450 (2015) 404–416. doi:10.1016/j.jcis.2015.03.042.
- [73] L. Lan, S. Chen, H. Li, H. Li, W. Wu, J. Deng, Y. Chen, Controllable synthesis of zone-distributed Pd over CeO<sub>2</sub>-ZrO<sub>2</sub>/Al<sub>2</sub>O<sub>3</sub> as advanced three-way catalyst, *J. Ind. Eng. Chem.* 58 (2018) 246–257. doi:10.1016/j.jiec.2017.09.034.
- [74] Z. Hu, A Pt-Rh synergism in Pt/Rh three-way catalysts, *Chem. Commun.* (1996) 879–880.
- [75] R. Di Monte, P. Fornasiero, S. Desinan, J. Kašpar, J.M. Gatica, J.J. Calvino, E. Fonda, Thermal stabilization of CexZr1-xO<sub>2</sub> oxygen storage promoters by addition of Al<sub>2</sub>O<sub>3</sub>: Effect of thermal aging on textural, structural, and morphological properties, *Chem. Mater.* 16 (2004) 4273–4285. doi:10.1021/cm048829q.
- [76] G. Li, Q. Wang, B. Zhao, M. Shen, R. Zhou, Effect of iron doping into

- CeO<sub>2</sub>-ZrO<sub>2</sub> on the properties and catalytic behaviour of Pd-only three-way catalyst for automotive emission control, *J. Hazard. Mater.* 186 (2011) 911–920. doi:10.1016/j.jhazmat.2010.11.080.
- [77] G. Ranga Rao, P. Fornasiero, R. Di Monte, J. Kašpar, G. Vlaic, G. Balducci, S. Meriani, G. Gubitosa, A. Cremona, M. Graziani, Reduction of NO over partially reduced metal-loaded CeO<sub>2</sub>-ZrO<sub>2</sub> solid solutions, *J. Catal.* 162 (1996) 1–9. doi:10.1006/jcat.1996.0254.
- [78] M. Ozawa, Role of cerium-zirconium mixed oxides as catalysts for car pollution: A short review, *J. Alloys Compd.* 275–277 (1998) 886–890. doi:10.1016/S0925-8388(98)00477-0.
- [79] M. Zhao, M. Shen, J. Wang, Effect of surface area and bulk structure on oxygen storage capacity of Ce<sub>0.67</sub>Zr<sub>0.33</sub>O<sub>2</sub>, *J. Catal.* 248 (2007) 258–267. doi:10.1016/j.jcat.2007.03.005.
- [80] R. Si, Y.W. Zhang, L.M. Wang, S.J. Li, B.X. Lin, W.S. Chu, Z.Y. Wu, C.H. Yan, Enhanced thermal stability and oxygen storage capacity for Ce<sub>x</sub>Zr<sub>1-x</sub>O<sub>2</sub> (x = 0.4–0.6) solid solutions by hydrothermally homogenous doping of trivalent rare earths, *J. Phys. Chem. C.* 111 (2007) 787–794. doi:10.1021/jp0630875.
- [81] T. Kollia, K. Rahkamaa-Tolonen, U. Lassi, A. Savimäki, R.L. Keiski, Influence of OSC material on the behaviour of metallic Pd catalysts in C<sub>2</sub>H<sub>4</sub> and CO oxidation as well as in NO reduction, *Top. Catal.* 30–31 (2004) 341–346. doi:10.1023/b:toca.0000029772.96623.81.
- [82] and R.J.G. Taeyoon Kim, John M. Vohs, Thermodynamic investigation of the redox properties for ceria - hafnia, ceria - terbia, and ceria - praseodymia solid solutions, *Ind. Eng. Chem. Prod. Res. Dev.* 45 (2006) 5561–5565. doi:10.1021/jp804089w.
- [83] M. Sun, W. Hu, T. Cheng, Y. Chen, P. Yao, M. Zhao, S. Yuan, Y. Chen, A novel insight into the preparation method of Pd/Ce<sub>0.75</sub>Zr<sub>0.25</sub>O<sub>2</sub>-Al<sub>2</sub>O<sub>3</sub> over high-stability close coupled catalysts, *Appl. Surf. Sci.* 467–468 (2019) 723–739. doi:10.1016/j.apsusc.2018.10.190.
- [84] J. Kašpar, P. Fornasiero, Nanostructured materials for advanced automotive de-pollution catalysts, *J. Solid State Chem.* 171 (2003) 19–29. doi:10.1016/S0022-4596(02)00141-X.
- [85] Y. Zhou, J. Deng, L. Xiong, J. Wang, S. Yuan, H. Zhang, Y. Chen, Synthesis and study of nanostructured Ce-Zr-La-RE-O (RE = Y, Nd and Pr) quaternary solid solutions and their supported three-way catalysts, *Mater. Des.* 130 (2017) 149–156. doi:10.1016/j.matdes.2017.05.059.
- [86] Q. Wang, B. Zhao, G. Li, R. Zhou, Application of rare earth modified Zr-based ceria-zirconia solid solution in three-way catalyst for automotive

- emission control, *Environ. Sci. Technol.* 44 (2010) 3870–3875.  
doi:10.1021/es903957e.
- [87] M. Uenishi, H. Tanaka, M. Taniguchi, I. Tan, Y. Sakamoto, S.I. Matsunaga, K. Yokota, T. Kobayashi, The reducing capability of palladium segregated from perovskite-type LaFePdOx automotive catalysts, *Appl. Catal. A Gen.* 296 (2005) 114–119. doi:10.1016/j.apcata.2005.08.031.
- [88] S.K. Matam, E.H. Otal, M.H. Aguirre, A. Winkler, A. Ulrich, D. Rentsch, A. Weidenkaff, D. Ferri, Thermal and chemical aging of model three-way catalyst Pd/Al<sub>2</sub>O<sub>3</sub> and its impact on the conversion of CNG vehicle exhaust, *Catal. Today.* 184 (2012) 237–244.  
doi:10.1016/j.cattod.2011.09.030.
- [89] EPA, Light-Duty Vehicles and Light-Duty Trucks : Clean Fuel Fleet Exhaust Emission Standards a, 2016.
- [90] D. Kim, S. Woo, J. Lee, O. Yang, The role of lanthanum oxide on Pd-only three-way catalysts prepared by co-impregnation and sequential impregnation methods, *Catal. Letters.* 70 (2000) 35–41.  
doi:10.1023/a:1019083704188.
- [91] S.K. Matam, E.H. Otal, M.H. Aguirre, A. Winkler, A. Ulrich, D. Rentsch, A. Weidenkaff, D. Ferri, Thermal and chemical aging of model three-way catalyst Pd/Al<sub>2</sub>O<sub>3</sub> and its impact on the conversion of CNG vehicle exhaust, *Catal. Today.* 184 (2012) 237–244.  
doi:10.1016/j.cattod.2011.09.030.
- [92] S. Lin, L. Yang, X. Yang, R. Zhou, Redox properties and metal-support interaction of Pd/Ce<sub>0.67</sub>Zr<sub>0.33</sub>O<sub>2</sub>-Al<sub>2</sub>O<sub>3</sub> catalyst for CO, HC and NO<sub>x</sub> elimination, *Appl. Surf. Sci.* 305 (2014) 642–649.  
doi:10.1016/j.apsusc.2014.03.153.
- [93] A. Baylet, S. Royer, P. Marécot, J.M. Tatibouët, D. Duprez, High catalytic activity and stability of Pd doped hexaaluminate catalysts for the CH<sub>4</sub> catalytic combustion, *Appl. Catal. B Environ.* 77 (2008) 237–247.  
doi:10.1016/j.apcatb.2007.07.031.
- [94] Paul Degobert, *Automobiles and pollution*, Society of Automotive Engineers, : Warrendale, Pa. : Editions Technip, 2013.  
doi:10.5860/choice.33-5728.
- [95] J. Kašpar, P. Fornasiero, N. Hickey, Automotive catalytic converters: Current status and some perspectives, *Catal. Today.* 77 (2003) 419–449.  
doi:10.1016/S0920-5861(02)00384-X.
- [96] L.P. Ma, H.J. Bart, P. Ning, A. Zhang, G. Wu, Z. Zengzang, Kinetic study of three-way catalyst of automotive exhaust gas: Modeling and application, *Chem. Eng. J.* 155 (2009) 241–247. doi:10.1016/j.cej.2009.07.045.

- [97] P. Taylor, M. Shelef, G.W. Graham, Shelef1994.Pdf, (2006) 37–41.
- [98] S.H. Oh, E.J. Bissett, Automotive applications of chemical reaction engineering and future research needs, *Stud. Surf. Sci. Catal.* 159 (2007) 17–26. doi:10.1016/s0167-2991(06)81533-8.
- [99] P. Kočí, M. Kubíček, M. Marek, Modeling of three-way-catalyst monolith converters with microkinetics and diffusion in the washcoat, *Ind. Eng. Chem. Res.* 43 (2004) 4503–4510. doi:10.1021/ie034137k.
- [100] C. Sellmer, V. Schmatloch, N. Kruse, NO dissociation on rhodium, *Catal. Letters.* 35 (1995) 165–174. doi:10.1007/BF00807014.
- [101] G.C. Mondragón Rodríguez, B. Saruhan, Effect of Fe/Co-ratio on the phase composition of Pd-integrated perovskites and its H<sub>2</sub>-SCR of NO<sub>x</sub> performance, *Appl. Catal. B Environ.* 93 (2010) 304–313. doi:10.1016/j.apcatb.2009.10.004.
- [102] G.C.M. Rodríguez, K. Kelm, S. Heikens, W. Grünert, B. Saruhan, Pd-integrated perovskites for TWC applications: Synthesis, microstructure and N<sub>2</sub>O-selectivity, *Catal. Today.* 184 (2012) 184–191. doi:10.1016/j.cattod.2011.12.026.
- [103] M. V Petrova, F.A. Williams, A small detailed chemical-kinetic mechanism for hydrocarbon combustion, 144 (2006) 526–544. doi:10.1016/j.combustflame.2005.07.016.
- [104] K. Taylor, Nitric oxide catalysis in automotive exhaust systems, *Catal. Rev.* 35 (1993) 457–481. doi:10.1080/01614949308013915.
- [105] J.H. Holles, M.A. Switzer, R.J. Davis, Influence of ceria and lanthana promoters on the kinetics of NO and N<sub>2</sub>O reduction by CO over alumina-supported palladium and rhodium, *J. Catal.* 190 (2000) 247–260. doi:10.1006/jcat.1999.2780.
- [106] A.S. Mamede, G. Leclercq, E. Payen, P. Granger, J. Grimblot, In situ raman characterisation of surface modifications during NO transformation over automotive Pd-based exhaust catalysts, *J. Mol. Struct.* 651–653 (2003) 353–364. doi:10.1016/S0022-2860(03)00111-X.
- [107] A. Renouprez, El Hamdaoui - CO and NO Interaction with Pd-Ag and Pd-Cr Bimetallic Catalysts.pdf, *J. Catal.* 148 (1994) 47–55.
- [108] T.R. Ward, R. Hoffmann, M. Shelef, Coupling nitrosyls as the first step in the reduction of NO on metal surfaces: the special role of rhodium, *Surf. Sci.* 289 (1993) 85–99. doi:10.1016/0039-6028(93)90890-V.
- [109] M. Hideaki, Reduction of NO by CO over Alumina-Supported Palladium Catalyst, *Ind. Eng. Chem. Prod. Res. Dev.* (1986) 419–424.
- [110] I. Twagirashema, M. Frere, L. Gengembre, C. Dujardin, P. Granger,

- Structural regeneration of LaCoO<sub>3</sub> perovskite-based catalysts during the NO + H<sub>2</sub> + O<sub>2</sub> reactions, *Top. Catal.* 42–43 (2007) 171–176.  
doi:10.1007/s11244-007-0173-3.
- [111] P. Granger, F. Dhainaut, S. Pietrzyk, P. Malfoy, A.S. Mamede, L. Leclercq, G. Leclercq, An overview: Comparative kinetic behaviour of Pt, Rh and Pd in the NO+CO and NO+H<sub>2</sub> reactions, *Top. Catal.* 39 (2006) 65–76.  
doi:10.1007/s11244-006-0039-0.
- [112] F. Dhainaut, S. Pietrzyk, P. Granger, Kinetics of the NO + H<sub>2</sub> reaction over supported noble metal based catalysts: Support effect on their adsorption properties, *Appl. Catal. B Environ.* 70 (2007) 100–110.  
doi:10.1016/j.apcatb.2005.11.029.
- [113] F. Dhainaut, S. Pietrzyk, P. Granger, Kinetic investigation of the NO reduction by H<sub>2</sub> over noble metal based catalysts, *Catal. Today.* 119 (2007) 94–99. doi:10.1016/j.cattod.2006.08.016.
- [114] T.P. Kobylinski, B.W. Taylor, The catalytic chemistry of nitric oxide. II. Reduction of nitric oxide over noble metal catalysts, *J. Catal.* 33 (1974) 376–384. doi:10.1016/0021-9517(74)90284-X.
- [115] K. Rahkamaa-Tolonen, T. Salmi, D.Y. Murzin, L. Barreto Dillon, H. Karhu, R.L. Keiski, J. Väyrynen, Investigation of NO reduction by H<sub>2</sub> on Pd monolith with transient and isotopic exchange techniques. I. H<sub>2</sub>/D<sub>2</sub> Exchange with H<sub>2</sub>O and NH<sub>3</sub>, *J. Catal.* 210 (2002) 17–29.  
doi:10.1006/jcat.2002.3668.
- [116] K. Paredis, L.K. Ono, F. Behafarid, Z. Zhang, J.C. Yang, A.I. Frenkel, B.R. Cuenya, Evolution of the structure and chemical state of Pd nanoparticles during the in situ catalytic reduction of NO with H<sub>2</sub>, *J. Am. Chem. Soc.* 133 (2011) 13455–13464. doi:10.1021/ja203709t.
- [117] D.C. Chambers, D.E. Angove, N.W. Cant, The formation and hydrolysis of isocyanic acid during the reaction of NO, CO, and H<sub>2</sub> mixtures on supported platinum, palladium, and rhodium, *J. Catal.* 204 (2001) 11–22.  
doi:10.1006/jcat.2001.3359.
- [118] S.H. Oh, T. Triplett, Reaction pathways and mechanism for ammonia formation and removal over palladium-based three-way catalysts: Multiple roles of CO, *Catal. Today.* 231 (2014) 22–32.  
doi:10.1016/j.cattod.2013.11.048.
- [119] N. Rankovic, A. Nicolle, D. Berthout, P. Da Costa, Kinetic modeling study of the oxidation of carbon monoxide-hydrogen mixtures over Pt/Al<sub>2</sub>O<sub>3</sub> and Rh/Al<sub>2</sub>O<sub>3</sub> catalysts, *J. Phys. Chem. C.* 115 (2011) 20225–20236.  
doi:10.1021/jp205476y.
- [120] T. Engel, G. Ertl, A molecular beam investigation of the catalytic oxidation

- of CO on Pd (111), *J. Chem. Phys.* 69 (1978) 1267–1281.  
doi:10.1063/1.436666.
- [121] J. Szanyi, D.W. Goodman, CO oxidation on palladium. 1. A combined kinetic-infrared reflection absorption spectroscopic study of Pd(100), *J. Phys. Chem.* 98 (1994) 2972–2977. doi:10.1021/j100062a038.
- [122] X. Xu, D.W. Goodman, An infrared and Kinetic Study of CO Oxidation on Model Silica-Supported Palladium Catalysts, *J. Phys. Chem.* 97 (1993) 7711–7718.
- [123] O. Balmes, A. Resta, D. Wermeille, R. Felici, M.E. Messing, K. Deppert, Z. Liu, M.E. Grass, H. Bluhm, R. Van Rijn, J.W.M. Frenken, R. Westerström, S. Blomberg, J. Gustafson, J.N. Andersen, E. Lundgren, Reversible formation of a PdC<sub>x</sub> phase in Pd nanoparticles upon CO and O<sub>2</sub> exposure, *Phys. Chem. Chem. Phys.* 14 (2012) 4796–4801. doi:10.1039/c2cp22873d.
- [124] S.F. Parker, The role of hydroxyl groups in low temperature carbon monoxide oxidation, *Chem. Commun.* 47 (2011) 1988–1990. doi:10.1039/c0cc04991c.
- [125] K. Föttinger, R. Schlögl, G. Rupprechter, The mechanism of carbonate formation on Pd-Al<sub>2</sub>O<sub>3</sub> catalysts, *Chem. Commun.* 3 (2008) 320–322. doi:10.1039/b713161e.
- [126] R. Rajasree, J.H.B.J. Hoebink, J.C. Schouten, Transient kinetics of carbon monoxide oxidation by oxygen over supported palladium/ceria/zirconia three-way catalysts in the absence and presence of water and carbon dioxide, *J. Catal.* 223 (2004) 36–43. doi:10.1016/j.jcat.2003.12.014.
- [127] S.G. M., G. K., The carbon monoxide combustion via silver, palladium and their alloy, *Zeitschrift Für Phys. Chemie Neue Folge.* 16 (1958) 39–63.
- [128] Y.F.Y. Yao, The oxidation of CO and hydrocarbons over noble metal catalysts, *J. Catal.* 87 (1984) 152–162. doi:10.1016/0021-9517(84)90178-7.
- [129] L. van de Beld, M.C. van der Ven, K.R. Westerterp, A kinetic study of the complete oxidation of ethene, propane and their mixtures on a Pd/Al<sub>2</sub>O<sub>3</sub> catalyst, *Chem. Eng. Process. Process Intensif.* 34 (1995) 469–478. doi:10.1016/0255-2701(95)00619-2.
- [130] C.F. Cullis, T.G. Nevell, Kinetics of the Catalytic Oxidation Over Palladium of Some Alkanes and Cycloalkanes., *Proc R Soc London Ser A.* 349 (1976) 523–534. doi:10.1098/rspa.1976.0087.
- [131] Y.Y. Yao, Oxidation of alkanes over noble metal catalysts, *Ind. Eng. Chem. Prod. Res. Dev.* 19 (1980) 293–298.
- [132] M. Aryafar, F. Zaera, Kinetic study of the catalytic oxidation of alkanes over nickel, palladium, and platinum foils, *Catal. Letters.* 48 (1997) 173–183.

doi:10.1023/a:1019055810760.

- [133] T. Sekiba, S. Kimura, H. Yamamoto, A. Okada, Development of automotive palladium three-way catalysts, *Catal. Today*. 22 (1994) 113–126. doi:10.1016/0920-5861(94)80096-0.
- [134] H. Tanaka, M. Misono, Advances in designing perovskite catalysts, *Curr. Opin. Solid State Mater. Sci.* 5 (2001) 381–387. doi:10.1016/S1359-0286(01)00035-3.
- [135] V.R. Choudhary, S. Banerjee, B.S. Uphade, Activation by hydrothermal treatment of low surface area ABO<sub>3</sub>-type perovskite oxide catalysts, *Appl. Catal. A Gen.* 197 (2000) 183–186. doi:10.1016/S0926-860X(99)00485-8.
- [136] G. Lafaye, J. Barbier, D. Duprez, Impact of cerium-based support oxides in catalytic wet air oxidation: Conflicting role of redox and acid-base properties, *Catal. Today*. 253 (2015) 89–98. doi:10.1016/j.cattod.2015.01.037.
- [137] P. Ciambelli, S. Cimino, G. Lasorella, L. Lisi, S. De Rossi, M. Faticanti, G. Minelli, P. Porta, CO oxidation and methane combustion on LaAl<sub>1-x</sub>FexO<sub>3</sub> perovskite solid solutions, 37 (2002) 231–241. doi:10.1063/1.2176389.
- [138] S. Royer, F. Bérubé, S. Kaliaguine, Effect of the synthesis conditions on the redox and catalytic properties in oxidation reactions of LaCo<sub>1-x</sub>FexO<sub>3</sub>, *Appl. Catal. A Gen.* 282 (2005) 273–284. doi:10.1016/j.apcata.2004.12.018.
- [139] N. Labhasetwar, G. Saravanan, S. Kumar Megarajan, N. Manwar, R. Khobragade, P. Doggali, F. Grasset, Perovskite-type catalytic materials for environmental applications, *Sci. Technol. Adv. Mater.* 16 (2015). doi:10.1088/1468-6996/16/3/036002.
- [140] . Irusta, M. P. Pina, M. Menendez, J. Santamaria, Catalytic combustion of volatile organic compounds, *J. Catal.* 179 (1998) 400–412. doi:10.1016/j.jhazmat.2004.03.019.
- [141] H. Tanaka, M. Taniguchi, M. Uenishi, N. Kajita, I. Tan, Y. Nishihata, J. Mizuki, K. Narita, M. Kimura, K. Kaneko, Self-regenerating Rh- and Pt-based perovskite catalysts for automotive-emissions control, *Angew. Chemie - Int. Ed.* 45 (2006) 5998–6002. doi:10.1002/anie.200503938.
- [142] E. Tzimpilis, N. Moschoudis, M. Stoukides, P. Bekiaroglou, Ageing and SO<sub>2</sub> resistance of Pd containing perovskite-type oxides, *Appl. Catal. B Environ.* 87 (2009) 9–17. doi:10.1016/j.apcatb.2008.08.020.
- [143] S. Royer, C. Ayrault, C. Carnevillier, F. Epron, P. Marécot, D. Duprez, Enthalpy recovery of gases issued from H<sub>2</sub> production processes: Activity and stability of oxide and noble metal catalysts in oxidation reaction under highly severe conditions, *Catal. Today*. 117 (2006) 543–548. doi:10.1016/j.cattod.2006.06.023.



- [144] E. Tzimpilis, N. Moschoudis, M. Stoukides, P. Bekiaroglou, Preparation, active phase composition and Pd content of perovskite-type oxides, *Appl. Catal. B Environ.* 84 (2008) 607–615. doi:10.1016/j.apcatb.2008.05.016.
- [145] Y. Zhang-Steenwinkel, L.M. Van Der Zande, H.L. Castricum, A. Blik, Step response and transient isotopic labelling studies into the mechanism of CO oxidation over La<sub>0.8</sub>Ce<sub>0.2</sub>MnO<sub>3</sub> perovskite, *Appl. Catal. B Environ.* 54 (2004) 93–103. doi:10.1016/j.apcatb.2004.02.008.
- [146] LUIS G. TEJUCA, J.L.G. Fierro, Structure and Reactivity of Perovskite-Type Oxides, *Adv. Catal.* 36 (1989) 237–328.
- [147] R. Zhang, H. Alamdari, S. Kaliaguine, Water vapor sensitivity of nanosized La(Co, Mn, Fe)<sub>1-x</sub>(Cu, Pd)<sub>x</sub>O<sub>3</sub> perovskites during NO reduction by C<sub>3</sub>H<sub>6</sub> in the presence of oxygen, *Appl. Catal. B Environ.* 72 (2007) 331–341. doi:10.1016/j.apcatb.2006.10.025.
- [148] M. Machida, K. Ochiai, K. Ito, K. Ikeue, Catalytic properties of novel La-Sr-Cu-O-S perovskites for automotive C<sub>3</sub>H<sub>6</sub>/CO oxidation in the presence of SO<sub>x</sub>, *Catal. Today.* 117 (2006) 584–587. doi:10.1016/j.cattod.2006.06.009.
- [149] S. Cimino, L. Lisi, R. Pirone, G. Russo, M. Turco, Methane combustion on perovskites-based structured catalysts, *Catal. Today.* 59 (2000) 19–31. doi:10.1016/S0920-5861(00)00269-8.
- [150] R. Ran, X. Wu, D. Weng, J. Fan, Oxygen storage capacity and structural properties of Ni-doped LaMnO<sub>3</sub> perovskites, *J. Alloys Compd.* 577 (2013) 288–294. doi:10.1016/j.jallcom.2013.05.041.
- [151] M.A. Peña, J.L.G. Fierro, Chemical structures and performance of perovskite oxides, *Chem. Rev.* 101 (2001) 1981–2017. doi:10.1021/cr980129f.
- [152] A. Glisenti, M. Pacella, M. Guiotto, M.M. Natile, P. Canu, Largely Cu-doped LaCo<sub>1-x</sub>Cu<sub>x</sub>O<sub>3</sub> perovskites for TWC: Toward new PGM-free catalysts, *Appl. Catal. B Environ.* 180 (2016) 94–105. doi:10.1016/j.apcatb.2015.06.017.
- [153] A.P.E. York, C.S. Cooper, K. Simmance, S.K. Wilkinson, Non-PGM Iron Perovskite Three-Way Gasoline Emissions Control Catalysts: Kinetics, Reaction Mechanism and Catalyst Sizing Study, *Top. Catal.* 63 (2019) 256–267. doi:10.1007/s11244-019-01197-8.
- [154] S. Keav, S. Matam, D. Ferri, A. Weidenkaff, Structured Perovskite-Based Catalysts and Their Application as Three-Way Catalytic Converters—A Review, *Catalysts.* 4 (2014) 226–255. doi:10.3390/catal4030226.
- [155] K.K. Hansen, E.M. Skou, H. Christensen, T. Turek, Perovskites as catalysts for the selective catalytic reduction of nitric oxide with propene: Relationship between solid state properties and catalytic activity, *J. Catal.*

- 199 (2001) 132–140. doi:10.1006/jcat.2000.3153.
- [156] X. Zhu, K. Li, L. Neal, F. Li, Perovskites as Geo-inspired Oxygen Storage Materials for Chemical Looping and Three-Way Catalysis: A Perspective, *ACS Catal.* 8 (2018) 8213–8236. doi:10.1021/acscatal.8b01973.
- [157] S.G. Francis, *Structure, Properties and Preparation of Perovskite Type Compounds*, 1969.
- [158] N. Guilhaume, M. Primet, Three-way catalytic activity and oxygen storage capacity of perovskite  $\text{LaMn}_{0.976}\text{Rh}_{0.024}\text{O}_{3+\delta}$ , *J. Catal.* 165 (1997) 197–204. doi:10.1006/jcat.1997.1481.
- [159] E.J. Baran, Structural chemistry and physicochemical properties of perovskite-like materials, *Catal. Today.* 8 (1990) 133–151. doi:10.1016/0920-5861(90)87015-u.
- [160] R. Leanza, I. Rossetti, L. Fabbrini, C. Oliva, L. Forni, Perovskite catalysts for the catalytic flameless combustion of methane. Preparation by flame-hydrolysis and characterisation by TPD-TPR-MS and EPR, *Appl. Catal. B Environ.* 28 (2000) 55–64. doi:10.1016/S0926-3373(00)00163-6.
- [161] Y. Zhang-Steenwinkel, J. Beckers, A. Blik, Surface properties and catalytic performance in CO oxidation of cerium substituted lanthanum-manganese oxides, *Appl. Catal. A Gen.* 235 (2002) 79–92. doi:10.1016/S0926-860X(02)00241-7.
- [162] Y. Teraoka, H.M. Zhang, K. Okamoto, N. Yamazoe, Mixed ionic-electronic conductivity of  $\text{La}_{1-x}\text{Sr}_x\text{Co}_{1-y}\text{Fe}_y\text{O}_{3-\delta}$  perovskite-type oxides, *Mater. Res. Bull.* 23 (1988) 51–58. doi:10.1016/0025-5408(88)90224-3.
- [163] A.R.J.H. Voorhoeve, D.W. Johnson, J.P. Remeika, P.K. Gallagher, *Perovskite Oxides : Materials Science in Catalysis* Published by : American Association for the Advancement of Science Stable URL : <http://www.jstor.org/stable/1743316>, *Adv. Sci.* 195 (2010) 827–833.
- [164] R.J. Bell, G.J. Millar, J. Drennan, Influence of synthesis route on the catalytic properties of  $\text{La}_{1-x}\text{Sr}_x\text{MnO}_3$ , *Solid State Ionics.* 131 (2000) 211–220. doi:10.1016/S0167-2738(00)00668-8.
- [165] P.K. Gallagher, D.W. Johnson, F. Schrey, Studies of some supported perovskite oxidation catalysts, *Mater. Res. Bull.* 9 (1974) 1345–1352. doi:10.1016/0025-5408(74)90057-9.
- [166] L. Wachowski, Influence of the method of preparation on the porous structure of perovskite oxides, *Surf. Coatings Technol.* 29 (1986) 303–311. doi:10.1016/0257-8972(86)90003-4.
- [167] M.S.G. Baythoun, F.R. Sale, Production of strontium-substituted lanthanum manganite perovskite powder by the amorphous citrate process, *J. Mater.*

- Sci. 17 (1982) 2757–2769. doi:10.1007/BF00543914.
- [168] H. Taguchi, S. Yamada, M. Nagao, Y. Ichikawa, K. Tabata, Surface characterization of LaCoO<sub>3</sub> synthesized using citric acid, *Mater. Res. Bull.* 37 (2002) 69–76. doi:10.1016/S0025-5408(01)00799-1.
- [169] Y.N. Lee, R.M. Lago, J.L.G. Fierro, J. González, Hydrogen peroxide decomposition over Ln<sub>1-x</sub>A<sub>x</sub>MnO<sub>3</sub> (Ln = La or Nd and A = K or Sr) perovskites, *Appl. Catal. A Gen.* 215 (2001) 245–256. doi:10.1016/S0926-860X(01)00536-1.
- [170] P.K. Gallagher, E.M. Vogel, F. Sehrey, EFFECTS OF THE Pt CONTENT OF La<sub>0.7</sub>Pb<sub>0.3</sub>MnO<sub>3</sub> ON ITS CATALYTIC ACTIVITY FOR THE OXIDATION OF CO IN THE PRESENCE OF SO<sub>2</sub>, *Mater. Res. Bull.* 10 (1975) 623–627.
- [171] J.L.G. Fierro, Structure and composition of perovskite surface in relation to adsorption and catalytic properties, *Catal. Today.* 8 (1990) 153–174. doi:10.1016/0920-5861(90)87016-V.
- [172] S. Kaliaguine, A. Van Neste, PROCESS FOR SYNTHESIZING METAL OXIDES AND METAL OXIDES HAVING A PEROWSKITE OR PEROWSKITE-LIKE CRYSTAL STRUCTURE USOO6770256B1, 2004.
- [173] Y. Wang, J. Ren, Y. Wang, F. Zhang, X. Liu, Y. Guo, G. Lu, Nanocasted synthesis of mesoporous LaCoO<sub>3</sub> perovskite with extremely high surface area and excellent activity in methane combustion, *J. Phys. Chem. C.* 112 (2008) 15293–15298. doi:10.1021/jp8048394.
- [174] Z. Sarshar, F. Kleitz, S. Kaliaguine, Novel oxygen carriers for chemical looping combustion: La<sub>1-x</sub>Ce<sub>x</sub>BO<sub>3</sub> (B = Co, Mn) perovskites synthesized by reactive grinding and nanocasting, *Energy Environ. Sci.* 4 (2011) 4258–4269. doi:10.1039/c1ee01716k.
- [175] M.M. Nair, F. Kleitz, S. Kaliaguine, Kinetics of Methanol Oxidation over Mesoporous Perovskite Catalysts, *ChemCatChem.* 4 (2012) 387–394. doi:10.1002/cctc.201100356.
- [176] R.J.H. Voorhoeve, J.P. Remeika, P.E. Freeland, B.T. Matthias, Rare-earth oxides of manganese and cobalt rival platinum for the treatment of carbon monoxide in auto exhaust, *Science* (80-. ). 177 (1972) 353–354. doi:10.1126/science.177.4046.353.
- [177] R.J.H. Voorhoeve, J.P. Remeika, D.W. Johnson, Rare-earth manganites: Catalysts with low ammonia yield in the reduction of nitrogen oxides, *Science* (80-. ). 180 (1973) 62–64. doi:10.1126/science.180.4081.62.
- [178] M.C. Lea, Disruption of the silver haloid molecule by mechanical force, *Am. J. Sci.* s3-43 (1892) 527–531. doi:10.2475/ajs.s3-43.258.527.

- [179] L. Takacs, M. Carey Lea, the Father of mechanochemistry, *Bull. Hist. Chem.* 28 (2003) 26–34.
- [180] L. Takacs, M. Carey Lea, the first mechanochemist, *J. Mater. Sci.* 39 (2004) 4987–4993. doi:10.1023/B:JMISC.0000039175.73904.93.
- [181] D. Braga, S.L. Gíaffreda, M. Curzi, L. Maini, M. Polito, F. Grepioni, Mechanical mixing of molecular crystals : AAAA green route to co-crystals and coordination networks, *J. Therm. Anal. Calorim.* 90 (2007) 115–123. doi:10.1007/s10973-007-8484-y.
- [182] V. V Boldyrev, *J Mat Syn and Proc Volume 8 issue 3-4 2000* V. V. Boldyrev; K. Tkáčová -- Mechanochemistry of Solids- Past, Present, and Prospects.pdf, 8 (2000).
- [183] Q. Zhang, F. Saito, Mechanochemical synthesis of LaMnO<sub>3</sub> from La<sub>2</sub>O<sub>3</sub> and Mn<sub>2</sub>O<sub>3</sub> powders, *J. Alloys Compd.* 297 (2000) 99–103. doi:10.1016/S0925-8388(99)00606-4.
- [184] J. Shu, S. Kaliaguine, Well-dispersed perovskite-type oxidation catalysts, *Appl. Catal. B Environ.* 16 (1998) L303. doi:10.1016/s0926-3373(97)00097-0.
- [185] J.P. Dacquin, C. Lancelot, C. Dujardin, P. Da Costa, G. Djega-Mariadassou, P. Beaunier, S. Kaliaguine, S. Vaudreuil, S. Royer, P. Granger, Influence of preparation methods of LaCoO<sub>3</sub> on the catalytic performances in the decomposition of N<sub>2</sub>O, *Appl. Catal. B Environ.* 91 (2009) 596–604. doi:10.1016/j.apcatb.2009.06.032.
- [186] J.L.G. Fierro, Physicochemical Properties of LaFeO<sub>3</sub>, *J. Chem. SOC., Faraday Trans.* 81 (1985) 2399–2407.
- [187] L.G. Tejuca, Properties of perovskite-type oxides II: Studies in catalysis, *J. Less-Common Met.* 146 (1989) 261–270. doi:10.1016/0022-5088(89)90384-6.
- [188] M. Futai, C. Yonghua, L. Hangzhou, CHARACTERIZATION OF PEROVSKITE-TYPE OXIDE CATALYSTS RECoO<sub>3</sub> BY TPR, 31 (1986) 47–53.
- [189] M. Crespin, W.K. Hall, The surface chemistry of some perovskite oxides, *J. Catal.* 69 (1981) 359–370. doi:10.1016/0021-9517(81)90171-8.
- [190] L. Simonot, F. Garin, G. Maire, A comparative study of LaCoO<sub>3</sub>, Co<sub>3</sub>O<sub>4</sub> and LaCoO<sub>3</sub>-Co<sub>3</sub>O<sub>4</sub>: I. Preparation, characterisation and catalytic properties for the oxidation of CO, *Appl. Catal. B Environ.* 11 (1997) 167–179. doi:10.1016/S0926-3373(96)00046-X.
- [191] J.L.G. Fierro, M.A. Peña, L. González Tejuca, An XPS and reduction study of PrCoO<sub>3</sub>, *J. Mater. Sci.* 23 (1988) 1018–1023. doi:10.1007/BF01154005.

- [192] R. Lago, G. Bini, M.A. Peña, J.L.G. Fierro, Partial oxidation of methane to synthesis gas using  $\text{LnCoO}_3$  perovskites as catalyst precursors, *Stud. Surf. Sci. Catal.* 110 (1997) 721–730. doi:10.1016/s0167-2991(97)81034-8.
- [193] Y. Nakamura, T.; Misono, M.; Yoneda, Catalytic Properties of Perovskite-type Mixed Oxides,  $\text{La}_{1-x}\text{Sr}_x\text{CoO}_3$ , *Bull. Chem. Soc. Jpn.* 55 (1982) 394–399.
- [194] P. Ciambelli, S. Cimino, L. Lisi, M. Faticanti, G. Minelli, I. Pettiti, P. Porta, La, Ca and Fe oxide perovskites : preparation , characterization and catalytic properties for methane combustion, 33 (2001) 193–203.
- [195] P.E. Marti, Influence of the A-site cation in  $\text{AMnO}_3 + x$  and  $\text{AFeO}_3 + x$  (  $A = \text{La}, \text{Pr}, \text{Nd}$  and  $\text{Gd}$  ) perovskite-type oxides on the catalytic activity for methane combustion, *Catal. Letters.* 26 (1994) 71–84.
- [196] T. Yasutake, Z. Hua-Min, Y. Noboru, OXYGEN-SORPTIVE PROPERTIES OF DEFECT PEROVSKITE-TYPE  $\text{La}_{1-x}\text{Sr}_x\text{Co}_{1-y}\text{Fe}_y\text{O}_{3-\delta}$ , *Chem. Lett.* 14 (1985) 1367–1370.
- [197] H.M.Zhang, Y. SHIMIZU, Y. Teraoka, N. MIURA, N. YAMAZOE, Oxygen sorption and catalytic properties of  $\text{La}_{1-x}\text{Sr}_x\text{Co}_{1-y}\text{Fe}_y\text{O}_3$  Perovskite-type oxides, *J. Ca.* 121 (1990) 432–440.
- [198] L. Lisi, G. Bagnasco, P. Ciambelli, S. De Rossi, A.P. Porta, G. Russo, M. Turco, Perovskite-Type Oxides II . Redox Properties of  $\text{LaMn}_{1-x}\text{Cu}_x\text{O}_3$  and  $\text{LaCo}_{1-x}\text{Cu}_x\text{O}_3$  and Methane Catalytic Combustion, 183 (1999) 176–183.
- [199] S. Ponce, M.A. Peña, J.L.G. Fierro, Surface properties and catalytic performance in methane combustion of Sr-substituted lanthanum manganites, 24 (2000) 193–205.
- [200] J.L.G.Fierro, J.M.D. Tascón, L.G. Tejuca, Physicochemical Properties of  $\text{LaMnO}_3$  : Reducibility of  $\text{O}_2$  Adsorption, *J. Catal.* 89 (1984) 209–216.
- [201] P. Ciambelli, S. Cimino, S. De Rossi, M. Faticanti, L. Lisi, G. Minelli, I. Pettiti, P. Porta, G. Russo, M. Turco,  $\text{AMnO}_3$  ( $A = \text{La}, \text{Nd}, \text{Sm}$ ) and  $\text{Sm}_{1-x}\text{Sr}_x\text{MnO}_3$  perovskites as combustion catalysts: structural, redox and catalytic properties, *Appl. Catal. B Environ.* 24 (2000) 243–253.
- [202] T. NITADORI, M. Misono, Catalytic Properties of  $\text{La}_{1-x}\text{A}'_x\text{FeO}_3$  ( $A' = \text{Sr}, \text{Ce}$ ) and  $\text{La}_{1-x}\text{Ce}_x\text{CoO}_3$ , *J. Catal.* 93 (1985) 459–466.
- [203] T. Nitadori, S. KURIHARA, M. Misono, Catalytic Properties of  $\text{La}_{1-x}\text{A}'_x\text{MnO}_3$  ( $A' = \text{Sr}, \text{Ce}, \text{Hf}$ ), *J. Catal.* 98 (1986) 221–228.
- [204] T. Yasutake, Y. Noboru, Masahiro YOSHIMATSU, T. SEIYAMA, OXYGEN-SORPTIVE PROPERTIES AND DEFECT STRUCTURE OF PEROVSKITE-TYPE OXIDES, *Chem. Lett.* (1984) 893–896.

- [205] Y. Teraoka, Hua-Min ZHANG, N. Yamazoe, Preparation of Perovskite-type Oxides with Large Surface Area by Citrate Process, *Chem. Lett.* (1987) 665–668.
- [206] G. Saracco, G. Scibilia, A. Iannibello, Methane combustion on Mg-doped LaCrO<sub>3</sub> perovskite catalysts, *Appl. Catal. B Environ.* 8 (1996) 229–244.
- [207] G. Saracco, F. Geobaldo, G. Baldi, Methane combustion on Mg-doped LaMnO<sub>3</sub> perovskite catalysts, *Appl. Catal. B Environ.* 20 (1999) 277–288.
- [208] S. Kaliaguine, V. Szabo, A. Van Neste, J.E. Gallot, M. Bassir, R. Muzychuk, Perovskite-type oxides synthesized by reactive grinding, *Appl. Catal. A Gen.* 209 (2001) 345–358. doi:10.4028/www.scientific.net/msf.377.39.
- [209] J. Kirchnerova, M. Alifanti, B. Delmon, Evidence of phase cooperation in the LaCoO<sub>3</sub> – CeO<sub>2</sub> – Co<sub>3</sub>O<sub>4</sub> catalytic system in relation to activity in methane combustion, *Appl. Catal. A Gen.* 231 (2002) 65–80.
- [210] L. Marchetti, L. Forni, Catalytic combustion of methane over perovskites, *Appl. Catal. B Environ.* 15 (1998) 179–187.
- [211] D. Ferri, L. Forni, Methane combustion on some perovskite-like mixed oxides, *Appl. Catal. B Environ.* 16 (1998) 119–126. doi:10.1007/BF01696563.
- [212] S. Royer, D. Duprez, S. Kaliaguine, Role of bulk and grain boundary oxygen mobility in the catalytic oxidation activity of LaCo<sub>1-x</sub>Fe<sub>x</sub>O<sub>3</sub>, *Appl. Catal. B Environ.* 234 (2005) 364–375. doi:10.1016/j.jcat.2004.11.041.
- [213] E.R.S. Winter, *The Reactivity of Oxide Surfaces*, (n.d.).
- [214] G.K. Boreskov, *The Catalysis of Isotopic Exchange in Molecular Oxygen*, 8 (n.d.).
- [215] K. Klier, Exchange Reactions Molecules, *J. Catal.* 2 (1963) 479–484.
- [216] J. Nováková, *Catalysis Reviews : Science and Engineering ISOTOPIC EXCHANGE OF OXYGEN O BETWEEN THE GASEOUS PHASE AND OXIDE*, *Catal. Rev.* 4 (1970) 77.
- [217] M. Cherry, M.S. Islam., C.R.A. Catlow, Oxygen Ion Migration in Perovskite-Type Oxides, *J. Solid State Chem.* 118 (1995) 125–132.
- [218] N.Q. Minh, Ceramic Fuel Cells, *J. Am. Ceram. Soc.* 76 (1993) 563.
- [219] C.H. Tascon, J. M. D.; Tejuca, L. G.; Rochester, Surface Interactions of NO and CO with La/MO<sub>3</sub> Oxides *J.*, 95 (1985) 558–566.
- [220] J.L. L. Petunchi, J. O.; Nicasro, Ethylene Hydrogenation over LaCoO<sub>3</sub> Perovskite, *J.C.S. CHEM. COMM.* 121 (1980) 467–468.
- [221] H.C. Yao, S. M., Nitric Oxide and Carbon Monoxide Chemisorption on

Cobalt-Containing Spinels, *J. Phys. Chemistry*. 79 (1974) 2490.

- [222] G.. Kremenec, J.M.L.. Nieto, J.M.D.. Tascon, L.G. Tejuca, Chemisorption and Catalysis on LaMO , Oxides, *J. Chem. SOC., Faraday Trans.* 81 (1985) 939–949.
- [223] M.. Iwamoto, Y.. Yoda, N.. Yamazoe, T. Seiyama, Metal Oxide Catalysts by Temperature Programmed Desorption. 4. Oxygen Adsorption on Various Metal Oxides, *J. Phys. Chem.* 82 (1978) 2564.
- [224] J.M.D. Tascón, L. González Tejuca, Adsorption of CO on Pd(100), *Zeitschrift Für Phys. Chemie Neue*. 121 (1980) 63–78.  
doi:10.1063/1.440430.
- [225] M.A. Pena, J.M.D. Tascon, J.L.G. Fierro, A Study of NO and CO Interactions with LaMnO<sub>3</sub>, *J. Colloid Interface Sci.* 119 (1987) 100–107.
- [226] A.O.M.. Olivan, M.A.. Pena, J.M.D.. Tascon, L. González Tejuca, A COMPARATIVE STUDY OF THE INTERACTIONS OF NO AND CO WITH LaCrO<sub>3</sub>, *J. Mol. Catal.* 45 (1988) 355–363.
- [227] Y. Yokoi, H. Uchida, Catalytic activity of perovskite-type oxide catalysts for direct decomposition of NO : Correlation between cluster model calculations and temperature-programmed desorption experiments, 42 (1998) 167–174.
- [228] Z. Zhao, X. Yang, Y. Wu, Comparative study of Nickel-based perovskite-like mixed oxide catalysts for direct decomposition of, 8 (1996).
- [229] C.T. Au, K.D. Chen, H.X. Dai, Y.W. Liu, J.Z. Luo, C.F. Ng, Oxidative Dehydrogenation of Ethane to Ethene over BaO- and BaBr<sub>2</sub>-Modified Ho<sub>2</sub>O<sub>3</sub> Catalysts, 308 (1998) 300–308.
- [230] T. ARAKAWA, N. OHARA, J. Shiokawa, Reduction of perovskite oxide LnCoO<sub>3</sub> (Ln = La-Eu) in a hydrogen atmosphere, *J. Mater. Sci.* 21 (1986) 1824–1827.
- [231] L. Carreiro, R. Kershaw, K. Dwight, A. Wold, STABILITY OF SEVERAL IRON AND RHODIUM TERNARY OXIDES IN A REDUCING ATMOSPHERE L., *Mater. Res. Bull.* 20 (1985) 619–627.
- [232] T. Katsura, T. Sugihara, K. Kitayama, N. Kimizuka, Thermodynamic properties of Fe-lanthanoid-O compounds at high temperatures, *J. Solid State Chem.* 23 (1978) 43–57.
- [233] E. Diaz, S. Ordóñez, A. Vega, J. Coca, Influence of catalyst treatments on the adsorption properties of  $\gamma$ -Al<sub>2</sub>O<sub>3</sub> supported Pt, Rh and Ru catalysts, *Microporous Mesoporous Mater.* 77 (2005) 245–255.  
doi:10.1016/j.micromeso.2004.09.008.
- [234] U. Lassi, R. Polvinen, S. Suhonen, K. Kallinen, A. Savimäki, M. Härkönen, M. Valden, R.L. Keiski, Effect of ageing atmosphere on the deactivation of

- Pd/Rh automotive exhaust gas catalysts: Catalytic activity and XPS studies, *Appl. Catal. A Gen.* 263 (2004) 241–248. doi:10.1016/j.apcata.2003.12.024.
- [235] M. Haneda, O. Houshito, T. Sato, H. Takagi, K. Shinoda, Y. Nakahara, K. Hiroe, H. Hamada, Improved activity of Rh/CeO<sub>2</sub>-ZrO<sub>2</sub> three-way catalyst by high-temperature ageing, *Catal. Commun.* 11 (2010) 317–321. doi:10.1016/j.catcom.2009.10.020.
- [236] G. Wang, R. You, M. Meng, An optimized highly active and thermo-stable oxidation catalyst Pd/Ce-Zr-Y/Al<sub>2</sub>O<sub>3</sub> calcined at superhigh temperature and used for C<sub>3</sub>H<sub>8</sub> total oxidation, *Fuel.* 103 (2013) 799–804. doi:10.1016/j.fuel.2012.08.051.
- [237] I. Önal, Thermal deactivation of Pt/Rh/ $\gamma$ -Al<sub>2</sub>O<sub>3</sub>/CeO<sub>2</sub> catalyst system, *Stud. Surf. Sci. Catal.* 68 (1991) 621–628. doi:10.1016/S0167-2991(08)62692-0.
- [238] P. Rodrigues De Almeida, A.L. Nakamura, J.R. Sodr , Evaluation of catalytic converter aging for vehicle operation with ethanol, *Appl. Therm. Eng.* 71 (2014) 335–341. doi:10.1016/j.applthermaleng.2014.06.069.
- [239] D.M. Fernandes, C.F. Scofield, A.A. Neto, M.J.B. Cardoso, F.M.Z. Zotin, The influence of temperature on the deactivation of commercial Pd/Rh automotive catalysts, *Process Saf. Environ. Prot.* 87 (2009) 315–322. doi:10.1016/j.psep.2009.05.002.
- [240] M. Moldovan, S. Rauch, G.M. Morrison, M. G ez, M. Antonia Palacios, Impact of ageing on the distribution of platinum group elements and catalyst poisoning elements in automobile catalysts, *Surf. Interface Anal.* 35 (2003) 354–359. doi:10.1002/sia.1541.
- [241] C.H. Bartholomew, Mechanisms of catalyst deactivation, *Appl. Catal. A Gen.* 212 (2001) 17–60. doi:10.1016/S0926-860X(00)00843-7.
- [242] Q. Wang, G. Li, B. Zhao, M. Shen, R. Zhou, The effect of La doping on the structure of Ce<sub>0.2</sub>Zr<sub>0.8</sub>O<sub>2</sub> and the catalytic performance of its supported Pd-only three-way catalyst, *Appl. Catal. B Environ.* 101 (2010) 150–159. doi:10.1016/j.apcatb.2010.09.026.
- [243] B. Seyfi, M. Baghalha, H. Kazemian, Modified LaCoO<sub>3</sub> nano-perovskite catalysts for the environmental application of automotive CO oxidation, *Chem. Eng. J.* 148 (2009) 306–311. doi:10.1016/j.cej.2008.08.041.
- [244] A. Glisenti, M. Pacella, M. Guiotto, M.M. Natile, P. Canu, Largely Cu-doped LaCo<sub>1-x</sub>Cu<sub>x</sub>O<sub>3</sub> perovskites for TWC: Toward new PGM-free catalysts, *Appl. Catal. B Environ.* 180 (2016) 94–105. doi:10.1016/j.apcatb.2015.06.017.
- [245] D.Y. Yoon, Y.J. Kim, J.H. Lim, B.K. Cho, S.B. Hong, I.S. Nam, J.W. Chung, Thermal stability of Pd-containing LaAlO<sub>3</sub> perovskite as a modern TWC, *J. Catal.* 330 (2015) 71–83. doi:10.1016/j.jcat.2015.07.013.



- [246] Z. Liu, J. Hao, L. Fu, T. Zhu, Study of Ag/La<sub>0.6</sub>Ce<sub>0.4</sub>CoO<sub>3</sub> catalysts for direct decomposition and reduction of nitrogen oxides with propene in the presence of oxygen, *Appl. Catal. B Environ.* 44 (2003) 355–370. doi:10.1016/S0926-3373(03)00103-6.
- [247] M.B. Katz, S. Zhang, Y. Duan, H. Wang, M. Fang, K. Zhang, B. Li, G.W. Graham, X. Pan, Reversible precipitation/dissolution of precious-metal clusters in perovskite-based catalyst materials: Bulk versus surface re-dispersion, *J. Catal.* 293 (2012) 145–148. doi:10.1016/j.jcat.2012.06.017.
- [248] Y. Nishihata, J. Mizuki, H. Tanaka, M. Uenishi, M. Kimura, Self-regeneration of palladium-perovskite catalysts in modern automobiles, *J. Phys. Chem. Solids.* 66 (2005) 274–282. doi:10.1016/j.jpcs.2004.06.090.
- [249] N. Labhasetwar, G. Saravanan, S. Kumar Megarajan, N. Manwar, R. Khobragade, P. Doggali, F. Grasset, Perovskite-type catalytic materials for environmental applications, *Sci. Technol. Adv. Mater.* 16 (2015). doi:10.1088/1468-6996/16/3/036002.
- [250] Q. Wang, G. Li, B. Zhao, M. Shen, R. Zhou, The effect of La doping on the structure of Ce<sub>0.2</sub>Zr<sub>0.8</sub>O<sub>2</sub> and the catalytic performance of its supported Pd-only three-way catalyst, *Appl. Catal. B Environ.* 101 (2010) 150–159. doi:10.1016/j.apcatb.2010.09.026.
- [251] S. Furfori, N. Russo, D. Fino, G. Saracco, V. Specchia, NO SCR reduction by hydrogen generated in line on perovskite-type catalysts for automotive diesel exhaust gas treatment, *Chem. Eng. Sci.* 65 (2010) 120–127. doi:10.1016/j.ces.2009.01.065.
- [252] J.P. Dacquin, C. Lancelot, C. Dujardin, C. Cordier-Robert, P. Granger, Support-induced effects of LaFeO<sub>3</sub> perovskite on the catalytic performances of supported Pt catalysts in DeNO<sub>x</sub> applications, *J. Phys. Chem. C.* 115 (2011) 1911–1921. doi:10.1021/jp1069779.
- [253] G.C. Mondragón Rodríguez, K. Kelm, B. Saruhan, H<sub>2</sub>-selective catalytic reduction of NO<sub>x</sub> activity and microstructural analysis of new BaTi<sub>0.95</sub>Pd<sub>0.05</sub>O<sub>3</sub> catalyst, *Appl. Catal. A Gen.* 387 (2010) 173–184. doi:10.1016/j.apcata.2010.08.012.
- [254] R. Zhang, A. Villanueva, H. Alamdari, S. Kaliaguine, Catalytic reduction of NO by propene over LaCo<sub>1-x</sub>Cu<sub>x</sub>O<sub>3</sub> perovskites synthesized by reactive grinding, *Appl. Catal. B Environ.* 64 (2006) 220–233. doi:10.1016/j.apcatb.2005.10.028.
- [255] B. Kucharczyk, W. Tylus, Effect of Pd additive on the activity of monolithic LaMnO<sub>3</sub>-based catalysts for methane combustion, *Catal. Today.* 137 (2008) 318–323. doi:10.1016/j.cattod.2007.11.049.
- [256] R. Zhang, A. Villanueva, H. Alamdari, S. Kaliaguine, SCR of NO by

- propene over nanoscale  $\text{LaMn}_{1-x}\text{Cu}_x\text{O}_3$  perovskites, *Appl. Catal. A Gen.* 307 (2006) 85–97. doi:10.1016/j.apcata.2006.03.019.
- [257] A. Schön, J.P. Dacquin, P. Granger, C. Dujardin, Non stoichiometric  $\text{La}_{1-y}\text{FeO}_3$  perovskite-based catalysts as alternative to commercial three-way-catalysts? – Impact of Cu and Rh doping, *Appl. Catal. B Environ.* 223 (2018) 167–176. doi:10.1016/j.apcatb.2017.06.026.
- [258] H.X. Dai, H. He, W. Li, Z.Z. Gao, C.T. Au, Perovskite-type oxide  $\text{ACo}_{0.8}\text{Bi}_{0.2}\text{O}_{2.87}$  ( $A = \text{La}_{0.8}\text{Ba}_{0.2}$ ): a catalyst for low-temperature CO oxidation, *Catal. Letters.* 73 (2001) 149–156.
- [259] I.S. Yakovleva, L.A. Isupova, S. V Tsybulya, A. V Chernysh, Mechanochemical synthesis and reactivity of  $\text{La}_{1-x}\text{Sr}_x\text{FeO}_{3-y}$  perovskites ( $0 \leq x \leq 1$ ), *J. Mater. Sci.* 39 (2004) 5517–5521.
- [260] L.A. Isupova, I.S. Yakovleva, V.A. Rogov, G.M. Alikina, V.A. Sadykov, Oxygen States in Oxides with a Perovskite Structure and Their Catalytic Activity in Complete Oxidation Reactions : System  $\text{La}_{1-x}\text{Ca}_x\text{FeO}_{3-y}$  ( $x = 0 - 1$ ), *Kinet. Catal.* 45 (2004) 473–480.
- [261] P. Porta, S. Cimino, S. De Rossi, M. Faticanti, G. Minelli, I. Pettiti, structural and redox properties, *Mater. Chem. Phys.* 71 (2001) 165–173.
- [262] W. Yang, R. Zhang, B. Chen, N. Bion, D. Duprez, S. Royer, Activity of perovskite-type mixed oxides for the low-temperature CO oxidation : Evidence of oxygen species participation from the solid, *J. Catal.* 295 (2012) 45–58. doi:10.1016/j.jcat.2012.07.022.
- [263] P. Esmaeilnejad-ahranjani, A. Khodadadi, H. Ziaei-azad, Y. Mortazavi, Effects of excess manganese in lanthanum manganite perovskite on lowering oxidation light-off temperature for automotive exhaust gas pollutants, *Chem. Eng. J.* 169 (2011) 282–289. doi:10.1016/j.cej.2011.02.062.
- [264] J. Beckers, G. Rothenberg, “ Hot Spot ” Hydrocarbon Oxidation Catalysed by Doped Perovskites — Towards Cleaner Diesel Power, *ChemPhysChem.* 6 (2005) 223–225. doi:10.1002/cphc.200400421.
- [265] V. Roche, E. Siebert, M.C. Steil, J.P. Deloume, Electrochemical promotion of propane deep oxidation on doped lanthanum manganites, *Ionics (Kiel).* 14 (2008) 235–241. doi:10.1007/s11581-007-0185-9.
- [266] N.A. Merino, B.P. Barbero, P. Grange, L.E. Cadús,  $\text{La}_{1-x}\text{Ca}_x\text{CoO}_3$  perovskite-type oxides : preparation , characterisation , stability , and catalytic potentiality for the total oxidation of propane, *J. Catal.* 231 (2005) 232–244. doi:10.1016/j.jcat.2005.01.003.
- [267] T. Asada, T. Kayama, H. Kusaba, H. Einaga, Y. Teraoka, Preparation of alumina-supported  $\text{LaFeO}_3$  catalysts and their catalytic activity for propane combustion, *Catal. Today.* 139 (2008) 37–42.

doi:10.1016/j.cattod.2008.08.006.

- [268] K.S. Song, D. Klvana, J. Kirchnerova, Kinetics of propane combustion over, *Appl. Catal. A Gen.* 213 (2001) 113–121.
- [269] F. Diehl, J. Barbier, D. Duprez, I. Guibard, G. Mabilon, Applied Catalysis B: Environmental Catalytic oxidation of heavy hydrocarbons over Pt / Al<sub>2</sub>O<sub>3</sub>. Influence of the structure of the molecule on its reactivity, *Appl. Catal. B, Environ.* 95 (2010) 217–227. doi:10.1016/j.apcatb.2009.12.026.
- [270] Z. Sui, L. Vradman, I. Reizner, M. V Landau, M. Herskowitz, Effect of preparation method and particle size on LaMnO<sub>3</sub> performance in butane oxidation, *Catal. Commun.* 12 (2011) 1437–1441. doi:10.1016/j.catcom.2011.06.001.
- [271] R. Spinicci, A. Tofanari, M. Faticanti, I. Pettiti, P. Porta, Hexane total oxidation on LaMO<sub>3</sub> ( M = Mn , Co , Fe ) perovskite-type oxides, *J. Mol. Catal. A Chem.* 176 (2001) 247–252.
- [272] C. Hwan, Strontium-Doped Perovskites Rival, *Science* (80-. ). 327 (2010) 1624. doi:10.1126/science.1184087.
- [273] J. Rodriguez-Mirasol, J.A. Moulijn, F. Kapteijn, Heterogeneous catalytic decomposition of nitrous oxide, *Appl. Catal. B, Environ.* 9 (1996) 25–64.
- [274] S. Furfori, S. Bensaid, N. Russo, D. Fino, Towards practical application of lanthanum ferrite catalysts for NO reduction with H<sub>2</sub>, *Chem. Eng. J.* 154 (2009) 348–354. doi:10.1016/j.cej.2009.03.009.
- [275] F. Dhainaut, S. Pietrzyk, P. Granger, Impact of thermal aging on the kinetic parameters of the NO/H<sub>2</sub> reaction on Pd/LaCoO<sub>3</sub>, *Langmuir.* 25 (2009) 13673–13679. doi:10.1021/la901840z.
- [276] Y. Renème, F. Dhainaut, P. Granger, Catalytic post-treatment of automotive exhaust gas from natural gas combustion engines: Potential interest of perovskite materials, *Top. Catal.* 52 (2009) 2007–2012. doi:10.1007/s11244-009-9401-3.
- [277] J.P. Dacquain, M. Cabié, C.R. Henry, C. Lancelot, C. Dujardin, S.R. Raouf, P. Granger, Structural changes of nano-Pt particles during thermal ageing: Support-induced effect and related impact on the catalytic performances, *J. Catal.* 270 (2010) 299–309. doi:10.1016/j.jcat.2010.01.006.
- [278] J.C. Menezes, S. Inkari, T. Bertin, J. Barbier, R. Noirotc, T. Seguelongd, Catalytic reduction of NO by propene in the presence of oxygen and water over La<sub>0.59</sub>Sr<sub>0.39</sub>MnO<sub>3</sub>-alumina mixtures, *Appl. Catal. B Environ.* 15 (1998) L1–L4.
- [279] J. Lentmaier, S. Kemmler-Sack, BIFUNCTIONAL YFeO<sub>3</sub>-BASED CATALYSTS USED IN THE SELECTIVE CATALYTIC REDUCTION

OF NITROGEN MONOXIDE IN THE PRESENCE OF EXCESS OXYGEN, *Mater. Res. Bull.* 33 (1998) 461–473.

- [280] United States Environmental Protection Agency, Light Duty Vehicle Emissions | Green Vehicle Guide | US EPA, (n.d.). <https://www.epa.gov/greenvehicles/light-duty-vehicle-emissions> (accessed May 12, 2021).
- [281] O. Ruetten, S. Pischinger, R. Weinowski, D. Gian, W. Betton, M. Bahn, Catalyst Aging Method for Future Emissions Standard Requirements, *SAE Int. Int.* (2010).
- [282] D. Gerçeker, Removal of hydrocarbons, carbon monoxide and nitric oxides in automotive exhaust with three-way catalytic converter, Middle East Technical University, 2013. doi:10.1037//0033-2909.126.1.78.
- [283] M. Uenishi, M. Taniguchi, H. Tanaka, M. Kimura, Y. Nishihata, J. Mizuki, T. Kobayashi, Redox behavior of palladium at start-up in the Perovskite-type LaFePdO<sub>x</sub> automotive catalysts showing a self-regenerative function, *Appl. Catal. B Environ.* 57 (2005) 267–273. doi:10.1016/j.apcatb.2004.11.011.
- [284] F.C. Gennari, T. Montini, P. Fornasiero, J.J. Andrade Gamboa, Reduction behavior of nanoparticles of Ce<sub>0.8</sub>Zr<sub>0.2</sub>O<sub>2</sub> produced by different approaches, *Int. J. Hydrogen Energy.* 33 (2008) 3549–3554. doi:10.1016/j.ijhydene.2007.12.006.
- [285] M. Nguéfacq, A.F. Popa, S. Rossignol, C. Kappenstein, Preparation of alumina through a sol-gel process. Synthesis, characterization, thermal evolution and model of intermediate boehmite, *Phys. Chem. Chem. Phys.* 5 (2003) 4279–4289. doi:10.1039/b306170a.
- [286] X.-D. Zhou, L.R. Pederson, Q. Cai, J. Yang, B.J. Scarfino, M. Kim, W.B. Yelon, W.J. James, H.U. Anderson, C. Wang, Structural and magnetic properties of LaMn<sub>1-x</sub>Fe<sub>x</sub>O<sub>3</sub> (0 < x < 1.0), *J. Appl. Phys.* 99 (2006) 08M918. doi:10.1063/1.2176389.
- [287] T.A. Nijhuis, A.E.W. Beers, T. Vergunst, I. Hoek, F. Kapteijn, J.A. Moulijn, Preparation of monolithic catalysts, *Catal. Rev. - Sci. Eng.* 43 (2001) 345–380. doi:10.1081/CR-120001807.
- [288] D.L. Mowery, R.L. McCormick, Deactivation of alumina supported and unsupported PdO methane oxidation catalyst: The effect of water on sulfate poisoning, *Appl. Catal. B Environ.* 34 (2001) 287–297. doi:10.1016/S0926-3373(01)00222-3.
- [289] R. Blume, M. Hävecker, S. Zafeirotos, D. Teschner, A. Knop-Gericke, R. Schlögl, P. Dudin, A. Barinov, M. Kiskinova, Oxidation of methanol on Ru catalyst: Effect of the reagents partial pressures on the catalyst oxidation

state and selectivity, *Catal. Today*. 124 (2007) 71–79.  
doi:10.1016/j.cattod.2007.02.030.

[290] O. Krocher, M. Widmer, M. Elsener, D. Rothe, Adsorption and desorption of SO<sub>x</sub> on diesel oxidation catalysts, *Ind. Eng. Chem. Res.* 48 (2009) 9847–9857. doi:10.1021/ie900882p.

[291] I. Arrizabalaga, O. Gómez-Laserna, J.A. Carrero, J. Bustamante, A. Rodríguez, G. Arana, J.M. Madariaga, Diffuse reflectance FTIR database for the interpretation of the spectra obtained with a handheld device on built heritage materials, *Anal. Methods*. 7 (2015) 1061–1070.  
doi:10.1039/c4ay02189d.



## APPENDICES

### APPENDIX A

#### CATALYST PREPARATION

##### A.1 Preparation of Ceria-Zirconia Oxide ( $\text{Ce}_{0.8}\text{Zr}_{0.2}\text{O}_2$ )

###### Chemicals:

Cerium (III) nitrate hexahydrate

Zirconyl nitrate hexahydrate ( $\text{N}_2\text{O}_7\text{Zr}$ aq) (Fluka, % 27 & Zr (gravimetric))

Hydrogen peroxide ( $\text{H}_2\text{O}_2$ ) (J.T. Baker, 30% v/v)

Ammonium hydroxide solution ( $\text{NH}_4\text{OH}$ ) (Aldrich, 33%  $\text{NH}_3$ )

Iso-propanol ( $\text{CH}_3\text{CHOHCH}_3$ ) (J.T. Baker)

###### Procedure:

1. Place 1lt deionized water in a beaker.
2. Tare 214.00 g of  $\text{CeN}_3\text{O}_9.6\text{H}_2\text{O}$  and place it into water
3. Tare 41.80 g of  $\text{N}_2\text{O}_7\text{Zr}$ .aq and place it into water (solution 1)
4. Stir the solution 1 for 30 min with magnetic stirrer at 300rpm
5. Measure 333ml  $\text{H}_2\text{O}_2$  and place it into a burette
6. Add  $\text{H}_2\text{O}_2$  into solution 1 dropwise within 1 hour. (rate: 1drop/sec) During this step stirring continues.
7. Measure 550ml of  $\text{NH}_4\text{OH}$  solution and place it into 2 lt beaker.
8. Place solution 1 into a burette and add solution 1 into of  $\text{NH}_4\text{OH}$  solution dropwise. (Solution 2)
9. Obtained solution 2 is settled for 48 hours in order to collect precipitates.
10. Product of solution 2 is washed and filtered with excess  $\text{CH}_3\text{CHOHCH}_3$

11. The filtrate is mixed with 250ml  $\text{CH}_3\text{CHOHCH}_3$  and placed into a reflux setup and refluxed for 6 hours
12. Refluxed product is placed into an oven and dried at  $150^\circ\text{C}$  for 12 h.
13. Dried powder is firstly grounded within a mortar
14. Obtained powder is placed into a furnace and calcined under dry air flow at  $600^\circ\text{C}$  for 5 hr.

## A.2 Preparation of Pseudoboehmite

### Chemicals:

Aluminum-tri-sec-butoxide (ATSB) ( $\text{Al}(\text{OC}_4\text{H}_9)_3$ ) (Aldrich, 97%)

Hydrochloric acid HCl (Aldrich, min 37%)

### Procedure:

1. 103.10 g of  $\text{Al}(\text{OC}_4\text{H}_9)_3$  hydrolyzed with 730 ml double distilled water.
2. 9.00 ml HCL is added to the beaker.
3. The mixture is stirred vigorously for 1 h while keeping at  $80^\circ\text{C}$ .
4. Product as gel is dried at  $150^\circ\text{C}$  for 48 h

The powder sample is grounded and calcined in the oven for at  $300^\circ\text{C}$  for 5 h with a heating rate of  $5^\circ\text{C}/\text{min}$

## A.3 Metal Impregnation on Ceria-Zirconia Oxide

### Chemicals:

Palladium (II) chloride solution (Aldrich,  $\text{PdCl}_2$ , 5 wt% solution in 10 wt% HCl)

Rhodium (III) nitrate solution (Aldrich,  $\text{Rh}(\text{NO}_3)_3$  ~ 10 wt% Rh in 5wt% nitric acid ( $\text{HNO}_3$ ))

### Procedure:



1. Place 6ml deionized water in a beaker, measure 0.62 ml of  $\text{Rh}(\text{NO}_3)_3$  and place it into water. (Solution 1)
2. Place 6ml deionized water in a beaker, measure 3.25 ml of  $\text{PdCl}_2$  solutions and place it into water (solution 2)
3. Place the solution 1 into a rotary evaporator and mix for 15 without heat or vacuum at 130rpm
4. Tare 7.50 g  $\text{Ce}_{0.8}\text{Zr}_{0.2}\text{O}_2$  and place it into rotary evaporator to mix with solution 1.
5. Operate the rotary evaporator at 80 °C under vacuum at ~450 mbar until all the liquid evaporates.
6. Place the product into an oven and dried at 150°C for 12 h (powder 1).
7. Place the solution 2 into a rotary evaporator and mix for 15 without heat or vacuum at 130rpm
8. Tare 15 g  $\text{Ce}_{0.8}\text{Zr}_{0.2}\text{O}_2$  and place it into rotary evaporator to mix with solution 2.
9. Operate the rotary evaporator at 80 °C under vacuum at ~450 mbar until all the liquid evaporates.
10. Place the product into an oven and dried at 150°C for 12 h (powder 2).
11. Dried powder 1 and powder 2 are mixed and grounded within a mortar.
12. Obtained powder is placed into a furnace and calcined under dry air at 500°C flow for 3 hr.

#### **A.4 Preparation of C1 Catalyst**

##### **Procedure:**

1. 15 g of metal impregnated ceria-zirconia mixed oxide and 36 g of  $\gamma$ -Al<sub>2</sub>O<sub>3</sub> are mixed in 75.77 ml of deionized water and ball-milled with 3 mm diameter alumina chips at 275 rpm for 24 hr in HDPE mortar.
2. Product is dried at 150°C for 12 h, grounded and calcined at 550°C for 1 h.
3. 3.6 g of pseudoboehmite is added and the mixture is solved in 81.09 ml deionized water and ball-milled for 30 min at 275 rpm.
4. 3.67 ml of nitric acid is added and slurry is ball-milled at same speed for 3 h (coating solution).
5. Monolith is dipped in to the coating solution and channels inside the monolith is opened by pressurized dry air (dipping process).
6. Dipping process is repeated until weight change stabilization.
7. Coated monolith is dried at 150°C for 12 h and calcined at 550°C for 1 h.
8. Calcined monolith is tared and obtained data is recorded as weight change of monolith on dry basis.

#### **A.5 Preparation of LaFe<sub>0.57</sub>Co<sub>0.37</sub>Pd<sub>0.06</sub>O<sub>3</sub>**

##### **Chemicals:**

Lanthanum (III) nitrate hexahydrate (La(NO<sub>3</sub>)<sub>3</sub>·6H<sub>2</sub>O), (Aldrich, 99.9%)

Cobalt (II) nitrate hexahydrate (Co(NO<sub>3</sub>)<sub>2</sub>·6H<sub>2</sub>O), (Aldrich, 98.0%)

Iron (III) nitrate nonahydrate (Fe(NO<sub>3</sub>)<sub>3</sub>·9H<sub>2</sub>O), (Aldrich, 99.5%)

Palladium (II) nitrate hydrate (Pd(NO<sub>3</sub>)<sub>2</sub>·xH<sub>2</sub>O), (Aldrich, 99.9%)

Citric acid monohydrate, C<sub>6</sub>H<sub>8</sub>O<sub>7</sub> \* H<sub>2</sub>O (Merck, 99.5%)

##### **Procedure:**

1. Place 0.130g Pd(NO<sub>3</sub>)<sub>2</sub> · 2H<sub>2</sub>O, 1.874g Fe(NO<sub>3</sub>)<sub>3</sub>·9H<sub>2</sub>O, 0.876g Co(NO<sub>3</sub>)<sub>2</sub>·6H<sub>2</sub>O, 3.523g La(NO<sub>3</sub>)<sub>3</sub> \* 6 H<sub>2</sub>O and 15ml deionized water in a beaker (Solution 1).

2. Stirr the solution 1 vigorously for 1 hour.
3. Place 10.3g  $C_6H_8O_7 \cdot H_2O$  and 20 ml deionized water in a beaker (Solution 2).
4. Stir the solution 2 vigorously for 1 hour.
5. Pour solution 2 into solution 1 under vigorous stirring.
6. Stir the obtained solution for 72 hours until the water evaporates and a jelly solution is obtained.
7. The product is placed into an oven and dried at  $150^\circ C$  for 12 h.
8. Dried powder is firstly grounded within a mortar
9. Obtained powder is placed into a furnace and calcined under dry air flow at  $700^\circ C$  for 24 hr.

#### **A.6 Preparation of $LaFe_{0.57}Co_{0.37}Rh_{0.06}O_3$**

##### **Chemicals:**

Lanthanum (III) nitrate hexahydrate ( $La(NO_3)_3 \cdot 6H_2O$ ), (Aldrich, 99.9%)

Cobalt (II) nitrate hexahydrate ( $Co(NO_3)_2 \cdot 6H_2O$ ), (Aldrich, 98.0%)

Iron (III) nitrate nonahydrate ( $Fe(NO_3)_3 \cdot 9H_2O$ ), (Aldrich, 99.5%)

Rhodium (III) nitrate solution hydrate ( $Rh(NO_3)_2 \cdot xH_2O$ ), (Aldrich, 99.9%)

Citric acid monohydrate,  $C_6H_8O_7 \cdot H_2O$  (Merck, 99.5%)

##### **Procedure:**

1. Place 0.126g ( $Rh(NO_3)_2 \cdot xH_2O$ ), 1.874g  $Fe(NO_3)_3 \cdot 9H_2O$ , 0.876g  $Co(NO_3)_2 \cdot 6H_2O$ , 3.523g  $La(NO_3)_3 \cdot 6H_2O$  and 15ml deionized water in a beaker (Solution 1).
2. Stirr the solution 1 vigorously for 1 hour.

3. Place 10.3g  $C_6H_8O_7 \cdot H_2O$  and 20 ml deionized water in a beaker (Solution 2).
4. Stir the solution 2 vigorously for 1 hour.
5. Pour solution 2 into solution 1 under vigorous stirring.
6. Stir the obtained solution for 72 hours until the water evaporates and a jelly solution is obtained.
7. The product is placed into an oven and dried at  $150^\circ C$  for 12 h.
8. Dried powder is firstly grounded within a mortar
9. Obtained powder is placed into a furnace and calcined under dry air flow at  $700^\circ C$  for 24 hr.

#### **A.7 Preparation of C2 Catalyst**

##### **Procedure:**

- 1) 1.27g  $LaFe_{0.57}Co_{0.37}Pd_{0.06}O_3$ , 0.19  $LaFe_{0.57}Co_{0.37}Rh_{0.06}O_3$ , 1.38g  $Ce_{0.8}Zr_{0.2}O_2$ , 1.97g  $Al_2O_3$  are mixed in 7.25 ml of deionized water and ball-milled with 3 mm diameter alumina chips at 275 rpm for 24 hr in HDPE mortar.
- 2) Product is dried at  $150^\circ C$  for 12 h, grounded and calcined at  $550^\circ C$  for 1 h.
- 3) 3.6 g of pseudoboehmite is added and the mixture is solved in 81.09 ml deionized water and ball-milled for 30 min at 275 rpm.
- 4) 3.67 ml of nitric acid is added and slurry is ball-milled at same speed for 3 h (coating solution).
- 5) Monolith is dipped in to the coating solution and channels inside the monolith is opened by pressurized dry air (dipping process).
- 6) Dipping process is repeated until weight change stabilization.
- 7) Coated monolith is dried at  $150^\circ C$  for 12 h and calcined at  $550^\circ C$  for 1 h.

- 8) Calcined monolith is tared and obtained data is recorded as weight change of monolith on dry basis

### **A.8 Preparation of C3 Catalyst**

#### **Procedure:**

- 1) 0.64g  $\text{LaFe}_{0.57}\text{Co}_{0.37}\text{Pd}_{0.06}\text{O}_3$ , 0.10  $\text{LaFe}_{0.57}\text{Co}_{0.37}\text{Rh}_{0.06}\text{O}_3$ , 1.38g  $\text{Ce}_{0.8}\text{Zr}_{0.2}\text{O}_2$ , 2.70g  $\text{Al}_2\text{O}_3$  are mixed in 7.25 ml of deionized water and ball-milled with 3 mm diameter alumina chips at 275 rpm for 24 hr in HDPE mortar.
- 2) Product is dried at 150°C for 12 h, grounded and calcined at 550°C for 1 h.
- 3) 3.6 g of pseudoboehmite is added and the mixture is solved in 81.09 ml deionized water and ball-milled for 30 min at 275 rpm.
- 4) 3.67 ml of nitric acid is added and slurry is ball-milled at same speed for 3 h (coating solution).
- 5) Monolith is dipped in to the coating solution and channels inside the monolith is opened by pressurized dry air (dipping process).
- 6) Dipping process is repeated until weight change stabilization.
- 7) Coated monolith is dried at 150°C for 12 h and calcined at 550°C for 1 h.
- 8) Calcined monolith is tared and obtained data is recorded as weight change of monolith on dry basis.

### **A.9 Preparation of C4 Catalyst**

#### **Procedure:**

- 1) 0.13g  $\text{LaFe}_{0.57}\text{Co}_{0.37}\text{Pd}_{0.06}\text{O}_3$ , 0.02  $\text{LaFe}_{0.57}\text{Co}_{0.37}\text{Rh}_{0.06}\text{O}_3$ , 1.38g  $\text{Ce}_{0.8}\text{Zr}_{0.2}\text{O}_2$ , 3.29g  $\text{Al}_2\text{O}_3$  are mixed in 7.25 ml of deionized water and ball-

milled with 3 mm diameter alumina chips at 275 rpm for 24 hr in HDPE mortar.

- 2) Product is dried at 150°C for 12 h, grounded and calcined at 550°C for 1 h.
- 3) 3.6 g of pseudoboehmite is added and the mixture is solved in 81.09 ml deionized water and ball-milled for 30 min at 275 rpm.
- 4) 3.67 ml of nitric acid is added and slurry is ball-milled at same speed for 3 h (coating solution).
- 5) Monolith is dipped in to the coating solution and channels inside the monolith is opened by pressurized dry air (dipping process).
- 6) Dipping process is repeated until weight change stabilization.
- 7) Coated monolith is dried at 150°C for 12 h and calcined at 550°C for 1 h.
- 8) Calcined monolith is tared and obtained data is recorded as weight change of monolith on dry basis.

## APPENDIX B

### NOBLE METAL LOADING CALCULATION

In order to calculate the noble metal loading of a certain catalyst the following formula should be used:

$$AL = \frac{WCDB * (C_{Rh} + C_{Pd})}{100 * V_{monolith}}$$

Where,

AL is actual noble metal loading of a certain catalyst

WCDB is weight change of monolith after coating process on dry basis

C<sub>Rh</sub> is the measured concentration of the rhodium by ICP-OES

C<sub>Pd</sub> is the measured concentration of the palladium by ICP-OES

Actual noble metal loadings of each catalyst are shown in Table B. 1

Table B. 1. Actual Noble Metal Loading Calculation

	<b>Weight Change on Dry Basis  (g)</b>	<b>Monolith Volume  (ft<sup>3</sup>)</b>	<b>Measured Rh  (wt. %)</b>	<b>Measured Pd  (wt. %)</b>	<b>Actual NM Loading  (g/ft<sup>3</sup>)</b>
C1	0.469	0.000174427	0.100	0.649	20.165
C2	0.473	0.000174427	0.101	0.649	20.332
C3	0.481	0.000174427	0.051	0.326	10.383
C4	0.471	0.000174427	0.010	0.065	2.038

## APPENDIX C

### MASS FLOW CONTROLLER CALIBRATION

All MFCs are calibrated once a year. Before each activity experiment, the flow through the reactor was checked. A soft bubble flow meter is used for calibration and flow control. All calibration points were measured in five replicates. The measurement accuracy is about 2%. The following formula was used to calculate the measurement accuracy;

$$Q^o = \frac{Q_1 + Q_2 + Q_3 + Q_4 + Q_5}{5}$$

$$\%acc = \frac{\frac{\sum_{i=1}^5 |Q^o - Q_i|}{5}}{Q^o} \times 100$$

Where,

$Q^o$  is mean of the measured values

$Q_i$  is the value of current measurement

In Table C. 1 each cylinder composition and MFC number are illustrated. In the calibration test soft bubble flow meter was used to measure the flow coming from MFC device. As experiment procedure, the flow is set from control station to related MFC device then the bubble is formed in front of the flowing stream within glass tube. Movement duration of the soft bubble through glass tube for certain volume is recorded. Calibration results for MFC 1-5 are shown in Figure C. 1, Figure C. 2, Figure C. 3, Figure C. 4 and Figure C. 5.



Table C. 1. Cylinders connected to MFC devices

MFC #	Cylinder Content	Cylinder Composition (%)
MFC 1	O <sub>2</sub>	100
MFC 2	NO	50
	N <sub>2</sub>	50
MFC 3	C <sub>3</sub> H <sub>6</sub>	0.33
	C <sub>3</sub> H <sub>8</sub>	0.11
	CO	8.87
	H <sub>2</sub>	2.04
	CO <sub>2</sub>	88.65
MFC 4	SO <sub>2</sub>	0.01
	N <sub>2</sub>	0.99
MFC 5	N <sub>2</sub>	100

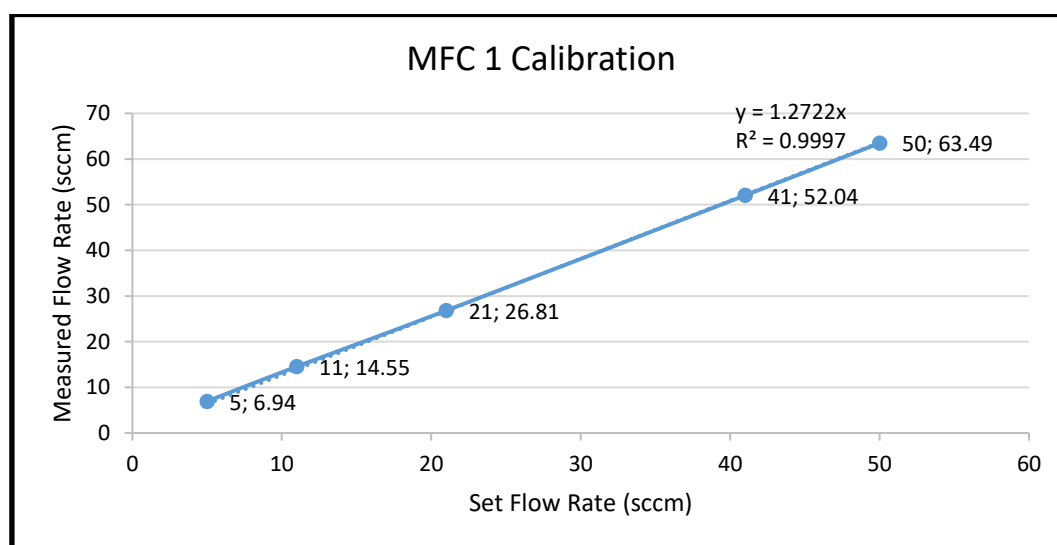


Figure C. 1. Calibration result of MFC1 connected to O<sub>2</sub> cylinder.

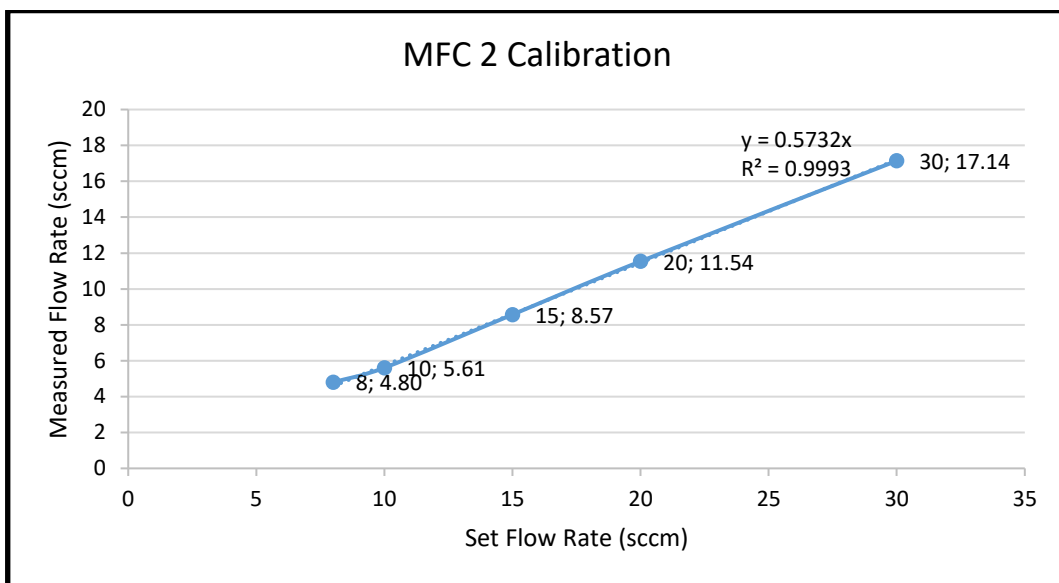


Figure C. 2. Calibration result of MFC2 connected to NO+N2 containing cylinder.

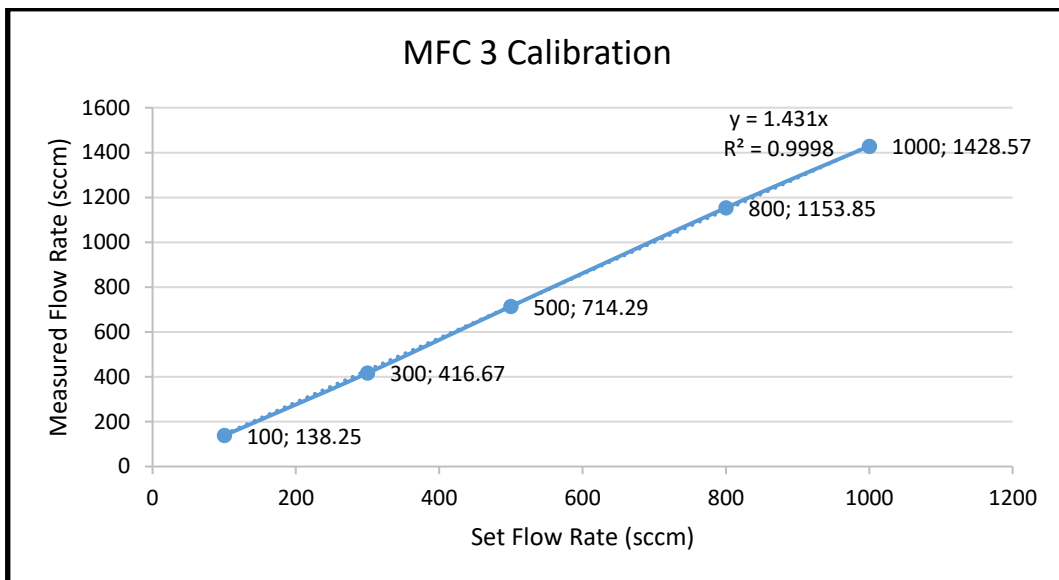


Figure C. 3. Calibration result of MFC3 connected to C<sub>3</sub>H<sub>6</sub>, C<sub>3</sub>H<sub>8</sub>, CO, H<sub>2</sub>, CO<sub>2</sub> containing cylinder.

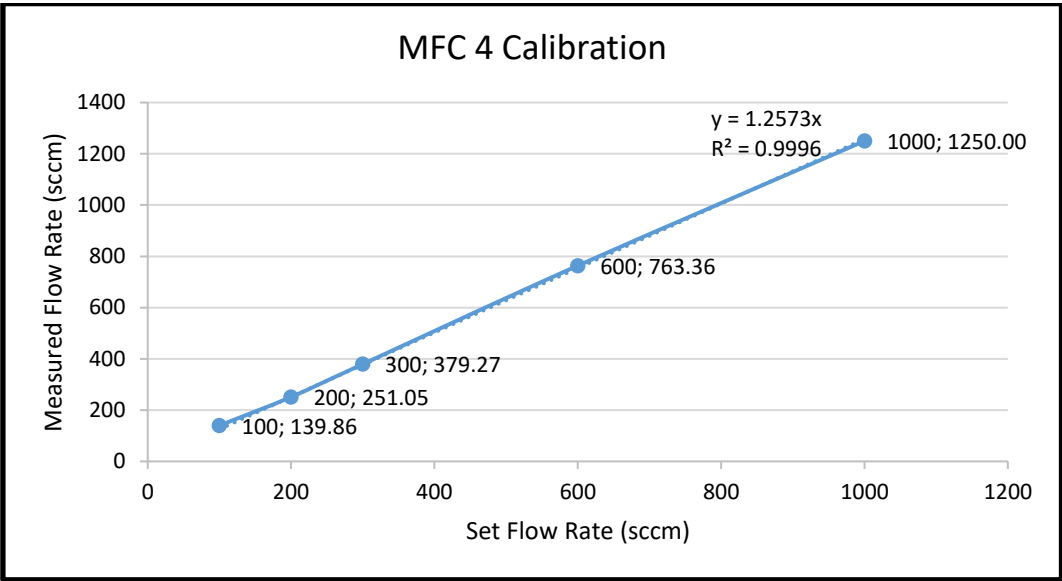


Figure C. 4. Calibration result of MFC4 connected SO<sub>2</sub>, and N<sub>2</sub>, containing cylinder

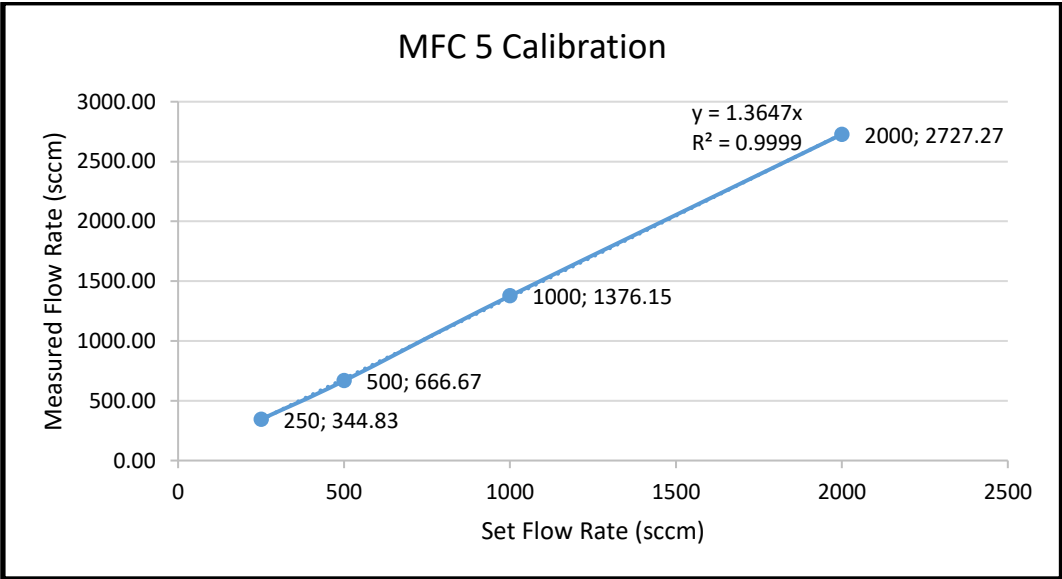


Figure C. 5. Calibration result of MFC5 connected N<sub>2</sub>, containing cylinder



## APPENDIX D

### MASS SPECTROMETER CALIBRATION

After calibrating the mass flow controllers mass spectrometer calibration was conducted. Mass spectrometry calibration was performed when experiments were suspended for 1 month or more. Mass spectrometry was never turned off in order to prevent the filament from cooling in tests performed on the same day. Mass spectrometry was operated under gas flow for 2-4 hours to stabilize again when it stopped for a maximum of half an hour. This duration was for the heating of the filament and the tests were continued when the signal levels required to start the experiment reached the desired value. When the mass spectrometer was stopped for more than half an hour, the stabilization duration reached 6 hours. In this study, 43, 1, 30, 41 and 64 m/z signals were used for determination of C<sub>3</sub>H<sub>8</sub>, H<sub>2</sub>, NO, C<sub>3</sub>H<sub>6</sub> and SO<sub>2</sub> concentrations, respectively. The overlaps made by the relevant compounds to the m/z signals referred from the mass spectrometry library is shown in Table D 1. The formulas used to sort out the effects of these overlaps are given between D1-D5. In these formulas S<sub>#</sub> o represents the signal obtained in m/z. k<sub>#</sub> represents the constants specific to the relevant equation. As seen in equations D1-D3, it is assumed that there is no interference for C<sub>3</sub>H<sub>8</sub>, H<sub>2</sub> and CO. For calibration study 6 calibration points were used. Calibration points were selected as 0%, 20%, 40%, 60%, 80% and 100% composition of the species for which 80% composition is same as reaction gas composition for that component. For example, NO concentration in reaction gas mixture is 1440 ppm and six calibration point were 0ppm, 360ppm, 720ppm, 1080ppm, 1440ppm and 1800ppm for NO. While changing the NO composition rest of the component's concentration was kept at reacting gas concentration. Calibration results are shown in Figure D. 1, Figure D. 2, Figure D. 3 and Figure D. 4, for C<sub>3</sub>H<sub>6</sub>, C<sub>3</sub>H<sub>8</sub>, H<sub>2</sub>, NO, respectively.

Table D 1. Relative intensities of peaks obtained each compound at specified m/z.  
Obtained from mass spectrometer library.

Compound	Relative Intensities				
	m/z= 1	m/z= 30	m/z= 41	m/z= 43	m/z= 64
SO <sub>2</sub>					100
NO		100			
C <sub>3</sub> H <sub>8</sub>		2.1	12.4	22.3	
C <sub>3</sub> H <sub>6</sub>			100		
O <sub>2</sub>					
H <sub>2</sub>	10				
N <sub>2</sub>					
H <sub>2</sub> O					
CO		0.2			
CO <sub>2</sub>					

$$C_{C_3H_8} = k_1 * S_{43} \quad (D1)$$

$$C_{H_2} = k_2 * S_1 \quad (D2)$$

$$C_{CO} = C_{NDIR} \quad (D3)$$

$$C_{NO} = k_4 * S_{30} - k_5 * C_{C_3H_8} - k_6 * C_{CO} \quad (D4)$$

$$C_{C_3H_6} = k_7 * S_{41} - k_8 * C_{C_3H_8} \quad (D5)$$

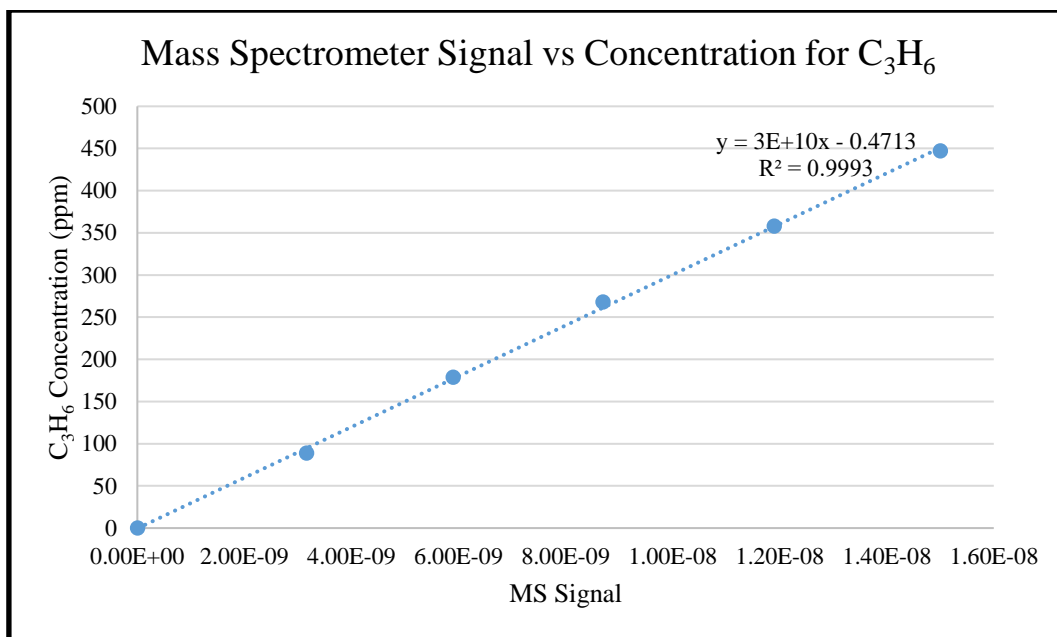


Figure D. 1 Mass spectrometer calibration result for C<sub>3</sub>H<sub>6</sub> (m/z = 41) for 0, 89, 179, 268, 358, 447 ppm concentration.

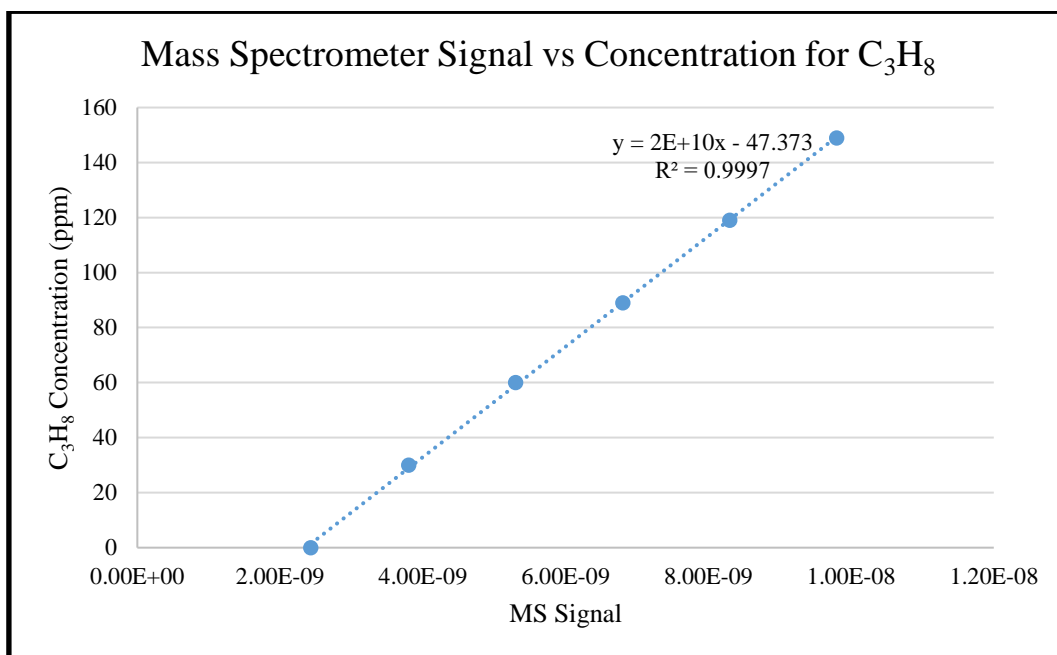


Figure D. 2. Mass spectrometer calibration result for C<sub>3</sub>H<sub>8</sub> (m/z = 43) for 0, 30, 60, 89, 119, 149 ppm concentration

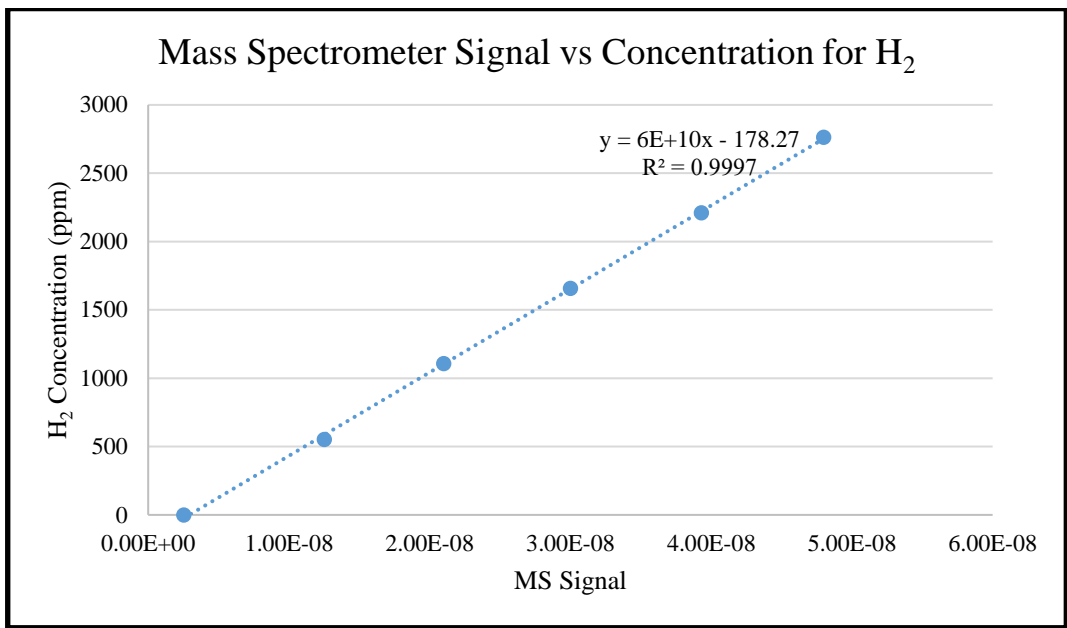


Figure D. 3. Mass spectrometer calibration result for H<sub>2</sub> (m/z = 1) for 0, 553, 1106, 1658, 2211, 2764 ppm concentration

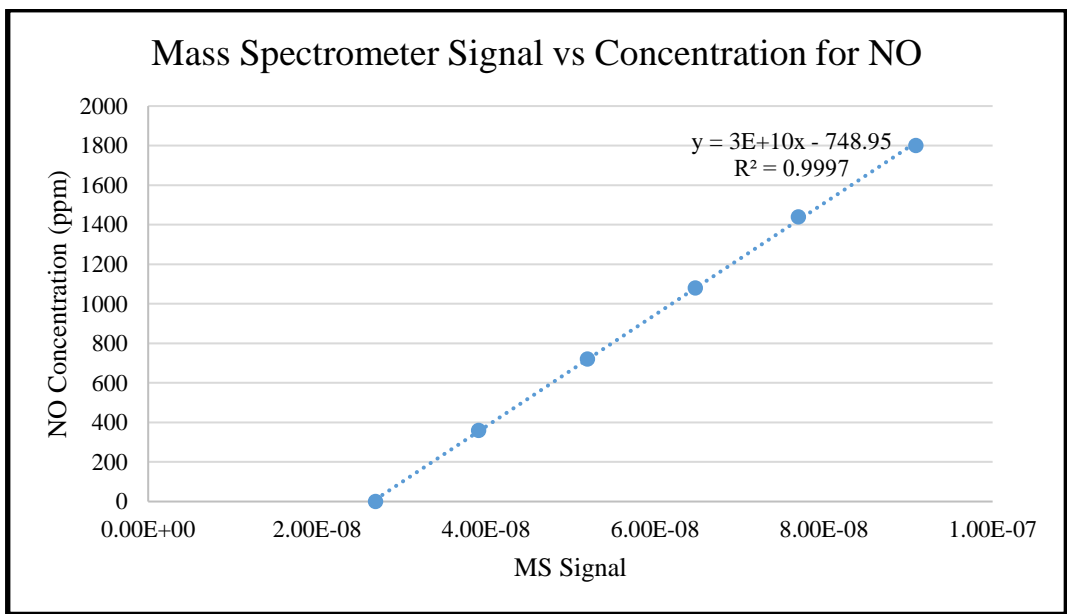


Figure D. 4. Mass spectrometer calibration result for NO (m/z = 30) for 0, 360, 720, 1080, 1440, 1800 ppm concentration



## APPENDIX E

### CATALYTIC PERFORMANCE TEST CALCULATIONS

#### E.1 Volumetric Gas Flow Rate Determination

Total gas flow rate ( $\dot{Q}$ ) is obtained from the result of multiplication of selected gas hourly space velocity (GHSV) by effective volume ( $V_{eff}$ ).

GHSV: 50000 h<sup>-1</sup> or 833.33 min<sup>-1</sup>

$D_{cat.}$ : 2.2 cm

$L_{cat.}$ : 1.3 cm

Frontal Open Area (foa) = 69%

$$V_{eff} = \frac{(\pi * D_{cat.}^2 * L_{cat.})}{4} * f_{oa} = 3.41 \text{ cm}^3$$

$$\dot{Q} = V_{eff} * \text{GHSV} = 2840 \text{ cm}^3 / \text{min}$$

In order to calculate the noble metal loading of a certain catalyst the following formula should be used:

#### E.2 MFC Flow Rate Calculation

In order to calculate the setting flow rate of an MFC device the following formula is used, according to this formula all setting flow rate are calculated in Table E. 1.

$$\dot{Q}_{MFC} = \frac{\text{Required Composition (ppm)} * \dot{Q}}{\text{Cylinder Composition (\%)} * 10000}$$

Table E. 1. MFC Setting Flow Rate

MFC #	Cylinder Content	Cylinder Composition %	Required Concentration in mixture (ppm)	MFC Set Flow Rate (ml/min)
MFC 1	O <sub>2</sub>	100	7700	21.87
MFC 2	NO	50	1500	8.52
	N <sub>2</sub>	50	Balance	
MFC 3	C <sub>3</sub> H <sub>6</sub>	0.33	370	320
	C <sub>3</sub> H <sub>8</sub>	0.11	120	
	CO	8.87	10000	
	H <sub>2</sub>	2.04	2310	
	CO <sub>2</sub>	88.65	100000	
MFC 4	SO <sub>2</sub>	0.01	20	568
	N <sub>2</sub>	0.99	Balance	
MFC 5	N <sub>2</sub>	100	Balance	balance

## APPENDIX F

### PERFORMANCES OF PEROVSKITE BASED CATALYST WITHOUT NOBLE METAL LOADINGS

In order to understand the noble metal effect on the perovskite-based catalyst performance three different catalysts were produced. Below the results obtained with these catalysts are presented. According to the results it can be interpreted that noble metals are crucial components for a catalyst to obtain remarkable three-way catalytic activity.

#### F.1 Performance and Characterization of $\text{LaFe}_{0.6}\text{Co}_{0.4}\text{O}_3$ Catalyst

The  $\text{LaFe}_{0.6}\text{Co}_{0.4}\text{O}_3$  perovskite-based catalyst (LaFeCo), wash-coated on a cordierite monolith, is comprised of  $\text{LaFe}_{0.6}\text{Co}_{0.4}\text{O}_3$ ,  $\text{Ce}_{0.8}\text{Zr}_{0.2}\text{O}_2$  and  $\gamma\text{-Al}_2\text{O}_3$ . Palladium and rhodium were not used in this catalyst. ICP-OES analysis also confirmed the absence of these metals. After the monolith coating process 0.493 g weight change was recorded for monolith on dry basis. Oxidation performance of monolithic catalyst LaFeCo on  $\text{H}_2$ , CO,  $\text{C}_3\text{H}_6$  was well enough to complete conversion, results are shown in Table F. 1. 50% conversion temperature for  $\text{H}_2$ , CO,  $\text{O}_2$ ,  $\text{C}_3\text{H}_6$  are 350, 380, 365 and 433 °C respectively. However,  $\text{C}_3\text{H}_8$  and NO conversions were maximum 50% and 17%, respectively. The fresh performance of the LaFeCo catalyst is too low to compare to the fresh performance of the C1 catalyst (shown in Figure F. 1). Moreover, considering the incomplete conversion in some compounds, no further studies have been performed on the LaFeCo catalyst.

Table F. 1. Catalytic activity of fresh LaFeCo monolithic catalyst

Species	T50 (°C)	Max. Conv. (%)
H <sub>2</sub>	350	100
CO	380	100
O <sub>2</sub>	365	87
C <sub>3</sub> H <sub>6</sub>	433	99
C <sub>3</sub> H <sub>8</sub>	600	50
NO	600	17

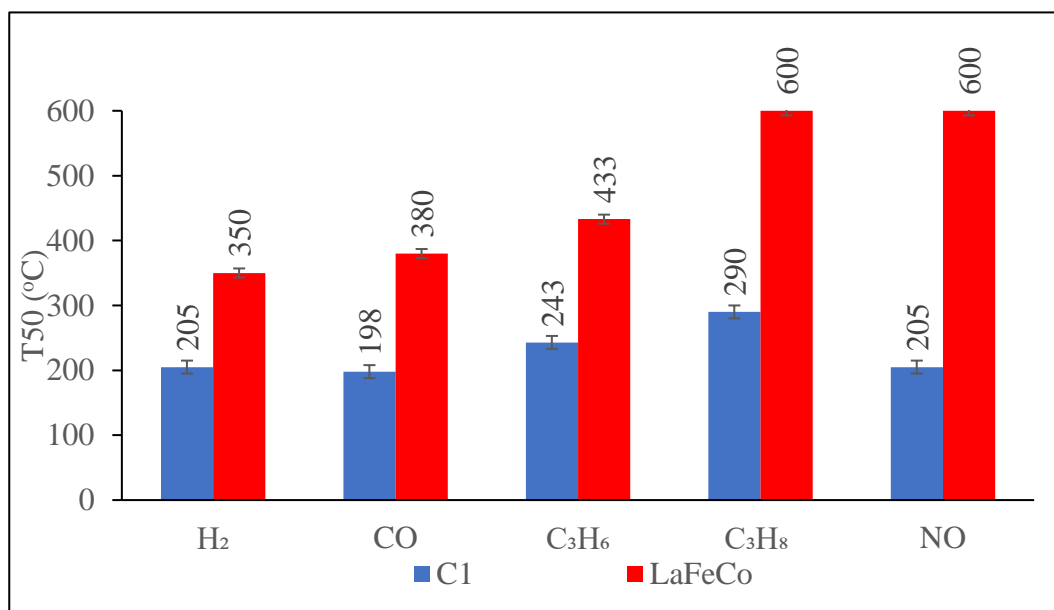


Figure F. 1. T50 temperatures comparisons of fresh monolithic C1 and LaFeCo catalysts

## F.2 Performance and Characterization of LaFe<sub>0.57</sub>Co<sub>0.37</sub>Mn<sub>0.06</sub>O<sub>3</sub> Catalyst

The LaFe<sub>0.57</sub>Co<sub>0.37</sub>Mn<sub>0.06</sub>O<sub>3</sub> perovskite-based catalyst (LaFeCoMn), wash-coated on a cordierite monolith, is comprised of LaFe<sub>0.57</sub>Co<sub>0.37</sub>Mn<sub>0.06</sub>O<sub>3</sub>, Ce<sub>0.8</sub>Zr<sub>0.2</sub>O<sub>2</sub> and  $\gamma$ -Al<sub>2</sub>O<sub>3</sub>. Prepared catalyst contains 0.75% nominal manganese loading. The effect of placing manganese on site B of perovskite on catalytic performance is studied with this catalyst. ICP-OES analysis also confirmed the absence of noble metals. After the monolith coating process 0.516 g weight change was recorded for monolith on dry basis, which meant 22.18 g/ft<sup>3</sup> nominal manganese loading. 50% conversion temperature for H<sub>2</sub>, CO, O<sub>2</sub>, C<sub>3</sub>H<sub>6</sub> are 319, 369, 382 and 426 °C respectively, (shown in Table F. 2. However, C<sub>3</sub>H<sub>8</sub> and NO conversions were maximum 51% and 20%, respectively. The placement of manganese on B site of perovskite did not produce a remarkable improvement in catalytic performance. Similar to that of the LaFeCo catalyst, the fresh performance of the LaFeCoMn catalyst is also too low to compare to the fresh performance of the C1 catalyst (shown in Figure F. 2, therefore no further studies have been performed on the LaFeCoMn catalyst.

Table F. 2. Catalytic activity of fresh LaFeCoMn monolithic catalyst

<b>Species</b>	<b>T50 (°C)</b>	<b>Max. Conv. (%)</b>
<b>H<sub>2</sub></b>	319	100
<b>CO</b>	369	100
<b>O<sub>2</sub></b>	382	87
<b>C<sub>3</sub>H<sub>6</sub></b>	426	99
<b>C<sub>3</sub>H<sub>8</sub></b>	591	52
<b>NO</b>	600	20

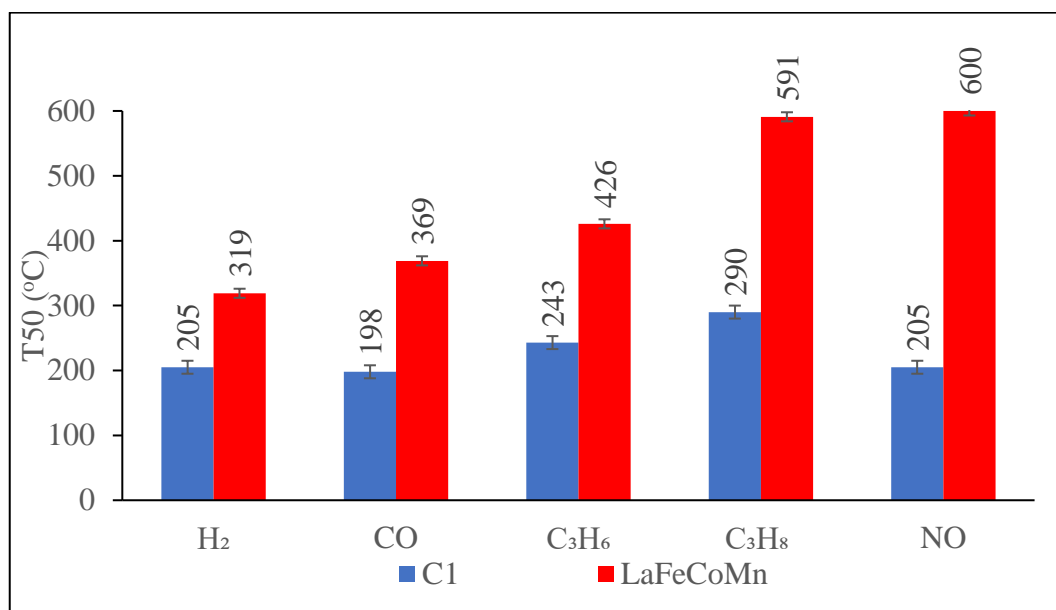


Figure F. 2. T50 temperatures comparisons of fresh monolithic C1 and LaFeCoMn catalysts

### F.3 Performance and Characterization of LaFe<sub>0.57</sub>Co<sub>0.37</sub>Ru<sub>0.06</sub>O<sub>3</sub> Catalyst

The LaFe<sub>0.57</sub>Co<sub>0.37</sub>Ru<sub>0.06</sub>O<sub>3</sub> perovskite-based catalyst (LaFeCoRu), wash-coated on a cordierite monolith, is comprised of LaFe<sub>0.57</sub>Co<sub>0.37</sub>Ru<sub>0.06</sub>O<sub>3</sub>, Ce<sub>0.8</sub>Zr<sub>0.2</sub>O<sub>2</sub> and  $\gamma$ -Al<sub>2</sub>O<sub>3</sub>. Prepared catalyst contains 0.75% nominal ruthenium loading. The effect of placing ruthenium on site B of perovskite on catalytic performance is studied with this catalyst. ICP-OES analysis also confirmed the absence of noble metals. 0.470g weight change was recorded for monolith on dry basis after coating process, which meant 20.30 g/ft<sup>3</sup> nominal ruthenium loading. 50% conversion temperature for H<sub>2</sub>, CO, O<sub>2</sub>, C<sub>3</sub>H<sub>6</sub> are 373, 238, 390 and 410 °C respectively, (shown in Table F. 3). However, C<sub>3</sub>H<sub>8</sub> and NO conversions were maximum 65% and 27%, respectively. It can be inferred from results that inclusion of ruthenium in to the catalyst formulation significantly improved CO but the reduction reaction performance of this catalyst is

not promising. Similar to that of the LaFeCo catalyst, the fresh performance of the LaFeCoRu catalyst is also too low to compare to the fresh performance of the C1 catalyst (shown in Figure F.3), therefore no further studies have been performed on the LaFeCoRu catalyst.

Table F. 3. Catalytic activity of fresh LaFeCoRu monolithic catalyst

<b>Species</b>	<b>T50 (°C)</b>	<b>Max. Conv. (%)</b>
<b>H<sub>2</sub></b>	373	100
<b>CO</b>	238	100
<b>O<sub>2</sub></b>	390	87
<b>C<sub>3</sub>H<sub>6</sub></b>	410	99
<b>C<sub>3</sub>H<sub>8</sub></b>	530	52
<b>NO</b>	600	20

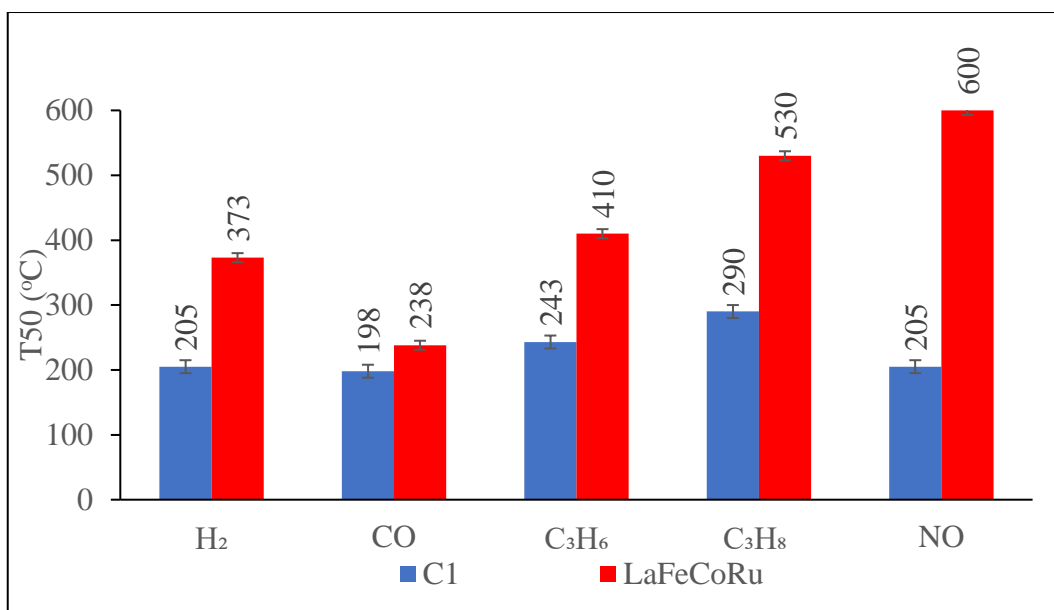


Figure F. 3. T50 temperatures comparisons of fresh monolithic C1 and LaFeCoRu catalysts



## APPENDIX G

### PERFORMANCES CURVES OF THE TESTED CATALYSTS

#### G.1 Performances Curves of fresh C1 Catalyst

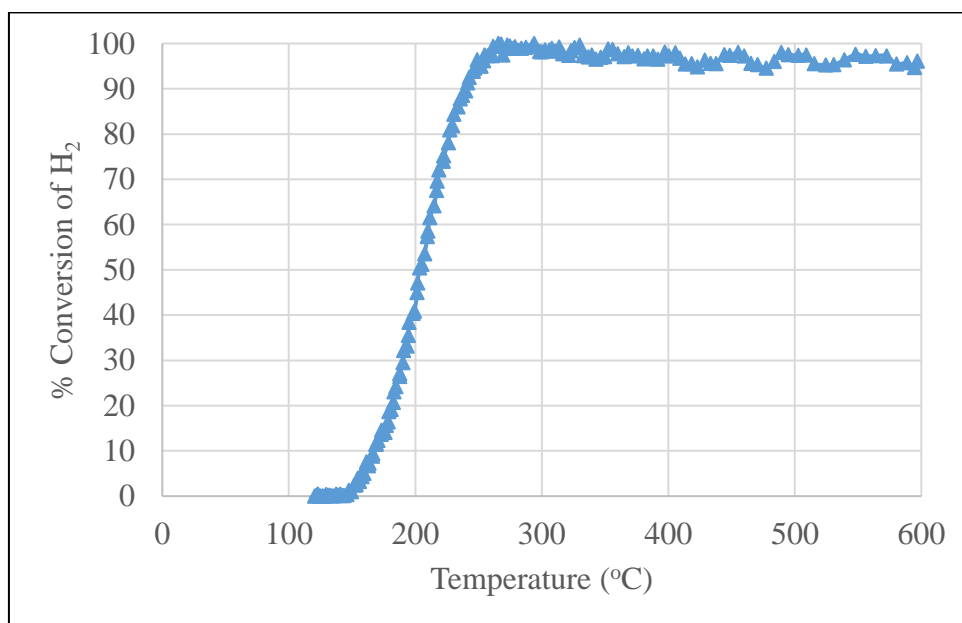


Figure G. 1. H<sub>2</sub> Conversion performance of fresh C1 Catalyst

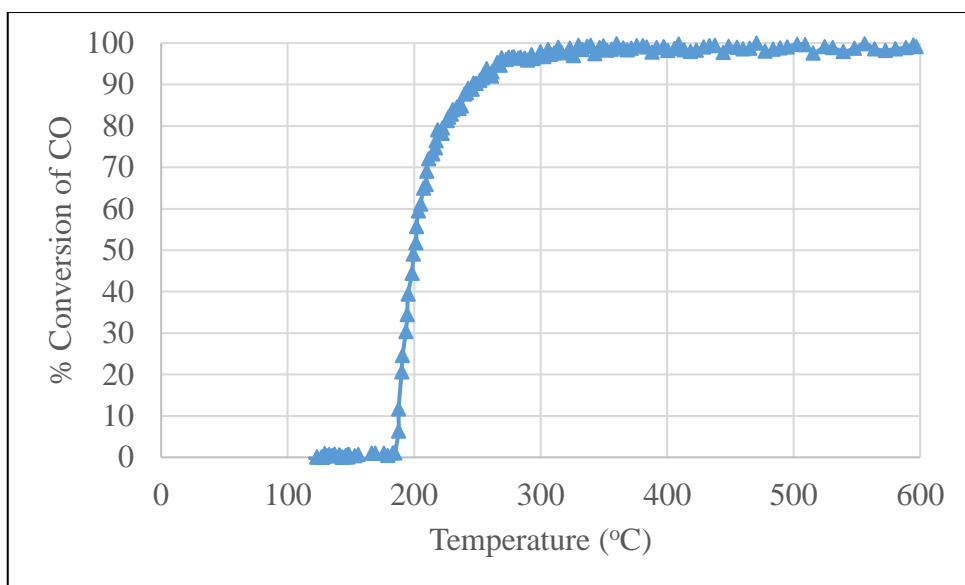


Figure G. 2. CO Conversion performance of fresh C1 Catalyst

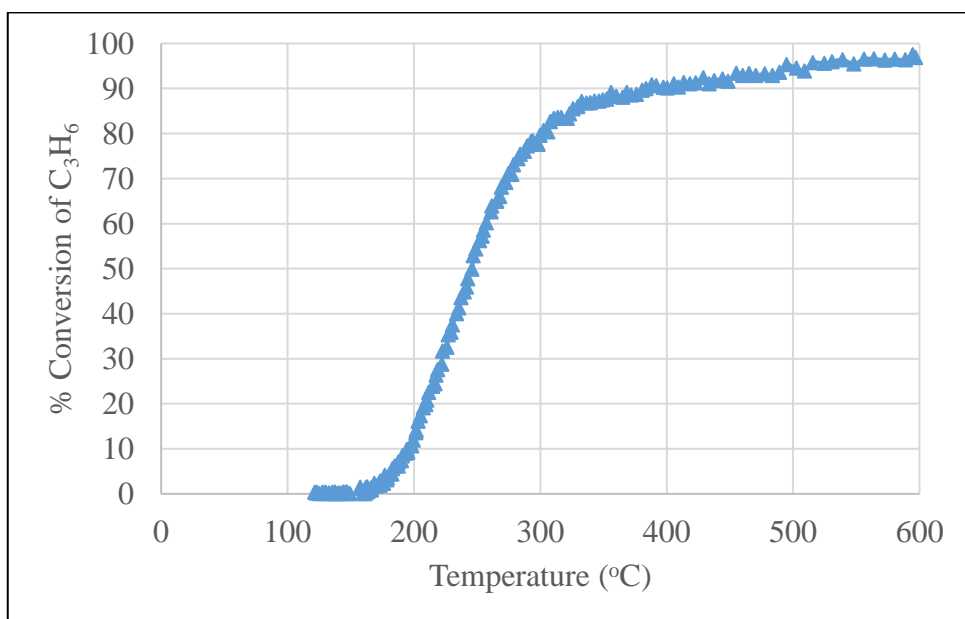


Figure G. 3. C<sub>3</sub>H<sub>6</sub> Conversion performance of fresh C1 Catalyst

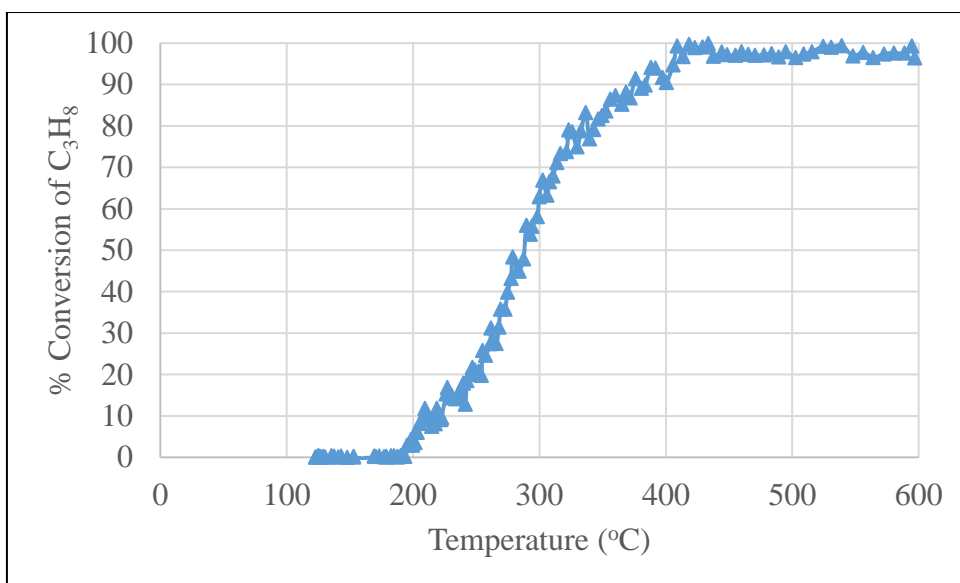


Figure G. 4. C<sub>3</sub>H<sub>8</sub> Conversion performance of fresh C1 Catalyst

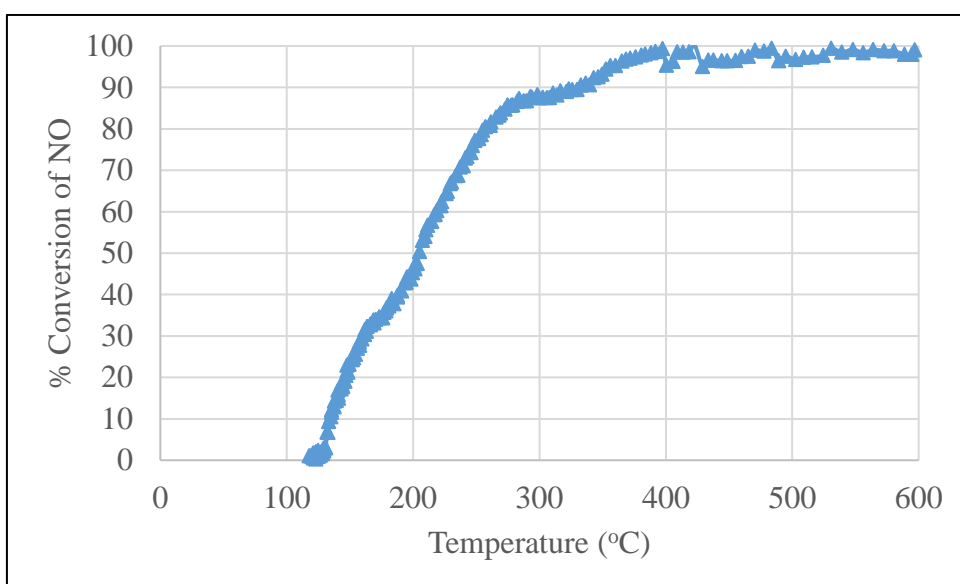


Figure G. 5. NO Conversion performance of fresh C1 Catalyst

## G.2 Performances Curves of fresh C2 Catalyst

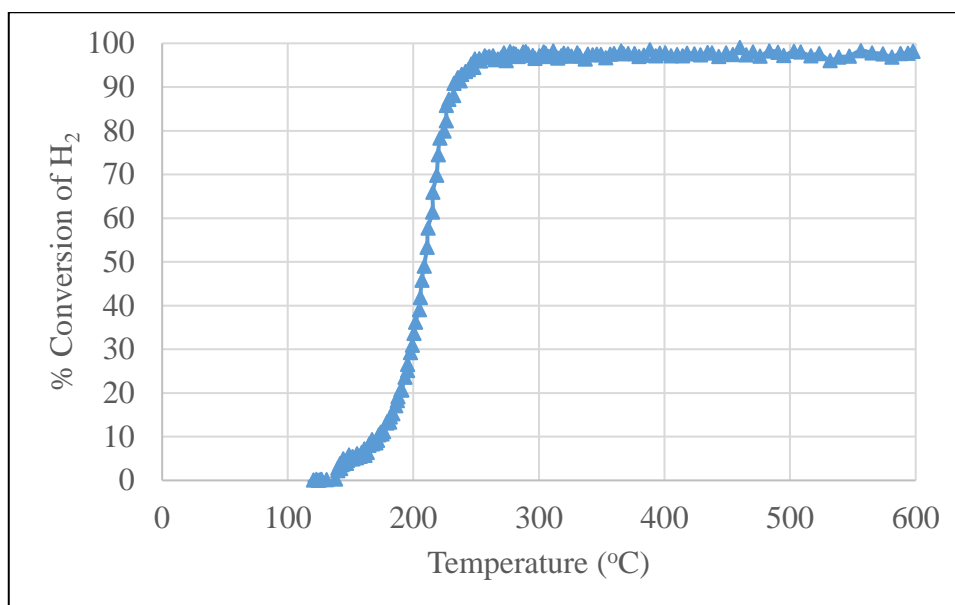


Figure G. 6. H<sub>2</sub> Conversion performance of fresh C<sub>2</sub> Catalyst

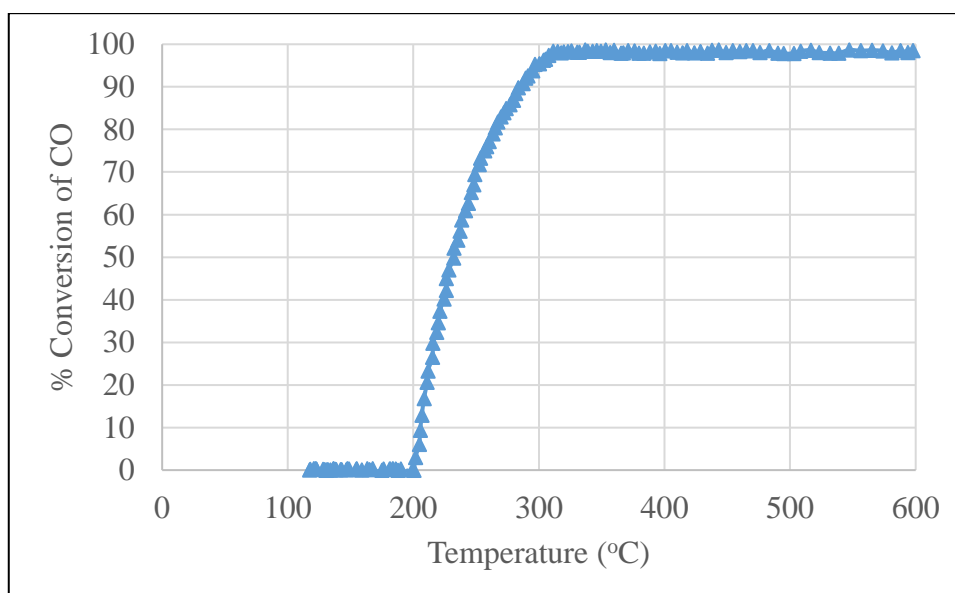


Figure G. 7. CO Conversion performance of fresh C<sub>2</sub> Catalyst

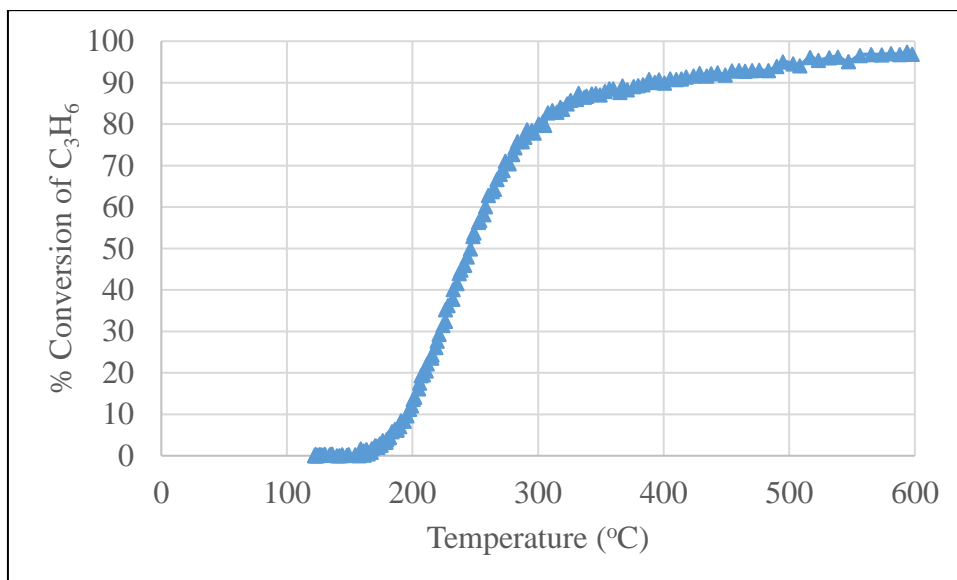


Figure G. 8.  $C_3H_6$  Conversion performance of fresh C2 Catalyst

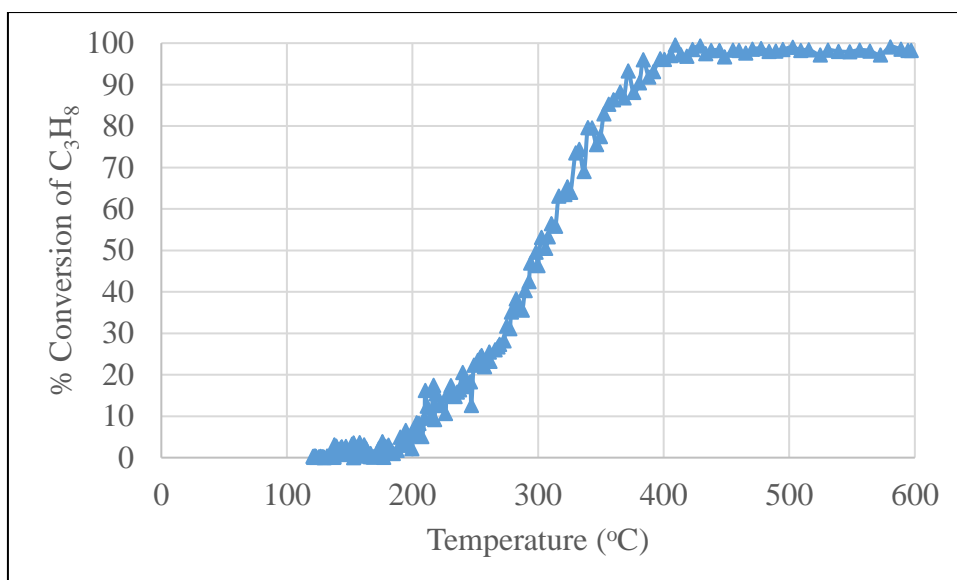


Figure G. 9.  $C_3H_8$  Conversion performance of fresh C2 Catalyst

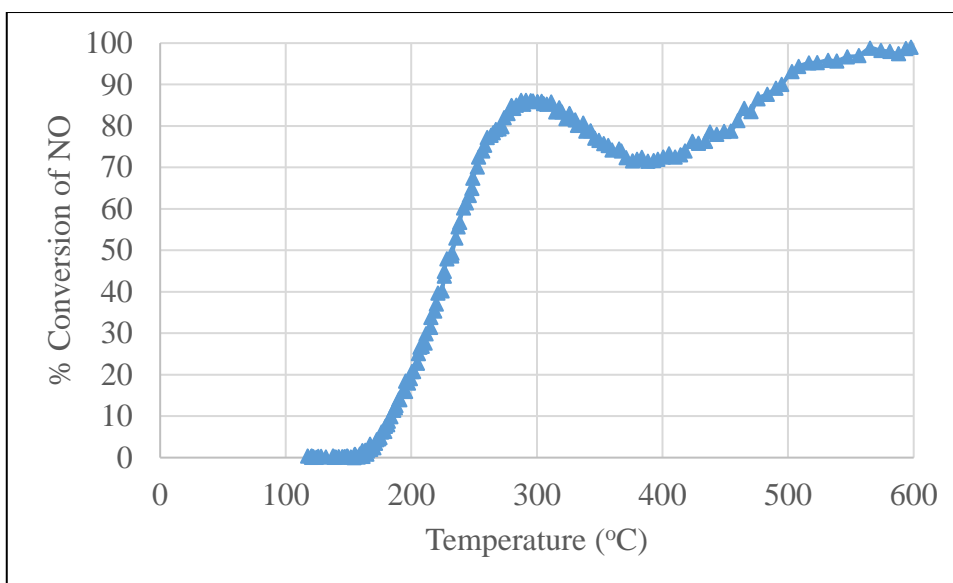


Figure G. 10. NO Conversion performance of fresh C2 Catalyst

### G.3 Performances Curves of fresh C3 Catalyst

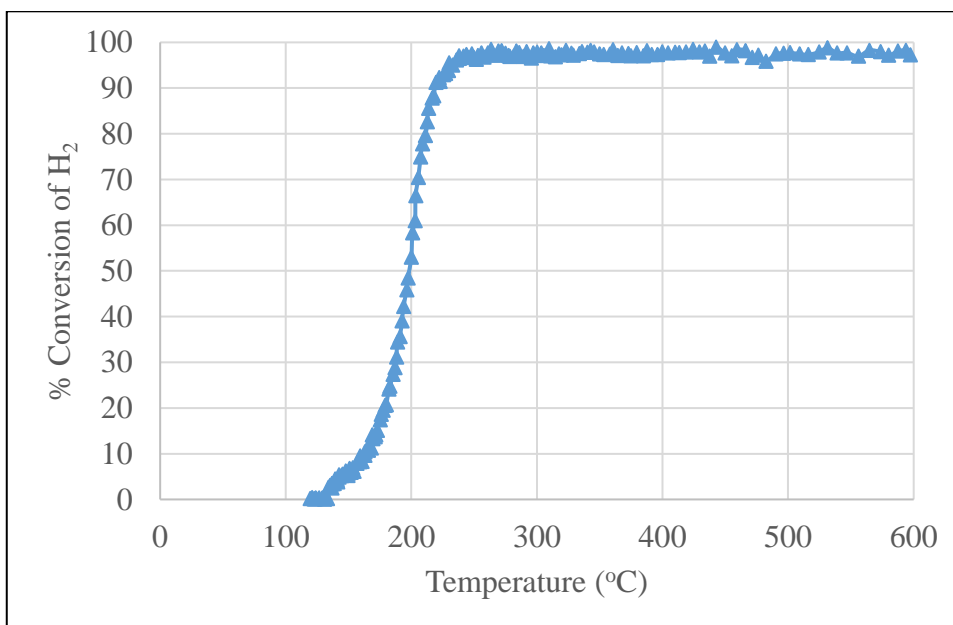


Figure G. 11. H<sub>2</sub> Conversion performance of fresh C3 Catalyst

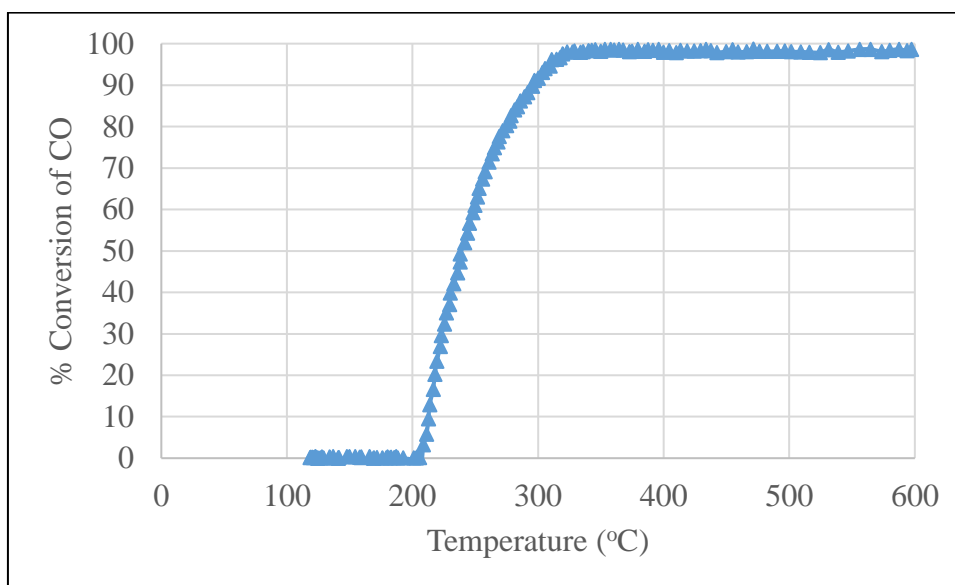


Figure G. 12. CO Conversion performance of fresh C3 Catalyst

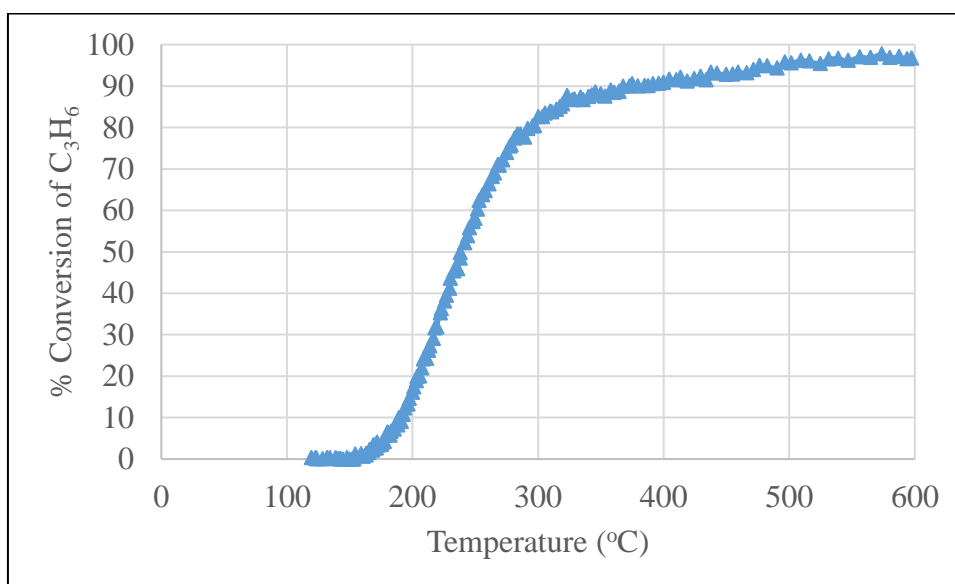


Figure G. 13. C<sub>3</sub>H<sub>6</sub> Conversion performance of fresh C3 Catalyst

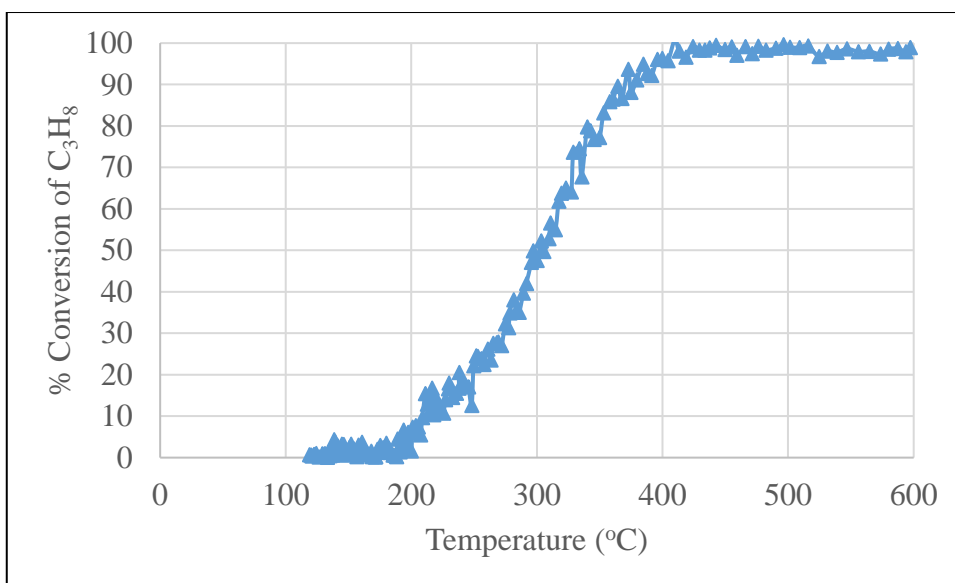


Figure G. 14. C<sub>3</sub>H<sub>8</sub> Conversion performance of fresh C3 Catalyst

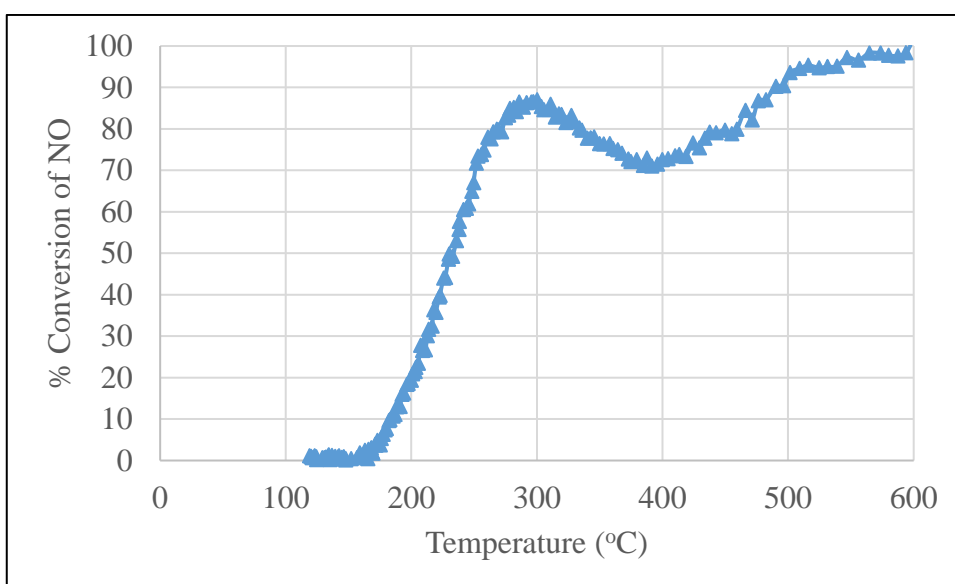


Figure G. 15. NO Conversion performance of fresh C3 Catalyst



#### G.4 Performances Curves of fresh C4 Catalyst

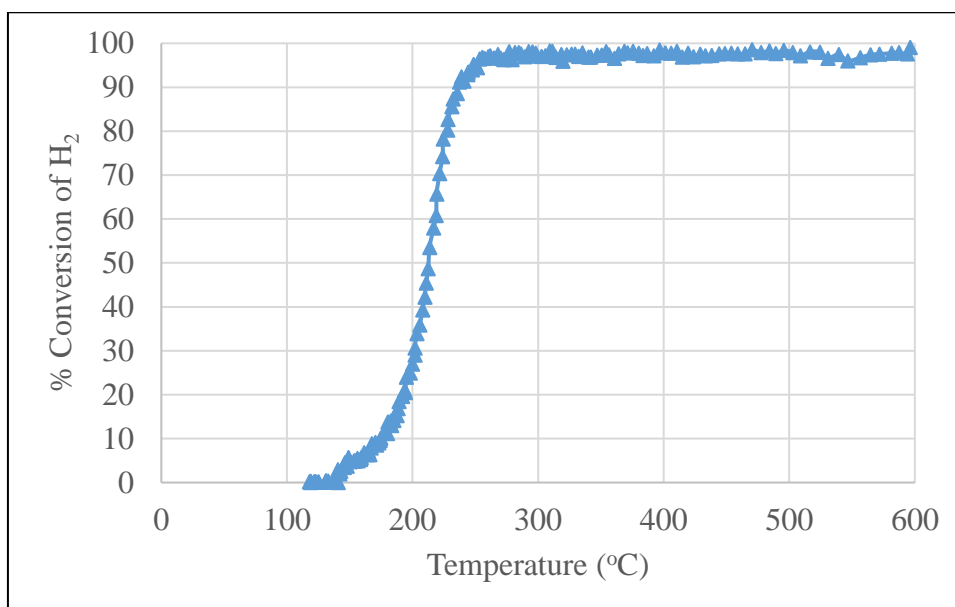


Figure G. 16. H<sub>2</sub> Conversion performance of fresh C4 Catalyst

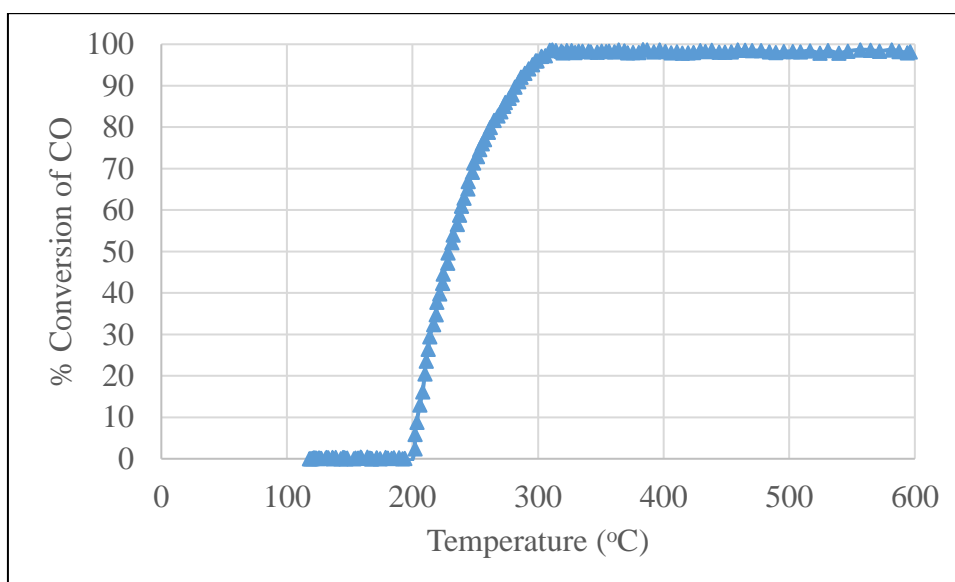


Figure G. 17. CO Conversion performance of fresh C4 Catalyst

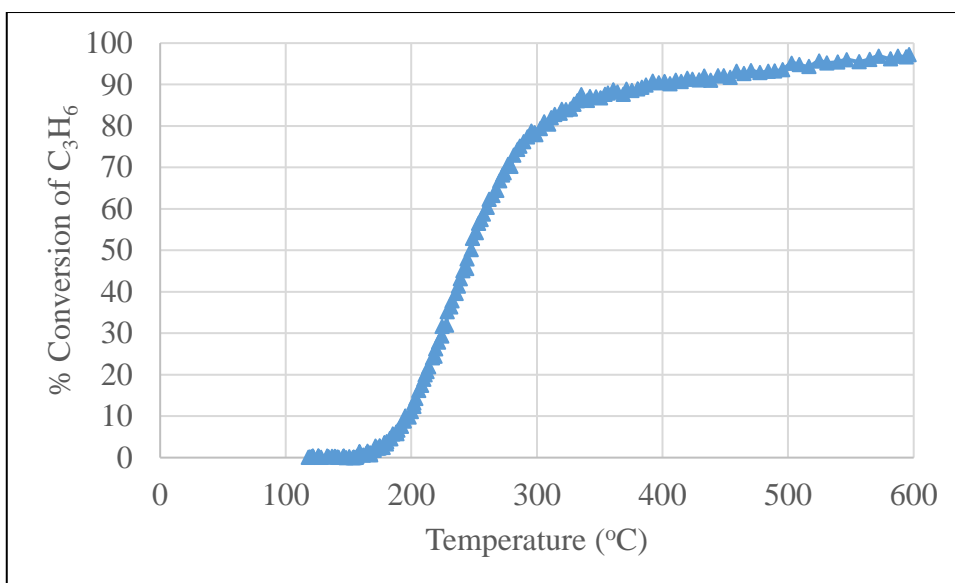


Figure G. 18. C<sub>3</sub>H<sub>6</sub> Conversion performance of fresh C4 Catalyst

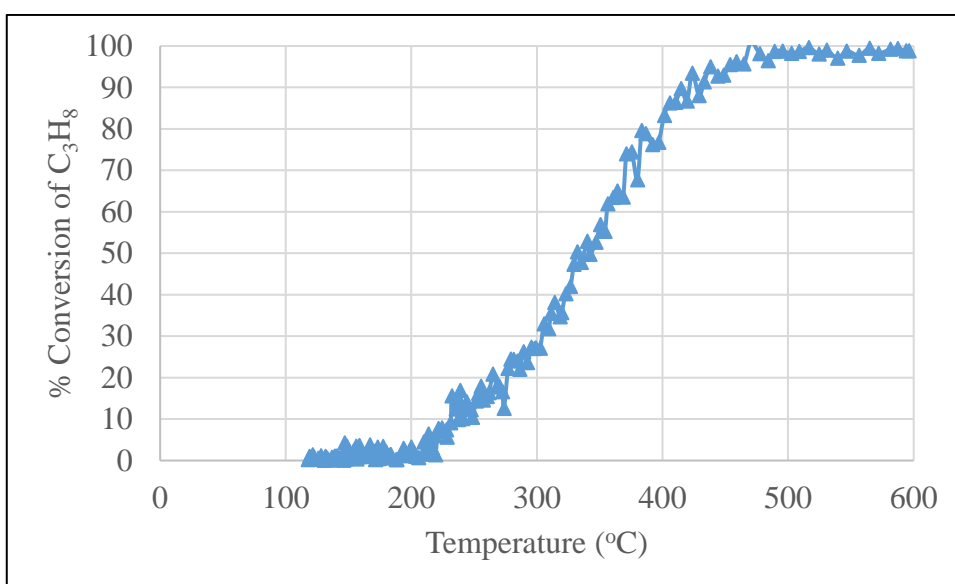


Figure G. 19. C<sub>3</sub>H<sub>8</sub> Conversion performance of fresh C4 Catalyst

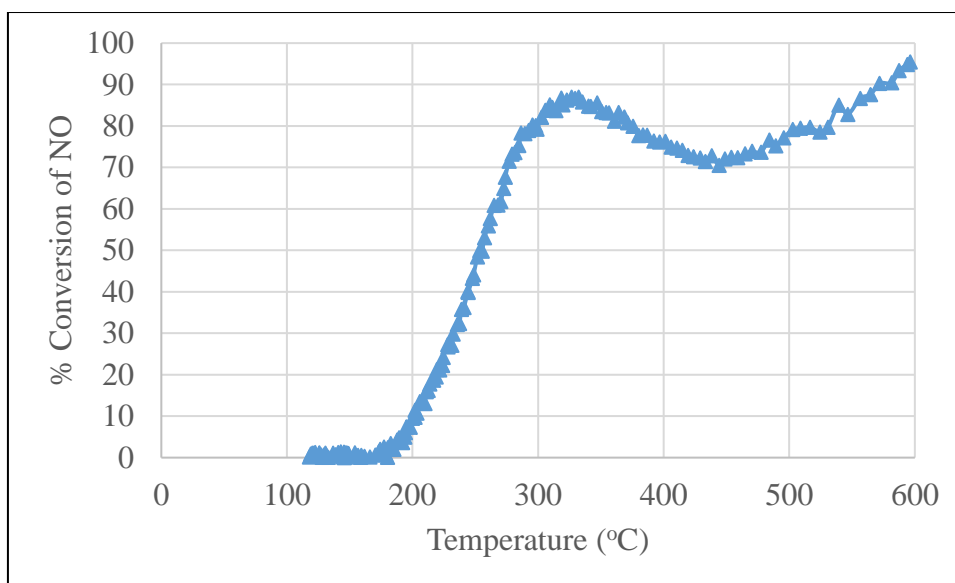


Figure G. 20. NO Conversion performance of fresh C4 Catalyst

**G.5 Performances Curves of Hydrothermally Aged C1 Catalyst**

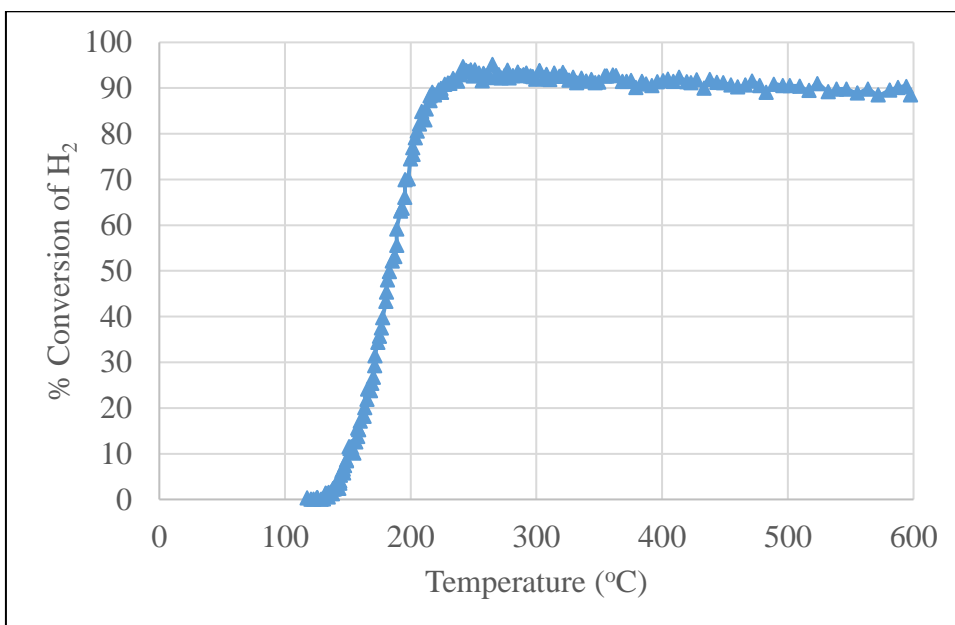


Figure G. 21. H<sub>2</sub> Conversion performance of hydrothermally aged C1 Catalyst

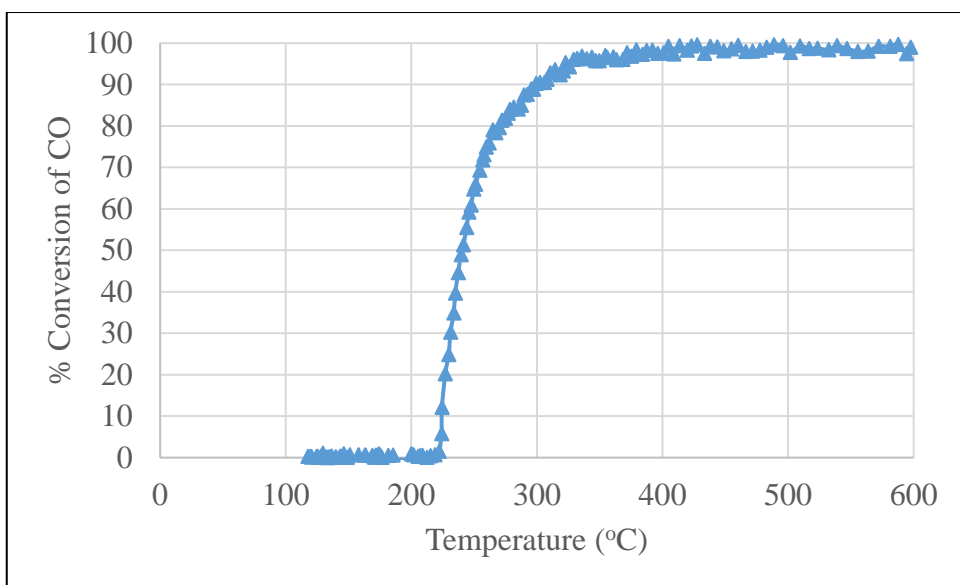


Figure G. 22. CO Conversion performance of hydrothermally aged C1 Catalyst

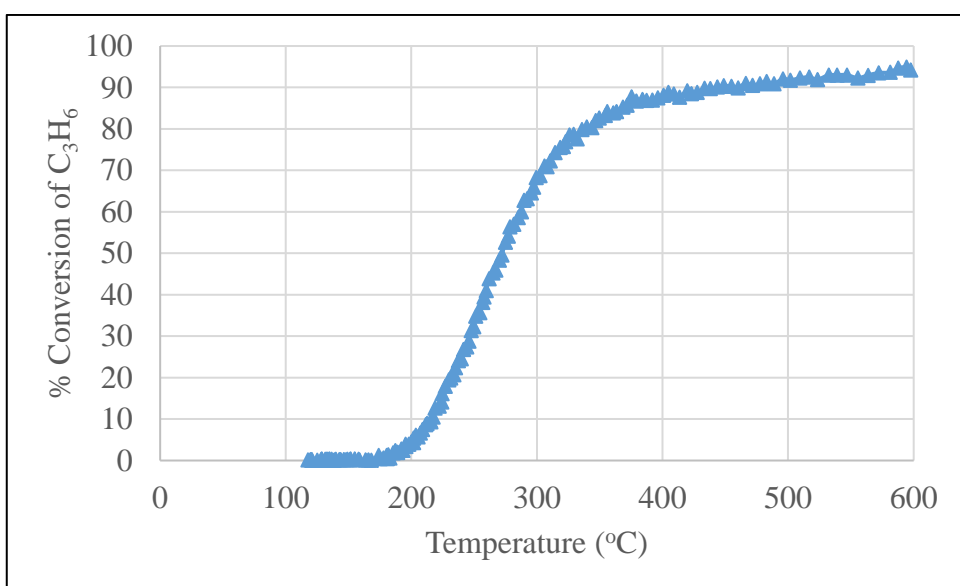


Figure G. 23. C<sub>3</sub>H<sub>6</sub> Conversion performance of hydrothermally aged C1 Catalyst

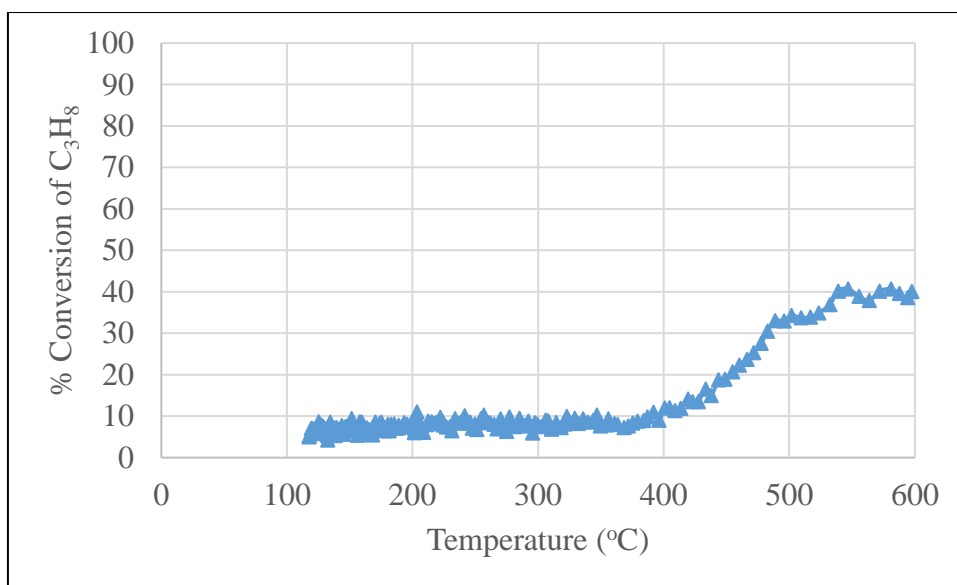


Figure G. 24. C<sub>3</sub>H<sub>8</sub> Conversion performance of hydrothermally aged C1 Catalyst

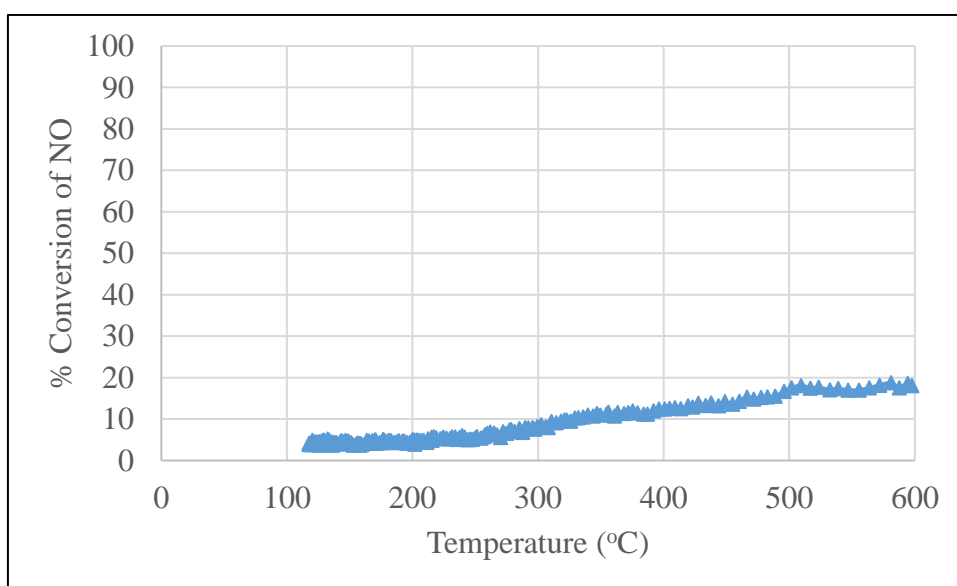


Figure G. 25. NO Conversion performance of hydrothermally aged C1 Catalyst

## G.6 Performances Curves of Hydrothermally Aged C2 Catalyst

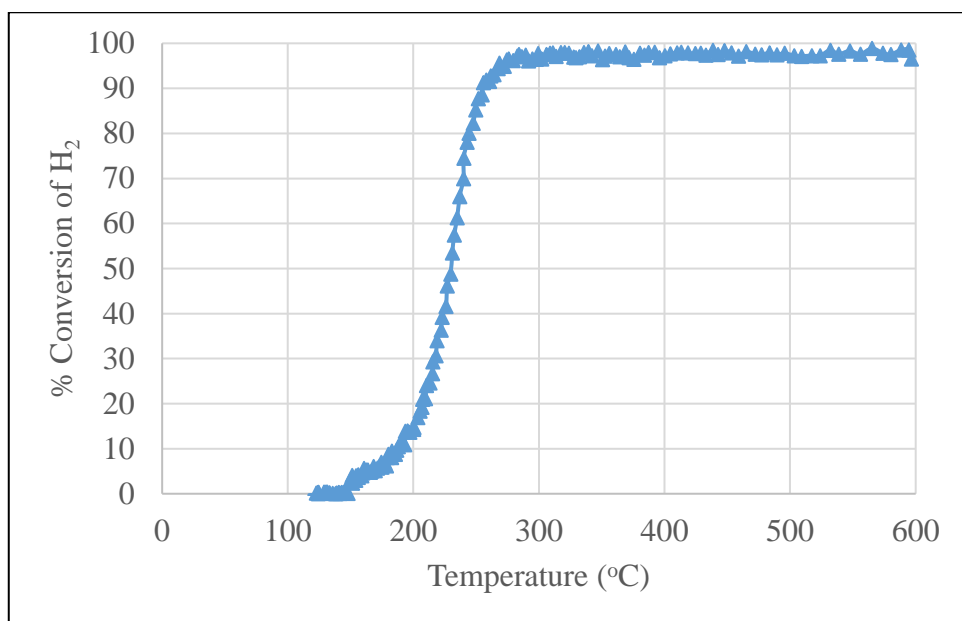


Figure G. 26. H<sub>2</sub> Conversion performance of hydrothermally aged C<sub>2</sub> Catalyst

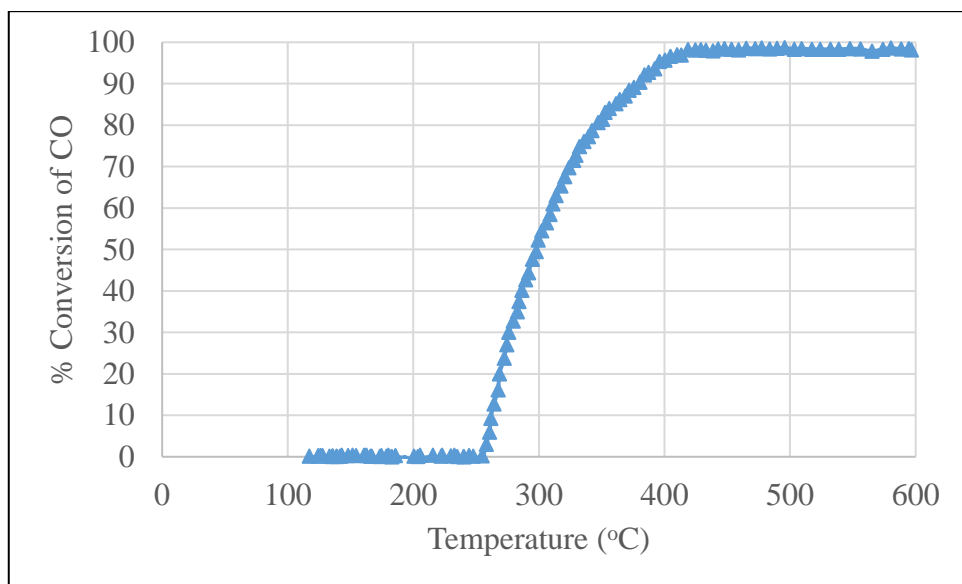


Figure G. 27. CO Conversion performance of hydrothermally aged C<sub>2</sub> Catalyst

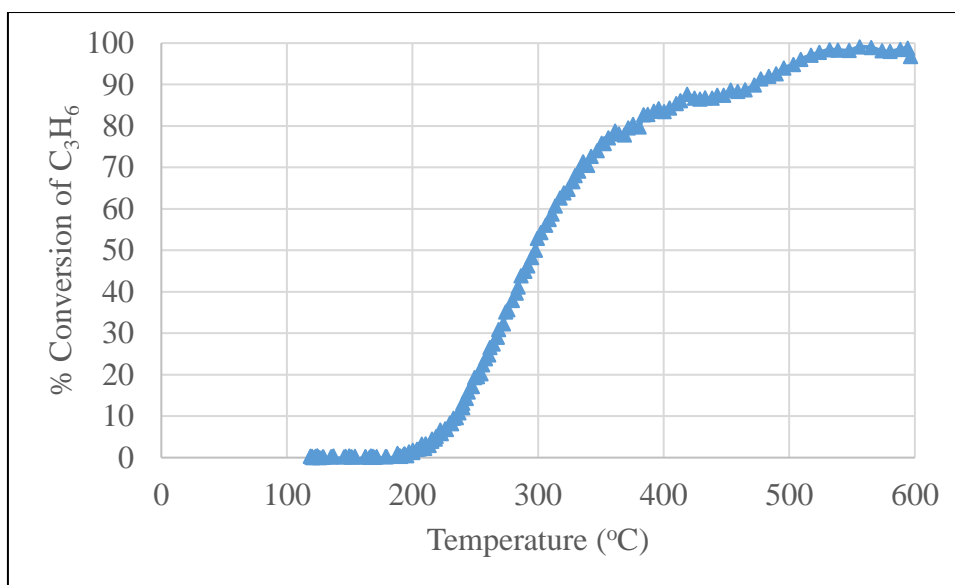


Figure G. 28.  $C_3H_6$  Conversion performance of hydrothermally aged C2 Catalyst

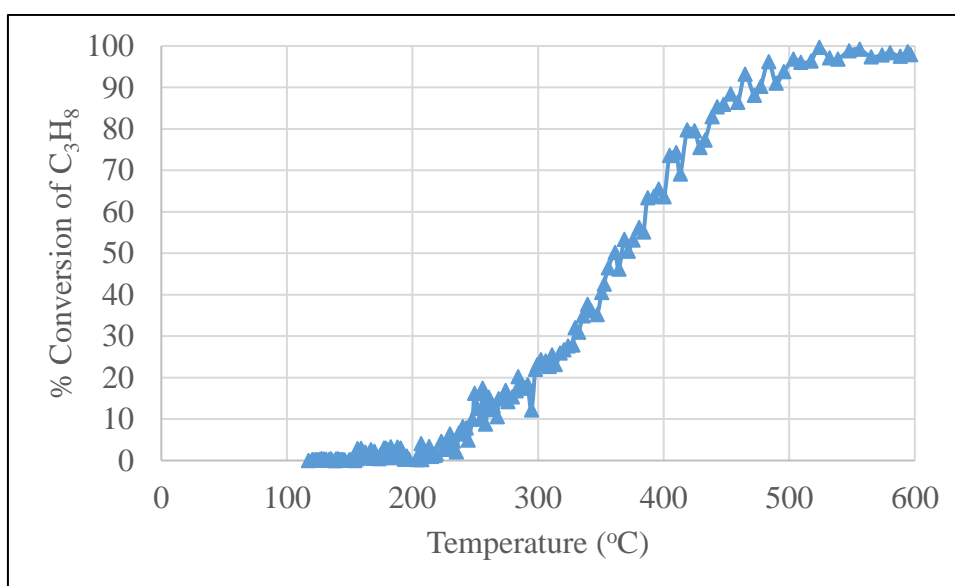


Figure G. 29.  $C_3H_8$  Conversion performance of hydrothermally aged C2 Catalyst

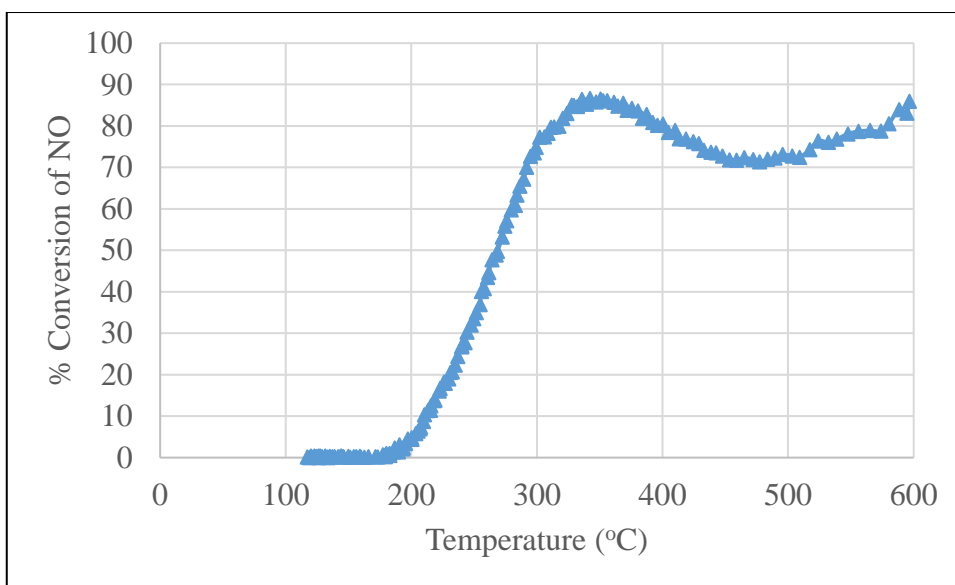


Figure G. 30. NO Conversion performance of hydrothermally aged C2 Catalyst

**G.7 Performances Curves of Hydrothermally Aged C3 Catalyst**

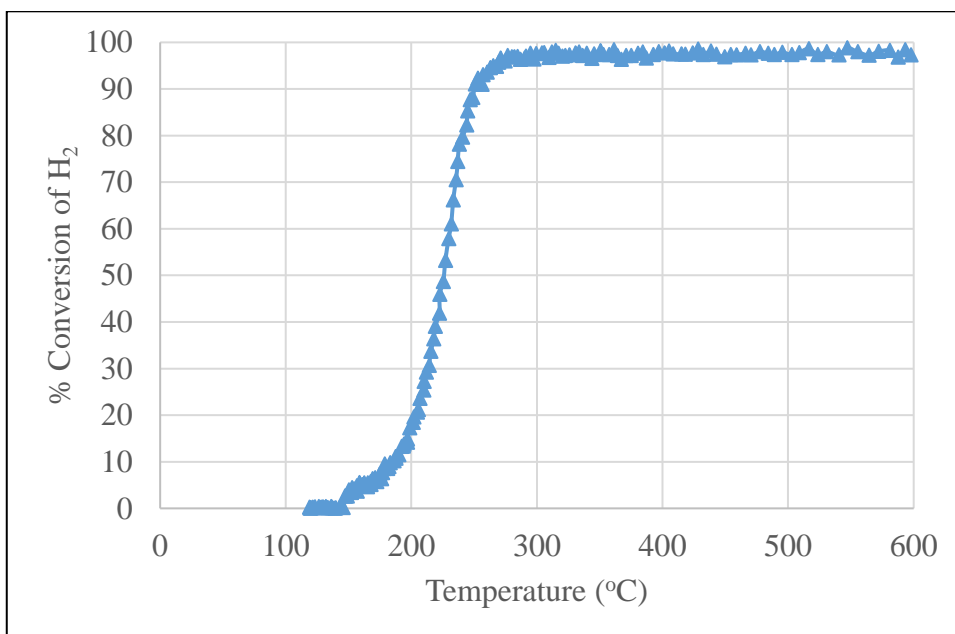


Figure G. 31. H<sub>2</sub> Conversion performance of hydrothermally aged C3 Catalyst



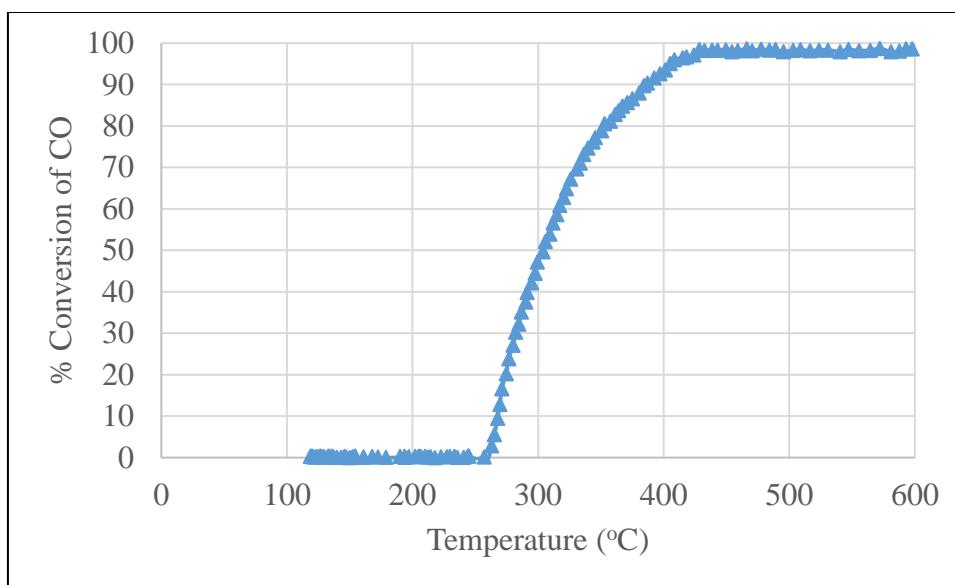


Figure G. 32. CO Conversion performance of hydrothermally aged C3 Catalyst

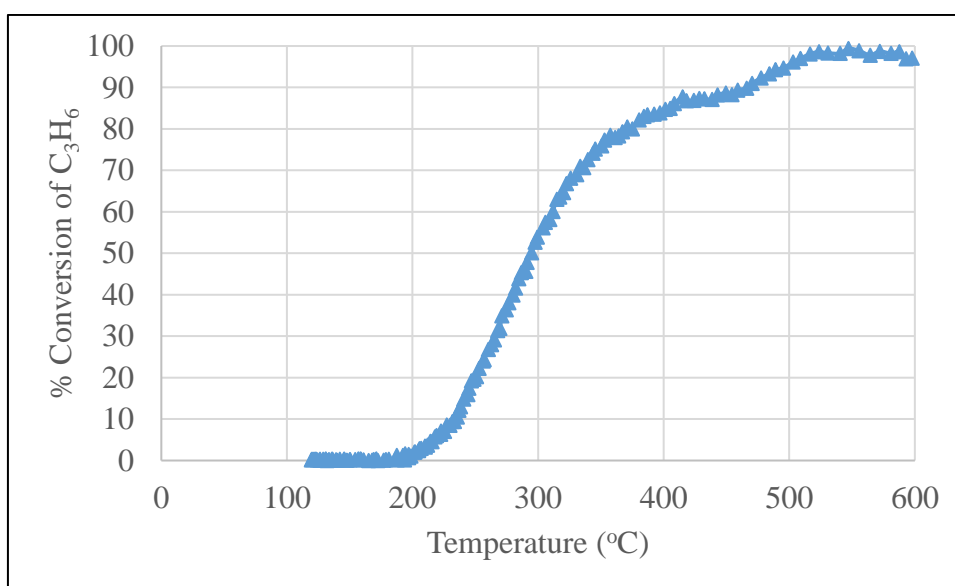


Figure G. 33. C<sub>3</sub>H<sub>6</sub> Conversion performance of hydrothermally aged C3 Catalyst

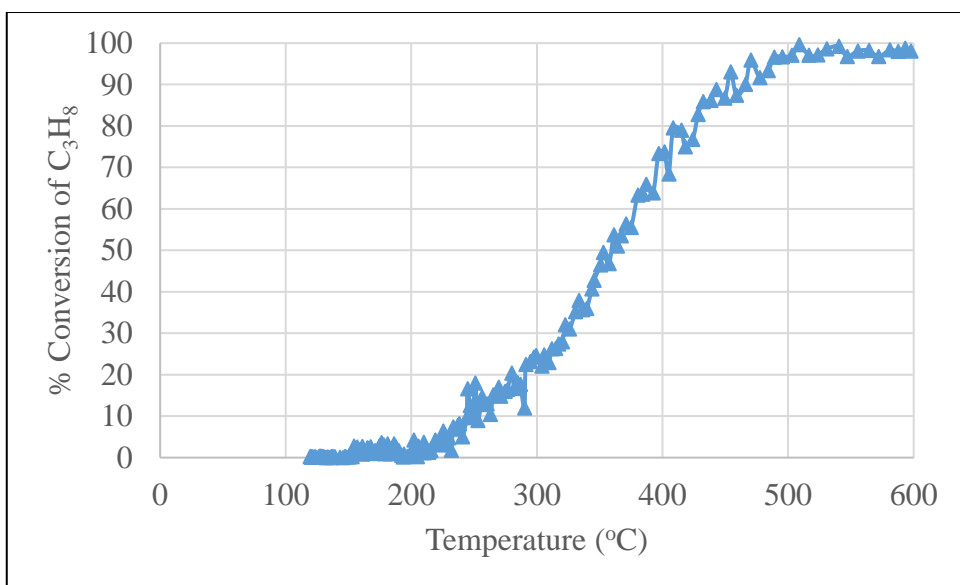


Figure G. 34.  $C_3H_8$  Conversion performance of hydrothermally aged C3 Catalyst

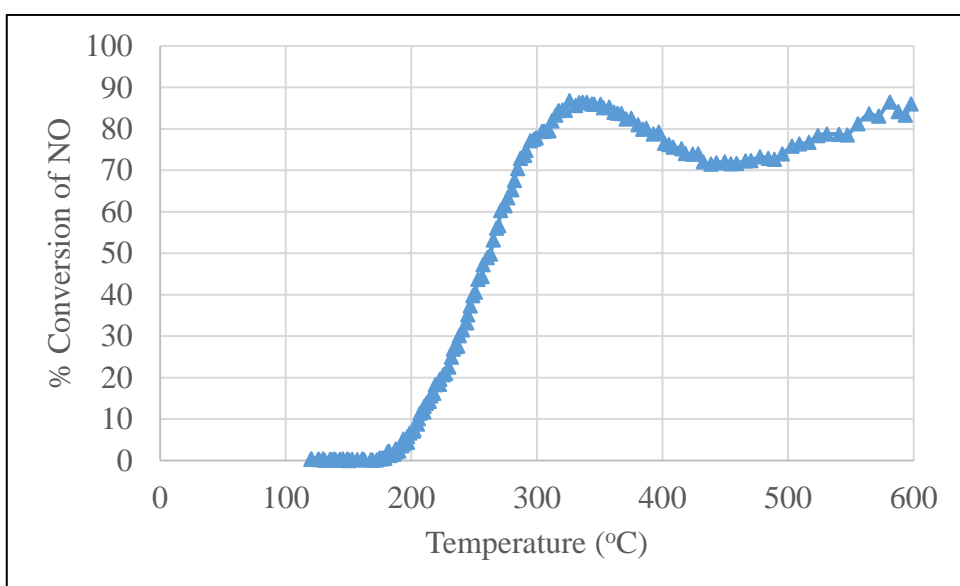


Figure G. 35. NO Conversion performance of hydrothermally aged C3 Catalyst

## G.8 Performances Curves of Hydrothermally Aged C4 Catalyst

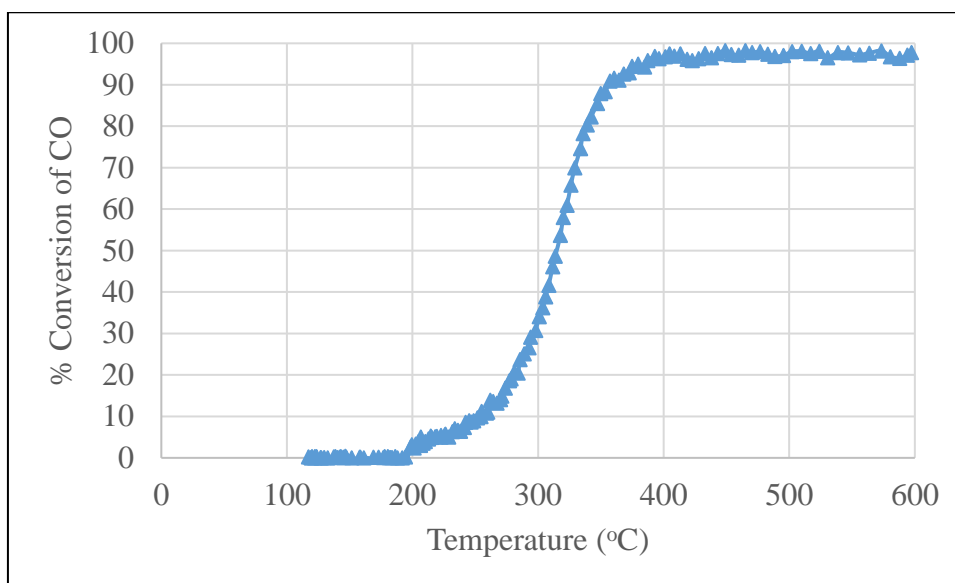


Figure G. 36. CO Conversion performance of hydrothermally aged C4 Catalyst

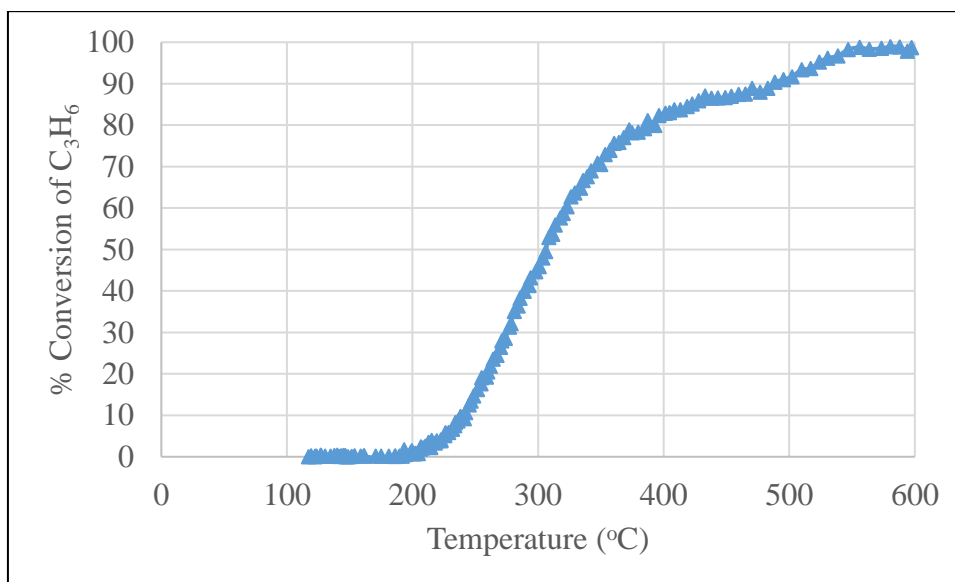


Figure G. 37. C<sub>3</sub>H<sub>6</sub> Conversion performance of hydrothermally aged C4 Catalyst

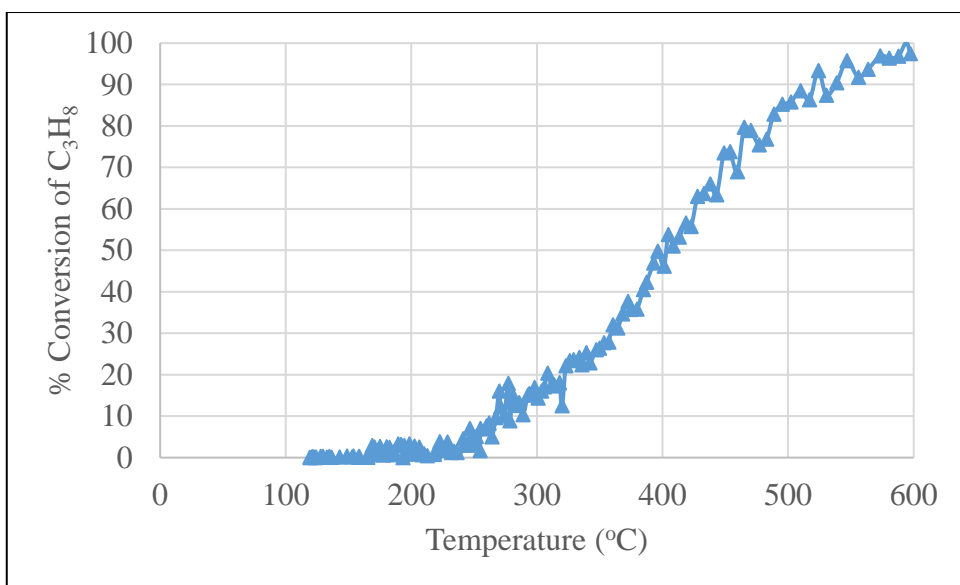


Figure G. 38. C<sub>3</sub>H<sub>8</sub> Conversion performance of hydrothermally aged C4 Catalyst

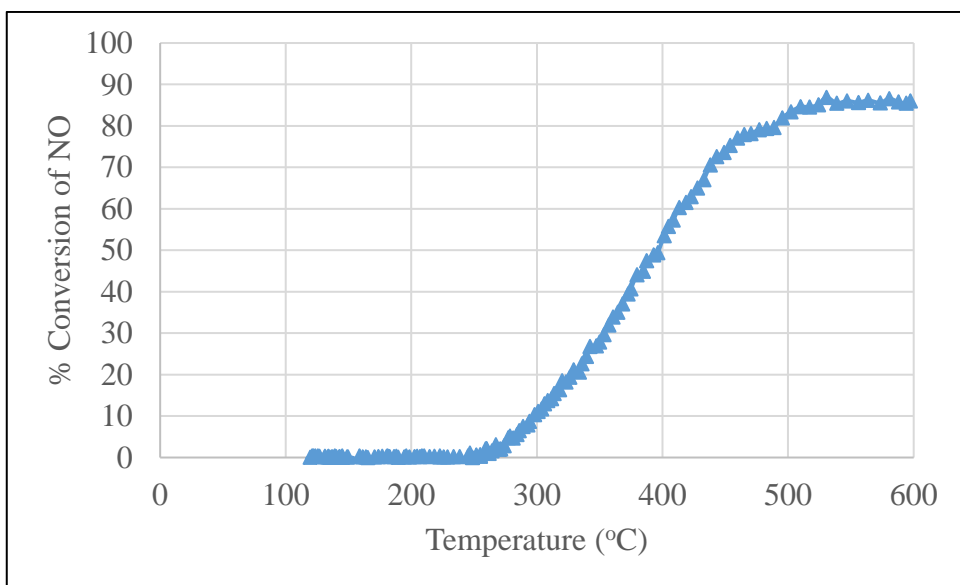


Figure G. 39. NO Conversion performance of hydrothermally aged C4 Catalyst

### G.9 Performances Curves of SO<sub>2</sub> Poisoned C1 Catalyst

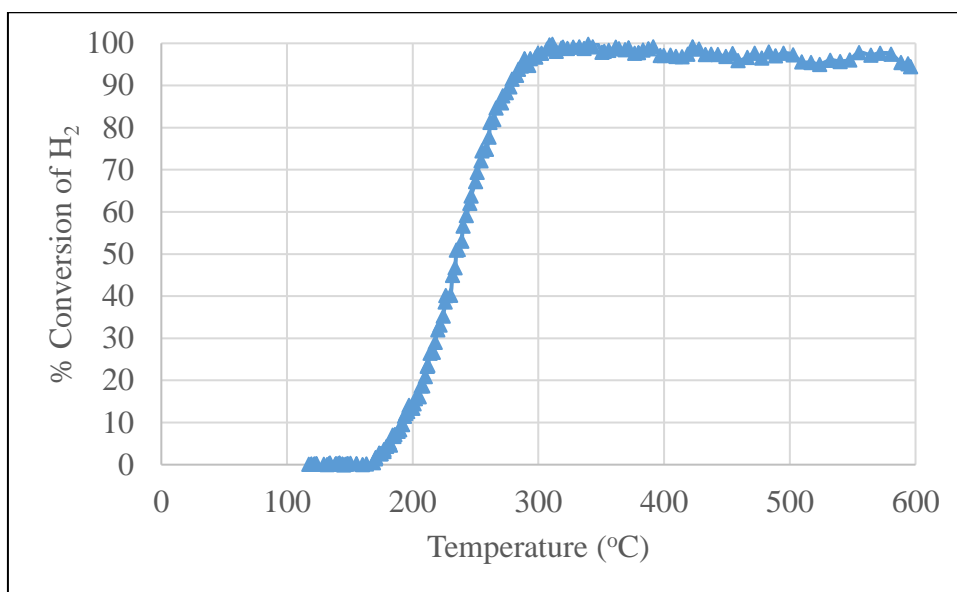


Figure G. 40. H<sub>2</sub> Conversion performance of SO<sub>2</sub> poisoned C1 Catalyst

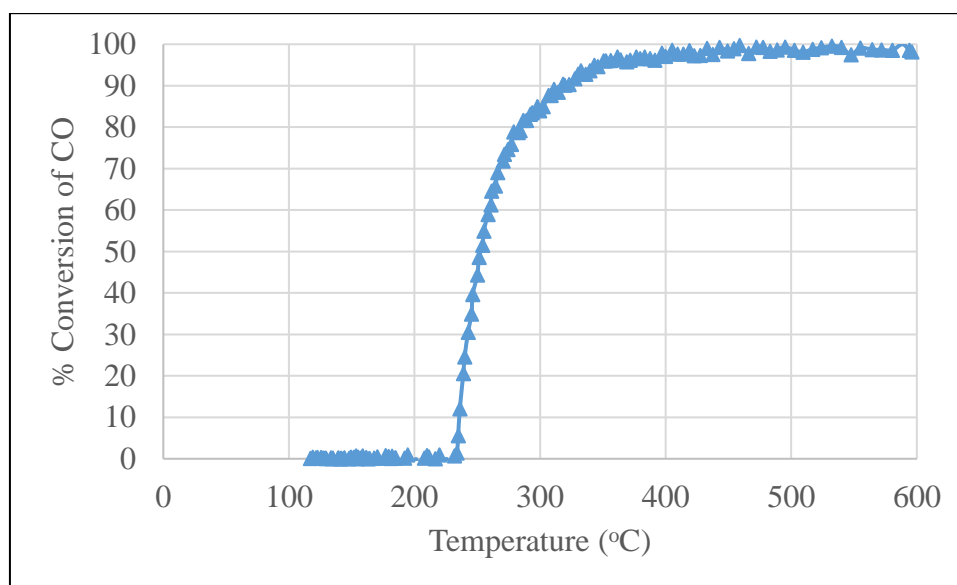


Figure G. 41. CO Conversion performance of SO<sub>2</sub> poisoned C1 Catalyst

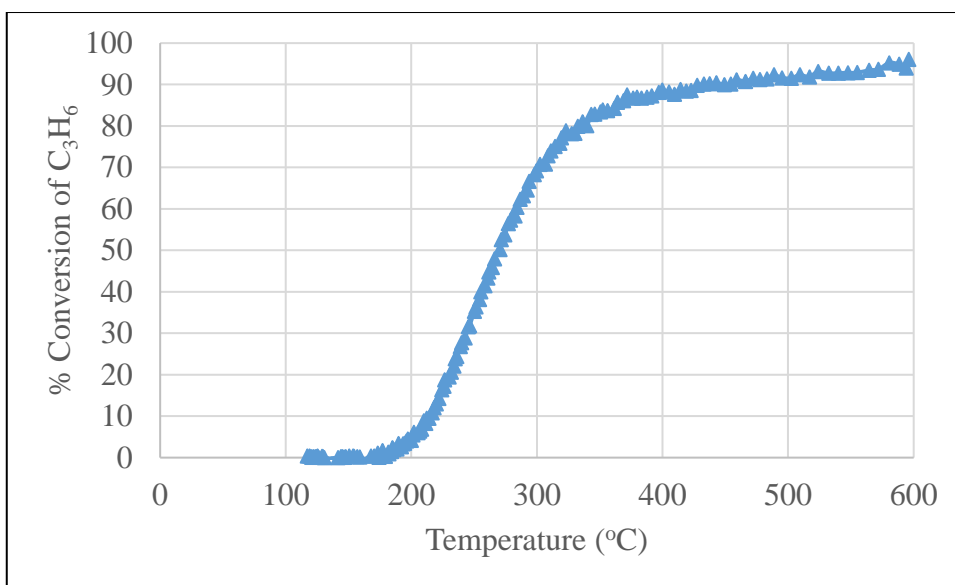


Figure G. 42.  $C_3H_6$  Conversion performance of  $SO_2$  poisoned C1 Catalyst

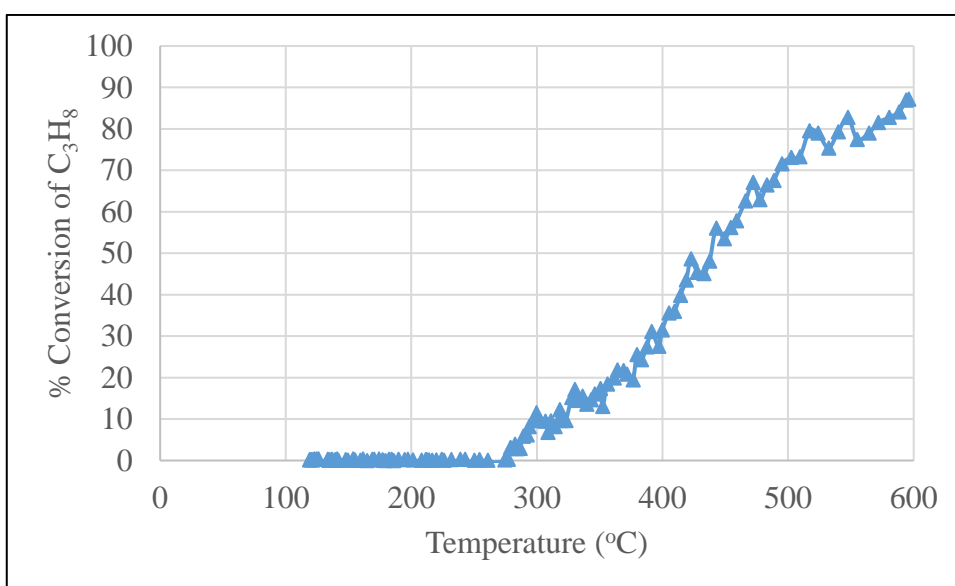


Figure G. 43.  $C_3H_8$  Conversion performance of  $SO_2$  poisoned C1 Catalyst

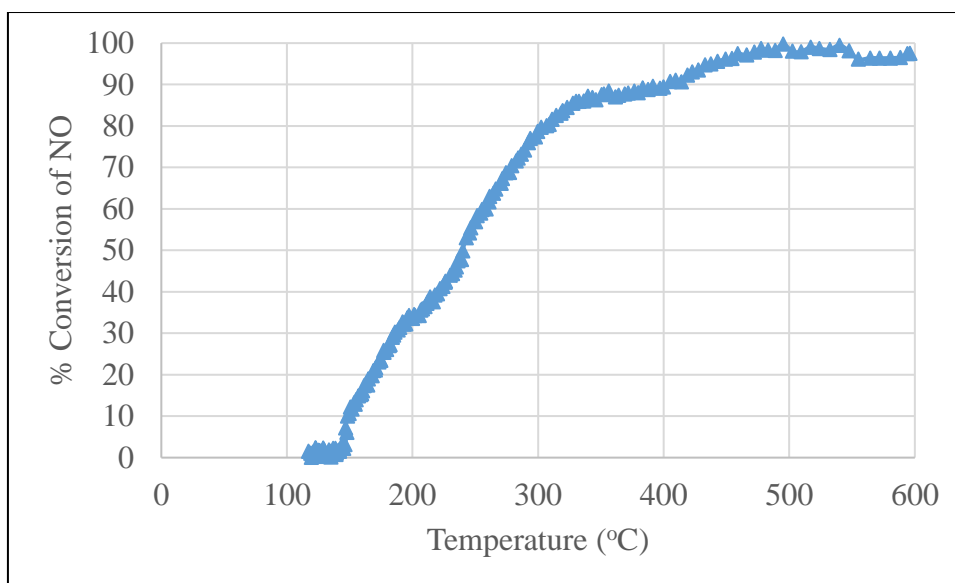


Figure G. 44. NO Conversion performance of SO<sub>2</sub> poisoned C1 Catalyst

### G.10 Performances Curves of SO<sub>2</sub> Poisoned C2 Catalyst

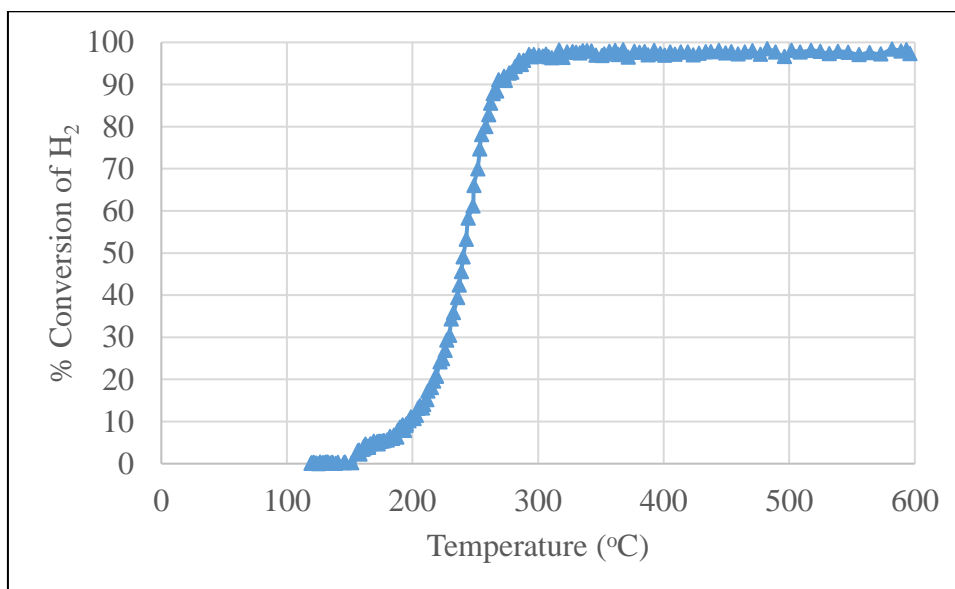


Figure G. 45. H<sub>2</sub> Conversion performance of SO<sub>2</sub> poisoned C2 Catalyst

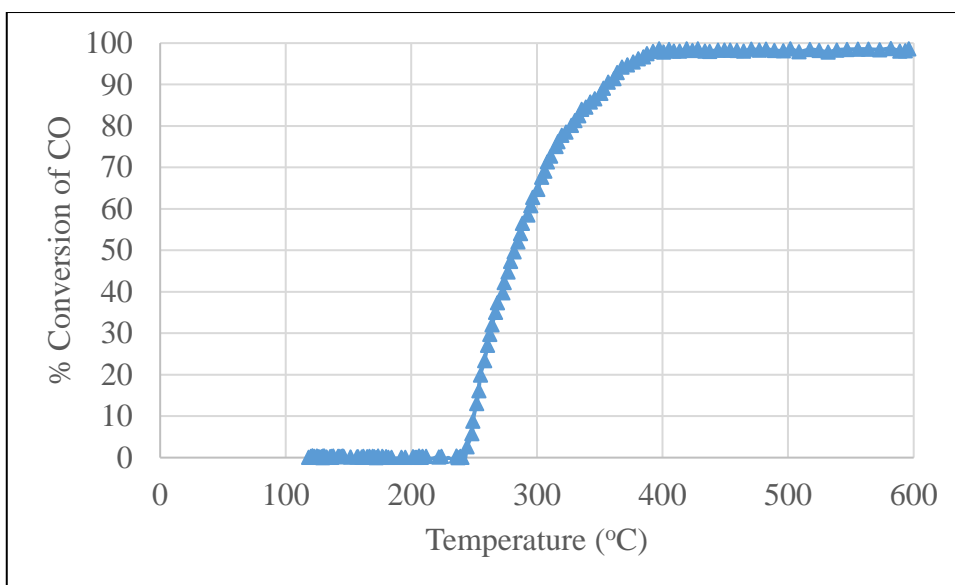


Figure G. 46. CO Conversion performance of SO<sub>2</sub> poisoned C<sub>2</sub> Catalyst

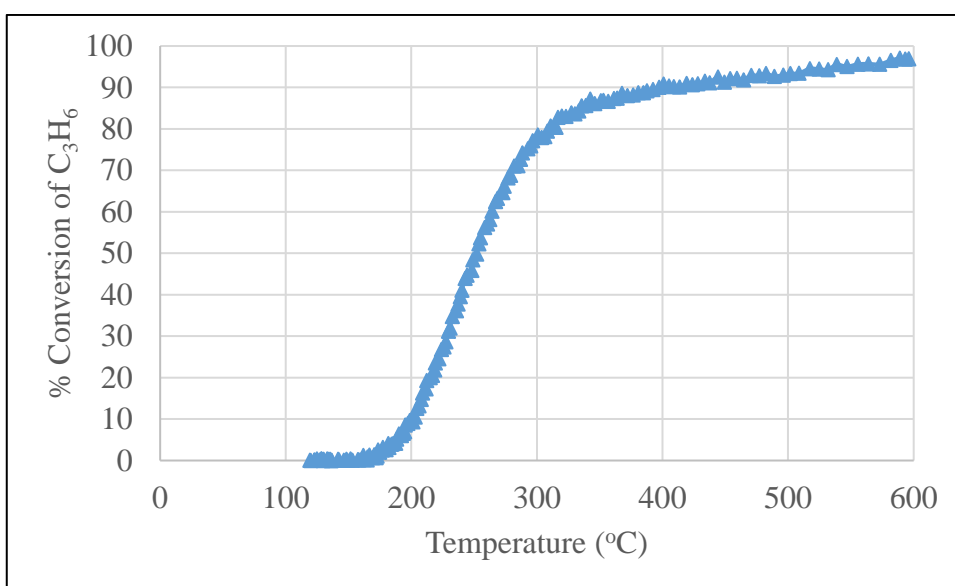


Figure G. 47. C<sub>3</sub>H<sub>6</sub> Conversion performance of SO<sub>2</sub> poisoned C<sub>2</sub> Catalyst



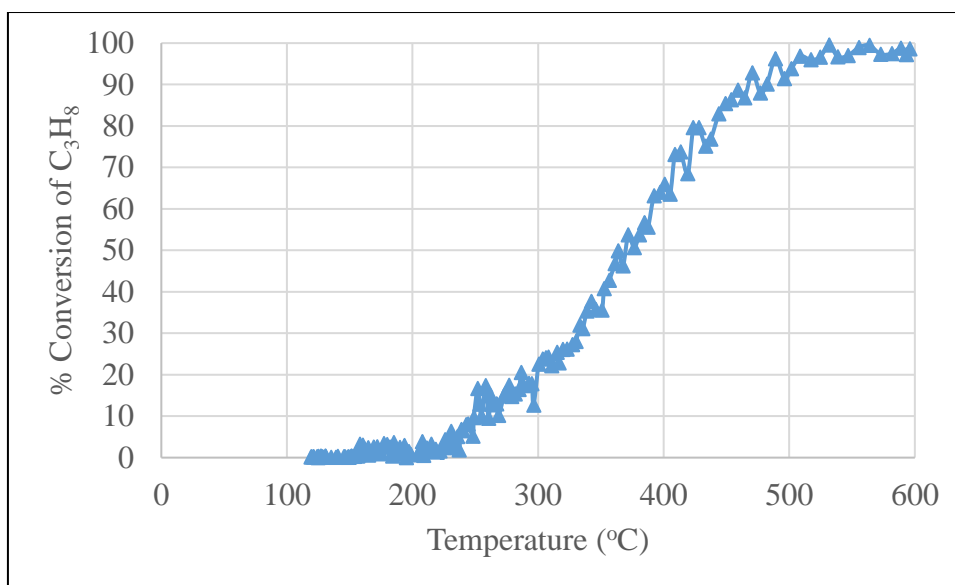


Figure G. 48. C<sub>3</sub>H<sub>8</sub> Conversion performance of SO<sub>2</sub> poisoned C2 Catalyst

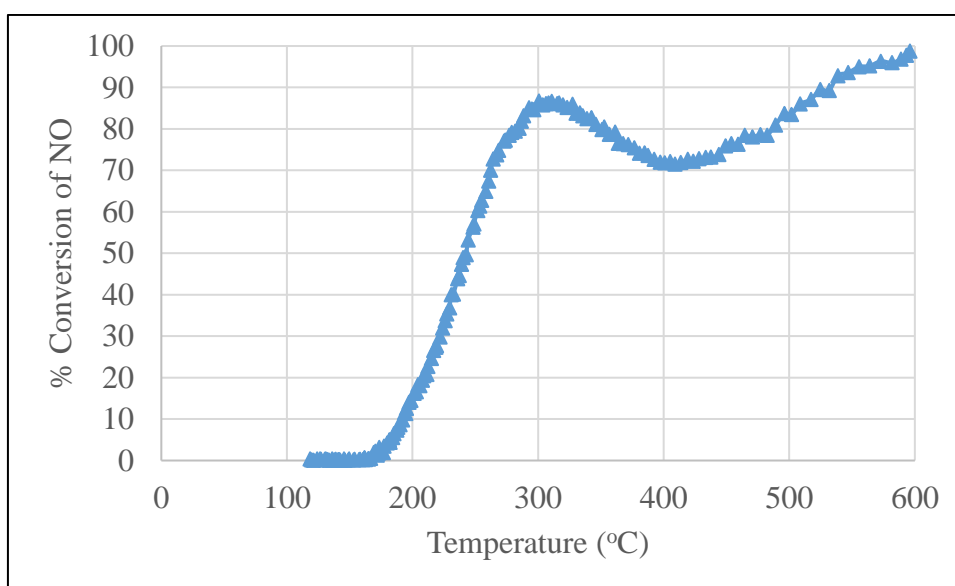


Figure G. 49. NO Conversion performance of SO<sub>2</sub> poisoned C2 Catalyst

### G.11 Performances Curves of SO<sub>2</sub> Poisoned C3 Catalyst

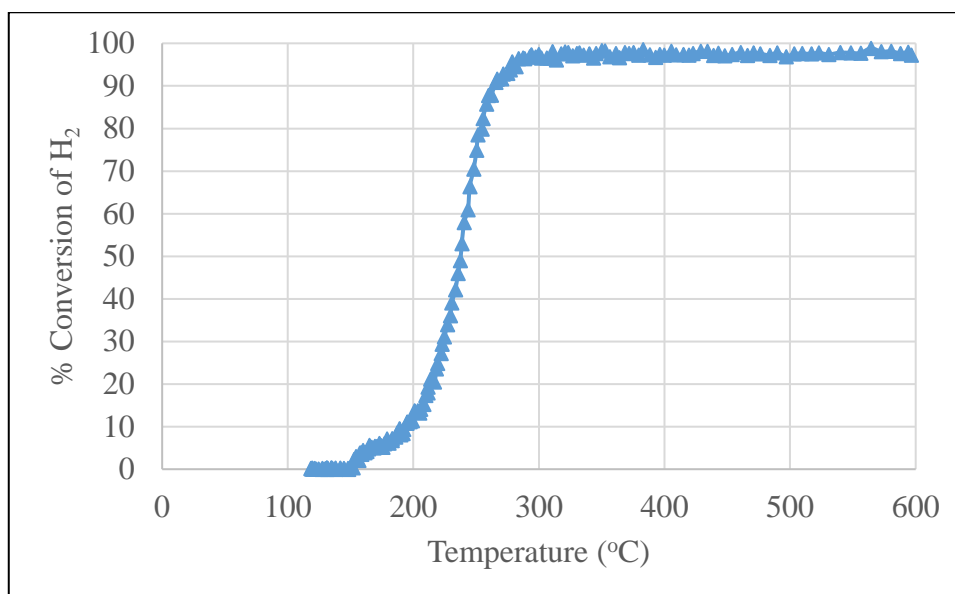


Figure G. 50. H<sub>2</sub> Conversion performance of SO<sub>2</sub> poisoned C3 Catalyst

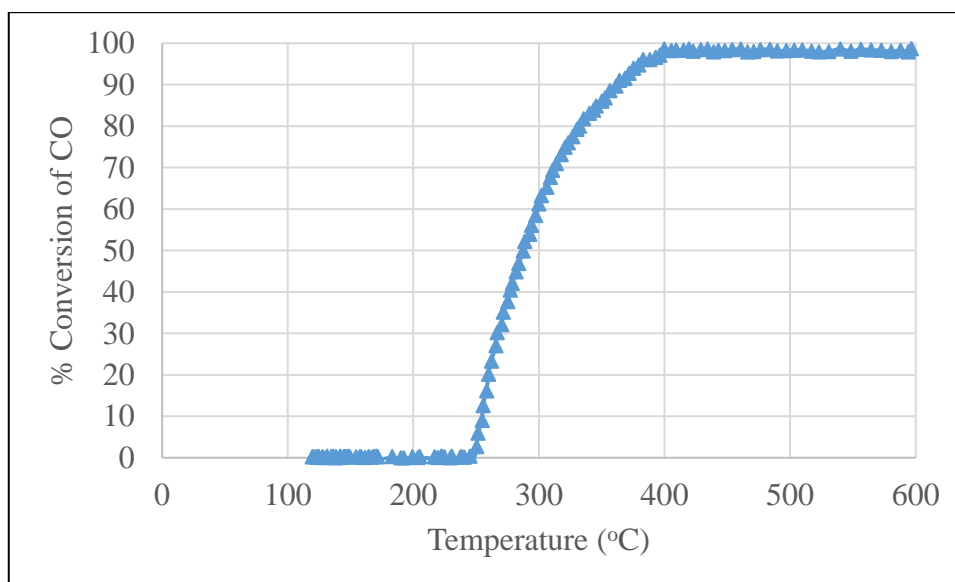


Figure G. 51. CO Conversion performance of SO<sub>2</sub> poisoned C3 Catalyst

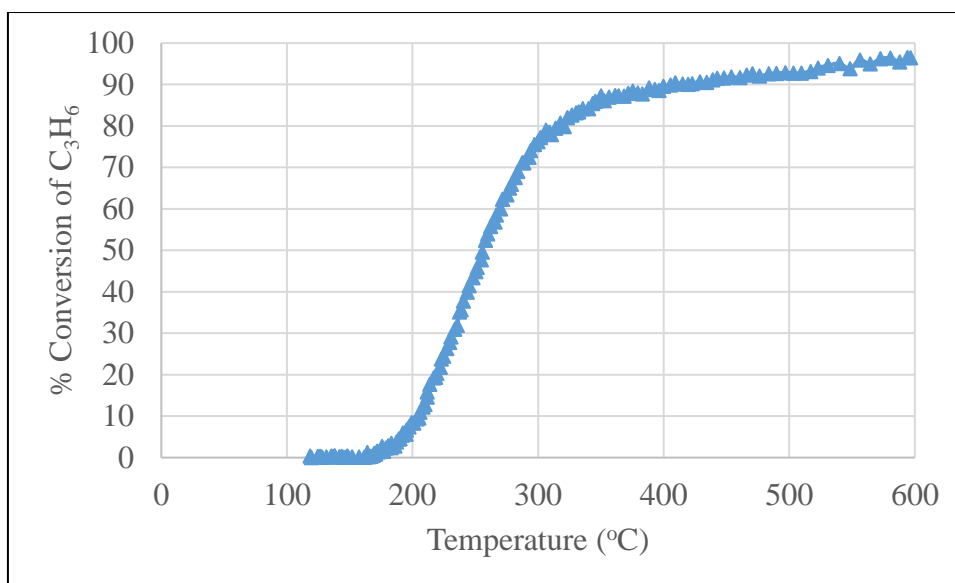


Figure G. 52. C<sub>3</sub>H<sub>6</sub> Conversion performance of SO<sub>2</sub> poisoned C3 Catalyst

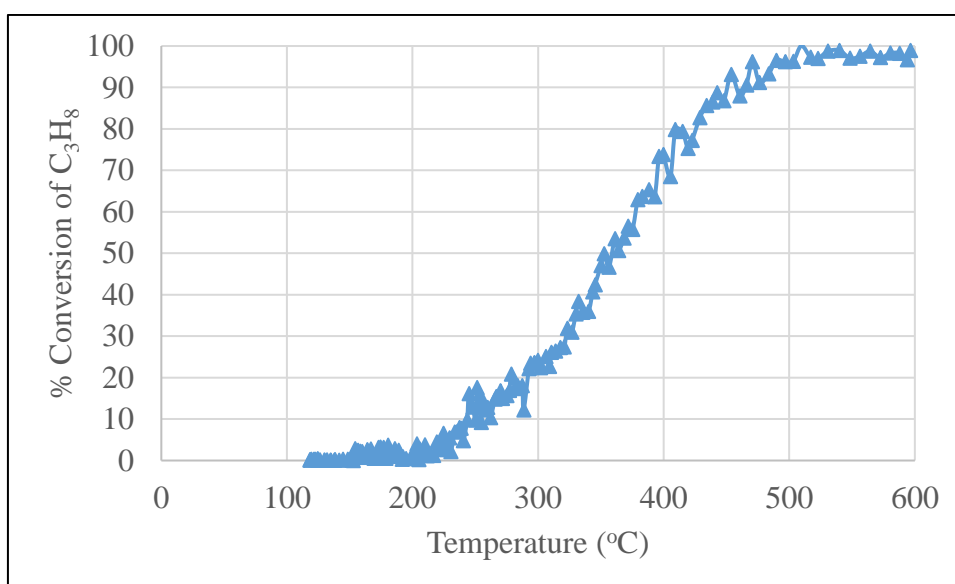


Figure G. 53. C<sub>3</sub>H<sub>8</sub> Conversion performance of SO<sub>2</sub> poisoned C3 Catalyst

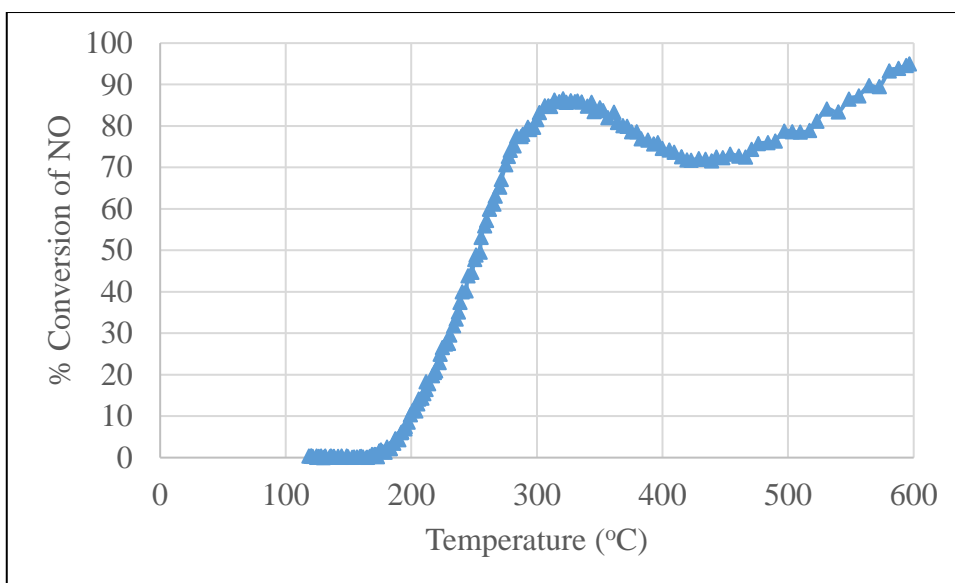


Figure G. 54. NO Conversion performance of SO<sub>2</sub> poisoned C3 Catalyst

**G.12 Performances Curves of SO<sub>2</sub> Poisoned C4 Catalyst**

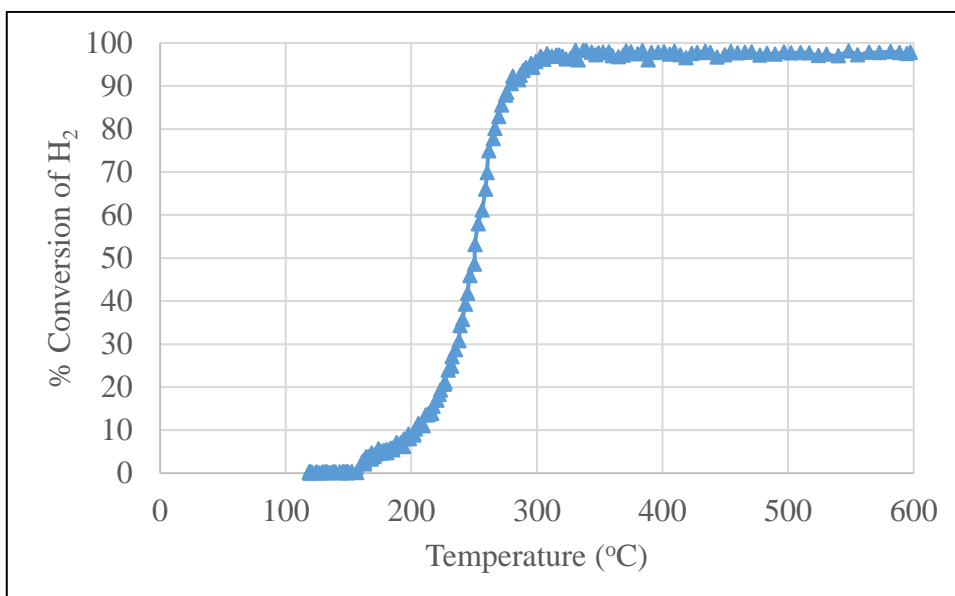


Figure G. 55. H<sub>2</sub> Conversion performance of SO<sub>2</sub> poisoned C4 Catalyst

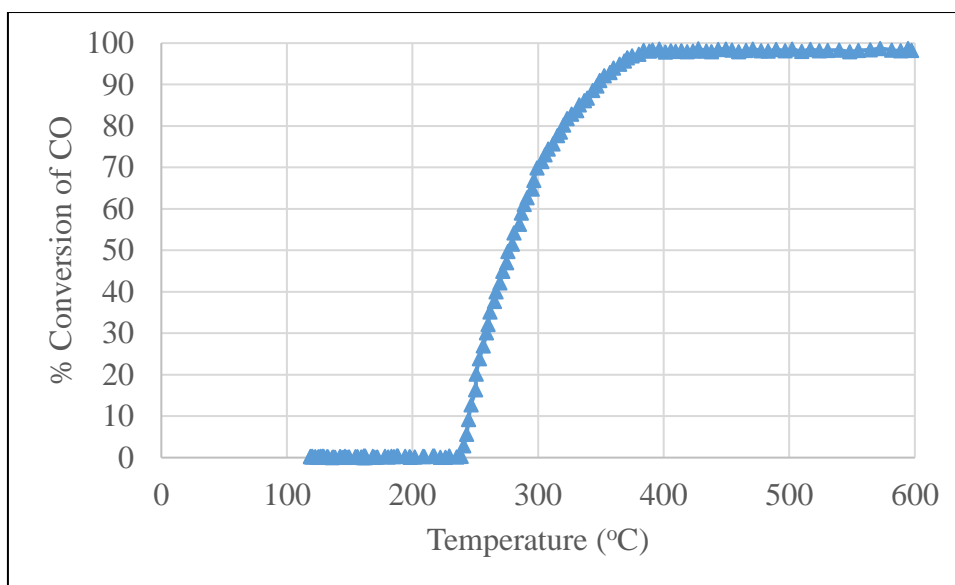


Figure G. 56. CO Conversion performance of SO<sub>2</sub> poisoned C4 Catalyst

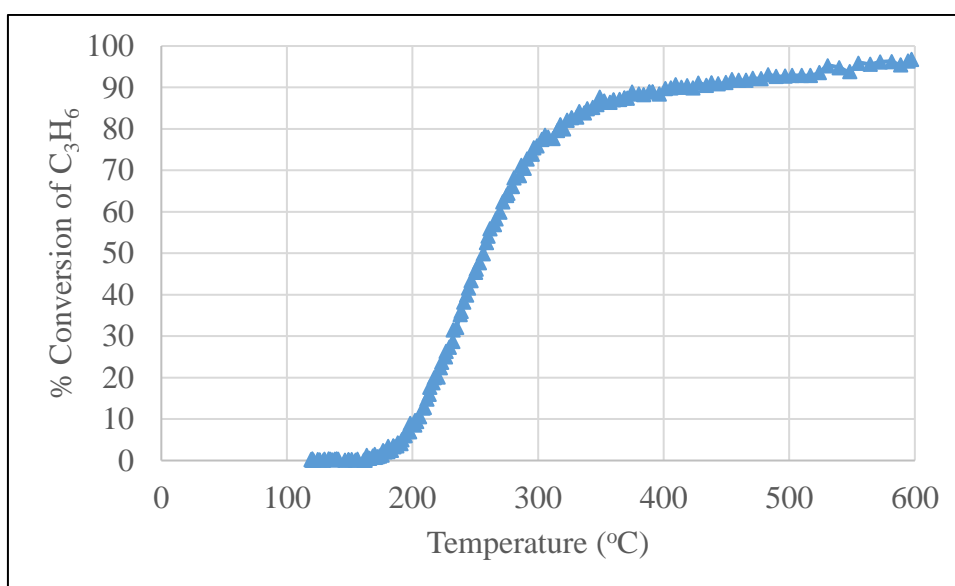


Figure G. 57. C<sub>3</sub>H<sub>6</sub> Conversion performance of SO<sub>2</sub> poisoned C4 Catalyst

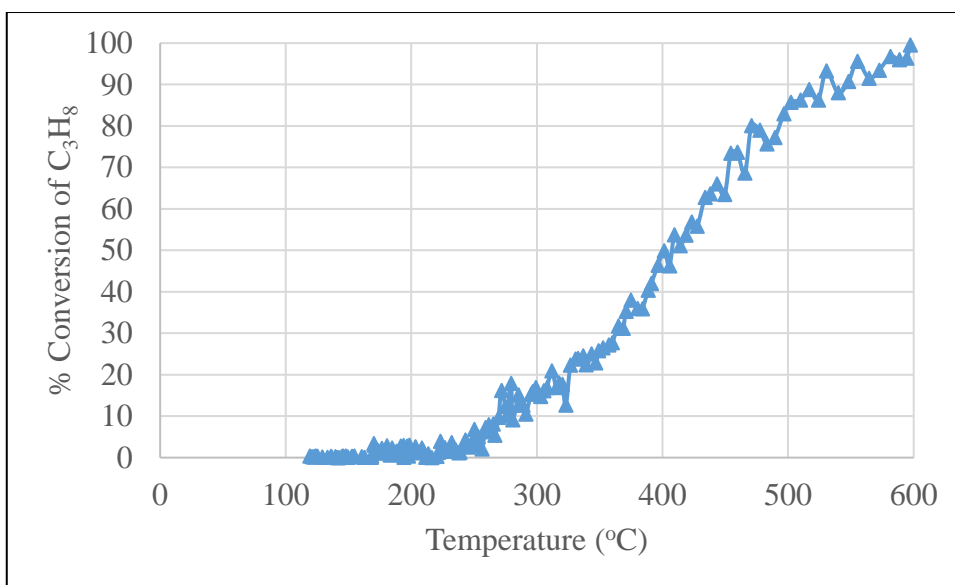


Figure G. 58. C<sub>3</sub>H<sub>8</sub> Conversion performance of SO<sub>2</sub> poisoned C4 Catalyst

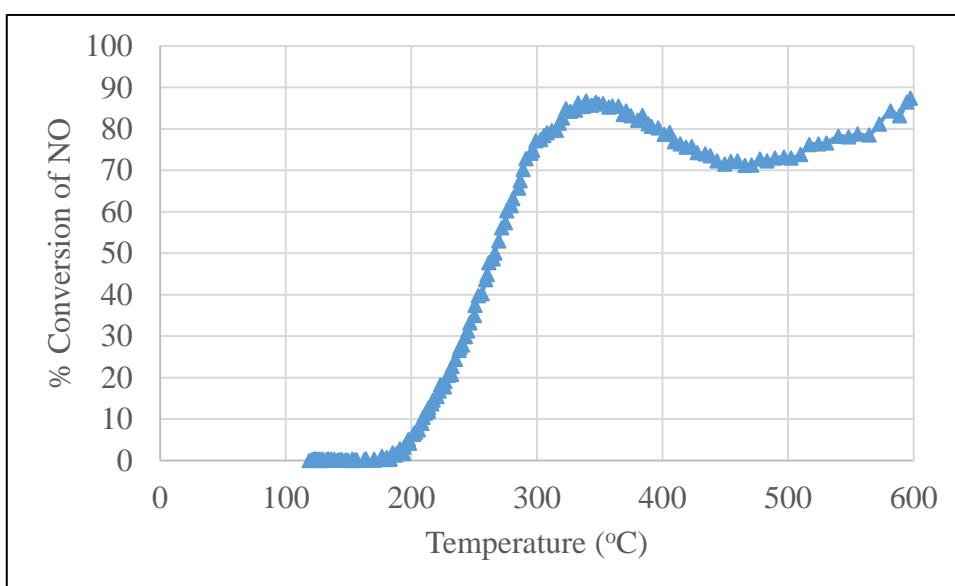


Figure G. 59. NO Conversion performance of SO<sub>2</sub> poisoned C4 Catalyst

## CURRICULUM VITAE

### PERSONAL INFORMATION

Surname, Name: Bayram, Bilal

### EDUCATION

<b>Degree</b>	<b>Institution</b>	<b>Year of Graduation</b>
MS	METU Chemical Engineering	2009
BS	METU Chemical Engineering	2006
High School	İncirlik High School, Adana	2001